Modeling of solar collector fields for solar heating plants in district heating systems

Federico Bava

PhD Thesis

Department of Civil Engineering
2017

DTU Civil Engineering Report R-365

DTU Civil Engineering
Department of Civil Engineering

Modeling of solar collector fields for solar heating plants in district heating systems

Federico Bava

PhD Thesis

06/06/2017

TECHNICAL UNIVERSITY OF DENMARK
DTU BYG

Supervisors:
Simon Furbo, Associate Professor, DTU Civil Engineering, Denmark
Jianhua Fan, Associate Professor, DTU Civil Engineering, Denmark
Jesper Tange, R&D Manager, Arcon Sunmark A/S, Denmark

Assessment Committee:
Toke Rammer Nielsen, Associate Professor, DTU Civil Engineering, Denmark
Björn Olof Harry Karlsson, Professor, Mälardalen University, Sweden
Jørgen Schultz, Senior Sustainability Consultant, Steensen Varming ApS, Denmark

Modeling of solar collector fields for solar heating plants in district heating systems

Publisher: Department of Civil Engineering,
Technical University of Denmark,
Brovej, building 118
2800 Kgs. Lyngby, Denmark

ISBN: 9788778774590
ISSN: 1601-2917
Report: BYG R-365

Preface

This thesis is submitted as fulfillment of the requirements for the Degree of Doctor of Philosophy at the Technical University of Denmark, Department of Civil Engineering. The thesis is the result of three years of research on simulation and modeling of large solar collector fields for district heating applications.

This thesis consists of two parts. Part I of the thesis summarizes the main methods and results of the research, and provides a perspective for future development. Part II consists of a number of published and submitted journal and conference articles, which describe in more detail the research.

Paper I: *Comparative test of two large solar collectors for solar field application*, Bava F. and Furbo S., Proceedings of EuroSun 2014 Conference.

Paper II: *Simulation of a solar collector array consisting of two types of solar collectors, with and without convection barrier*, Bava F., Furbo S. and Perers B., Proceedings of International Conference on Solar Heating and Cooling for Buildings and Industry SHC 2014.

Paper III: *A numerical model for pressure drop and flow distribution in a solar collector with U-connected absorber pipes*, Bava F. and Furbo S., Solar Energy 134 (2016) 264–272.

Paper IV: *A numerical model to evaluate the flow distribution in a large solar collector field,* Bava F., Dragsted J. and Furbo S., Solar Energy 143 (2017) 31–42.

Paper V: *A numerical model to evaluate the flow distribution in large solar collector fields in different operating conditions*, Bava F., Dragsted J. and Furbo S., Proceedings of EuroSun 2016 Conference.

Paper VI: *Development and validation of a detailed TRNSYS-Matlab model for large solar collector fields for district heating applications*, Bava F. and Furbo S., Energy 135C (2017) 698-708.

Paper VII: *Impact of different improvement measures on the thermal performance of a solar collector field for district heating*, Bava F. and Furbo S., currently under review at *Energy* journal.

To my father,

everything good I accomplish is because you taught me,
any mistake I make is because I did not listen enough.

Acknowledgments

I am most grateful to Simon Furbo and Jianhua Fan for always being available and open for supervision and scientific discussion.

I would like to thank the entire Solar Group at the Department of Civil Engineering at the Technical University of Denmark for the constructive talks and meetings.

I am also thankful to the technical personnel of the Department, especially to Claus Aagaard and Martin Dandanell for helping me in building up experimental setups.

I would like to express my gratitude to the company Arcon-Sunmark A/S, in particular to the R&D Manager Jesper Tange and the former CEO Søren Elisiussen, for the availability in sharing the company's experience; Martin Poulsen, for being a precious reference during my external stay; Jan Birk, for the help with the experiments on the field; Martin Pejstrup, for replying to the way too many emails I sent; Mathias Brassøe, Dan Mathiasen and Niels Kjær, for the lunch breaks.

I would like to thank the company Høje Taastrup Fjernvarme, for granting me access to their collector field to carry out experiments and collect data.

I would like to thank the Marie-Curie Actions – Initial Training Network research program of the European Union which supported my PhD study and gave me the chance to meet all the amazing people of the SolNet-SHINE project.

Federico Bava

Kongens Lyngby, 6 June 2017.

Finally, I feel the need and obligation to say thanks to those people who in one way or another contributed to make these three years an unforgettable experience. To everyone their own responsibilities...

Pater, gratias tibi ago, cum vir sis qui fieri vellem.
Grazie Mamma, perché hai sempre messo noi prima di tutto.
Grazie Silvia, per il tuo coraggio e la tua pazienza.
Grazie Alberto, per il supporto IT nel corso degli anni.
Grazie zio Gianpaolo e zia Marisa, per la forza con cui vivete ogni giorno.
Tak Mark, fordi du har været min danske bror.
Tak Janne, fordi "I love you too!".
Tak Jonas, for den smittende latter og maratonløbet.
Thanks to the members of the Ghost House, permanent and passing by. In particular:
thanks Gaby, for the friend you have always been;
gracias Maria1 y Toni, por vuestra puerta siempre abierta;
gracias Maria2, por enseñarme la importancia del medio ambiente;
gracias Jorge, por "knock-knock-knockin' on heaven's doooor";
thanks Timi, for the shelter in the deepest need;
thanks Tivi, because "if you don't finish your PhD, I'll kick you!".
Grazie Claudio, per essere l'amico di una vita e quello di quartiere ...e per il trapano.
Grazie Nicolàs e Davìd, nonostante vederci tutti assieme sia ormai impossibile.
Grazie Edu, per il sangue versato assieme e per i ringraziamenti.
Grazie Fra, perché non mi hai mai pestato, nonostante avessi potuto.
Grazie Waz, per la tua testardaggine ad essere mio amico.
Grazie Dàvid e Cri, perché mi avreste invitato al Noma, se solo fosse stato aperto.
Gracias Eva, por haber hecho mi estancia en Aalborg mejor de lo que esperaba.
Gracias Meritxell, por los días en Barcelona y por la paella que ojalá comeré.
Grazie Manu, perché sei un bomber.
Thanks Nicolàs and Yoann, for all the PÁ-PÁMs across Europe, Korea and Japan.
Tak Christian, på trods af det første forfatterskab.
Thanks Kaya, for the pizza recipe, the jokes I seldom understood and the good talks.
Thanks to Nicola, Matteo, Paul, Christoph, Bastian and Antoine, for the unexpectedly many sunny afternoons spent playing beach volleyball.
Grazie Giògià, "pevché se non fai la tintavella da Nevone non sei nessuno!".
Grazie Betta, perché lo sai meglio di molti altri.
Grazie Romanina, per le chiacchierate corse al Ruffini e le diagnosi a distanza.
Grazie Lox ed Eli, perché prima o poi verrete a trovarmi a Copenhagen.
Grazie Ire, per essere più che la farmacista di quartiere, (forse) tuo malgrado.
Thanks Tian, for feeding me whenever hunger hit.
Thanks Kata, Katerina and Jitka, for the extra beds in Czech.
Grazie Bob, perché volevi essere citata nei ringraziamenti.
Thanks to the PhDs and PostDocs of the Section, for being another good reason not to have lunch in the canteen.
Tak til mine kammerater fra danske klasser, fordi I delte denne umulige udfordring, og modstod min dårlige udtale. Især tak til Amanda og Alejandro.
Thanks Misha, for each kilometer we biked.

Abstract

Currently Denmark represents a unique example for a mature and commercial market for large solar collector fields supplying district heating systems. The country hosted 77 % of the collector area installed in Europe for this type of applications at the end of 2015. The year 2016 saw a further growth, with 31 new solar heating plants and 5 plant extensions, which totaled 495,000 m^2 of solar collectors. Among these new plants, it is worth mentioning the world's largest solar collector field put in operation in Silkeborg, with a collector area of 156,000 m^2. This development is expected to continue in the next future.

In a scenario where both the number and the size of solar heating plants increase, even small performance improvements in relative terms can lead to a large increase in the overall energy production in absolute terms. For this reason it is relevant to identify the operating conditions, the collector field layouts and the plant control strategies that give the best performance. If correct sizing, control strategy and design improvements can be evaluated in advance and implemented already in the planning phase, later and more expensive interventions can be avoided. Hence it is important to be able to predict the behavior and thermal performance of these installations in an accurate way. This can be done through detailed simulation models.

However, in most simulation models the solar collector field is treated with little detail, usually simplifying it with a single collector having as aperture area the area of the entire collector field. Another simplification is to assume that the collector efficiency is independent of the operating conditions at which the collectors operate.

Two flat plate collectors for collector field applications were tested in different operating conditions of flow rate and tilt angle. The only difference between the two collectors was a polymer foil interposed between absorber and glass cover in one of them, acting as a convection barrier. The experimental results showed that a change in flow regime in the absorber pipes was the main factor affecting the collector efficiency, with variations up to 4 %. Simulation models were developed and validated, to estimate this effect for collectors which could not be experimentally tested in a variety of operating conditions. Additionally, a new collector model, able to account for flow regime-dependent collector efficiency, was developed within the software TRNSYS.

To consider the flow distribution in a solar collector array, two different numerical models were developed in Matlab. The first consisted of a hydraulic model for calculating the pressure drop and flow distribution in a harp collector with U-type configuration, as those usually installed in solar collector fields in Denmark. The results showed that turbulent flow made the flow distribution more uniform compared to laminar flow. The second model treated flow distribution in solar collector arrays. The simulation results showed that it was possible to achieve uniform flow distribution by installing balancing valves, regardless of the operating conditions and layout of the collector array. In case of regular layouts and moderate number of collector rows, balancing valves were not strictly necessary. Both hydraulic models were validated against measurements or data from literature.

Finally, a detailed simulation model for an entire solar heating plant, making use of the above mentioned models, was developed in TRNSYS. The successful validation of the model highlighted the priority of accurate measurements and inputs when dealing with simulation. Special attention should be given to solar radiation sensors, heat exchangers and collector efficiency.

The simulation results showed that differences between actual operating conditions and inputs to control strategy can significantly penalize the performance of the plant. Hence aspects such as shadows from row to row and incidence angle modifier should be considered. If accurate input to the control strategy is not economically feasible, a feedback control on the field outlet temperature could be a valid alternative and simultaneously make the control more robust. On the other hand, weather forecast-based controls seemed not to offer significant advantages, compared to the additional investment cost and the more complex control they required. Regarding the solar collector fluid, a glycol concentration able to prevent or limit to a minimum the use of frost protection operation in the solar collector loop gave better results than lower concentrations, as the higher frost protection guaranteed by the former outweighed the better thermophysical properties of the latter. For Danish weather conditions, a 35 % propylene glycol/water mixture seemed to be the more appropriate solution among the tested fluids.

Table of Contents

List of Figures

List of Tables

Nomenclature

A	Collector area	$[\mathrm{m}^2]$
a_1	Heat loss coefficient at $(T_m - T_{amb}) = 0$	$[\mathrm{W/(m^2\,K)}]$
a_2	Temperature dependence of the heat loss coefficient	$[\mathrm{W/(m^2\,K^2)}]$
c_p	Specific heat	$[\mathrm{J/(kg\,K)}]$
E_{DH}	Energy delivered to the DH network	[MWh]
$E_{DH,w}$	Energy to the DH network, weighted on the temperature difference $\Delta T_{s\text{-}DH}$	[MWh]
E_{el}	Electricity consumption	[MWh]
E_{frost}	Energy from DH to collector field for frost protection	[MWh]
G	Total solar irradiance on the collector plane	$[\mathrm{W/m^2}]$
K_θ	Incidence angle modifier	$[-]$
$\dot{m}$	Mass flow rate	[kg/s]
N	Number of collector rows	$[-]$
Q_{sol}	Theoretical power output from the solar collector field	[W]
Re	Reynolds number	$[-]$
T	Temperature	[°C]
T_{amb}	Ambient temperature	[°C]
T_m	Mean temperature	[°C]
T_{in}	Inlet temperature of the solar collector fluid	[°C]
T_{out}	Outlet temperature of the solar collector fluid	[°C]
$T_{setpoint}$	Set point outlet temperature for the collector field	[°C]
V	Volume flow rate	$[\mathrm{m^3/h}]$
V'	Dimensionless volume flow rate	$[-]$

Greek symbols

Δp	Pressure difference	[Pa]
$\Delta T_{s\text{-}DH}$	Difference between DH supply temperature and temperature of the fluid supplied from the solar heating plant to the DH network	[K]
η	Collector efficiency	$[-]$
η_0	Peak collector efficiency	$[-]$

Acronyms

CHP	Combined heat and power (plant)
DH	District heating
FEP	Fluorinated ethylene propylene
IAM	Incidence angle modifier
MLR	Multiple linear regression
RMSD	Root-mean-square deviation

Part I

Introduction and summary

"A model must be wrong, in some respects,
else it would be the thing itself.
The trick is to see where it is right."
— Henry A. Bent

Chapter 1

Introduction

1.1 The threat of climate change

The correlation between CO_2-emissions and climate change, with all the risks that the latter entails, has been acknowledged by most countries and by the vast majority of the scientific community. In this respect, a preliminary international treaty was reached at the United Nations Conference on Environment and Development in Rio de Janerio in 1992 [1]. This treaty, the United Nations Framework Convention on Climate Change (UNFCCC), set the goal of stabilizing greenhouse gas concentrations *at a level that would prevent dangerous anthropogenic interference with the climate system*. The agreement led to the signature of the Kyoto Protocol [2] in 1998, where precise goals for the reduction of greenhouse gases were set for the subscribing countries. More recently, the Paris Agreement [3], currently ratified by 118 of the 197 Parties to UNFCCC, brought back the attention on the urgent necessity of reducing significantly carbon emissions, to avoid irreversible climate change and extreme weather events.

Besides the will and need of reducing the effects of climate change, other reasons, such as depletion of limited natural resources, environmental protection, energy independence from politically unstable countries, long-term economics, push toward a phase-out of fossil fuels.

Nowadays, 86 % of the primary energy consumption worldwide is based on fossil fuels [4]. Hence, it is reasonable to assume that a radical change of the energy sector cannot rely on a single technology, but will require the smart interaction of a variety of different measures, technologies and energy sources.

1.2 District heating in Europe

The final energy consumption in the EU-28 in 2014 was about 1100 million tonnes of oil equivalent (corresponding to 46 EJ) [5]. This amount have been roughly stable since the '90s and is expected to remain such also in the next years. Figure 1.1 shows how the final energy consumption is distributed among the different sectors.

Buildings account approximately for 40 % of total final energy consumption and around 55 % of electricity consumption in the EU-28 [6]. So, buildings are the largest end-use sector, followed by transport, industry and agriculture. Residential buildings represent around two thirds of the consumption of buildings [6].

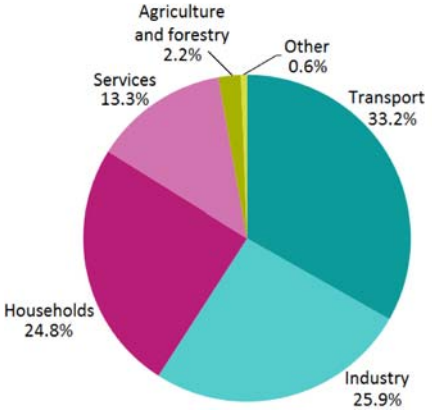

Figure 1.1: Final energy consumption breakdown into sectors in EU-28, 2014 [5].

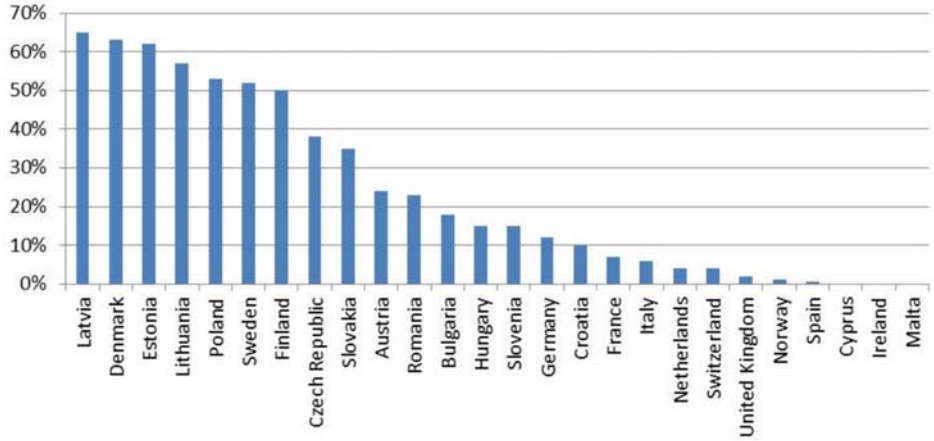

Figure 1.2: Share of the population served by district heating in 2013 [8].

Approximately 80 % of the energy demand of European residential buildings is used for space heating and domestic hot water preparation [6]. An efficient way to provide heat to buildings in densely populated areas is through district heating (DH). A DH network is an expensive infrastructure to build, but the resulting energy savings justify the investment cost. The network is usually supplied by one or more centralized plants, which have a higher efficiency than individual boilers. Secondly, a wider variety of fuels, including municipal solid waste, can be used to generate the heat supplying the network. Additionally, the economies of scale of these large plants allow more sophisticated and efficient emission reduction systems to be installed. The spread of DH in Europe varies significantly from country to country, with shares as high as 60 % in Scandinavian and Baltic countries. Figure 1.2 shows the percentage of the population served by DH in different European countries. On average, only 13 % of the residential and service sector heat market is covered by DH [7].

As space heating and domestic hot water preparation require relatively low temperatures, solar thermal collectors seem to be a perfect candidate to cover this demand in a sustainable and efficient way. It is not uncommon to see solar collectors installed on the roof of single-family houses.

Although these two technologies are not new, their integration, i.e. solar collector

Figure 1.3: Silkeborg solar collector field (source: Arcon-Sunmark A/S).

fields supplying DH networks, is relatively recent and still rare, except for a few countries. In fact, solar thermal plants for DH applications represented less than 1 % of the total installed water collector capacity at the end of 2014 [9]. Of the approximately 5000 DH networks currently in operation in Europe only about 150 are solar assisted DH systems [10]. This situation may change in the future, as the European Union has set a target of 1 % solar fraction in DH by 2020 and of 5 % by 2050 [11].

1.3 Solar district heating in Denmark

1.3.1 Background

Although the first collector fields for DH applications in Denmark date back to the late '80s, it was from 2006 that the market of solar heating plants for DH started to grow significantly. This was encouraged by the increasingly cheaper solar heating technology, which became a more viable alternative to the highly taxed natural gas.

Nowadays, Denmark is a unique example for a mature and commercial market for solar DH. The country is leader in this sector, with 77 % of the collector area installed in European large solar heating plants at the end of 2015 [9]. At the end of 2016, Denmark had installed more than $1,300,000\,m^2$ of collectors and had 104 plants in operation [12]. Among these, it is worth mentioning the world's largest solar collector field put in operation at the end of 2016 in Silkeborg with a collector area of $156,000\,m^2$ [13] (see Figure 1.3).

Several factors have contributed to the strong development of this technology in the Scandinavian country [14]:

- long time tradition and widespread use of DH,
- ambitious Danish plan on phasing out fossil fuels,

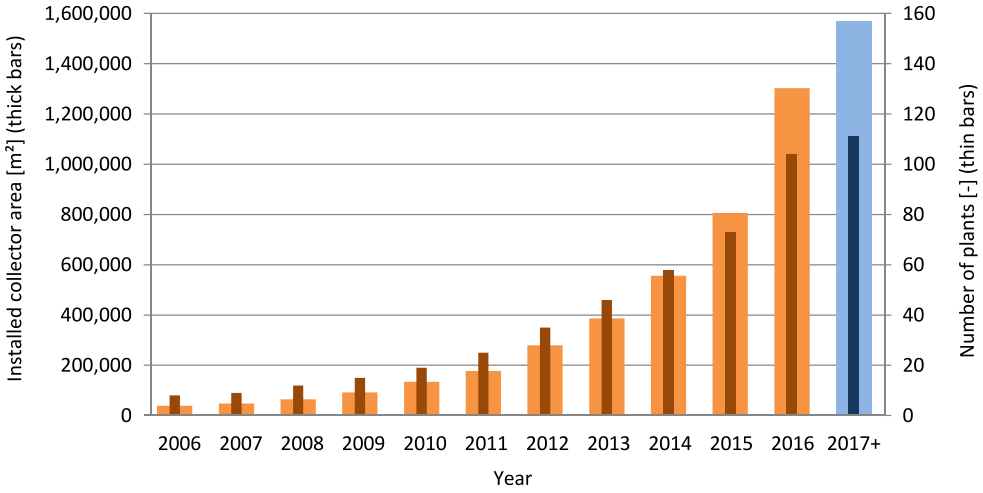

Figure 1.4: Historical development of solar collector fields for DH applications in Denmark: installed collector area and number of operating (orange) and upcoming (blue) plants at the end of 2016 [12].

- high taxation on fossil fuels,
- low price and high performance of the collector fields,
- competitive heat production price,
- interaction with liberal electricity market.

The above mentioned reasons of the success of solar DH in Denmark are discussed in more detail in Sections 1.3.1.1–1.3.1.5.

Despite the impressive growth in recent years, as shown in Figure 1.4, large-scale collector fields still provide a minor contribution to the overall DH demand. In 2015, of the 127 PJ produced by DH plants, solar energy produced little more than 0.8 PJ, representing 0.7 % of the total gross production [15]. Considering the newly installed capacity of solar collector fields since 2015 (Figure 1.4), it can be estimated that solar thermal energy will increase its contribution to DH by about 2.3 times in 2017 compared to 2015.

Typical solar DH systems have a yearly solar fraction of 15–20 % [16]. This is generally the value reached by a system, where the solar collector field has been sized to cover the DH heat demand in summer, so that almost no auxiliary energy is needed in this season. A short-term heat storage (usually a steel tank) provides sufficient flexibility to match the hourly/daily oscillations of demand and supply. Higher solar fractions can be reached, but this requires the installation of a seasonal heat storage, usually in the form of a water pit. The storage is charged in summer, when excess solar heat is produced, and discharged later on during the autumn and winter months. Examples of plants equipped with water pit seasonal heat stores are Dronninglund ($60,000\,m^3$), Marstal ($75,000\,m^3$), Gram ($120,000\,m^3$) and Vojens ($200,000\,m^3$, Figure 1.5). A borehole seasonal storage of $19,000\,m^3$ is installed in Brædstrup DH plant [17].

Figure 1.5: Vojens solar collector field with the water pit seasonal storage under construction (source: Arcon-Sunmark A/S).

1.3.1.1 Long tradition in district heating

The presence of a DH network is a necessary prerequisite for the installation of a large solar collector field, which can use the network as heat sink.

The history of DH in Denmark goes back to the '20s and '30s, when the first DH systems were developed based on waste heat from local electricity production [18]. Since then, DH expanded considerably and by the '70s approximately 30 % of the Danish houses were connected to DH networks [18].

Until 1979, no specific law regulating the heating supply existed in Denmark and most consumers had small oil-fired boilers or other forms of individual heating. Deeply affected by the international oil crises in the '70s and in order to secure a market for the natural gas which had been recently discovered in the North Sea, Denmark introduced its first *law on heating supply* in 1979. The goal of the law was to improve the energy security by reducing the dependency on imported oil and introducing the concept of public heating planning. Each municipality was required to provide information about the present status of the existing heating supply method and options for future heating supply. Based on the collected information, the country was divided in zones, supplied either by DH or by natural gas. The possibility of utilizing surplus heat from cogeneration power plants led to the *cogeneration agreement* in 1986, which made small-scale CHP plants a major energy policy priority. Simultaneously, electric heating was banned, although new low energy buildings are still exempt [18].

A revised law on heating supply in 1990 promoted the conversion of existing coal- and gas-fired DH plants to CHP plants, and the increased use of biomass and biofuels. Besides the conversions of existing plants, new CHP plants were built to supply new DH networks installed in a number of larger villages, the so called *green-field plants*. Policy and financial subsidies supported the use of biomass. The *Biomass Agreement* in 1993 set the requirement of 1.2 million tons of straw and 0.2 million tons of wood

chips to be used annually in power plants by the end of 2000 [18].

Nowadays, DH supplies more than 60 % of all private Danish buildings [18]. An important role in the integration of solar energy into the Danish DH networks has been played by the relatively low temperatures at which the networks are operated. Forward temperatures are usually in the range 70−80 °C, while return temperatures are around 35−45 °C [16]. The low temperatures improve the efficiency of the solar collectors, making the integration of solar heating plants into DH systems even more appealing and cost-effective.

Currently, two thirds of the DH demand is covered by 55 municipally owned utilities, while the remaining part is covered by 340 consumer owned cooperatives [19]. Regardless of the ownership, DH companies must be non-profit. Consequently, customers pay only for the heat and there is no reason for keeping good and innovative ideas in-house, which means that these are often replicated by other DH companies. In general, there is a close cooperation and strong exchange of information and experiences among the DH companies, which gather in the Danish District Heating Association [19].

1.3.1.2 Danish energy policy

Denmark is currently the EU-28 country with the lowest level of energy intensity, i.e. units of gross energy consumption per unit of gross domestic product [5], and has one of the highest shares of renewable energy covering the national energy consumption. In 2015, renewable energy sources represented 30 % of the total energy consumption and 65 % of the gross electricity production. The main contribution came from biomass and waste (67 % of the total renewable energy production), while wind energy represented 49 % of the gross electricity production [15]. Compared to 1990 levels, the adjusted greenhouse gas emissions decreased by 30 % [20].

However, Denmark has set even more ambitious goals. In March 2012 the Danish government drew up an energy agreement with the large majority of the Parliament with the aim to completely rid use of fossil fuels by 2050 [21]. In November 2016 a new government broadly reconfirmed the goal, but stressing that this transition had to be cost-effective, contributing to growth and employment, without unnecessarily high costs for the society [22]. An intermediate milestone has been set for 2030, when half of the energy demand should be covered by renewable energies. A more detailed energy plan is expected to be released in autumn 2017 [22].

To achieve its ambitious goal, Denmark will act on several fronts. A key role will be played by more efficient energy consumption, with a special focus on the residential sector. Secondly, electrification will be strongly encouraged with new electricity transmission lines between Denmark and the neighboring countries, and investments will be made for the development of smart grids. Thirdly, renewable energies (biomass, wind, solar and wave energy) will be promoted for both electricity and heat production. Finally, investments in research, development and innovation will be made to improve existing technologies and to overcome challenges such as efficient energy storage, smart regulation of the electrical grid and green means of transportation [23].

Concerning heat production, the exact mix of the energy sources is not yet clearly defined, but the energy plan refers to district heating, heat pumps, biomass and solar thermal energy. A key role should be played by the reduction in heat demand from the buildings, which is estimated in about 30 %. Solar heating is expected to have a more

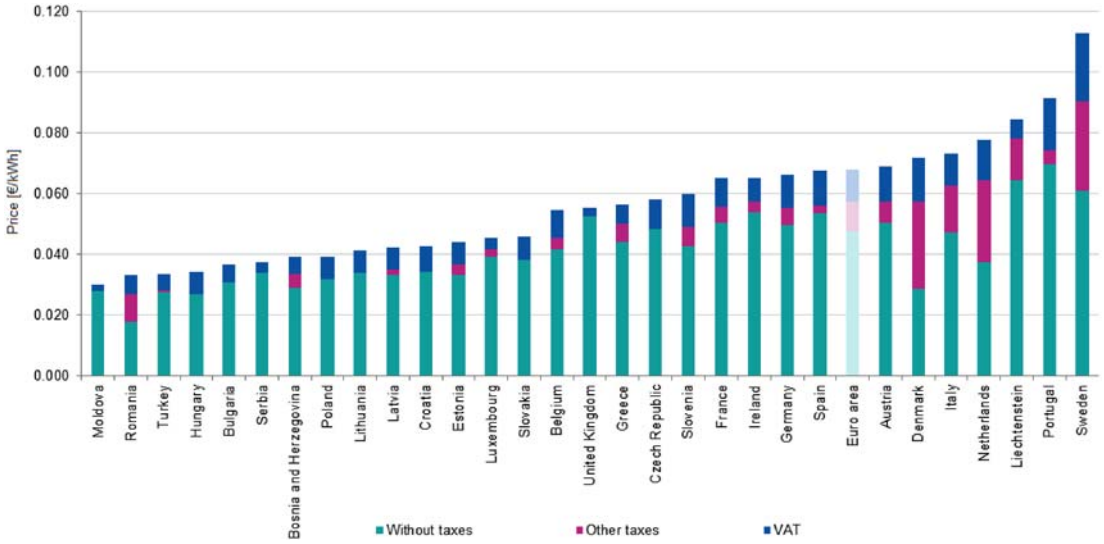

Figure 1.6: Natural gas prices for household consumers in 2016 (1st semester) [25].

relevant role in small district heating areas, while larger cities are more likely to attract waste-to-energy and biomass plants because of the scale advantage. Depending on the considered scenario among those assumed as more realistic, solar thermal should contribute between 7 % and 16 % to the overall DH demand in 2050, with a production between 8 PJ and 17 PJ respectively [24].

1.3.1.3 Taxation on fossil fuels

During the 1970s and '80s, taxes were applied to fuels used for heating generation with the intention to encourage the use of sustainable energy sources and efficient energy utilization. Therefore, biomass and biogas were exempted from taxes. When oil and gas prices dropped at the end of the '80s, the tax level was increased for these fuels [18]. This ensured that consumers continued to be motivated to use energy in a responsible way and prefer environmentally friendly energy sources.

Nowadays, natural gas is the main fossil fuel used for heating purposes. This is due to the large spread of CHP plants, many of which are gas-fired. Although still present in some DH plants, coal has been progressively decreasing, while oil gives a negligible contribution [15]. Natural gas is the most commonly used fossil fuel also in individual heating systems [15].

Figure 1.6 shows the natural gas prices for household consumers in different European countries. Despite being one of the countries with the lowest prices for natural gas before taxes, Denmark has traditionally applied such a high taxation on this fossil fuel, to make its final price for private consumers one of the highest in Europe.

Similar production prices and tax level are found for DH plants. In case of using natural gas in a CHP plant, this is taxed with an energy tax, a CO_2-tax, a NO_x-tax and a methane tax. Although the exact calculation is more complicated, this can be simplified saying that in 2016, when the natural gas had a price of about 0.32 €/m^3(see Figure 1.6), the total taxes on the this fossil fuel for CHP use were approximately 0.36 €/m^3. In case of a gas-fired boiler, the fuel was taxed with an energy tax, a CO_2-tax and a NO_x-tax. In this case, an added tax of 0.33 €/m^3 can be roughly estimated. Regardless of the

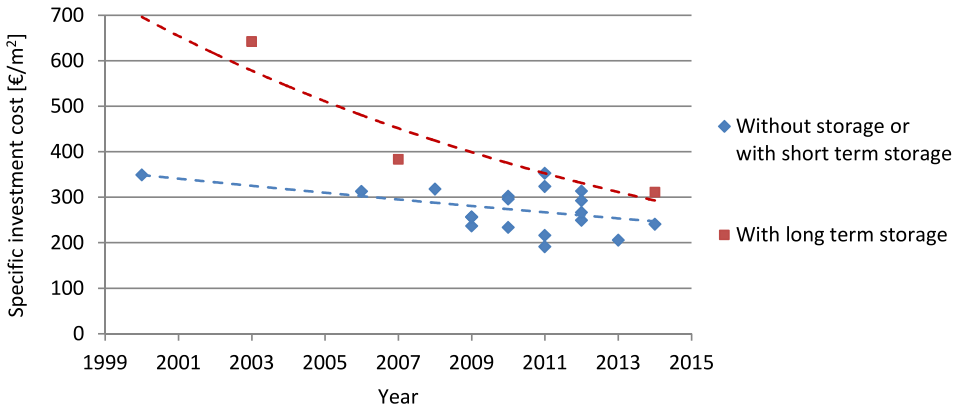

Figure 1.7: Historical evolution of the investment cost per unit area of solar collector in large-scale solar collector fields [28].

generation technology, it can be concluded that taxation on natural gas in Denmark makes this fossil fuel at least twice as expensive.

Indicative production prices for heating in 2015 can be estimated to be 0.063 €/kWh for a CHP plant and 0.059 €/kWh for a gas-fired boiler plant, based on price of natural gas of 0.28 €/m^3 [26].

1.3.1.4 High performance and low cost

Due to economies of scale, large collector fields are characterized by low specific cost. It is not only the low land price contributing to the good economics of these plants. Enhancements in the production and installation have progressively decreased the investment cost of these systems, with current prices ranging between 200 € and 300 € per square meter of collector for a turn-key system. Figure 1.7 shows the historical evolution of the investment cost per unit area of collector for large solar collector fields from 2000 to 2014. Also collector fields equipped with seasonal storage have seen a remarkable cost reduction, due to the improved know-how and to the larger storage volumes, which decrease the specific cost.

Another important factor in the economics of these installations is played by the type of ownership and financing which is usually adopted. The collector field is generally owned and operated by the DH company [27]. A loan guarantee is usually given by the local municipality, which has almost no risk in doing so, as consumers are bound to a contract obliging them to be customers of the DH company. The income for the DH company is secured and used to pay the loan [27]. With this guarantee and stable economic boundary conditions, low interest rates can be obtained, keeping low low the cost of the heat supplied by the collector field.

On the other hand, the performance of these installations is fairly high. Measured yearly thermal performances in the period 2012–2015 ranged between 313 kWh and 577 kWh per square meter of collector aperture area, with averages for all plants between 414 kWh/m^2 and 463 kWh/m^2 [29]. The efficiency of the collector fields, defined as the ratio between its yearly thermal performance and the solar radiation on the collector plane, was as high as 45−50 % for recently installed plants and down to 30 % for older ones.

The combination of high performance and low cost of large collector fields has led to very competitive heat production prices. On average, these installations produce heat at around 0.045 €/kWh, in some cases the price can be as low as 0.03 €/kWh [30, 31]. Comparing these values with the average production prices of gas-fired DH plants (see Section 1.3.1.3), it is easy to understand why many DH companies have opted for solar heating plants.

The Danish company Arcon-Sunmark A/S, one of the main manufacturers of large-scale solar collectors in the world, has played a key role in the strong development of this technology in Denmark, where they have installed the very vast majority of the large solar collector fields for DH applications. In recent years, the successful story of this technology has allowed the company to open new markets, not only in Europe, but also in the rest of the world.

1.3.1.5 Interaction with liberal electricity market

In 2015 wind energy represented 42 % of the national electricity supply [15] and its share is expected to increase further in the future. High shares of electricity production from an intermittent energy source as wind entail technological and economic challenges for the electrical grid. First of all, as electricity cannot be directly stored, mechanisms that can increase the flexibility and regulation capability of the grid are needed. These mechanisms must be able to absorb the excess electricity, when there is plenty of wind energy production, and vice versa ensure efficient power generation in case of little wind. Transmission lines already connect the Danish electrical grid to Sweden, Norway and Germany. So, when the wind electricity production is higher than the demand, the excess electricity is sold to the neighboring countries, to be instantaneously used or converted in potential energy and stored in the Norwegian water reservoirs. The reservoirs can be emptied later, to cover the higher electricity demand in peak hours. However, the transmission and accumulation capacity is limited.

Secondly, the need for power generation from thermal power plants and CHP plants decreases. So, the profit of CHP plants coming from the electricity market is reduced and this can increase the cost of the heat for DH. Because of their fast capacity regulation, CHP plants are expected to become more a backup and balancing mechanism, than the suppliers of the base load of the electrical grid. Hence, CHP plants would run only when the balance of the electrical grid and the electricity prices make their operation economically convenient. On the other hand, heating supply is required by the DH network throughout the year, also in summer for domestic hot water preparation. The need to cover the heat demand may force a CHP plant to operate, even when the electricity prices and/or the operation mode which the plant must operate at makes its operation expensive and not very efficient.

In this scenario, a solar thermal plant can play an important role. This plant provides very cheap heat, regardless of the electricity price. When equipped with a short-term storage, the plant can cover most of the heat demand during the summer season, so that the CHP plant can be shut down. If the solar thermal plant has also a seasonal storage, the time frame during which it can cover the heat demand is significantly increased. Additionally, in periods of high wind electricity production and hence low electricity prices, the storage can be used to balance the grid. Electricity can be converted and stored in the storage, or used to run a heat pump to discharge the storage [32, 33, 16].

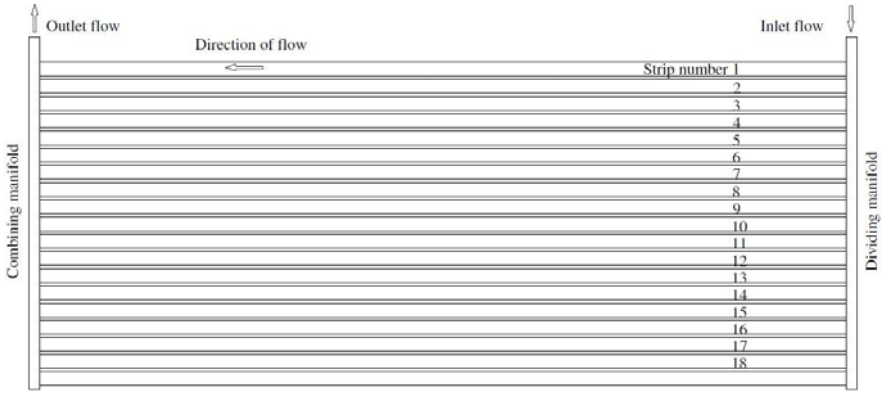

Figure 1.8: Sketch of a typical Arcon-Sunmark collector.

1.3.2 Typical design

1.3.2.1 Solar collectors

The wide majority of large solar collector fields for DH applications is made of flat plate collectors. These collectors have undergone a strong development during the years with regard to quality, efficiency increase and cost reduction [34]. The collectors used in these installations have relatively large aperture areas ($12-14\,m^2$ [16]), which make the installation faster and more cost-effective.

Before 2015, the Danish market was dominated by two collector manufacturers, Arcon Solar A/S and Sunmark Solutions. Both companies produced flat plate harp collectors, with similar design, although differences existed in terms dimensions, materials and production method. After the fusion of the two companies into Arcon-Sunmark A/S [35], all collectors manufactured and installed in Denmark were produced according to the same design, with minor differences among the single models. The collectors and the collector fields investigated in this thesis were characterized by this design, which is described in the present section.

The collectors had external dimensions of $2.27 \times 5.97 \times 0.14\,m$, corresponding to a gross area of $13.57\,m^2$ and an aperture area of $12.56\,m^2$. The absorber consisted of 18 horizontal strips covered by a selective coating. The absorber strips were made of aluminum, because they are easier to handle and cheaper compared to copper [36]. A 5.80 m long copper pipe was laser-welded below each absorber strip. The 18 absorber pipes connected two copper manifolds, running along the sides of the collector. The inlet and outlet of the collector were at the top corners of the module, which made them easy to connect to one another, when several collectors are installed side by side in a collector row. Both absorber pipes and manifolds had circular cross sections. A scheme of the collector hydraulic is shown in Figure 1.8.

The external cover was made of an anti-reflective treated glass with a thickness of 3.2 mm. Back and side of the collector were insulated by 75 mm and 30 mm of mineral wool respectively. The casing of the collector was made of aluminum.

The collector could be equipped with a foil of fluorinated ethylene propylene (FEP) mounted between absorber and glass cover. The polymer foil acted as a convection barrier to decrease the heat losses from the front of the collector. Compared to a double glass cover, this solution was significantly cheaper and lighter. The Arcon-Sunmark

Figure 1.9: An Arcon-Sunmark HT-SA 35/10 collector at the Technical University of Denmark.

collector models which were equipped with polymer foil were named HTHEATstore (or HT-SA for older models), while those without foil were named HTHEATboost (or HT-A for older models). The collector name was completed by a two number code, where the first number denoted the nominal diameter (in millimeters) of the collector manifolds, and the second the diameter of the absorber pipes. As an example, the collector name HT-SA 35/10 identifies a collector equipped with FEP foil, and having a manifold diameter of 35 mm and a absorber pipe diameter of 10 mm (see Figure 1.9). When referring to a solar collector in this thesis, these names are used to identify the specific model, without necessarily describing the collector characteristics every time.

1.3.2.2 Solar collector arrays

In a solar assisted DH system, the solar collector field is usually installed next to the heating plant supplying the DH network. From a technical point of view, solar heat can be combined with all other fuels for DH, but some of them are more suitable for environmental and economic reasons [37]. The auxiliary energy system often relies on natural gas (boilers or CHP plants) or biomass [38, 39]. The contribution of most solar heating plants to the yearly DH demand is relatively low, no more than 15–20 % [16]. This is generally the solar fraction which can be reached by plants which are not equipped with seasonal storage.

The inlet and outlet temperature at which the collector field operates are related respectively to the return and supply temperature of the DH network. The difference between inlet/outlet temperatures of the collector field and return/supply temperatures of the DH consists mainly of the temperature drop across the heat exchanger, which couples the solar collector loop (primary side) to the DH network (secondary side). Typical supply and return temperatures in Danish DH networks are in the intervals $35-45\,^{\circ}\mathrm{C}$ and $70-80\,^{\circ}\mathrm{C}$ respectively [16].

The control strategy of the collector field aims at reaching a constant outlet temperature, by continuously regulating the total flow rate based on the measured solar irradiance [40]. For this purpose, more pyranometers are installed across the collector

field. In case of very large solar collector fields, the presence of more sensors is required by the fact that, in case of moving clouds (and consequently moving shadows on the ground), different parts of the collector field may receive different radiations. Nevertheless, even small collector fields are equipped with more pyranometers for redundancy, so that, in case of failure of one sensor, the collector field does not run the risk of stagnation.

Ideally, the outlet temperature of the collector field should be approximately equal to the supply temperature of the DH network. However, in periods of low solar irradiance, when sufficiently high temperature cannot be achieved, the additional energy can be provided by the auxiliary energy system. In this case, the collector field operates with a target outlet temperature lower than the DH supply temperature, which increases the efficiency of the solar collectors [41].

The solar collectors are installed on the ground, arranged in rows of $10-25$ modules in series [16], which are then connected in parallel. The distribution pipes connecting the different collector series are made of preinsulated steel pipes, buried underground. The pipe diameter progressively decreases, as part of the flow rate is diverted to the collector rows. Unlike pipes for DH networks, the distribution pipes in a solar collector field must cope with much higher and more frequent temperature variations. To deal with thermal expansion cycles of the pipes without risk of breakage, the installation of expansions fittings, such as expansion bellows or lyre loops, is carefully studied in the designing phase of the collector field. Wires to detect potential leakages can be embedded in the pipe insulation [16].

To maximize its performance, a collector field should be designed so that the outlet temperature of every row is the same. This is achieved, when the flow rate in each row is approximately proportional to the row collector area. In this thesis this proportionality between row flow rate and row collector area will be referred to as *uniform flow distribution*. To obtain the desired flow distribution in the collector array, mechanical balancing valves are installed and properly regulated at the inlet of each collector row. Because the valves are regulated in nominal operating conditions, i.e. high solar irradiance, high flow rate, nominal inlet and outlet temperatures, deviations in flow distribution may occur when the actual operating conditions differ from the nominal ones.

Other ways to reach a uniform flow distribution exist, such as adopting a Tichelmann (or reverse return) connection or making sure that the pressure drop across the collector rows is much higher than that in the distribution pipes. However, these methods are applicable only in case of collector arrays characterized by regular layouts. Hence, mechanical valves are the most common solution adopted, as these are very effective and offer a higher flexibility, in case of irregular array layout, or if later adjustment is required. An example of fairly irregular layout is given by Brædstrup I solar collector field (see Figure 1.10).

To avoid freezing of the heat transfer fluid in the solar collector loop in case of low ambient temperatures, propylene glycol/water mixtures are used [41]. As higher concentrations of glycol entail poorer fluid properties in terms of specific heat, heat transfer and viscosity, a lower concentration assuring anti-freezing protection only to a certain extent may be preferred. If the fluid temperature approaches its freezing point, the pump of the solar collector loop starts and the fluid circulates, with or without injection of auxiliary heat (frost protection operation).

(a) Aerial picture. (b) Layout.

Figure 1.10: Brædstrup I solar collector field [42].

1.4 Aim and scope

The aim of the research carried out within this PhD study was to develop detailed simulation models of large solar collector fields for DH applications. Although its goal made this PhD study strongly simulation-oriented, the developed models were validated by comparison with measurements. This was done to guarantee the reliability of the single models, as well as the overall model of the solar heating plant.

The focus of this study was on solar heating plants installed in Denmark, given the unquestionable leadership that this country has had in the last years in this kind of installations. As solar heating plants increase in number and in size, it is important to be able to predict their behavior and performance in the most accurate way. If correct sizing, control strategy and design improvements can be accurately evaluated in advance and implemented already in the planning phase, later and more expensive interventions can be avoided.

Hence, the developed models aimed at addressing aspects which are often neglected by simpler models, such as influence of the operating conditions on the collector efficiency, flow distribution in the different rows of the collector field, thermal capacity of the components, shadow effect from collector row to collector row. So this PhD study included:

- Study of the effect of different collector designs and operating conditions on the collector efficiency (Chapter 2). This goal included:
  - efficiency tests of collectors for collector field applications,
  - analysis of how different operating conditions affect the collector efficiency,

  - development of stand-alone simulation models of solar collectors, to evaluate the collector efficiency in different operating conditions,
  - identification of the most relevant conditions that influence the collector efficiency,
  - development of simulation models for solar collectors, which take into account these relevant aspects and can be integrated in software for system simulation.

- Evaluation of the flow distribution in a collector array (Chapter 3). This goal included:
  - development and validation of a model to evaluate the pressure drop and flow distribution in solar collectors for collector field applications,
  - development and validation of a model to evaluate the flow distribution in a collector array of known design,
  - studying how different operating conditions and array designs affect the flow distribution.

- Accurate modeling of a solar heating plant (Chapter 4). This was done by:
  - integrating the above mentioned models into a system model simulating the entire solar heating plant,
  - validating the system model against measurements from an actual plant,
  - evaluating the impact of the higher degree of detail introduced in the modeling on the model accuracy.

- Identify the impact that different improvement measures in terms of operating conditions and control strategy have on the performance of the solar heating plant (Chapter 4). These included:
  - different temperature levels in the collector field,
  - accurate inputs to the control strategy,
  - feedback control on the field outlet temperature,
  - integration of weather forecast into the control strategy,
  - use of different fluids in the solar collector loop.

The programs TRNSYS and Matlab were the main software used to develop the models, and were chosen because of their wide usage. Because dissemination was considered one of the main pillars of scientific research, the developed models were made publicly available whenever allowed by copyright.

Chapter 2

Operating conditions and collector efficiency

2.1 Introduction

In most applications and studies on solar collectors, the collector efficiency parameters are assumed constant. Besides the mean fluid temperature, the collector efficiency is assumed to vary only depending on environment-related variables, such as solar irradiance, ambient temperature and incidence angle, as shown in (Eq. 2.1):

$$\eta = \eta_0 K_\theta - a_1 \frac{T_m - T_{amb}}{G} - a_2 \frac{(T_m - T_{amb})^2}{G} \tag{2.1}$$

where

η is the collector efficiency $[-]$,

η_0 is the peak collector efficiency $[-]$,

K_θ is the incidence angle modifier $[-]$,

a_1 is the heat loss coefficient at $(T_m - T_{amb}) = 0\,\mathrm{K}$ $\left[\mathrm{W/(m^2\,K)}\right]$,

a_2 is the temperature dependence of the heat loss coefficient $\left[\mathrm{W/(m^2\,K^2)}\right]$,

T_m is the mean temperature of the solar collector fluid $[°\mathrm{C}]$,

T_{amb} is the ambient temperature $[°\mathrm{C}]$,

G is the total irradiance on the collector plane $\left[\mathrm{W/m^2}\right]$.

More detailed efficiency expressions may include the distinction between beam and diffuse radiation and wind speed [43].

Among the different operating conditions which can affect the collector efficiency, the type of fluid and the flow rate have a great importance, especially if these determine a change in flow regime in the absorber pipes of the collector. With the collector geometry and the fluid parameters given in their works, Kummer [44] calculated a decrease of the collector peak efficiency of 2 %, when using a 50 % ethylene glycol/water mixture instead of water; Qin [45] 3.8 %, when comparing a 40 % propylene

(a) Collector HT-A 35/10. (b) Collector HT-SA 35/10.

Figure 2.1: Tested solar collector HT-A 35/10 (a) and HT-SA 35/10 (b) at the Department of Civil Engineering at the Technical University of Denmark.

glycol/water mixture and water; Eisenmann et al. [46] 3 %, , when comparing a glycol mixture in laminar flow and water in turbulent flow. The effect of the flow regime (not necessarily related to a change in fluid type) on the collector efficiency was also confirmed by experimental investigations [47, 48]. A change in flow regime from laminar to turbulent may cause an increase of the collector efficiency of 3–8 % [47].

Most collectors are tested using water as heat transfer fluid and in condition of turbulent flow. If the collectors were supplied with propylene glycol/water mixtures, laminar regime may take place, reducing its efficiency.

This chapter summarizes the study on the effect of the flow regime on the collector efficiency and the measures that were taken to account for this when modeling a solar collector. Additionally, the effect of a polymer foil used as convection barrier inside a solar collector is described.

2.2 Testing and modeling of solar collectors

The efficiency of two solar collectors for collector field applications was experimentally investigated in different operating conditions of flow rate and tilt angle. The collectors were the models HT-A 35/10 and HT-SA 35/10 (see Section 1.3.2.1), and are shown in Figure 2.1. The only difference between the two was a FEP foil interposed between absorber and glass cover in the HT-SA model, acting as a convection barrier.

The collectors were tested according to the steady-state method described in the standard ISO 9806 [43]. The tested operating conditions were: tilt angle of 45° and flow rates of 5, 10 and 25 l/min (corresponding to 0.3, 0.6 and 1.5 m^3/h); tilt angles of 30° and 60° and flow rate of 25 l/min. The solar collector fluid was a 40 % propylene glycol/water mixture.

Testing a collector in many different conditions is time consuming and not always practical. Hence, a simulation model able to calculate the collector efficiency in different conditions can be very convenient. Such a model was created in *Soleff*, software developed at Technical University of Denmark [49]. The model results were validated against measurements, to verify that the software was suitable for simulation of large solar collectors for collector field applications and to prove the model reliability.

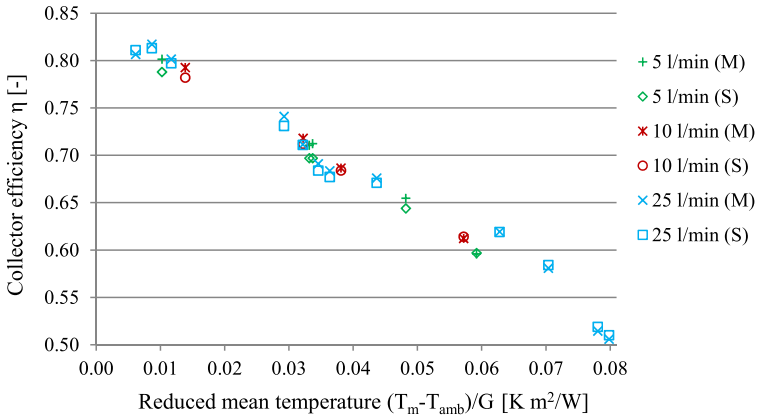

Figure 2.2: Comparison between measured (M) and simulated (S) efficiencies of the HT-A 35/10 collector.

Part of the experimental measurements and simulation results are presented in Figure 2.2. The diagram shows the comparison between measured and simulated efficiencies for the HT-A 35/10 collector at different tilt angles and flow rates. Similar results were obtained for the HT-SA 35/10 collector. For sake of clarity, and because it was found that the condition affecting more strongly the collector efficiency was the flow regime, Figure 2.2 does not specify the tilt angle of the single data points. Additionally, to keep the diagram as clear and simple as possible, the efficiency points characterized by transitional flow regime (i.e., Reynolds number Re=2200−2400) are not reported in Figure 2.2. The complete results of this study can be found in Paper I.

Figure 2.2 shows that a good agreement between measured and calculated efficiencies was found, when the flow regime was either laminar (Re<2000) or turbulent (Re>3800). This proved the suitability of the software and the model in these flow conditions. Additionally, it was found that the peak efficiency of the collector was not significantly affected by the flow rate, as long as this did not entail a change in flow regime. Conversely, transition from laminar to turbulent flow increased the peak efficiency by up to 4 % [50]. For this reason, the diagram shows that the efficiency points at 5 and 10 l/min, characterized by laminar flow, were mainly aligned. On the other hand, the efficiency points at 25 l/min presented a sort of discontinuity, when the ratio $(T_m - T_{amb})/G$ was higher than 0.06 K m^2/W. In these conditions of flow rate and temperature the flow in the absorber pipes became turbulent, resulting in higher collector efficiencies compared to those obtained at lower fluid temperatures. The discontinuity caused by the change in flow regime prevented fitting the data with a quadratic efficiency expression (Eq. 2.1).

Regarding the effect of the FEP foil on the collector efficiency, the results showed that the presence of the foil reduced the heat losses by 19–25 %, but the additional layer also reduced the solar irradiance reaching the absorber by 2–4 % [50]. As a result, the HT-SA model presented lower heat loss coefficients, but also lower peak efficiencies compared to the HT-A model. Hence, the latter performed better at lower temperatures, while the former at higher temperatures. As the temperature rise along a collector row is relatively high (30−40 K), a mixed composition of collectors with and without polymer foil may be an optimal solution. Installing collectors without

Table 2.1: Comparison between measurements and TRNSYS collector types.

Parameter	Type 832	Type 1290	Type 539
Deviation in useful energy output (all four days)	-2.3 %	-0.32 %	-0.31 %
Maximum deviation in useful energy output over one day test	-5.6 %	-0.69 %	-0.69 %
RMSD of outlet temperature (all four days)	0.16 K	0.14 K	0.12 K
Maximum RMSD of outlet temperature over one day test	0.17 K	0.21 K	0.15 K

foil in the first part of the array and collectors with foil in the second part would allow exploiting the advantageous characteristics of both models. A study on a collector row consisting of both types of collectors is presented in Paper II, both in terms of energy performance and economics.

2.3 TRNSYS Type 330

2.3.1 Development and characteristics of Type 330

As seen in Section 2.2, a change in flow regime can have a strong impact on the collector efficiency. Additionally, if a collector experiences different flow regimes within the range of its operating conditions, then its efficiency cannot be accurately described by a single efficiency expression. For example, if the ranges of temperatures and flow rates of the collector field by Høje Taastrup are considered (see Section 4.2), solar collectors will experience laminar flow in approximately one third of the cases. For this reason, a new type component of solar collector, with flow regime-dependent efficiency, was developed in this study, in order to be used within the software TRNSYS.

Validated and reliable collector types already exist in TRNSYS. For this reason, the new type was created by editing the source code of one of these. The main collector types in TRNSYS are Type 832 [51], Type 539 and Type 1290 [52]. To select the most suitable type, these were compared to measurements from a HT-SA 35/10 collector (see Section 3.2). The efficiency of the collector was determined according to the quasi-dynamic test method described in the standard ISO 9806 [43]. The collector was tested with a water flow rate of 1.5 m^3/h and at four different temperature levels during four days. The measured data were analyzed and fitted through a multiple linear regression (MLR) to determine the collector efficiency parameters. These, together with the measured inlet temperature, flow rate, solar irradiance and ambient temperature, were given as input to the three TRNSYS collector types. It must be noted that, as Type 539 internally calculates the incidence angle modifier for diffuse radiation, its source code was modified to accept the value determined by the MLR.

The deviation in useful energy gains and the root-mean-square deviation (RMSD) of the collector outlet temperatures between the measured data and the output of the three collector types are shown in Table 2.1.

Type 832 presented the highest deviations, both in terms of outlet temperature (if

calculated over the four days) and energy gain. Type 539 showed the best agreement with the measurements, followed by Type 1290. Type 1290 and Type 832 are perfectly compatible with the quasi-dynamic test method described in the standard [43], as they offer the possibility of giving as input the wind speed and sky temperature effects on the collector efficiency. However, these parameters are expected to play a negligible role in glazed flat plate collectors [53] and are not usually provided in technical datasheets. Consequently, given the slightly better agreement between measured data and the output of Type 539, this was chosen as starting type to develop the new collector model, Type 330.

Type 330 differs from the original Type 539 in the following aspects:

- The incidence angle modifier for diffuse radiation can be specified by the user.

- Two sets of efficiency coefficients (η_0, a_1 and a_2) and test parameters (flow rate and fluid specific heat to which the efficiency coefficients refer to) can be given as input. The user needs also to specify the number of absorber pipes and the pipe diameter. Assuming that the inlet flow is uniformly distributed in the absorber pipes, fluid velocity and Reynolds number are calculated in each collector node. In fact, the collector is divided in a user-defined number of nodes in the flow direction, to solve the differential equations resulting from the energy balance on the collector. Depending on the flow regime in each node, one set of efficiency coefficients or the other is used. Transition from laminar to turbulent regime is assumed to take place at Re=2300.

- The thermophysical properties (density and viscosity) defined in the type refer to a 35 % propylene glycol/water mixture (Eqs. 8–9 in Paper IV), but they can be easily changed by the users according to their needs.

- The incidence angle modifier (IAM) for direct radiation is calculated through the cosine formula in the range $0°-80°$. In the range $80°-90°$, the IAM value is obtained through linear interpolation between $IAM(80°)$ and 0. Type 539 works in the same way, but the linearization occurs for angles larger than $60°$. Depending on the information available in the collector test report, the user can specify the range of incidence angles for which the IAM expression fitting the test data should be used.

2.3.2 Use of Type 330

In solar collector test reports the collector efficiency parameters are given only for a specific combination of fluid type and flow rate. The tested fluid is usually water, and water was used in the efficiency tests of the Arcon-Sunmark collectors considered in this thesis. The flow rate should be chosen in such a way that the flow regime in the absorber pipe(s) does not change across the range of tested temperatures [43].

On the other hand, to use all the features of Type 330, two sets of efficiency coefficients (one for laminar and one for turbulent flow) were needed, as explained in Section 2.3.1. For this purpose the software Soleff (see Section 2.2) was used. The collector chosen to be modeled was a HTHEATstore 35/08, as those installed in Høje Taastrup solar collector field (see Section 4.2).

Table 2.2: Declared and simulated efficiencies of a HTHEATstore 35/08 collector based on gross area (13.57 m^2).

	Fluid	η_0 $[-]$	a_1 $[W/(m^2\,K)]$	a_2 $[W/(m^2\,K^2)]$
Declared efficiency [54]	water	0.757	2.199	0.007
Soleff efficiency (test conditions)	water	0.757	2.260	0.006
Soleff efficiency (turbulent)	35 % glycol	0.756	2.318	0.006
Soleff efficiency (laminar)	35 % glycol	0.727	2.357	0.005

Based on the actual collector design (see Section 1.3.2.1) and test conditions [54], a model of the collector was developed in Soleff, so to match the efficiency expression stated in the test report [54]. The maximum deviation between the two efficiency curves was lower than 0.2 % in the range $0-0.10\,K\,m^2/W$ for factor $(T_m - T_{amb})/G$. In this way, the collector design parameters used by the software were determined and only the operating conditions were changed afterwards. More specifically, the Soleff model was used to evaluate the efficiency of a HTHEATstore 35/08 collector, when this was supplied with a 35 % propylene glycol/water mixture, both at a high ($2\,m^3/h$) and a low ($0.7\,m^3/h$) flow rate. These two flow rates were chosen, because they guaranteed respectively turbulent and laminar flow in the temperature range at which a collector field usually operates. In this way, the resulting efficiency curves were characterized by the same flow regime throughout the temperature range and did not present anomalous discontinuities. The coefficients of the declared and simulated efficiencies are listed in Table 2.2.

Chapter 3

Flow distribution

3.1 Introduction

The size of solar collector fields in Denmark has been constantly increasing in the last years. In 2012 the largest solar collector field in operation was Marstal, with a collector area of about $33,000\,m^2$, although this plant consisted of three fields, built in different years. The single largest collector field was Gråsten, with about $20,000\,m^2$ collector area. Two years later the record passed to Dronninglund ($37,500\,m^2$), and the following year to Vojens II ($52,500\,m^2$, see Figure 1.5), extension of an existing collector field. In 2016 the collector field in Silkeborg won the title with a collector area of $157,000\,m^2$ (see Figure 1.3).

When collector arrays become increasingly larger, the risk of non-uniform flow distribution from one row to another increases. Non-uniform flow distribution is not desirable for different reasons. First of all, it decreases the performance of the collector field, because different collector rows reach different outlet temperatures. Mixing flows at different temperatures causes a lower temperature rise across the collector field compared to the case with identical outlet temperatures.

Secondly, a uniform temperature distribution across the collector array is crucial in critical conditions, such as incipient stagnation and frost protection operation. A collector row supplied by a lower flow rate is likely to run into stagnation and/or freezing earlier than other collector rows. This is a risk for the entire collector field and decreases its performance. In fact, a collector row supplied by a lower flow rate may reach high outlet temperatures, which can trigger an alarm signal and interrupt the normal operation of the collector field, with consequent loss of useful energy production.

Uniform flow distribution also plays an important role in case of anti-freezing operation. Propylene glycol/water mixtures ensure a frost protection down to several degrees below $0\,°C$, depending on the glycol concentration. If the fluid temperature in the collectors decreases dangerously close to the freezing point, the primary pump is turned on and the solar collector fluid is circulated across the collector field. Depending on the measured collector temperatures and ambient temperature, the frost protection operation may operate with or without injection of heat from the secondary side to the solar collector loop. A uniform flow distribution in all the rows ensures protection of the system, as collector rows supplied by lower flow rates are more likely to experience freezing in case of extended cold periods.

In large solar collector fields in Denmark, balancing valves are installed at the inlet of each collector row and their setting is chosen so to give a uniform flow distribution in nominal operating conditions, i.e. high solar irradiance, high flow rate, nominal inlet and outlet temperatures. However, due to the non-linear relation between flow rate and pressure drop, and the variation of the fluid thermophysical properties with the temperature, deviations in flow distribution can be expected if the operating conditions differ from the nominal ones [55].

Flow distribution in solar thermal systems has been the topic of many investigations, both at collector level [56, 57, 58, 59, 60] and array level [55, 61, 62]. However, it was not possible to find a flexible tool or model, able to solve the flow distribution problem in scenarios different from those for which the model had been developed. For this reason, a model to evaluate the flow distribution for different collector array designs was developed. This chapter briefly describes the development and validation of the model, while the complete analysis is presented in Paper III, IV and V.

3.2 Hydraulic model for solar collectors

To calculate the flow distribution in a collector array, the relation between flow rate and pressure drop in each component of the system needs to be known. In a collector field it is possible to distinguish three main types of hydraulic components: solar collectors, pipes and fittings (bends, tee junctions, valves, changes in flow area, etc.). Correlations for pipes and fittings are usually found in literature or in product catalogs. Finding this information for solar collector is less straightforward. First of all, the pressure drop characteristic curve is often missing in collector datasheets. Even when present, the conditions used during the test may be different from those in real-world operation, both in terms of fluid type and fluid temperature. In such cases, the test results cannot be directly used without introducing a systematic error [63]. For this reason a hydraulic model of a flat plate harp collector was developed. The model was developed in Matlab and, given its flexibility, it can be easily customized according to the user's needs.

The model was based on the design of U-type harp collectors, as described in Section 1.3.2.1. Buoyancy effect was neglected and the flow was assumed isothermal. This simplification could be done due to the characteristics of the flow which usually takes place in large collectors in collector field applications. The collectors are usually arranged in rows of $10-25$ modules [16], so the temperature rise in each collector is relatively low, while the flow rate is relatively high. If the velocity in the collector pipes is high compared to the temperature rise across the collector, then the flow distribution is dominated by friction and buoyancy can be neglected [60].

The model was validated in terms of pressure drop across the collector against measurements and in terms of flow distribution against other model results found in literature [58]. The validation of the model in terms of overall pressure drop was done comparing the model results with measurements carried out on an Arcon-Sunmark HT-SA 35/10 collector (see Section 1.3.2.1). The collector piping was made of copper and had circular cross sections. The 18 absorber pipes were 5.80 m long, had an inner diameter of 9.1 mm and an intermediate spacing of 122 mm. The manifolds had an inner diameter of 32.9 mm.

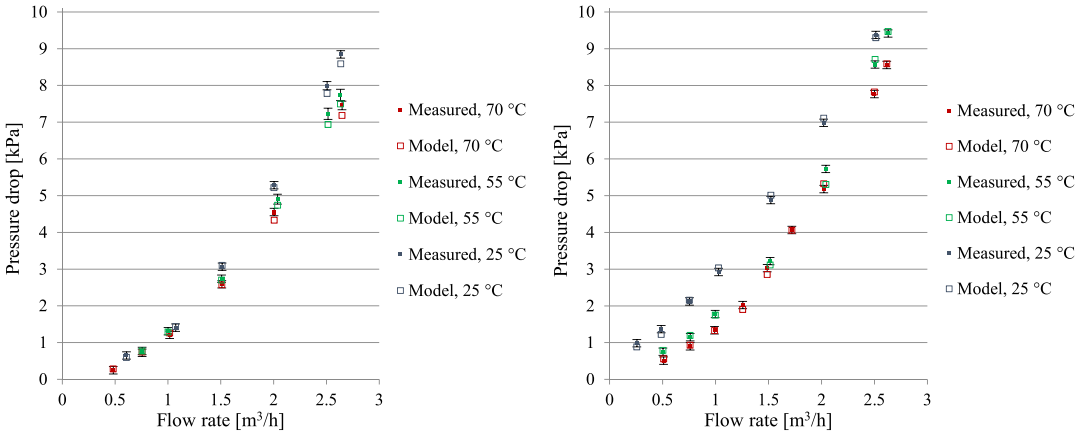

(a) Water. (b) 50 % propylene glycol/water mixture.

Figure 3.1: Comparison between measured and modeled pressure drops.

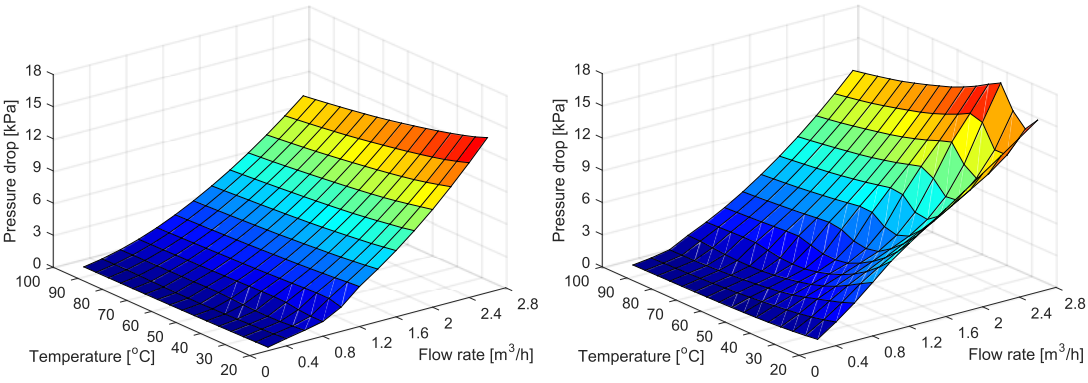

(a) Water. (b) 35 % propylene glycol/water mixture.

Figure 3.2: Pressure drop in Arcon-Sunmark HTHEATstore 35/08 collector.

Measurements were performed using water and a 50 % propylene glycol/water mixture, at different flow rates and fluid temperatures. The comparison between measured and calculated pressure drops is shown in Figure 3.1.

The validated model could then be used to assess the flow distribution and the pressure drop in similarly designed collectors in different operating conditions. Two examples of output of the model in terms of pressure drop are given in Figure 3.2. The two diagrams show the pressure drop as function of the flow rate and fluid temperature. The diagrams refer to an Arcon-Sunmark HTHEATstore 35/08 collector [54], when this is supplied with water (Figure 3.2a) and with a 35 % propylene glycol/water mixture (Figure 3.2b). In terms of hydraulic design, the only difference between an HTHEATstore 35/08 and a HT-SA 35/10 collector was the diameter of the absorber pipes, which was 7.3 mm in the former and 9.1 mm in the latter.

As expected, the pressure drop in the collector supplied with water was significantly lower, due to the lower viscosity of water compared to the glycol/water mixture. For the thermophysical properties, refer to (Eqs. 3–4) in Paper III for water, and

to (Eqs. 8–9) in Paper IV for the glycol/water mixture.

The two pressure drop diagrams reveal also something about the flow regime which takes place in the collector absorber pipes in different operating conditions of flow rate and fluid temperature. At high flow rates and high temperatures the Reynolds number in the absorber pipe was fairly high and the flow was turbulent. When decreasing the flow rate and/or the fluid temperature, the surfaces shown in Figure 3.2 present some sort of discontinuity, which marks the start of the transition region. This is particularly evident in the case of the glycol/water mixture in Figure 3.2b. If the flow rate and/or the fluid temperature are further decreased, the laminar region is entered. Let us assume that a collector array made of HTHEATstore 35/08 is operated between 50 °C and 95 °C. If water was used as solar collector fluid, the flow regime in the collector absorber pipes would be turbulent, almost regardless of the flow rate. Conversely, if the 35 % glycol/water mixture was used, the flow would be turbulent regardless of the fluid temperature, only at flow rates higher than 2 m^3/h. At lower flow rates and depending on the fluid temperature, the absorber pipes would experience transitional or laminar flow.

Hence, the diagram can be used to identify how often, in which conditions and which fraction of the collector array experiences non-turbulent flow, and consequently, when a lower performance can be expected.

3.3 Model for flow distribution in a collector array

3.3.1 Numerical model

The collector model previously described was used as part of a hydraulic model simulating an entire collector array. In the model the pressure drop along straight pipes was calculated through the well known Darcy-Weisbach equation and correlations for the friction factor found in literature (see (Eqs. 1–3) in Paper IV) [64, 65, 66, 67]. For fittings, such as bends, tee junctions, changes of flow section area, etc., correlations from Idelchik [68] were used. The relation between flow and pressure drop in the balancing valves, installed at the inlet of each collector row to achieve uniform flow distribution, was provided by the valve manufacturer [69]. Finally, for the corrugated pipes connecting to each other the collectors of the same row, experimental results made available by the company Arcon-Sunmark A/S were used.

Based on the above mentioned correlations between flow rate and pressure drop, the hydraulic model for flow distribution in solar collector arrays was developed in Matlab. The core of the model consists of the solution of a set of equations (Eq. 12 in Paper IV), imposing the conservation of mass across the collector field and the uniformity of pressure drop along the different hydraulic paths. Given a preliminary assumption on the flow distribution, the set of equations is solved iteratively, until convergence is reached.

Two different methods are implemented to estimate the temperature profile along the collector rows, which determines the fluid properties. In the first method, one inlet and one outlet temperature must be defined as input, and a linear temperature profile is assumed along the collector row. The second method does not require an outlet temperature to be defined, as this is calculated for each row, as function of the flow rate passing through it. Required inputs are in this case the collector efficiency

Figure 3.3: Aerial picture of Høje Taastrup solar collector field (source: Arcon-Sunmark A/S).

coefficients and weather conditions, such as solar irradiance and ambient temperature. The temperature profile across each collector row is then calculated according to (Eqs. 10–11) in Paper IV.

3.3.2 Høje Taastrup solar collector field

The collector field near Høje Taastrup (20 km west of Copenhagen) was taken as basis to develop the hydraulic model and used for the validation. A detailed description of the entire solar heating plant is given in Section 4.2. In this Section the description focuses only on the hydraulic characteristics of the solar collector loop, as these are relevant for understanding the boundary conditions of the flow distribution model.

An aerial picture of the collector field is shown in Figure 3.3, while the layout of the collector array is presented in Figure 3.4. The collector field consisted of 240 solar collectors HTHEATstore 35/08 (see Section 1.3.2.1), for a total collector gross area of 3257 m^2. As shown in Figure 3.4, the collectors were arranged in two identical subfields. Each subfield consisted of 12 collector rows, with a row distance of 5.5 m, and each row was made up of 10 collectors.

The supply pipes ran along the outer sides of the collector field, while a single return pipe collected the fluid in the middle of the field. The diameter of the distribution pipes progressively decreased, as part of the flow rate was diverted to the collector rows. Balancing valves were installed at the inlet of each collector row to guarantee a uniform flow distribution.

Depending on the solar irradiance and the outlet temperature set point, the flow rate to the collector field ranged between 8 and 67 m^3/h. The fluid in the collector loop was a 35 % propylene glycol/water mixture.

To measure the flow distribution in the collector field (i.e. the flow rate in each collector row), a differential pressure sensor was used. This could be done as the in-

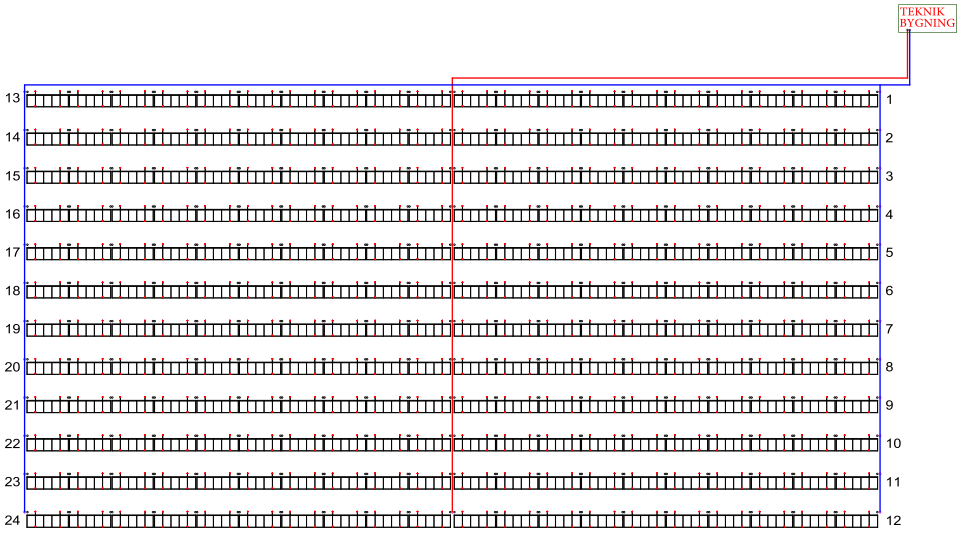

Figure 3.4: Layout of Høje Taastrup collector field (adapted from Arcon-Sunmark).

stalled balancing valves had two measuring points, one before and one after the valve member. Measuring the pressure drop across the valve and knowing the relation between flow rate and pressure drop for each setting of the valve, the row flow rate was calculated. The fluid temperature, needed to calculate the fluid density and viscosity, and correct the valve characteristic accordingly, was also measured.

Measuring the row flow rate in this way has the obvious advantage that this method is not invasive and does not require any modification of the existing piping system. However, this simplicity of measurement comes with the drawback of a higher measurement error, compared to a regular flow meter. This ranged between 5 % and 7 % in the performed tests (refer to Figure 4 in Paper IV). Some preliminary field measurements showed that the balancing valves gave a fairly uniform flow distribution, so that the differences in the measured row flow rates were smaller than the measurement error. Consequently, the measurements were repeated, after inducing a stronger maldistribution in the eastern subfield, by modifying the valve settings in the first 10 collector rows.

With the modified valve settings, the flow distribution in the field was measured at flow rates of 14, 30 and 50 m^3/h. Additionally, two manometers in the primary loop – one installed after the pump and the other right before the inlet to the heat exchanger – were used to measure the pressure drop across the collector field.

3.3.3 Output of the model

The model was validated both in terms of overall pressure drop and flow distribution, as described in Section 3.3.2. The comparison between measurements and model results is shown in Figure 3.5. Figure 3.5a presents the measured and calculated pressure drops as function of the flow rate. The reason why the pressure difference was not null at null flow rate was the hydrostatic pressure between the two manometers (see Section 3.3.2), which had an elevation difference of 1.36 m.

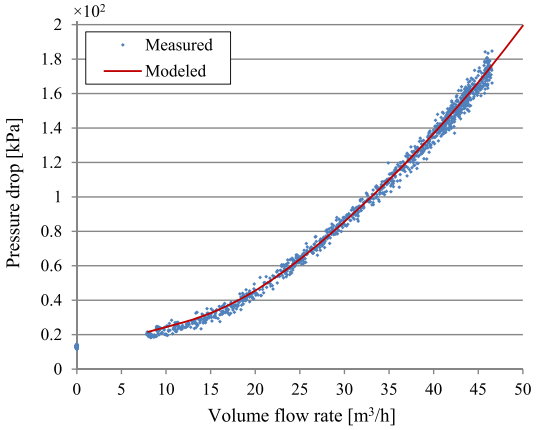

(a) Measured and modeled pressure drop across the collector array.

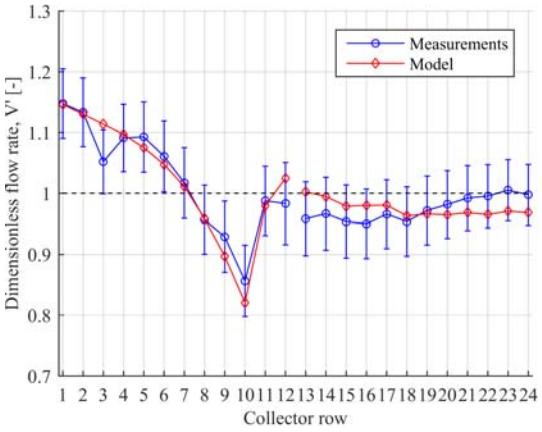

(b) Measured and modeled flow distribution in the collector array at a flow of 30 m^3/h.

Figure 3.5: Validation of the flow distribution model for solar collector arrays.

Figure 3.5b presents the flow distribution in one of the validation tests, more specifically that using a flow rate of 30 m^3/h. Both modeled and measured row flow rates (the latter including error bars) are shown in terms of dimensionless flow rate, which was defined by (Eq. 3.1) as the ratio between the actual row flow rate and the flow rate that each collector row should receive in case of perfectly uniform flow distribution. It must be remembered that, according to the definition given in Section 1.3.2, *uniform flow distribution* refers to the proportionality between the flow rate in each collector row and the row collector area, and not necessarily to an identical flow rate in each collector row.

$$V_i' = \frac{V_i}{\frac{A_{row,i}}{A_{field}} \sum_{i=1}^{N} V_i} \tag{3.1}$$

where

V' is the dimensionless volume flow rate in a collector row $[-]$,

V is the actual volume flow rate in the collector row $[m^3/h]$,

A is the area either of the collector row or of the collector field, depending on the subscript $[m^2]$,

i subscript denotes the collector row $[-]$,

N is the total number of collector rows $[-]$.

As a good agreement between model and measurements was found, the model was regarded suitable to investigate the flow distribution in solar collector arrays with different layouts and under different operating conditions.

First, the flow distribution in Høje Taastrup collector field was simulated, assuming that the actual settings of the balancing valves were used, and that the inlet and outlet temperatures were 55 °C and 95 °C respectively. The flow distribution for the

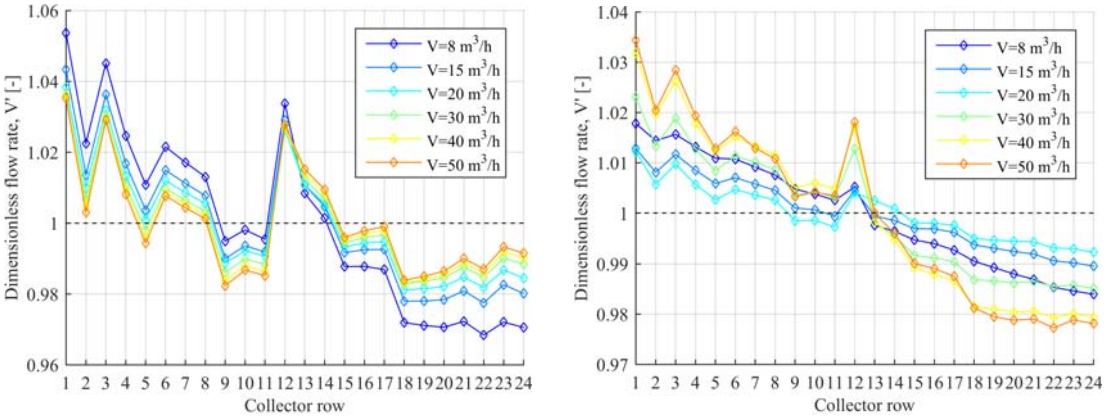

(a) Normal operation: T_{in}=55 °C, T_{out}≈95 °C.

(b) Constant fluid temperature T=-13 °C.

Figure 3.6: Modeled flow distributions in Høje Taastrup solar collector field for different field flow rates.

considered flow rates is shown in Figure 3.6a. Compared to the validation scenario (Figure 3.5b), the flow distribution was significantly more uniform due to the correct valve settings. As can be seen, the higher the flow rate, the more uniform the flow distribution. This could be expected, because the settings of the balancing valves had been chosen so to give a uniform distribution when the collector field was supplied with a flow rate of 55 m^3/h. Although flow rates different from 55 m^3/h caused a higher maldistribution, the balancing valves maintained the flow distribution within an acceptable range. Even at fluid temperatures close to the freezing point of the glycol/water mixture, the flow distribution remained fairly uniform (Figure 3.6b).

The flow distribution in collector arrays characterized by different layouts was also investigated. In Sweden there have been experiences of relatively small collector fields with regular layout, obtaining a uniform flow distribution without the use of balancing valves. This was achieved by simply keeping constant the diameter of the supply and return pipes along their entire length. This assured that the pressure drop across the collector rows was much higher than that in the distribution pipes. So one of the simulated scenarios consisted of applying the same approach to the collector field by Høje Taastrup. However, because the western subfield was farther away than the eastern one from the primary pump, a flow unbalance between the two subfields would occur, if the balancing valves were removed. Hence, in the new layout (Figure 3.7a) it was also assumed that the technical building was in a centered position compared to the of the field. The resulting flow distribution is shown in Figure 3.7b.

Due to the new symmetry of the collector array and to the constant pipe diameters, the flow distribution was fairly uniform, with deviations comparable to the scenario with normal operation (Figure 3.6a). The absence of the balancing valves and the larger pipe diameters decreased the pressure drop in the collector field by 20–25 % compared to the original design. However, to make a fair comparison, the additional pipe length on the secondary side between the newly located technical building and the north-east corner of the field, where the connection to the DH network lies, should be considered. In this case the resulting net reduction in pressure drop was 7–15 %.

Other arrays, characterized by a larger number of collector rows connected in par-

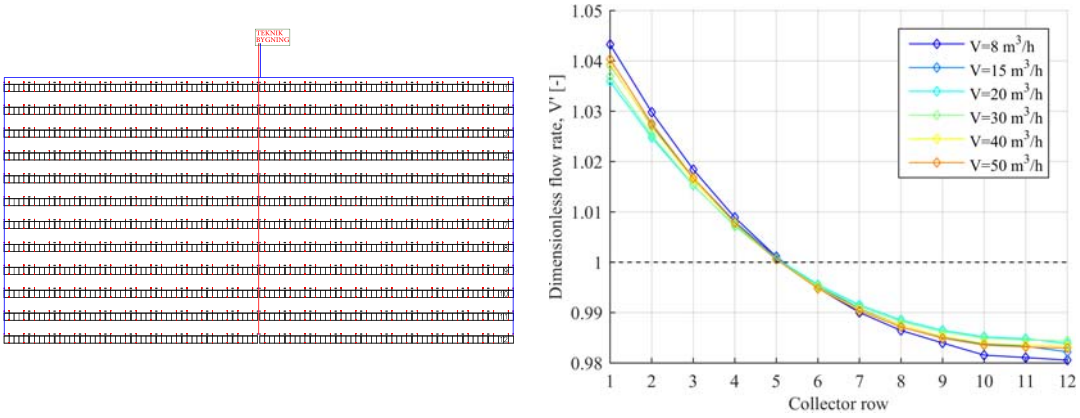

(a) Layout of the collector field.

(b) Modeled flow distribution.

Figure 3.7: Alternative configuration of Høje Taastrup collector field: symmetric array, constant diameters of the distribution pipes and no balancing valves.

allel or by a more irregular layout, were also simulated, to assess the effect that the absence of balancing valves would have in these cases. In Figure 3.8 two of the simulated layouts and the resulting flow distributions are shown. For both layouts, two cases were considered. In the first the pipe diameter was kept constant along the entire length of the distribution pipes, while in the second the diameter was progressively decreased, as the flow was diverted to the different collector rows. For sake of simplicity, only two flow rates, those giving the most and the least flow uniform distribution, are shown in the diagrams. A more detailed analysis of these configurations is presented in Paper IV and Paper V.

Results from several simulations based on regular array layouts (such as those shown in Figures 3.7a and 3.8a) indicated that, in absence of balancing valves, the rule of thumb (Eq. 3.2) is generally valid:

$$\frac{\max(V_i) - \min(V_i)}{\min(V_i)} \approx 0.5 \frac{\Delta p_{distr.pipes}}{\Delta p_{row}} \tag{3.2}$$

where

$\max(V_i)$ is the highest volume flow rate in a collector row $\left[\mathrm{m^3/h}\right]$,

$\min(V_i)$ is the lowest volume flow rate in a collector row $\left[\mathrm{m^3/h}\right]$,

$\Delta p_{distr.pipes}$ is the pressure drop along the longest distribution pipe (supply and return) [Pa],

Δp_{row} is the pressure drop in a collector row supplied by the average flow rate [Pa].

Additionally, assuming that the collector efficiency was independent of the collector flow rate, it was found that the reduction in thermal performance of a collector array due to flow maldistribution was relatively small. Figure 3.9 shows the effect of flow maldistribution on the power output of a collector field consisting of HTHEATstore 35/08 collectors [54]. The degree of flow maldistribution is expressed in terms of root-mean-square deviation (RMSD) between the actual dimensionless row flow rates

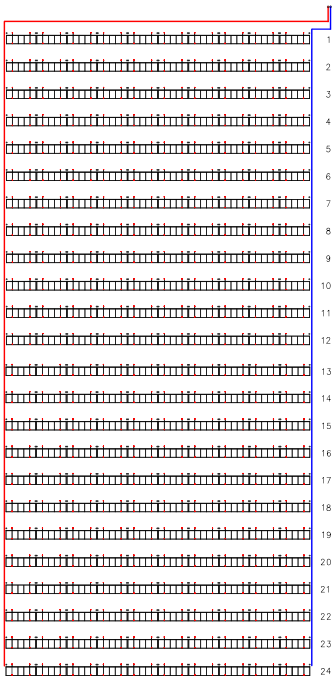

(a) Layout of the collector field.

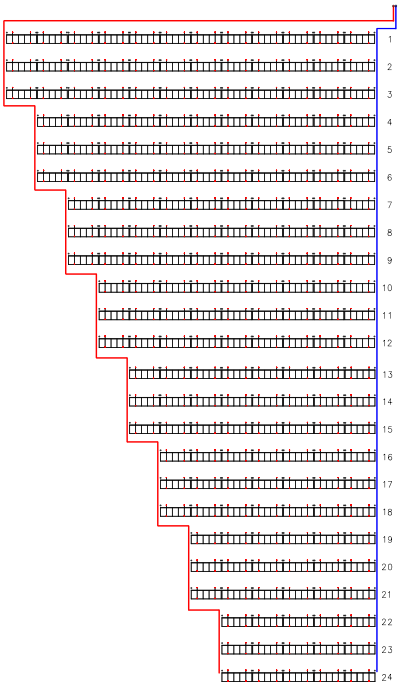

(b) Layout of the collector field.

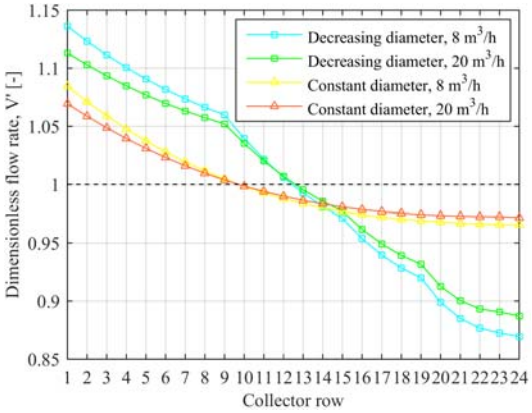

(c) Modeled flow distribution for layout (a).

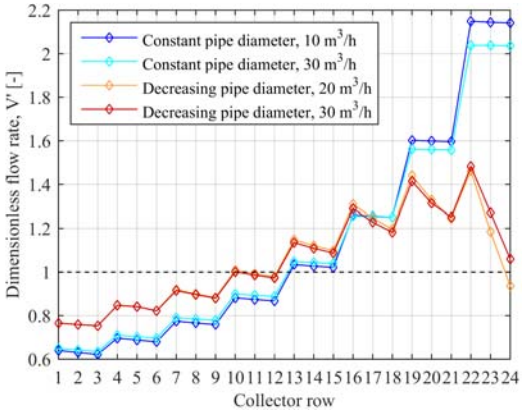

(d) Modeled flow distribution for layout (b).

Figure 3.8: Array layouts and resulting flow distributions: 24 identical collector rows connected in parallel (a, c); 24 differently composed collector rows connected in parallel (b, d).

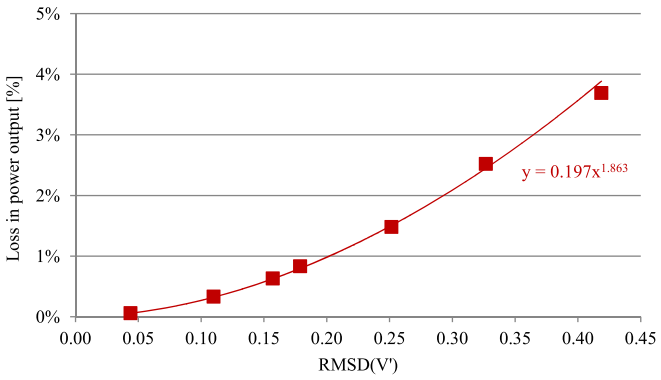

Figure 3.9: Reduction in power output of a collector field as function of the flow maldistribution, assuming T_{in}=50 °C and T_{out}≈90 °C.

and the dimensionless row flow rates in case of perfectly uniform distribution. It can be seen that severe levels of maldistribution are necessary to significantly affect the thermal power output of a collector field.

Chapter 4

Modeling of solar heating plants

4.1 Introduction

Although several simulation tools exist to model large solar collector fields for DH applications [70, 71, 72, 73, 74, 75, 76, 77, 78], TRNSYS was identified as the most suitable software to this purpose, due to the existing libraries of available components [75, 52, 79] and its high flexibility. As seen in Section 2.3.1, users can also create their own components, or customize existing ones by editing the source code. Additionally, TRNSYS has been widely used for simulation of solar thermal systems and many models have been validated against measurements [80, 81, 82, 83, 84, 85, 86].

In the wide majority of the studies found in literature the collector field was treated with little detail, usually modeled by a single collector component, one supply pipe and one return pipe. Consequently, the flow distribution across the collector field was not considered, and the plug flow in the distribution pipes was not accurately modeled, likely leading to an advance or delay of the model response compared to reality. Another simplification was the assumption of a constant efficiency expression, although this can be affected by the collector operating conditions, in particular by the flow regime in the absorber pipes, as seen in Chapter 2. Other aspects which are often neglected are thermal capacity of the components, distinction between beam and diffuse radiation and shadow effect from one row to another.

To investigate the effect of these different aspects on the accuracy of the simulation, a detailed model of a large solar heating plant for DH application was developed, validated and finally used to investigate possible improvement measures. The present chapter summarizes the key points of this study, while the complete analysis is presented in Paper VI and VII.

4.2 Description of Høje Taastrup solar heating plant

The TRNSYS model was developed based on the solar heating plant by Høje Taastrup. As the layout of collector field has been already described in Section 3.3.2, this section summarizes only the key characteristics of the collector field and focuses on the remaining components of the solar heating plant and on the control strategy.

The collector field was made of two subfields of 12 collector rows (see Figure 3.4 in Section 3.3.2) and each row consisted of 10 HTHEATStore 35/08 collectors [54] resulting in a total gross collector area of 3257 m^2. The collectors had a tilt angle of 43° and

an orientation of 2.5° W. The solar collector fluid was a 35 % propylene glycol/water mixture.

The operating temperatures depended on the return and supply temperature in the DH network. The DH return temperature was about 40 °C in winter and 50 °C in summer. The DH supply temperature varied from the lowest temperature of 70 °C (in summer) to the highest temperature of 90 °C (in winter), depending on the ambient temperature. However, during the first year of operation (2015) the outlet temperature from the collector field in summer was about 95 °C, so considerably higher than the nominal DH supply temperature. Because no auxiliary heating plant was located near the collector field, the temperature from the solar heating plant had to be as close as possible to DH supply temperature, if the energy was to be delivered to the DH network.

The flow rate in the collector field varied between 8 and 67 m^3/h, depending on the solar irradiance, which was measured by silicon cell pyranometers [87]. However, it was known – and was confirmed in this study – that the accuracy of this kind of sensors was not very high and tended to decrease over time, underestimating the actual solar irradiance. Hence, secondary standard [88] thermopile pyranometers were added to measure the total radiation on the collector plane. A first class [88] thermopile pyranometer equipped with shadow ring was used to measure the diffuse radiation.

From the solar collector loop (primary side) thermal energy was transferred to a water loop (secondary side) by a plate heat exchanger. The secondary side was connected to the DH network by 550 m long transmission pipes. Both primary and secondary side were equipped with a bypass for pre-heating purposes. In the primary loop the bypass connected the return pipe from the collector field to the supply pipe to the field (*Bypass 1* in Figure 4.1), and was used to recirculate the heat transfer fluid across the collector field, without it passing through the heat exchanger. The primary bypass was used at the start-up of the plant, when the collector field needed to reach a certain temperature set point before heat could be delivered to the secondary side. In the secondary loop the bypass was located at the end of the transmission pipes (*Bypass 2* in Figure 4.1), before the connection with the DH network. Also in this case, the bypass was used to recirculate the water in the transmission pipes, until it reached a temperature compatible with the DH network. If on the other hand the water from the forward transmission pipe was at a temperature higher than the DH supply temperature, this could be tempered mixing it with colder water from the DH return, intercepted through a shunt (*Shunt pump* in Figure 4.1).

The control strategy of the solar heating plant aimed at reaching a constant outlet temperature at the end of the forward transmission pipe. To achieve this, the quantity Q_{sol}, i.e. the theoretical power output from the collector field, was calculated according to (Eq. 4.1), based on the instantaneous solar irradiance measured on the collector plane (G). Then, the primary flow rate was regulated based on the value of Q_{sol} according to (Eq. 4.2), to achieve a constant field outlet temperature, ideally identical to the outlet temperature set point ($T_{setpoint}$).

$$Q_{sol} = A_{field} \left(G\,\eta_0 - a_1 \cdot (T_m - T_{amb}) - a_2 \cdot (T_m - T_{amb})^2 \right) \tag{4.1}$$

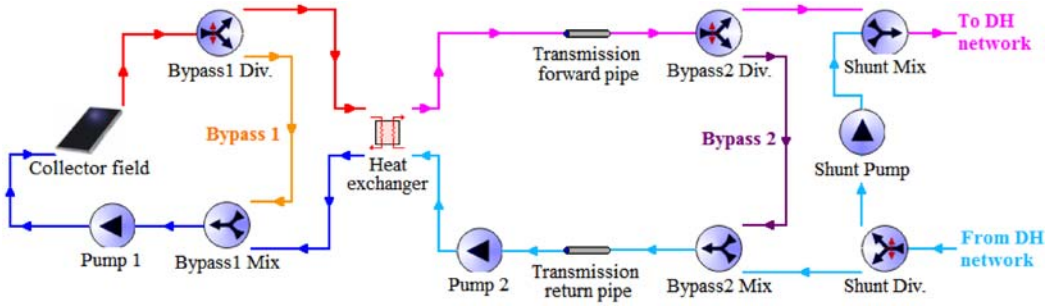

Figure 4.1: Scheme of Høje Taastrup solar heating plant.

$$\dot{m} = \min\left[\dot{m}_{max}, \max\left[\dot{m}_{min}, \frac{Q_{sol}}{c_p \cdot (T_{setpoint} - T_{in})}\right]\right] \tag{4.2}$$

It must be noted that in (Eq. 4.1) the temperature T_m is the average between the measured inlet temperature to the collector field and the outlet temperature set point, and not the actual outlet temperature. The outlet temperature set point was equal to the DH supply temperature, increased by a certain amount, to take into account the temperature drop across the heat exchanger and other factors, such as thermal losses from the pipes. In (Eq. 4.2) the flow rates $\dot{m}_{max}$ and $\dot{m}_{min}$ are the maximum and minimum flows the primary pump could supply.

The primary pump turned on, when either Q_{sol} was higher than a certain value, or one of the sensors installed at the outlet of the monitored collector rows measured a fluid temperature higher than a certain set point. When the field outlet temperature was higher than a certain threshold, the primary bypass was closed and the secondary pump was turned on.

The 35 % glycol/water mixture in the primary loop ensured frost protection down to -16 °C. If the fluid temperature fell below a first set point, the primary pump would start and recirculate the warmer fluid stored in the distribution pipes through the primary bypass and across the collector field. If the fluid temperature still decreased below a second set point, heat would be transferred from the DH network to the collector field through the heat exchanger, until a minimum fluid temperature was reached in all monitored collector rows.

4.3 TRNSYS-Matlab model

4.3.1 Development of the model

All components used in the simulation model (Figure 4.2) belonged to well-established TRNSYS libraries [75, 52, 79], with the only exception of the solar collectors, for which the in-house developed Type 330 was used (see Section 2.3).

Each Type 330 in the model represented one of the 24 collector rows which made up the collector field. Types 709 [52] were used to model all distribution pipe segments between the collector rows in the primary loop, and the transmission pipes in the secondary loop. So the exact field layout and plug flow were reproduced. Additionally, the Matlab model evaluating the flow distribution in the collector array (see Section 3.3) was integrated into the TRNSYS model through Type 155 [75]. At each

simulation time step Type 155 passed the necessary inputs from TRNSYS to Matlab, which calculated the flow distribution in the different collector rows and returned the result back to TRNSYS.

As the pipe Type 709 did not consider the thermal mass of the pipe material, which may be relevant for the bigger pipes, the thermal capacity Type 306 [79] was added to the longest distribution and transmission pipes, i.e. the supply pipe to the western subfield, the common return pipe from the collector field and the transmission pipes between the heat exchanger and the DH network (see Figure 4.2).

The soil temperature to calculate the heat losses from the buried pipes was evaluated through Type 77 [75]. The plate heat exchanger between primary and secondary side was modeled through Type 5b [75], as this component offered the possibility of defining a variable heat transfer coefficient. This was accurately determined based on measurements from the heat exchanger installed in Høje Taastrup plant.

The control strategy was implemented through the use of Equation blocks, to define correlations such as (Eq. 4.1) and (Eq. 4.2). Differential controllers of Type 2d [75] set the turn-on/off conditions of the pumps. Type 93 [75] was used to introduce time delay and weather forecast (Section 4.4.3). Controller Type 23 [75] was used to model the PID control (Section 4.4.2).

The model was run with two different types of weather data. Actual weather data measured at Høje Taastrup plant during the summer 2015 were used for the validation of the model. Instantaneous values of all monitored parameters were recorded with one minute time step. On the other hand, the yearly simulations made use of the Meteonorm weather data for the location of Copenhagen-Taastrup, contained in the standard TRNSYS library [75]. Both measured data and Meteonorm data were used in the investigated scenarios implementing weather forecast (Section 4.4.3) and PID control (Section 4.4.2). In these cases the Meteonorm data were used to calculated the yearly performance of the solar heating plant, while the measured data were used to verify the stability of the control strategy. In fact, being the Meteonorm data interpolations of hourly values, they did not present fast fluctuations in solar irradiance, which were needed to evaluate the behavior of the control, which was relevant in case of rapidly varying irradiance in the above mentioned scenarios.

The shadow effect from row to row was taken into account through the shadow mask Type 30 [75]. The so corrected diffuse and beam irradiance were given as input to all collector rows except the front ones, which were not shaded.

4.3.2 Validation of the model

For the validation of the model, measured weather data (irradiance and ambient temperature) and return temperature from the DH network were used as input, while all other quantities were calculated by the model. Because there was a distinct difference in measured irradiance between the thermopile pyranometers and the silicon cell pyranometers (Figure 4.3), the measurements from the two types of sensors had to be used appropriately. The total irradiance measured by the silicon cell pyranometers was used in the control strategy, as in the actual plant. The total and diffuse irradiance measured by the thermopile pyranometers were given as input to the shadow mask Type 30, which used them to calculate the actual irradiance on the collectors.

When using the collector efficiencies for a 35 % glycol/water mixture (see Table 2.2) as input to the TRNSYS model, the modeled outlet temperature from the collector

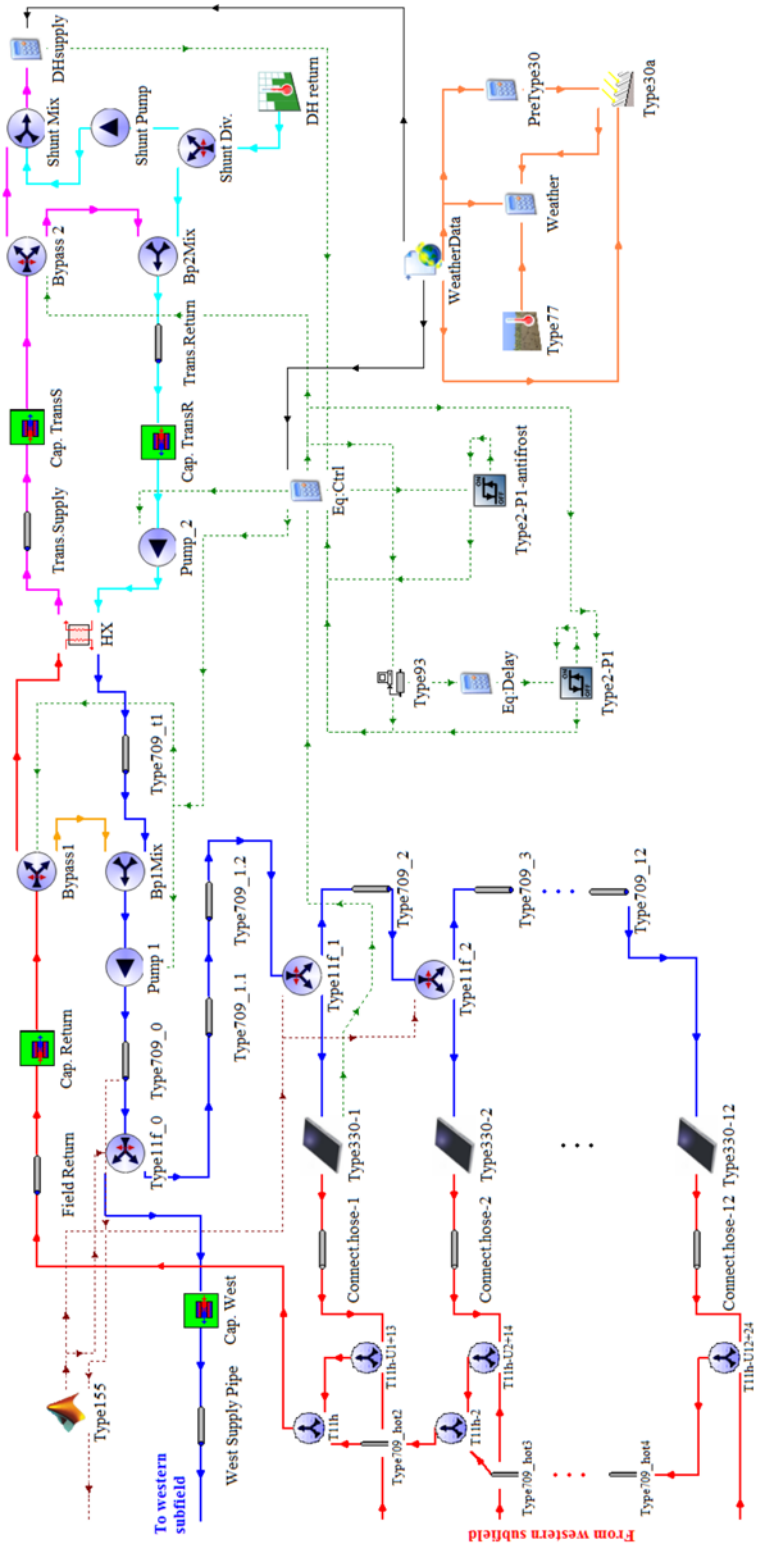

Figure 4.2: Detail of the TRNSYS-Matlab model. For sake of clarity, only 3 of the 24 collector rows are shown. Blue and red connections represent the supply and return pipes of the solar collector loop; purple and light blue connections represent the supply and the return pipes of the secondary side.

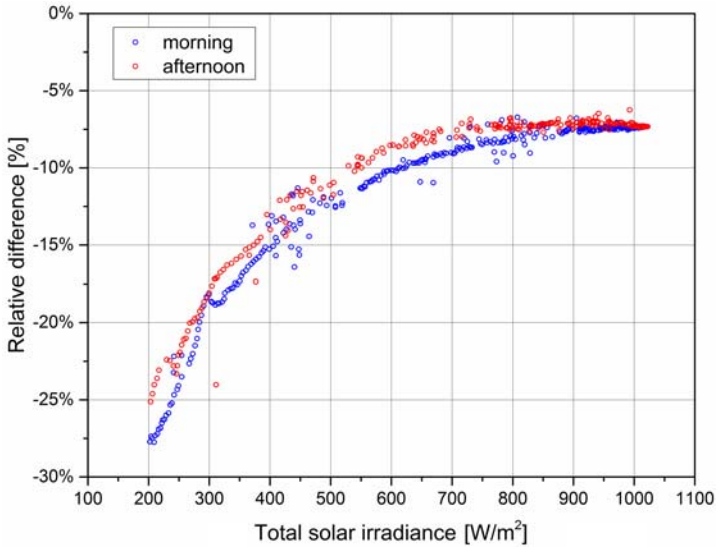

Figure 4.3: Relative difference in solar irradiance between silicon cell and thermopile pyranometer. The imperfect overlap of morning and afternoon data was likely due to slightly different orientations of the pyranometers.

field was always higher than the measured. A good agreement between the two could be found, if the peak collector efficiency in turbulent conditions was reduced by 5.5 % points, from 75.6 % to 70.1 %, corresponding to a relative decrease of 7.3 %. The same relative variation was assumed for the peak efficiency in laminar conditions.

Field inspections suggested that the disagreement between model and measurements could be partly caused by a difference between the actual collector efficiency and the efficiency from Soleff (Table 2.2). In particular, dirt on the glass cover of the collectors could be responsible for a decreased peak efficiency of the collectors. Hence, a glass pane of the same type as used in the HTHEATstore 35/08 collectors was tested. Its transmittance was measured before and after being exposed in the collector field for six months, from the end of October 2016 to the end of April 2017. The test was performed measuring the solar irradiance above and below the glass pane by means of two secondary standard pyranometers [88]. The utilized test rig is shown in Figure 4.4. Comparing the measurements before and after the six month period, a decrease of about 1 % point in the glass transmittance was found. Longer exposure periods may cause a further decrease in the glass transmittance. The further efficiency decrease required to match modeled and measured outlet temperature may have been caused by condensation of water (Figure 4.5) and outgassing particles from the insulation material on the inner side of the glass pane, higher heat losses caused by moist insulation, deviation between the actual collector performance and test report efficiency, etc. However, these aspects were not further investigated. Additionally, the accuracy of the measurements, such as accuracy of the measuring equipment (flow meter, pyranometers, temperature sensors) and orientation of the pyranometers, could also contribute to the disagreement.

The accuracy of the model was evaluated by comparing simulated and measured temperatures, energy outputs and flow rates under different weather conditions. The main results of the validations are summarized in Table 4.1 and Figure 4.6.

Figure 4.4: Experimental setup for testing the transmittance of a glass pane.

Figure 4.5: Condensation on glass pane of a collector in Høje Taastrup field.

Table 4.1 presents an overview of the comparison between measurements and model in terms of energy output from the collector field, energy delivered to the DH network, flow rate in the solar collector loop, fluid temperatures at the inlet/outlet of the collector field and at the end of the forward transmission pipe. Taking into account the accuracy of the measuring equipment and the variation of the density and specific heat of the heat transfer fluids at temperatures different from the nominal ones, the uncertainty of the measured energy outputs and cumulated flow rates can be calculated through the formula for propagation of error. So, the uncertainty of the measured energy outputs can be estimated to be about 1.5 %, while that of the mass flow rate about 0.8 %. Regarding the uncertainty on the RMSD of the considered temperatures, the accuracy of temperature sensors (0.25 K) can be assumed.

Figure 4.6 presents graphically the comparison between measured and modeled data for two days with different weather conditions. In particular the diagrams show the data from July 13, which was characterized by moving clouds (*cloudy* in Table 4.1) which caused sudden variations of the solar irradiance, and July 14, characterized mainly by clear sky.

A good agreement between model and measurements was generally found. Apart from the overcast day July 12, the model differed from the measurements no more than 1 % in terms of energy output and cumulated primary flow.

However, days characterized by sudden variations of solar irradiance (July 13 and 17) presented higher temperature deviations than clear sky days. A reason for this was that the recorded data were instantaneous values measured once a minute, with no information of what happened between one recording and the next. When the measured data were given as input to the TRNSYS model, these were assumed constant during the simulation time step. This is a reasonable assumption, if the inputs change slowly, such as in clear or overcast sky conditions. Higher deviations are likely to occur in case of higher frequency changes, such as sudden variations of the solar irradiance caused by moving clouds.

Also the different response times of the real pump and the pump model might play

Table 4.1: Comparison between measurements (M) and simulation results (S) for Høje Taastrup solar heating plant.

		12/07/2015	13/07/2015	14/07/2015	16/07/2015	17/07/2015
Weather condition		overcast	cloudy	sunny	sunny	cloudy
Field gross energy output (M)	MWh	2.42	6.63	11.4	11.7	8.63
Field gross energy output (S)	MWh	2.34	6.58	11.4	11.8	8.62
Deviation in gross energy output	%	-3.3 %	-0.8 %	0 %	0.9 %	-0.1 %
Energy delivered DH (M)	MWh	2.31	6.48	11.4	11.6	8.44
Energy delivered to DH (S)	MWh	2.27	6.47	11.3	11.7	8.45
Deviation in energy to DH	%	-1.7 %	-0.2 %	-0.9 %	0.9 %	0.1 %
Cumulated primary flow (M)	kg	$8.24 \cdot 10^4$	$1.79 \cdot 10^5$	$2.92 \cdot 10^5$	$2.99 \cdot 10^5$	$2.29 \cdot 10^5$
Cumulated primary flow (S)	kg	$8.03 \cdot 10^4$	$1.78 \cdot 10^5$	$2.95 \cdot 10^5$	$3.02 \cdot 10^5$	$2.29 \cdot 10^5$
Deviation in primary flow	%	-2.5 %	-0.6 %	1.0 %	1.0 %	0 %
RMSD($T_{\text{supply to field}}$)	K	1.37	1.20	1.33	1.10	1.28
RMSD($T_{\text{return from field}}$)	K	2.82	2.37	1.48	1.76	2.59
RMSD($T_{\text{supply to DH}}$)	K	3.77	2.20	1.43	1.89	2.29

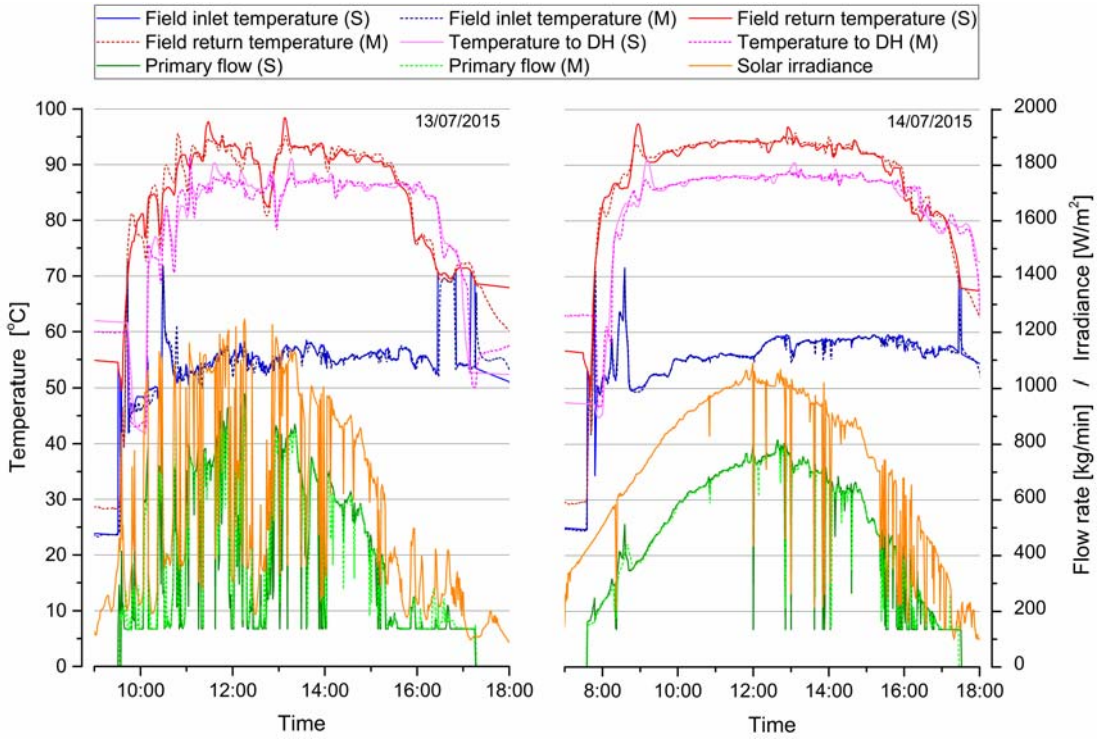

Figure 4.6: Comparison between measurements (M) and simulation results (S) based on the data from 13–14 July 2015.

a role. According to (Eq. 4.2), the pump in TRNSYS reacted instantly to any change in the value of Q_{sol}, while a real pump would have a certain inertia. The difference in response time can play a role in case of fast variations of the pump speed, caused by sudden changes of the solar irradiance.

Figure 4.6 shows that the larger deviations between measured and calculated field outlet temperature occurred in the early morning, especially in cloudy days. A possible explanation might be the simplified modeling of the collector heat capacity. In fact, according to the standard ISO 9806 [43], the collector heat capacity was accounted for through a single lumped parameter, without distinction between fluid and solid parts of the collector. This could limit the capability of reproducing accurately the dynamic response of the collector in case of large variations in absorber and fluid temperature. Additionally, among the collector coefficients determined by the quasi-dynamic test method [43], the collector thermal capacity is not always accurately identifiable, because the constant inlet temperature used in the test limits the dynamic response of the collector [89]. Finally, the thermal capacity determined by the test method is affected by the residence time of the fluid in the collector, and hence may change with the flow rate.

In case of July 12 (overcast sky conditions) a lower agreement with the measurements and model was found. The calculated gross energy output from the collector field and the energy delivered to the DH network were 3.5 % and 1.7 % lower than the measured. This was mainly caused by the lower cumulated flow rate in the simulation compared to the measurements (-2.6 %). In fact, although the measured and calculated profiles of the flow rates were extremely similar to each other, the measurements presented few sudden and brief peaks of flow rate, which did not appear in the model, because not justified by the recorded irradiance. Based on the above, the difference in response time between pyranometers and pumps, and the fact that the recorded data were instantaneous values may explain these peaks in the measured flow rates. Also the higher temperature deviations can be explained in this way. In fact, a difference between measured and calculated flow rates affects differently the plug flow in the real plant and in the model, causing a shift and mismatch of the temperature profiles. Finally, it should be noted that the energy production on this day was very low (only 2.42 MWh), so even modest absolute differences between model and measurements caused stronger relative differences, compared to days with higher energy output.

4.4 Investigated scenarios

After being validated, the TRNSYS-Matlab model was used to evaluate the effect of a number of optimization measures which could be applied to solar heating plants. These measures included variation of the temperature levels in the collector field, accurate input to the control strategy, feedback control on the field outlet temperature, control strategy based on weather forecast and use of different solar collector fluids.

When different scenarios were investigated, their performance was compared in terms of:

- energy delivered to the DH network, E_{DH};
- temperature-weighted energy to the DH network, $E_{DH,w}$, defined as $E_{DH,w} = E_{DH} \cdot (1 - 0.008\,\Delta T_{s\text{-}DH}^2)$, where $\Delta T_{s\text{-}DH}$ was the difference between the DH supply

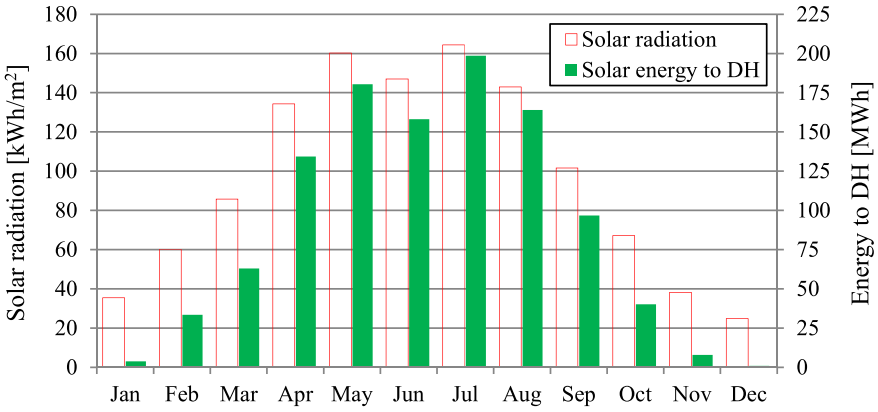

Figure 4.7: Monthly solar radiation on the collector plane (left axis) and energy delivered to the DH network (right axis) in the reference case.

temperature and the temperature at which energy from the solar heating plant was delivered to the network;

- electricity consumption of the pumps, E_{el}.

A reference case was first identified, according to what is described in Section 4.2. In this scenario the yearly energy output from the collector field was 1.13 GWh, the energy delivered to the DH (E_{DH}) was 1.08 GWh and the weighted energy to the DH ($E_{DH,w}$) was 1.05 GWh. The electricity consumption of the pumps (E_{el}) was 15.3 MWh. Frost protection operation (see Section 4.2) was active for approximately ten minutes during the entire year and did not require heat transfer from secondary to primary side.

The monthly energy delivered by the solar heating plant to the DH network, as well as the solar radiation on the collector plane, is shown in Figure 4.7. It can be seen that the performance of the plant was very poor in winter, partly because of the worse weather conditions, partly because of the higher temperatures required at the outlet of the collector field and the absence of an auxiliary heating plant nearby.

4.4.1 Lower outlet temperature set points

Because the heat demand from the DH network is higher in winter, an attempt was made to improve the energy output of the plant in this season. For this reason, the outlet temperature set point for the collector field was reduced, assuming that the lower temperature delivered to the DH network could be compensated by higher temperatures in the network. The set point was progressively lowered, down to a minimum value equal to the set point in summer time.

Nevertheless, if no other action was taken, this measure did not considerably improve the output of the field during winter. Considering the period November-March, the energy delivered to the DH network (E_{DH}) increased no more than 0.6 %.

4.4.2 Improved control strategy

The correlations (Eq. 4.1) and (Eq. 4.2), which regulated the flow rate in the solar collector field, assumed that the pyranometers received the same solar irradiance as

Table 4.2: Yearly energy output from the solar heating plant and electricity consumption of the pumps in different scenarios.

Case	E_{DH} [GWh]	$E_{DH,w}$ [GWh]	E_{el} [MWh]
Reference case	1.08	1.05	15.3
Accurate input	1.08	1.07	12.6
PID control	1.08	1.06	12.8

the collectors. However, unlike the pyranometers, which were installed on top of the collectors, a collector row could be shaded by the row in front. Secondly, the IAM of the collectors was not used in (Eq. 4.1). Another simplification was to assume a constant temperature drop across the heat exchanger. So the outlet temperature set point for the collector field was calculated adding a constant temperature rise to the DH supply temperature.

When these aspects were considered and the resulting corrected inputs were used for control purposes, the performance of the plant improved, as seen in Table 4.2 by comparing the *Reference case* and the *Accurate input* case. The weighted energy delivered to the DH network increased by 2 %, while electricity consumption decreased by 17 %. In fact, using the shaded solar radiation instead of the total unshaded radiation in (Eq. 4.1) decreased the value of Q_{sol} compared to the reference case, so resulting in a lower pumping energy. Additionally, the field outlet temperature became more constant, as can be seen in Figure 4.8, because the solar irradiance used by the control strategy was closer to the actual radiation reaching the collector absorber. Finally, the accurate estimation of the solar radiation and of the temperature drop across the heat exchanger allowed the collector field to reach the right temperature level required by the DH network, so improving the plant performance in terms of weighted energy to the DH.

Even if shadow effect, IAM and exact temperature drop across the heat exchanger were taken into account, the type of control described in Section 4.2 would still lack robustness. In fact, this control strategy represents an open-loop control, where the actual field outlet temperature plays no role in terms of control during normal operation. As long as the measured irradiance and the collector parameters used by the control strategy are representative of the actual conditions of the collector field, a good operation can be expected. Conversely, in case of a mismatch between inputs to the control strategy and real-world conditions – such as inaccurate reading of the pyranometers or collector efficiency different from the theoretical one – a disagreement between field outlet temperature and set point can be expected. So, an additional scenario was investigated where a PID feedback control was added on the field outlet temperature to correct the flow rate calculated by (Eq. 4.2), in the case that the field outlet temperature differed from the set point. The investigated scenario (*PID control* in Table 4.2 and Figure 4.8) used the same definition of Q_{sol} as the reference case (without considering shadow effect and IAM), while the outlet temperature set point was the same as in the *Accurate input* case.

Comparing the scenario implementing the PID control and that using accurate input in the control strategy, it can be noted that they were characterized by very similar performance, both in terms of energy (Table 4.2) and temperature profiles (Figure 4.8).

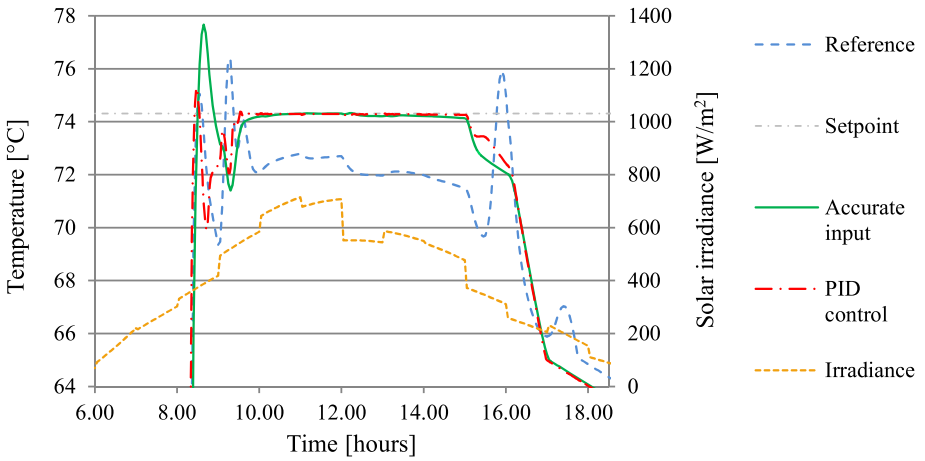

Figure 4.8: Outlet temperature from the collector field in different scenarios and solar irradiance on the collector plane on June 11.

Although in the *PID control* scenario the solar irradiance on the collector field was overestimated compared to the *Accurate input* scenario, the feedback control compensated for the inaccurate input parameters, decreasing the flow rate and achieving a field outlet temperature very close to the desired set point.

As higher accuracy of the input parameters is likely to be more complex and more expensive in terms of equipment, the integration of a PID controller seemed a more robust, flexible and economical solution.

4.4.3 Weather forecast

Assuming that the weather conditions at the plant location could be accurately forecast, the TRNSYS model was used to verify whether and how weather forecast could be used to improve the control strategy of the plant.

Two types of weather forecast were implemented: a short-term and a long-term forecast. These were tested using measured weather data from Høje Taastrup collector field, as they offered more high-frequency variability of solar irradiance compared to the Meteonorm weather data in TRNSYS (see Section 4.3.1).

In the short-term forecast, the upcoming solar irradiance was used to anticipate the regulation of the primary pump (see (Eqs. 4.1–4.2)), in the attempt of making the field outlet temperature more stable in case of moving clouds. However, the temperature profile did not become more constant.

In the long-term forecast, an additional requirement was added for start-up of the primary pump. The theoretical energy output from the collector field over a time interval, calculated based on the upcoming weather conditions, had to guarantee the operation of the collector field between nominal inlet and outlet temperatures at least at the lowest flow rate the primary pump could supply. This requirement was meant to avoid the start-up of the plant, in the case that the upcoming weather conditions would not allow operation for a minimum period of time. Although this was achieved in particular days characterized by mainly overcast sky with few and short sunny moments, the effect on the plant performance in the long term was negligible, with the electricity consumption reduced by only 0.1 %.

Table 4.3: Yearly energy output from the solar heating plant and electricity consumption of the pumps for different solar collector fluids.

Fluid	E_{DH} [GWh]	$E_{DH,w}$ [GWh]	E_{frost} [MWh]	E_{el} [MWh]
35 % glycol	1.08	1.07	0	12.6
22 % glycol	1.08	1.07	5	13.1
water	1.10	1.09	83	13.4

Hence, implementation of weather forecast in the control strategy did not seem to justify the additional cost and complexity of the control system, also considering that in reality forecast weather would have some uncertainty, which was avoided in the model.

4.4.4 Fluid types

Propylene glycol/water mixtures are commonly used in Danish solar collector fields made of flat plate collectors. The higher the glycol concentration, the lower is the freezing point. However, the fluid properties become poorer in terms of specific heat and heat transfer, and the pumping power increases due to the higher viscosity. Hence, different solar collector fluids were simulated, to identify the best compromise between fluid properties and frost protection. Beside the 35 % glycol/water mixture, simulations were run using water and a 22 % propylene glycol/water mixture (freezing point of -8 °C).

The use of different fluids entailed different collector efficiencies (calculated through the Soleff model, see Section 2.3.2), temperature set points for frost-protection operation (Section 4.2), characteristics of the primary pump and fluid properties.

The energy output and electricity consumption of the solar heating plant for the different fluids are listed in Table 4.3.

The use of water and of the 22 % glycol/water mixture increased the energy output of the plant because of the higher collector efficiency. Additionally, the higher maximum flow rate of the primary pump limited the overheating of collector fluid above the set point temperature in summer, so improving the performance of the collector field. In winter however heat had to be transferred from the DH network to the collector field for frost protection purposes (E_{frost}). In the case of water 83 MWh were injected into the collector field in winter, while the extra energy production achieved mainly in spring-summer was only 24 MWh. In the case of the 22 % glycol/water mixture the net balance was positive, but so small (+4 MWh) that it did not seem to justify the higher risk of freezing and the lower value that heat is likely to have in summer compared to winter.

The electricity consumption of the pumps increased. In fact, although the lower viscosity of the two fluids reduced the electricity consumption of the primary pump during normal operation, the secondary pump consumed more electricity because of the higher maximum flow rates of the primary pump and the matched flow between primary and secondary pump. Additionally, the pumps ran more often for frost protection purposes.

Chapter 5

Conclusions and recommendation

A number of simulation models for large solar collector fields and solar heating plants for DH applications were developed and validated against measurements.

Both measurements and simulation results showed that the flow regime in a solar collector significantly affected the collector efficiency. Hence its effect should be taken into account when modeling collector fields, where different flow regimes are expected to take place. A new TRNSYS collector type (Type 330) was developed to consider this aspect, as well as to match more closely the collector technical specifications usually presented in the collector datasheets.

A hydraulic model for calculating the pressure drop and flow distribution in a harp collector with U-type configuration was developed, validated and made publicly available. The results showed that turbulent flow made the flow distribution more uniform compared to laminar flow. Because turbulent flow also enhanced the heat transfer, this flow regime should be aimed for when designing and operating a solar collector.

The simulation results obtained through the hydraulic model for collector arrays showed that, when properly set, balancing valves achieved fairly uniform flow distribution, regardless of the operating conditions and layout of the collector array. However, in case of a regular layout and moderate number of collector rows, balancing valves were not strictly necessary.

Another option to achieve uniform outlet temperature from the different collector rows can be the use of thermo-differential valves installed in correspondence of the combining tee junction between the collector row outlet and the return distribution pipe. These valves do not require any electronics and automatically regulate based on the temperature differences [90]. They offer an active and more robust regulation of the row flow rate, and can compensate for external disturbances, such as different solar radiation on the collector rows due to different shading or increased hydraulic resistance in specific rows due to partial clogging of the pipes. Additionally, they prevent thermosyphon effect between the warmer distribution pipes and the colder collector row outlet at night.

From the development, validation and simulation results of the TRNSYS-Matlab models for solar heating plants, the following conclusions could be drawn. Accurate measurements and inputs are crucial for validation purposes. Special attention should be given to solar radiation sensors (accuracy, orientation, tidiness), heat exchangers

(nominal and actual heat transfer coefficient) and actual collector efficiency. In this respect, an in-situ test procedure to determine the efficiency of solar collector fields is currently under investigation at the company AEE INTEC in collaboration with the University of Innsbruck. To maintain a high collector efficiency, cleaning of the glass covers at least once a year is advisable to remove external soiling. Additionally, measures should be taken to avoid or reduce water condensation on the inner side of the glass covers, especially in collectors equipped with FEP foil. For this purpose ventilation holes should be placed between FEP foil and glass cover.

Considering the flow distribution improved the accuracy of the model, but required much longer programming and computing time, so this aspect should be taken into account, if justified by the aimed level of accuracy. Heat capacity may be considered for long and bulky transmission pipes. For shorter pipes or heat exchangers its role was negligible. The control strategy should have input data as close to reality as possible (e.g., shadows from row to row and IAM should be considered). If this solution is not convenient, a feedback control on the field outlet temperature can be a valid alternative and simultaneously make the control more robust. On the other hand, weather forecast-based controls seemed not to offer significant advantages, compared to the additional investment cost and the more complex control they require. Regarding the solar collector fluid, higher glycol concentrations in the solar collector fluid gave better results than lower concentrations, as the higher frost protection guaranteed by the former outweighed the better thermophysical properties of the latter.

Bibliography

[1] United Nations, "United Nations Framework Convention on Climate Change," 1992. Online at http://unfccc.int/resource/docs/convkp/conveng.pdf, accessed on 13/05/2017.

[2] United Nations, "Kyoto Protocol To the United Nations Framework Convention on Climate Change," 1998. Online at http://unfccc.int/resource/docs/convkp/kpeng.pdf, accessed on 13/05/2017.

[3] United Nations, "Paris Agreement," 2015. Online at http://unfccc.int/paris_agreement/items/9485.php, accessed on 13/05/2017.

[4] British Petroleum, "BP Statistical Review of World Energy 2016," 2016. Online at http://www.bp.com/content/dam/bp/pdf/energy-economics/statistical-review-2016/bp-statistical-review-of-world-energy-2016-full-report.pdf, accessed on 13/05/2017.

[5] Eurostat, "Consumption of energy," 2016. Online at http://ec.europa.eu/eurostat/statistics-explained/index.php/Consumption_of_energy#Further_Eurostat_information, accessed on 09/01/2017.

[6] L. Gynther, B. Lappillone, and K. Pollier, "Energy efficiency trends and policies in the household and tertiary sectors. An analysis based on the ODYSSEE and MURE databases," 2015. Online at http://www.odyssee-mure.eu/publications/br/energy-efficiency-in-buildings.html, accessed on 13/05/2017.

[7] U. Persson, *District heating in future Europe: Modelling expansion potentials and mapping heat synergy regions*. Ph.D. Thesis, Chalmers University of Technology, 2015.

[8] European Commission, "Review of available information accompanying the document Communication from the Commission to the European Parliament, the Council, the European Economic and Social Committee and the Committee of the Regions on an EU Strategy for Heating and Cooling." Brussels, Belgium, 2016. Online at https://ec.europa.eu/energy/sites/ener/files/documents/1_EN_autre_document_travail_service_part1_v6_0.pdf, accessed on 13/05/2017.

[9] F. Mauthner, W. Weiss, and M. Spörk-Dür, "Solar Heat Worldwide: Markets and Contribution to the Energy Supply 2014," 2016. Online at http://www.iea-shc.org/data/sites/1/publications/Solar-Heat-Worldwide-2016.pdf, accessed on 13/12/2016.

[10] J.-O. Dalenbäck and S. Werner, "Solar District Heating: Boundary Conditions and Market Obstacles," 2012. Online at http://www.solar-district-heating.eu, accessed on 13/12/2016.

[11] M. Schubert, C. Holter, and R. Soell, "Solar District Heating (SDH): Technologies used in large scale SDH plants in Graz, Operational experiences and further developments," in *Proceedings of 12th International Symposium on District Heating and Cooling*, (Tallinn, Estonia), pp. 140–142, 2010.

[12] D. Trier. Personal communication with D. Trier (PlanEnergi), 2016.

[13] S. Wittrup, "Verdens største solfangeranlæg i drift i Silkeborg," *Ingeniøren*, 10 Jan 2017. Online at http://ing.dk/artikel/verdens-stoerste-solfangeranlaeg-drift-silkeborg-191730, accessed on 13/05/2017.

[14] S. Furbo, B. Perers, and F. Bava, "Thermal performance of solar district heating plants in Denmark," in *Proceedings of EuroSun 2014 Conference*, (Aix-les-Bains, France), 2015. http://dx.doi.org/10.18086/eurosun.2014.19.11.

[15] Danish Energy Agency, "Energistatistik 2015," 2016. Online at http://ens.dk/service/statistik-data-noegletal-og-kort/maanedlig-og-aarlig-energistatistik, accessed on 13/05/2017.

[16] J. Windeleff and J. E. Nielsen, "Solar District Heating in Denmark." Danish Energy Authority, PlanEnergi, 2014.

[17] PlanEnergi, "Long term storage and solar district heating," 2016. Online at http://ens.dk/sites/ens.dk/files/Forskning_og_udvikling/sol_til_fjernvarme_brochure_endelig.pdf, accessed on 13/05/2017.

[18] Danish Energy Agency, "Regulation and planning of district heating in Denmark," 2016. Online at http://ens.dk/sites/ens.dk/files/Globalcooperation/regulation_and_planning_of_district_heating_in_denmark.pdf, accessed on 13/05/2017.

[19] Danish District Heating Association, "Danish District Heating Association," 2014. Online at http://www.danskfjernvarme.dk, accessed on 13/05/2017.

[20] Danish Energy Agency, "The Danish Energy Model: Innovative, Efficient and Sustainable," 2014. Online at http://ens.dk/en/our-responsibilities/global-cooperation/danish-energy-model, accessed on 10/01/2017.

[21] Danish Ministry of Energy, Utilities and Climate, "Aftale mellem regeringen (Socialdemokraterne, Det Radikale Venstre, Socialistisk Folkeparti) og Venstre, Dansk Folkeparti, Enhedslisten og Det Konservative Folkeparti om den danske energipolitik 2012-2020," 2012. Online at http://old.efkm.dk/energi-forsynings-klimapolitik/dansk-energi-forsynings-klimapolitik/energiaftale, accessed on 13/05/2017.

[22] Danish Government, "Regeringsgrundlag - For et friere, rigere og mere trygt Danmark," 2016. Online at http://www.stm.dk/multimedia/Regeringsgrundlag2016.pdf, accessed on 13/05/2017.

[23] Danish Government, "Our Future Energy," 2011. Online at http://stateofgreen.com/files/download/387, accessed on 13/05/2017.

[24] Danish Energy Agency, "Fjernvarmens rolle i den fremtidige energiforsyning," 2014. Online at http://ens.dk/sites/ens.dk/files/Vindenergi/fjernvarme_-_analyse_2014_web.pdf, accessed on 13/05/2017.

[25] Eurostat, "Natural gas price statistics," 2016. Online at http://ec.europa.eu/eurostat/statistics-explained/index.php/Natural_gas_price_statistics#Further_Eurostat_information, accessed on 12/01/2017.

[26] John Tang, "Nettoafregning for decentral kraftvarme: Beregningseksempler og konsekvenser af nettoafregning." Danish District Heating Association, 2015. Online at http://www.danskfjernvarme.dk/~/media/danskfjernvarme/gronenergi/analyser/2015-03-27nettoafregning-beregninger.pdf, accessed on 13/05/2017.

[27] P. A. Sørensen, "Solar District Heating Guidelines: Ownership and financing," 2012. Online at http://solar-district-heating.eu, accessed on 30/03/2017.

[28] J. E. Nielsen. Personal communication with J. E. Nielsen (PlanEnergi), 2016.

[29] S. Furbo, J. Dragsted, B. Perers, F. Bava, and K. P. Nielsen, "Variations of yearly thermal performance of Danish solar heating plants - measured and calculated," in *Proceedings of 4th International Solar District Heating Conference (SDH 2016)*, (Billund, Denmark), 2016. Online at http://solar-district-heating.eu/NewsEvents/SDHConference2016.aspx, accessed on 30/03/2017.

[30] Danish District Heating Association, "Solvarme dæmper prisen på energibesparelser," 2016. Online at http://www.danskfjernvarme.dk/nyheder/nyt-fra-dansk-fjernvarme/161220-solvarme-laegger-daemper-paa-prisen-energibesparelser, accessed on 16/01/2017.

[31] J. E. Nielsen, "Solar District Heating: Experiences from Denmark," 2014. Online at http://www.alpconv.org/it/organization/groups/past/wgenergy/default.html, accessed on 13/05/2017.

[32] P. A. Sørensen, M. V. Jensen, and N. From, "Smart district heating using the SUNSTORE concept," *Strojarstvo*, vol. 54, no. 6, pp. 455–461, 2012.

[33] A. V. Novo, J. R. Bayon, D. Castro-Fresno, and J. Rodriguez-Hernandez, "Review of seasonal heat storage in large basins: Water tanks and gravelwater pits," *Applied Energy*, vol. 87, no. 2, pp. 390–397, 2010. http://dx.doi.org/10.1016/j.apenergy.2009.06.033.

[34] J. Fan, Z. Chen, S. Furbo, B. Perers, and B. Karlsson, "Efficiency and lifetime of solar collectors for solar heating plants," in *Proceedings of ISES Solar World Congress 2009*, (Johannesburg, South Africa), pp. 331–340, 2009.

[35] T. Peschel, "Arcon and Sunmark merge," *Sun&Wind Energy*, 5 Feb 2015. Online at http://www.sunwindenergy.com/solar-thermal/arcon-sunmark-merge, accessed on 13/05/2017.

[36] J.-O. Dalenbäck and S. Werner, "Solar District Heating Guidelines: Market for Solar District Heating," 2012. Online at http://www.solar-district-heating.eu, accessed on 13/12/2016.

[37] P. A. Sørensen, "Solar District Heating Guidelines: Solar heat combined with other fuels," 2012. Online at http://solar-district-heating.eu, accessed on 30/03/2017.

[38] J.-O. Dalenbäck, "Large scale solar heating and cooling systems in Europe," in *Proceedings of ISES Solar World Congress 2007*, (Beijing, China), pp. 799–803, 2007. http://dx.doi.org/10.1007/978-3-540-75997-3_151.

[39] Danish District Heating Association, "Solarheatdata.eu," 2017. Online at http://www.solarheatdata.eu, accessed on 08/02/2017.

[40] A. Heller, *Large scale solar district heating evaluation, modelling and designing*. Ph.D. Thesis, Technical University of Denmark, 2000.

[41] Arcon-Sunmark A/S, "Drifts- og vedligeholdelsesmanual. Manual til Arcon-Sunmark solanlæg," 2015.

[42] P. A. Sørensen, P. Kristensen, S. Furbo, F. Ulbjerg, L. Holm, and T. Schmidt, "Optimeret solvarmeproduktion i et liberaliseret elmarked - Demonstration af fuldskalaanlæg i Brædstrup," 2009. Online at http://energinet.dk/SiteCollectionDocuments/Danskedokumenter/Forskning-PSO-projekter/6369Optimeretsolvarmeproduktion-demoBr%C3%A6dstrup.pdf, accessed on 13/05/2017.

[43] ISO, "ISO Standard 9806: Solar energy - Solar thermal collectors - Test methods." International Organization for Standardization (ISO), Geneva, Switzerland, 2014.

[44] J. P. Kummer, *Thermal performance of three freeze protection methods as applied to a large solar energy system*. Ph.D. Thesis, University of Wisconsin, 1986.

[45] L. Qin, *Analysis, modeling and optimum design of solar domestic hot water systems*. Ph.D. Thesis, Technical University of Denmark, 1998.

[46] W. Eisenmann, K. Vajen, and H. Ackermann, "Optimization of the material content of parallel flow flat-plate solar collector absorbers using a nomograph representation," in *Proceedings of ISES Solar World Congress 2003*, (Göteborg, Sweden), 2003.

[47] R. Hausner and H. Fechner, "Influence of the flow condition (laminar/turbulent) in the fluid tube on the collector efficiency factor of a fin absorber," in *Proceedings of EuroSun 1998 Conference*, (Portoroz, Slovenia), 1998.

[48] F. Bava and S. Furbo, "Comparative test of two large solar collectors for solar field application," in *Proceedings of EuroSun 2014 Conference*, (Aix-les-Bains, France), 2014. http://dx.doi.org/10.18086/eurosun.2014.16.03.

[49] P. B. Rasmussen and S. Svendsen, "SolEff, Program til beregning af solfangeres effektivitet." Laboratoriet for Vanneisolering - Technical University of Denmark, 1996.

[50] F. Bava, J. E. Nielsen, S. Knabl, A. Brunger, S. Furbo, and C. Fink, "Results of IEA SHC Task 45: Large Scale Solar Heating and Cooling Systems. Subtask A: Collectors and Collector Loop," *Energy Procedia*, vol. 91, pp. 546–556, 2016. http://dx.doi.org/10.1016/j.egypro.2016.06.197.

[51] M. Haller, M. Haller, B. Perers, C. Bale, J. Paavilainen, A. Dalibard, S. Fischer, and E. Bertram, "TRNSYS Type 832 v5.01 Dynamic Collector Model by Bengt Perers Updated Input-Output Reference," 2013.

[52] TESS, "TESSLibs 17 Component Libraries for the TRNSYS Simulation Environment," 2012. Online at www.tess-inc.com, accessed on 30/03/2017.

[53] B. Perers, "Dynamic method for solar collector array testing and evaluation with standard database and simulation programs," *Solar Energy*, vol. 50, no. 6, pp. 517–526, 1993. http://dx.doi.org/10.1016/0038-092X(93)90114-4.

[54] SP Technical Research Institute of Sweden, "Solar Keymark Certificate HTHE-ATstore 35/08 No. SP SC0843-14." Borås, Sweden, 2016. Online at http://www.solarkeymark.dk, accessed on 13/12/2016.

[55] J. E. Rohde and R. H. Knoll, "Analysis of a solar collector field water flow network." Lewis Research Center, 1976. Online at http://ntrs.nasa.gov/search.jsp?R=19760024583, accessed on 13/12/2016.

[56] J. P. Chiou, "The effect of nonuniform fluid flow distribution on the thermal performance of solar collector," *Solar Energy*, vol. 29, no. 6, pp. 487–502, 1982.

[57] X. A. Wang and L. G. Wu, "Analysis and performance of flat-plate solar collector arrays," *Solar Energy*, vol. 45, no. 2, pp. 71–78, 1990.

[58] G. Jones and N. Lior, "Flow distribution in manifolded solar collectors with negligible buoyancy effects," *Solar Energy*, vol. 52, no. 3, pp. 289–300, 1994.

[59] V. Weitbrecht, D. Lehmann, and A. Richter, "Flow distribution in solar collectors with laminar flow conditions," *Solar Energy*, vol. 73, no. 6, pp. 433–441, 2002.

[60] J. Fan, L. J. Shah, and S. Furbo, "Flow distribution in a solar collector panel with horizontally inclined absorber strips," *Solar Energy*, vol. 81, no. 12, pp. 1501–1511, 2007. http://dx.doi.org/10.1016/j.solener.2007.02.001.

[61] R. Dorantes, G. García, C. Salazar, H. Oviedo, H. González, R. Alanis, E. Salazar, and I. R. Martín-Dominguez, "Thermal and hydraulic design of a solar collector field for a primary school pool," *Energy Procedia*, vol. 57, pp. 2515–2524, 2014. http://dx.doi.org/10.1016/j.egypro.2014.10.262.

[62] S. Knabl, C. Fink, P. Ohnewein, F. Mauthner, and R. Hausner, "Requirements and guidelines for collector loop installation," 2014. Online at http://task45.iea-shc.org/fact-sheets, accessed on 13/12/2016.

[63] P. Kovacs, M. Persson, P. Wahlgren, and S. Jensen, "Quality assurance in solar thermal heating and cooling technology - Pressure drop over a solar flat plate collector using various heat transfer fluids," 2012. Online

at http://www.estif.org/solarkeymarknew/images/downloads/QAiST/qaist%20d2.2_r2.13%20pressure%20drop.pdf, accessed on 13/05/2015.

[64] P. R. H. Blasius, "Das Aehnlichkeitsgesetz bei Reibungsvorgangen in Flüssigkeiten," *Forschungsheft*, vol. 131, pp. 1–41, 1913.

[65] C. Colebrook, "Turbulent flow in pipes, with particular reference to the transition region between smooth and rough pipe laws," *Journal of the Institution of Civil Engineers*, vol. 11, pp. 133–156, 1939.

[66] S. Haaland, "Simple and Explicit Formulas for the Friction Factor in Turbulent Flow," *Journal of Fluids Engineering (ASME)*, vol. 105, no. 1, pp. 89–90, 1983.

[67] D. D. Joseph and B. H. Yang, "Friction factor correlations for laminar, transition and turbulent flow in smooth pipes," *Physica D*, vol. 239, pp. 1318–1328, 2010. http://dx.doi.org/10.1016/j.physd.2009.09.026.

[68] I. Idelchik, *Handbook of hydraulic resistance*. CRC press, 3rd ed., 1994.

[69] IMI Hydronic Engineering, "STAD Balancing valves DN 15-50," 2015. Online at http://www.imi-hydronic.com/en/products-solutions/balancing-and-control/balancing-valves, accessed on 13/12/2016.

[70] A. Le Denn, "Solar District Heating Guidelines: Calculation tools and methods," 2014. Online at http://solar-district-heating.eu, accessed on 13/12/2016.

[71] J. E. Nielsen and R. Battisti, "Solar District Heating Guidelines: Feasibility study," 2012. Online at http://solar-district-heating.eu, accessed on 13/12/2016.

[72] PlanEnergi, "Fjernsol II," 2013. Online at http://www.solarkey.dk/fjernsol.htm, accessed on 13/05/2017.

[73] L. Deschaintre, "Development of a solar district heating online calculation tool," *Energy Procedia*, vol. 48, pp. 1065–1075, 2014. http://dx.doi.org/10.1016/j.egypro.2014.02.121.

[74] CIT Energy Management, "Sunstore4 Tool," 2013. Online at http://sunstore4.eu/use-results/sunstore4-tool, accessed on 13/05/2017.

[75] S. A. Klein et al., "TRNSYS 17 A Transient System Simulation program." Solar Energy Laboratory, University of Wisconsin-Madison, 2012. Online at http://www.trnsys.com, accessed on 13/01/2017.

[76] EMD International A/S, "energyPRO," 2016. Online at http://www.emd.dk/energypro, accessed on 13/05/2017.

[77] Vela Solaris, "Polysun Simulation Software," 2016. Online at http://www.velasolaris.com, accessed on 13/05/2017.

[78] Natural Resources Canada, "RETScreen," 2016. Online at http://www.nrcan.gc.ca/energy/software-tools/7465, accessed on 13/05/2017.

[79] P. Schwarzbözl, "A TRNSYS Model Library for Solar Thermal Electric Components (STEC). Reference Manual," 2007. Online at http://sel.me.wisc.edu/trnsys/trnlib/stec/stec.htm, accessed on 30/03/2017.

[80] M. S. Saleem, A. Haider, and N. Abas, "Review of Solar Thermal Water Heater simulations using TRNSYS," in *Proceedings of 2nd International Conference on Power Generation Systems and Renewable Energy Technologies (PGSRET 2015)*, (Islamabad, Pakistan), pp. 68–73, 2015. http://dx.doi.org/10.1109/PGSRET.2015.7312251.

[81] A. M. Abdel Dayem, M. Nabil Metwally, A. S. Alghamdi, and E. M. Marzouk, "Numerical simulation and experimental validation of integrated solar combined power plant," *Energy Procedia*, vol. 50, pp. 290–305, 2014. http://dx.doi.org/10.1016/j.egypro.2014.06.036.

[82] M. Biencinto, R. Bayón, E. Rojas, and L. González, "Simulation and assessment of operation strategies for solar thermal power plants with a thermocline storage tank," *Solar Energy*, vol. 103, pp. 456–472, 2014. http://dx.doi.org/10.1016/j.solener.2014.02.037.

[83] M. Biencinto, L. González, and L. Valenzuela, "A quasi-dynamic simulation model for direct steam generation in parabolic troughs using TRNSYS," *Applied Energy*, vol. 161, pp. 133–142, 2016. http://dx.doi.org/10.1016/j.apenergy.2015.10.001.

[84] S. Raab, D. Mangold, and H. Müller-Steinhagen, "Validation of a computer model for solar assisted district heating systems with seasonal hot water heat store," *Solar Energy*, vol. 79, no. 5, pp. 531–543, 2005. http://dx.doi.org/10.1016/j.solener.2004.10.014.

[85] B. Sibbitt, D. McClenahan, R. Djebbar, J. Thornton, B. Wong, J. Carriere, and J. Kokko, "The performance of a high solar fraction seasonal storage district heating system - Five years of operation," *Energy Procedia*, vol. 30, pp. 856–865, 2012. http://dx.doi.org/10.1016/j.egypro.2012.11.097.

[86] F. Bava, S. Furbo, and B. Perers, "Simulation of a Solar Collector Array Consisting of two Types of Solar Collectors, with and Without Convection Barrier," *Energy Procedia*, vol. 70, pp. 4–12, 2015. http://dx.doi.org/10.1016/j.egypro.2015.02.091.

[87] SolData, "SolData 80spc Pyranometer - Data and application notes," 2016. Online at http://www.soldata.dk/pyr-80spc.htm, accessed on 30/03/2017.

[88] ISO, "ISO Standard 9060: Solar energy - Specification and classification of instruments for measuring hemispherical solar and direct solar radiation." International Organization for Standardization (ISO), Geneva, Switzerland, 2003.

[89] W. Kong, B. Perers, J. Fan, S. Furbo, and F. Bava, "A new Laplace transformation method for dynamic testing of solar collectors," *Renewable Energy*, vol. 75, pp. 448–458, 2015. http://dx.doi.org/10.1016/j.renene.2014.10.026.

[90] N. V. Ruth. Personal communication with Nico van Ruth (Conico Valves b.v.), 2017.

Part II

Papers

"Video meliora proboque,
deteriora sequor."
— Ovidius

Paper I

Comparative test of two large solar collectors for solar field application

Federico Bava and Simon Furbo

Proceedings of EuroSun 2014 Conference

Conference Proceedings

EuroSun 2014
Aix-les-Bains (France), 16 – 19 September 2014

Comparative test of two large solar collectors for solar field application

Federico Bava[1] and Simon Furbo[1]

[1] DTU Civil Engineering, Technical University of Denmark, Brovej, Building 118, 2800 Kgs. Lyngby (Denmark)

Abstract

Two large flat plate solar collectors for solar heating plants were tested according to the standard norm EN 12975-2. The two collectors were almost identical, the only difference being a thin FEP (fluorinated ethylene propylene) foil interposed between the absorber and the glass cover in one of them, in order to decrease convection losses. The efficiencies of the collectors were tested for different flow rates and tilt angles. The effect of the change from laminar to turbulent regime was investigated as well. Numerical models of the two collectors were developed with the software Soleff and their results were compared to the experimental measurements. The experimental results showed that the FEP foil caused a decrease in the optical efficiency of 2-4 percent. Nevertheless, the collector with the FEP foil performed better when the mean temperature of the solar collector fluid was sufficiently high. Additionally, the collector efficiency of both collectors increased at higher flow rates and tilt angles. The models developed in Soleff fit the experimental results with an average error of 1% in case of fully laminar and turbulent flow, so that they are likely to be suitable to simulate the collector performances in untested conditions. On the other hand, the software proved to be inadequate to study the collector efficiency in the transition region between laminar and turbulent regime.

Keywords: solar collector, solar heating plant, efficiency, tilt angle, flow rate, flow regime, FEP, Soleff

1. Introduction

By the end of 2013 Denmark had already installed almost 400,000 square meters of thermal collectors for solar heating plants, while another 350,000 square meters were to be built in the near future (Windeleff and Nielsen, 2014; Furbo et al., 2014). In a scenario still characterized by strong growth in the installed solar collectors' capacity, even an efficiency improvement of few percent would lead to a large increase in the overall energy production in absolute terms. For this reason, knowing in which conditions a collector performs best is of key importance. Nevertheless, the technical specification sheets released by collector manufacturers usually state the collector efficiency only for one operating condition, which can differ from those actually used in solar plant applications, so introducing uncertainty when predicting the performance of real installations.

This study focused on an experimental test of two large flat plate solar collectors (models HT-SA 35-10 and HT-A 35-10), produced by the Danish company ARCON Solar A/S. The only difference between the two collectors was the presence of a FEP (fluorinated ethylene propylene) foil interposed between the absorbing plate and the glass cover in the model HT-SA only. The idea of using a polymer foil as convection barrier dates back to the 70's (Wilson, 1978), but has seldom been implemented. The presence of the foil reduces the convection losses, as the air between absorber and glass circulates in two different layers of convective cells, one above and the other below the foil. The heat losses from the collector cover are therefore lower than in the collector without foil, due to the additional thermal resistance given by the convective heat transfer coefficient between air and FEP foil. On the other hand, as the foil is not completely transparent, it slightly reduces the solar irradiance reaching the absorber. Consequently, there is a certain temperature below which the collector without foil performs better than the other, as the transmittance of the cover plays a more significant role than the thermal losses.

Selection and/or peer review under responsibility of EuroSun2014 Scientific Committee
doi:10.18086/eurosun.2014.16.03 Available at http://proceedings.ises.org

The technical specification sheets (Arcon Solar, 2010; SP Technical Research Institute of Sweden, 2011) state the collector efficiency when a 25 (litres min^{-1}) flow rate of pure water is supplied to a 60° tilted collector, conditions which are very unlikely to be found in a Danish solar collector field. However, this incongruity is tolerated by the present standard for solar collector testing (EN 12975-2), which does not prescribe strict operating conditions at which to evaluate the efficiency.

The two collectors were tested at different flow rates and tilt angles, using a mixture of propylene glycol and water with a mass concentration of 40%. In fact, the efficiency of a solar collector is influenced by the volume flow rate, as shown by Chiou (1982) and Wang and Wu (1990) for vertical pipe collectors and by Fan and Furbo (2008) for horizontal pipe collectors. Regarding the tilt angle, both semi-empirical correlations (Klein, 1980; Agarwal and Larson, 1981) and experimental measurements (Furbo and Holck, 1995) show that the top heat losses decrease when tilting a flat plate collector.

The experimental determination of the collector efficiency equation is of key importance when assessing the actual performance of the collectors in certain operating conditions. As experimental tests are usually time consuming and expensive, it may be useful to have a model that is able to estimate the collector efficiency, so that it can be used to predict its value also in conditions that differ from those tested. In this study, such a model was created in Soleff, software developed at Technical University of Denmark (Rasmussen and Svendsen, 1996), and compared to the experimental measurements.

2. Materials and method

2.1 Experimental part

The two investigated solar collectors were manufactured by the Danish company ARCON Solar A/S. More specifically they were the flat plate collectors HT-SA 35-10 and HT-A 35-10. The collectors were largely identical in terms of design and technical specifications and the only relevant difference was a 0.025 mm thick FEP foil. The different appearance of the two collectors can be seen in Fig. 1.

Fig. 1: Solar collector HT-A 35-10 (left) and HT-SA 35-10 (right) at the Department of Civil Engineering at the Technical University of Denmark.

The collectors were installed beside each other, so that they experienced identical weather conditions. They both had an orientation of 9.5° West with respect to South, while the tilt angle could be changed through the use of semi-mobile scaffolding. Both collectors had external dimensions of 2.27 x 5.96 x 0.14 m with a total gross area of 13.57 m^2, while the aperture area was equal to 12.56 m^2. The absorber consisted of 18 aluminium strips covered by a selective coating. Each collector had two manifolds with a diameter of 35 mm, placed vertically along the sides and connected by 18 horizontal copper tubes with a diameter of 10 mm, laser-welded below the absorber strips. The external cover was made of an anti-reflective treated glass with a thickness of 3.2 mm. The insulation consisted of mineral wool, with a thickness of 75 mm below and 30 mm along the edges. The stated efficiencies, based on the aperture area and using a pure water flow of 25 (litres min^{-1}) and a 60° tilt angle, are given by the equations (Eq.1) and (Eq.2) for the model HT–A and HT–SA respectively (Arcon Solar, 2010; SP Technical Research Institute of Sweden, 2011).

$$\eta_{HT-A,60°,25} = 0.845 - 2.94 \cdot \frac{T_m - T_a}{G} - 0.013 \cdot \frac{(T_m - T_a)^2}{G} \qquad \text{(Eq.1)}$$

$$\eta_{HT-SA,60°,25} = 0.827 - 1.18 \cdot \frac{T_m - T_a}{G} - 0.032 \cdot \frac{(T_m - T_a)^2}{G} \qquad \text{(Eq.2)}$$

where η [-] is the collector efficiency,

T_m [°C] is the mean fluid temperature inside the collector,

T_a [°C] is the ambient temperature,

G [W m^{-2}] is the global solar irradiance on the collector plane,

the subscripts of η have the following meaning: *HT-A*/*HT-SA* refer to the collector model; the first numerical subscript denotes the tilt angle (in degrees), while the second numerical subscript the flow rate (in litres per minute).

The solar collectors were installed and tested in a solar collector test facility at the Technical University of Denmark. The fluid flow rates to the collectors were measured by two electromagnetic flow meters manufactured by Kamstrup (model MP240 and MP115 for the collector HT-A and HT-SA respectively). The inlet temperatures were measured by type TT thermocouples using a copper-constantan junction, while the temperature differences between outlet and inlet temperature were measured by thermopiles with five copper-constantan junctions at each measuring point. The total radiation on the collector plane was measured independently for each collector by a CM11 pyranometer, produced by Kipp & Zonen and fully compliant with the norm ISO 9060, while the diffuse radiation was measured by a similar pyranometer equipped with a shadow band.

The collectors were tested with a tilt angle of 45° at 5, 10 and 25 (litres min^{-1}) between 2011 and 2012, and then with tilt angles of 30° and 60° at 25 (litres min^{-1}) in 2013, using a propylene glycol/water mixture with a 40% weight concentration as solar collector fluid. The collector efficiency expressions were evaluated according to the steady-state method described in the norm EN 12975-2, so at least four independent data points were obtained for at least four different temperature levels, in a range between 20 °C and 100 °C. These data points were then interpolated by means of regression according to the method of least squares.

As different flow rates and temperature levels might cause changes in flow regime and therefore affect the heat transfer between absorber and solar collector fluid, pressure drop tests were performed on the HT-SA collector in 2014, in order to identify in which range of Reynolds numbers the transition from laminar to turbulent regime occurred. Such tests were carried out using a TA-SCOPE differential pressure sensor, manufactured by TA Hydronics, and supplying the collector with water at approximately 20-30 °C and varying the flow rate between 10 and 30 (litres min^{-1}). As the pressure drop measurements were taken at the inlet and outlet of the collector, the contribution given by the inlet/outlet connections and manifolds needed to be estimated and subtracted, in order to identify the pressure drop due to the horizontal pipes only. The pressure drops given by inlet/outlet connections and manifolds were evaluated using correlations found in literature (Idelchik, 1994). When the pressure drop across the horizontal pipes was isolated, the Darcy friction factor was evaluated according to (Eq.3).

$$f = \frac{2 D \cdot \Delta p}{L \cdot \rho \cdot w^2} \qquad \text{(Eq.3)}$$

where f [-] is the Darcy friction factor,

D [m] is the inner diameter of the horizontal pipe,

Δp [Pa] is the pressure drop across the horizontal pipe,

L [m] is the length of the horizontal pipe,

ρ [kg m^{-3}] is the fluid density evaluated at the mean fluid temperature across the collector,

w [m s^{-1}] is the mean fluid velocity in the horizontal pipe.

The incidence angle modifier was evaluated according to the test procedure suggested in the norm EN 12975-2, but the tangent formula (Eq.4) was used in place of the cosine formula, as the former proved to fit the experimental data more accurately than the latter.

$$IAM = 1 - \tan^{p}\left(\frac{\Theta}{2}\right) \qquad \text{(Eq.4)}$$

where Θ [°] is the angle of incidence,

p [-] is the characteristic coefficient.

2.2 Soleff simulation

The calculation of the experimental efficiency curves is of key importance to assess the actual performance of the collectors under given operating conditions. It could be both interesting and useful to have a model able to evaluate the collector efficiency also in conditions that differ from those tested. Such models were created using Soleff, a solar collector simulation software developed at Technical University of Denmark (Rasmussen and Svendsen, 1996).

Soleff requires a large number of input parameters, ranging from design characteristics of the collector to operating and weather conditions. Regarding the weather conditions, measured data were used whenever available. The earth radiation temperature and the sky temperature were assumed equal to the ambient temperature and to the ambient temperature decreased by 20 K respectively. Most of the collector characteristics were found either in the collector datasheets or in literature (Rasmussen and Svendsen, 1996; Furbo and Shah, 2003). Input parameters for which the exact value could not be found were assumed according to common values found in literature and iteratively modified in order to obtain the best fit with the experimental data.

Despite the large number of different aspects which is considered by Soleff, this software cannot take into account the complexity of the real-world operation. For example, the software assumes uniform flow distribution in the different pipes, constant fluid properties across the collector and sudden change from laminar to turbulent flow regime at a Reynolds number (*Re*) of approximately 2200. The last one proved to be the less accurate simplification, as measured efficiencies obtained for Reynolds numbers between 2200 and 2400 were always lower than those computed by the Soleff models (which assumes turbulent regime in this range). Then, increasing slightly the pipe diameter in the simulation models, the flow was forced to be laminar and the efficiency in this case was calculated. So, the experimental results could be compared to those returned by the simulation models, in both cases where turbulent and laminar flow was assumed.

3. Results

3.1. Experimental part

The coefficients of the efficiency expressions based on the experimental results and according to the standard norm EN 12975-2 are listed in Tab. 1, where η_0 represents the optical efficiency, a_1 the first order heat loss coefficient and a_2 the second order heat loss coefficient.

Tab. 1: Coefficients of the efficiency expressions according to the experimental results.

Case	Collector model	Fluid type	Flow rate [litres min^{-1}]	Tilt [°]	η_0 [-]	a_1 [W m^{-2} K^{-1}]	a_2 [W m^{-2} K^{-2}]
1	HT-A	40% glycol	5	45	0.835	3.13	0.0143
2	HT-A	40% glycol	10	45	0.843	3.55	0.0070
3	HT-A	40% glycol	25	45	0.845	3.80	-
4	HT-A	40% glycol	25	60	0.850	3.71	-
5	HT-A	40% glycol	25	30	0.832	4.04	-
6	HT-SA	40% glycol	5	45	0.818	2.76	0.0096
7	HT-SA	40% glycol	10	45	0.804	2.26	0.0107
8	HT-SA	40% glycol	25	45	0.810	2.83	-
9	HT-SA	40% glycol	25	60	0.806	2.74	-
10	HT-SA	40% glycol	25	30	0.805	3.13	-

The efficiency curves from Tab.1 can be seen in Fig. 2 (constant tilt angle and variable flow rate) and Fig. 3 (constant flow rate and variable tilt angle). Comparing the different efficiency equations, it can be noted that the optical efficiency was mainly independent of both flow rate and tilt angle. However, it was strongly influenced by the presence of the FEP foil, which caused a decrease of between 2 and 4 percent.

Nevertheless, the presence of the foil reduced the heat losses by approximately 0.6-1.1 W m^{-2} K^{-1}, so that for temperatures higher than a specific value (which can be defined as *intersection reduced temperature*), the HT-SA collector performed better than the HT-A model. Another evident remark is the absence of the second order heat loss coefficient in the efficiency expressions referring to 25 (litres min^{-1}) flow rate, which is discussed in more detail in section 4.

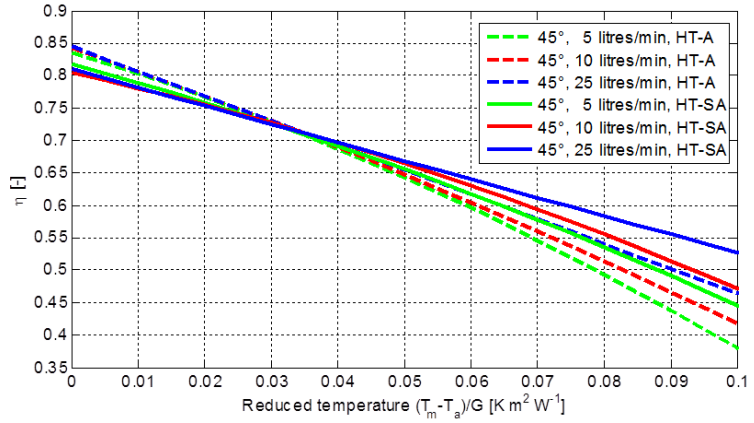

Fig. 2: Efficiency curves at different flow rates for the HT collectors at 45° tilt and for a total solar irradiance G=1000 W m^{-2}.

As Fig. 2 shows, the larger the flow rate was, the higher the efficiency. The difference in efficiency between 5 and 10 (litres min^{-1}) flow rates and the 25 (litres min^{-1}) case became more significant at high temperatures, because of the presence of the second order heat loss coefficient, which was missing in the efficiency expressions for 25 (litres min^{-1}).

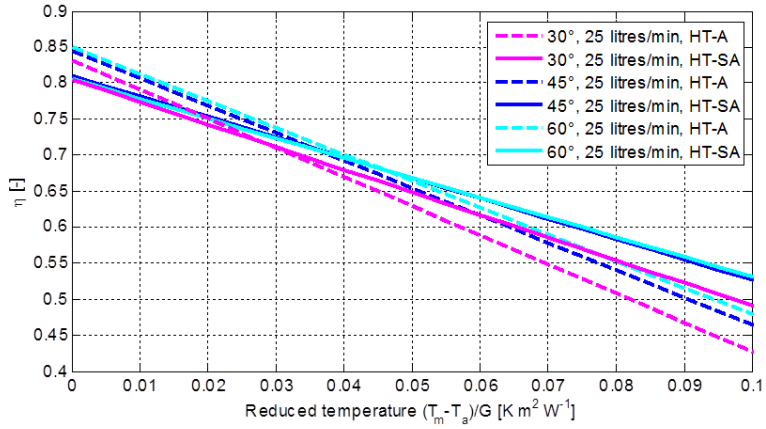

Fig. 3: Efficiencies curves at different tilts for the HT collectors at 25 (litres min^{-1}).

From Fig. 3, it may be seen that the larger the tilt angle, the higher the efficiency. Nevertheless, the relation between tilt angle and efficiency was not linear for either of the collectors. In fact, taking 45° tilt as a reference, decreasing the angle to 30° (-33%) caused an increase in the first order heat loss coefficient by about 10%, while a tilt of 60° (+33%) caused the same coefficient to decrease by only about 3%. In fact, in Fig. 3 it is clear that the efficiency curves for the 45° and 60° tilt angles are very close to each other, and they almost overlap in the case where the FEP foil is present. The optical efficiency of the HT-A collector at 30° tilt was unexpectedly lower than at other tilt angles, which might be due to the slightly different weather conditions from test to test.

The IAM was measured in all the different operating conditions and the values of the *p* exponent are listed in Tab. 2. Despite the scattered values, characterized by a standard deviation of approximately 0.12 for both collectors, the results showed clearly that the presence of the FEP foil reduced the optical properties of the cover, as the HT-A collector had a higher IAM curve than the HT-SA model in every operating condition. On the other hand, tilt angle and flow rate did not appear to influence the IAM in a specific way, so that if a single value of the *p* exponent needed to be chosen, the simplest approximation would consist in using the arithmetic mean, which is equal to 3.9 and 3.6 for the solar collector HT-A and HT-SA respectively.

Tab. 2: Exponent *p* in the tangent formula of the incidence angle modifier.

Tilt angle [°]	Flow rate [litres min^{-1}]	*p* exponent	
		HT-A	HT-SA
45°	5	4.05	3.72
45°	10	3.78	3.42
45°	25	3.73	3.68
60°	25	3.94	3.68
30°	25	3.78	3.54
Mean		3.85	3.61
Standard deviation		0.12	0.11

Regarding the pressure drop measurements and the following analysis to calculate the Darcy friction factor, the results of three independent series of tests are represented in Fig. 4. These results show how the friction factor calculated in all the three series of tests presented the same trend, where three different regions can be identified. The first region (Re<2000) is characterized by a steep decrease of the friction factor as the Reynolds number increases and corresponds to the laminar regime. The second (2000<Re<3000) represents the transition region and presents a slight increase of the friction factor with the Reynolds number. The third (Re>3000) is the turbulent region and shows again a decreasing trend of the friction factor as function of the Reynolds number, but much less steep than in the laminar regime.

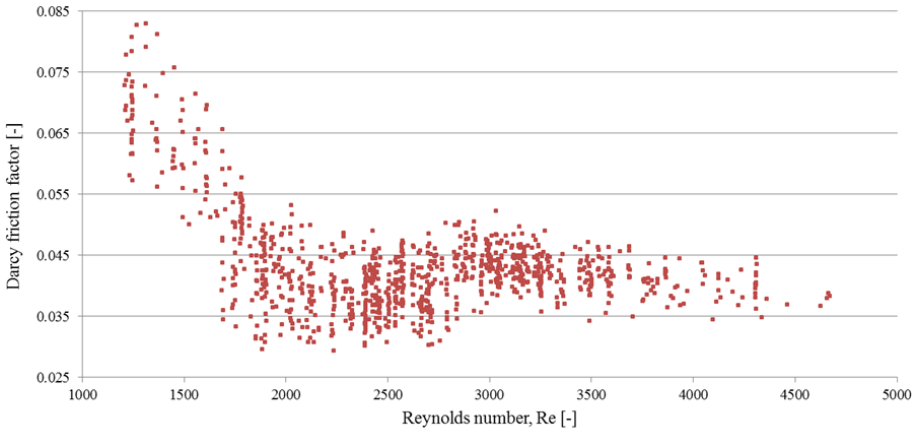

Fig. 4: Calculated Darcy friction factor as function of the Reynolds number in the horizontal pipes of the HT-SA collector.

3.2. Comparison between experimental efficiency results and Soleff simulation

The simulation models developed in Soleff were used to evaluate the theoretical efficiency of the two collectors, based on the weather and operation conditions measured during the efficiency tests. The measured and the theoretical efficiency points for the different flow rate and tilt angle conditions are shown in Fig. 5 and Fig. 6. For the sake of clarity, the efficiency points computed by the Soleff models at operating conditions corresponding to Reynolds numbers between 2200 and 2400 are not represented in Fig. 5 and Fig. 6, but are shown independently in Fig. 7.

From Fig. 5 and Fig. 6 it can be noted that the simulation models fit the experimental data points in the laminar (Re<2000) and turbulent regime (Re>3800). The average relative difference between experimental efficiency values and simulated ones is 1% for both the HT-A and HT-SA collector, while the maximum deviation is equal to 2.2% for the HT-A model and 1.8% for the HT-SA model. From the diagrams it is possible to notice that the experimental efficiency points at 5 and 10 (litres min^{-1}) are mainly aligned and then could be accurately interpolated by quadratic efficiency curves (cases 1, 2, 6 and 7 in Tab. 1). On the other hand, efficiency points obtained for 25 (litres min^{-1}) flow rate presented some kind of discontinuity when the ratio $(T_m-T_a)/G$ was between 0.044 and 0.051 K m^2 W^{-1}. In fact the efficiency values for this temperature level were higher than what would be expected from the extrapolated curve fitting the efficiency points obtained for lower values of $(T_m-T_a)/G$.

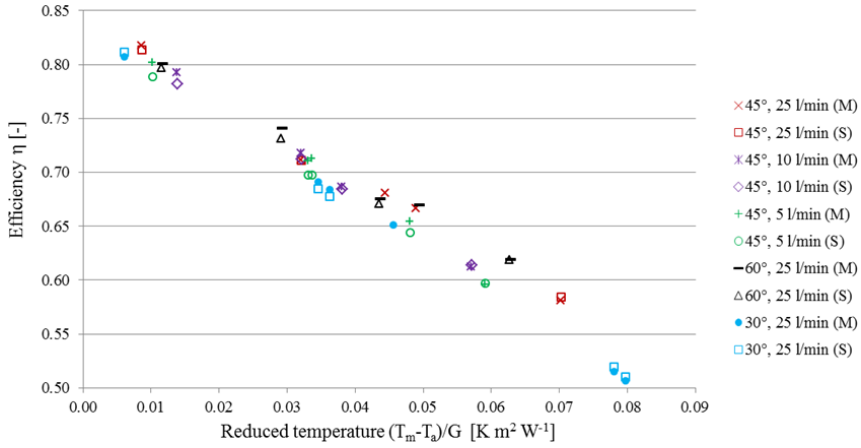

Fig. 5: Comparison between measured (M) and simulated (S) efficiencies of the HT-A collector at different tilts and flow rates.

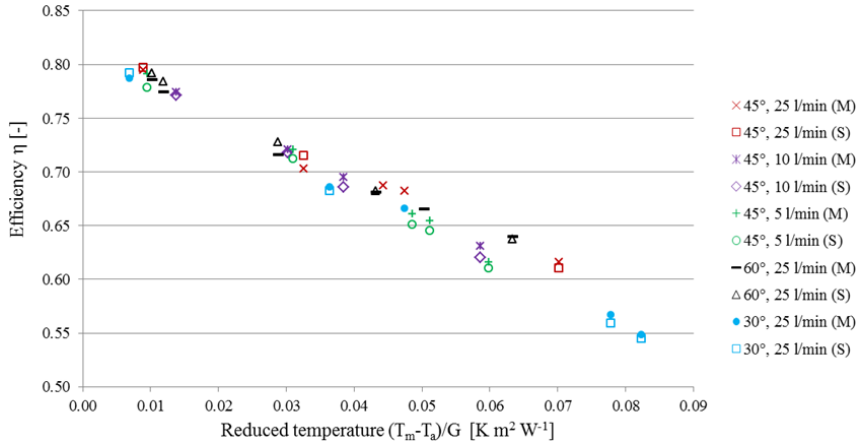

Fig. 6: Comparison between measured (M) and simulated (S) efficiencies of the HT-SA collector at different tilts and flow rates.

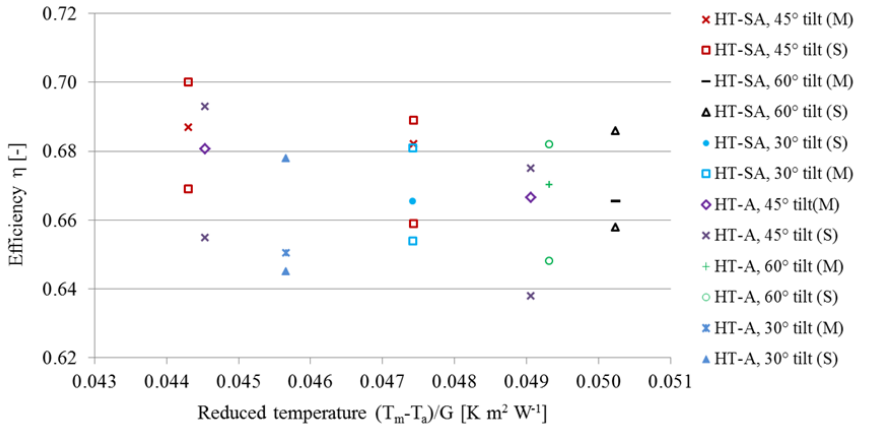

Fig. 7: Comparison between measured (M) and simulated (S) efficiencies of HT-A and HT-SA collector for a flow rate of 25 (litres min^{-1}) and Reynolds numbers between 2200 and 2400. In each couple of simulated efficiency points the higher was obtained for turbulent flow and the lower was obtained forcing the Soleff models to assume laminar flow conditions.

In fact, the measured points with a value of the ratio $(T_m\text{-}T_a)/G$ between 0.044 and 0.051 K m^2 W^{-1} and 25 (litres min^{-1}) flow rate had Reynolds numbers between 2200 and 2400, which is usually considered to be characterized by transitional flow according to literature (Idelchik, 1994). These efficiency points showed intermediate characteristics between laminar and turbulent regime, both in terms of pressure drop (see Fig. 4) and from the efficiency point of view (Fig. 7). In fact, as can be seen in Fig. 7, the efficiencies measured in this range of Reynolds number were always higher than those computed by the Soleff models for laminar flow, but lower than those obtained for turbulent flow.

4. Discussion

As expected, the experimental results (Tab. 1) showed that the presence of the FEP foil negatively affected the transmittance of the collector cover, causing a decrease in the optical efficiency as well as a lower IAM curve (Tab. 2). On the other hand, neither the tilt angle nor the fluid flow rate had any major influence on the optical efficiency. However, as the FEP foil also reduced the heat losses, there exists a certain value of reduced mean temperature above which the HT-SA collector performed better than the HT-A. As the fluid temperature generally increases from relatively low (~40 °C) to relatively high values (~85 °C) along a row in a solar heating field, a mixed composition of solar collectors with and without FEP foil seems to be the best solution, using collectors without foil in the first part of the array and collectors with foil in the second part, in order to optimally exploit their different characteristics.

Regarding the effect of the **flow rate**, the efficiency expressions for 5 and 10 (litres min^{-1}) had the usual quadratic form, while those found for a flow rate of 25 (litres min^{-1}) were linear. Analysing the single efficiency data points, it was found that the efficiencies measured at the highest temperature level were the main reason for the bending of the curves in the 5 and 10 (litres min^{-1}) cases, while efficiencies calculated at lower temperatures were largely aligned. This result was expected, as heat losses in a solar collector increase more than linearly with the temperature difference between fluid and external environment, due to the radiation contribution, which becomes increasingly important at higher temperatures, the convection losses, which increase due to the lower viscosity of air between absorber and cover, and secondarily the conduction losses, as the thermal conductivity of mineral wool increases with temperature. Conversely, no bending appeared in the diagrams regarding 25 (litres min^{-1}) flow rate. The reason of this unexpected behaviour was found in the combination of high fluid velocity and low kinematic viscosity at the highest temperature level, resulting in large Reynolds numbers and turbulent flow regime. This different flow regime led to a much higher heat transfer coefficient than laminar flow and hence was able to counteract the increased thermal losses. If measurements at higher temperature levels had been taken, a quadratic form of the efficiency expression would most likely have been found for 25 (litres min^{-1}) flow rate as well. In fact, only for the case at 30° tilt a mean temperature of 100 °C was reached, while for the other cases the higher temperature was about 85 °C. Temperatures as high as 120 °C could have been safely investigated, thanks to the glycol content and the pressurized system (~200 kPa). Much attention should be paid when using these linear equations (cases 3-5 and 8-10 in Tab. 1) outside the temperature range for which they were calculated, because extrapolation of the curves for higher values of the ratio $(T_m-T_a)/G$ would most likely overestimate the actual efficiency of the collector.

Another consequence of the change in flow regime was the discontinuity in the efficiency curves at 25 (litres min^{-1}) flow rate, which could be observed for reduced temperatures between 0.045 and 0.051 K m^2 W^{-1} (Fig. 5 and Fig. 6), corresponding to a mean fluid temperature of approximately 65 °C and Reynolds numbers in the range 2200-2400. Comparison with the results returned by the Soleff models (Fig. 7), pressure drop measurements (Fig. 4) and literature (Idelchick, 1994) proved that the two collectors experienced transitional flow regime along the horizontal pipes in this flow rate and temperature conditions. In case of flow rates of 10 and 5 (litres min^{-1}), turbulent flow cannot be achieved in practice, as it would require a fluid temperature higher than 95 °C, which is the upper limit in normal operating conditions.

Even when no flow regime transition occurs, higher fluid velocities cause better heat transfer between pipe walls and fluid, so that the larger the flow rate, the higher the efficiency (Fig. 2). Additionally, given the same weather conditions, higher flow rates entailed a lower fluid temperature rise across the collector and hence lower losses.

Considering the effect of the **tilt angle**, Fig. 3 shows that the larger the tilt angle, the higher the efficiency. This trend was in agreement with theory, as both convection and radiation losses are expected to decrease when tilting a flat plate collector. In fact, when a collector is tilted, convective losses decrease due to the reduced number of convective cells between the absorber and cover. Additionally, the view factor of the aperture area toward the earth surface increases, while the view factor toward the sky is reduced. Since the radiation temperature of the sky is lower than that of the earth, a higher tilt positively affects the efficiency by reducing the radiation losses. However, the experimental results show that the efficiency increase was very small when the collectors were tilted from 45° to larger angles, especially for the model HT-SA. This was most likely due to the fact that already at 45° tilt the FEP foil played a more significant role than the tilt

in reducing convection losses. Consequently, a further increase in the tilt did not result in an important enhancement.

The models developed in **Soleff** proved to be reasonably accurate when the flow regime was either completely laminar (Re<2000) or turbulent (Re>3800), fitting the experimental data with an average error of 1%, while the maximum error was equal to 2.2% and 1.8% for the HT-A and HT-SA model respectively. As the results returned by Soleff were compared to experimental measurements in a variety of operating conditions (flow rate, tilt angle and fluid temperature), the models are likely to be able to predict the efficiency of the two collectors with similar degree of accuracy also in other conditions. On the other hand, Soleff was inadequate to simulate the collector efficiency in case of transitional flow, as the software presents a step-change from laminar to turbulent correlations for the convective heat transfer coefficient at a Reynolds number of approximately 2200. Conversely, pressure drop measurements carried out on the HT-SA collector showed that the horizontal pipes experienced transition from laminar to turbulent regime in a range of Reynolds number between 2000 and 3000 (Fig. 4). Experimental collector efficiency obtained in the same range of Reynolds numbers were in agreement with these pressure drop measurements, as the collectors presented efficiency values in between those computed by the Soleff models assuming laminar and turbulent regime (Fig. 7). Though, no clear quantitative relation could be found between the theoretical Reynolds number of the flow and the relative position of the experimental efficiency with respect to the two Soleff efficiency points. This means, for example, that an efficiency point characterized by a higher Reynolds number was not necessarily closer to the corresponding Soleff efficiency point obtained for turbulent flow. In fact, transition from laminar to turbulent regime is a process which is not fully understood yet and fluid-dynamic properties of transitional flows are not simply function of the Reynolds number, but are influenced by local irregularities and disturbances.

5. References

Arcon Solar A/S, 2010. ARCON solfanger - type HT-SA 35/10.

Agarwal, V.K., Larson, D. C., 1981. Calculation of the top loss coefficient of a flat plate collector. Solar Energy 27, 69-71.

Chiou, J.P., 1982. The effect of non-uniform fluid flow distribution on the thermal performance of solar collector. Solar Energy 6, 487-502.

Fan, J., Furbo, S., 2008. Buoyancy effects on thermal behavior of a flat-plate solar collector. Journal of Solar Energy Engineering 130.

Furbo, S., Holck, O., 1995. Efficiencies of solar collectors for different tilts. Measurements. Report SR 95-7, Thermal Insulation Laboratory, Technical University of Denmark.

Furbo, S., Perers, B., Bava, F., 2014. Thermal performance of solar district heating plants in Denmark, in EuroSun 2014 Conference Proceedings, Aix-les-Bains, France.

Furbo, S., Shah L.J., 2003. Thermal advantages for solar heating systems with a glass cover with antireflection surfaces. Solar Energy 74, 513-523.

Idelchik, I.E., 1994. Handbook of hydraulic resistance, third ed. CRC press.

Klein, S.A. In: Duffie, J.A, Beckman, W.A. 1991. Solar engineering of thermal processes. New York.

Rasmussen, P.B., Svendsen, S., 1996. SolEff Program til beregning af solfangeres effektivitet. Thermal Insulation Laboratory, Technical University of Denmark.

SP Technical Research Institute of Sweden, 2011. Technical Report Ref. PX12871-01.

Wang, X.A., Wu, L.G., 1990. Analysis and performance of flat plate solar collector arrays. Solar Energy 2, 71-78.

Wilson, J.D.C., 1978. Film glazings for solar collectors. E.I. du Pont de Nemours & Co.

Windeleff, J., Nielsen, J.E., 2014. Solar District Heating in Denmark. Danish Energy Authority and PlanEnergi.

Paper II

Simulation of a solar collector array consisting of two types of solar collectors, with and without convection barrier

Federico Bava, Simon Furbo and Bengt Perers

Energy Procedia 70 (2015) 4–12

Proceedings of International Conference on Solar Heating and Cooling for Buildings and Industry SHC 2014

Available online at www.sciencedirect.com

ScienceDirect

Energy Procedia 70 (2015) 4 – 12

Energy Procedia

International Conference on Solar Heating and Cooling for Buildings and Industry, SHC 2014

Simulation of a solar collector array consisting of two types of solar collectors, with and without convection barrier

Federico Bava*, Simon Furbo, Bengt Perers

DTU Civil Engineering, Technical University of Denmark. Brovej, Building 118, Kgs. Lyngby 2800, Denmark

Abstract

The installed area of solar collectors in solar heating fields is rapidly increasing in Denmark. In this scenario even relatively small performance improvements may lead to a large increase in the overall energy production. Both collectors with and without polymer foil, functioning as convection barrier, can be found on the Danish market. Depending on the temperature level at which the two types of collectors operate, one can perform better than the other. This project aimed to study the behavior of a 14 solar collector row made of these two different kinds of collectors, in order to optimize the composition of the row. Actual solar collectors available on the Danish market (models HT-SA and HT-A 35-10 manufactured by ARCON Solar A/S) were used for this analysis. To perform the study, a simulation model in TRNSYS was developed based on the Danish solar collector field in Braedstrup. A parametric analysis was carried out by modifying the composition of the row, in order to find both the energy and economy optimum.

Peer-review by the scientific conference committee of SHC 2014 under responsibility of PSE AG

Keywords: solar collector; flat plate collector; solar heating field; FEP foil; TRNSYS; collector row; row composition; economic analysis

1. Introduction

At the end of 2013 Denmark had already installed around 350,000 square meters of thermal solar collectors in solar heating plants in district heating areas, with further 250,000 square meters planned for 2014 [1,2] . In a scenario still characterized by a strong growth in the installed solar collector capacity, even relatively small improvements may lead to a large increase in the overall energy production in absolute terms. For this reason

* Corresponding author. Tel.:+45 45251891.
E-mail address: febav@byg.dtu.dk

Peer-review by the scientific conference committee of SHC 2014 under responsibility of PSE AG
doi:10.1016/j.egypro.2015.02.091

research and development into the optimization of the collector characteristics and solar field design play key roles. Solar collectors in Denmark have seen a significant enhancement in performance in the last years [3] and efforts are still being made for further improvement, as new collector models prove [4,5]. Nevertheless, efficient components do not always guarantee the best performance possible, unless the overall system is well designed and operated.

Collectors installed in Danish solar collector fields for district heating applications are usually large flat plate collectors, connected in rows having between 10 and 25 modules each [1]. These collectors are either produced by ARCON Solar A/S or SUNMARK Solutions A/S, and may have a polymer foil between absorber and glass, functioning as a convection barrier to decrease the heat losses (in ARCON collectors only). On the other hand, as the polymer foil is not completely transparent, it slightly reduces the solar irradiance reaching the absorber. Consequently, if two collectors differ only for the presence of the convection barrier, there is a certain temperature below which the model without foil performs better than the other. For this reason, the choice of a collector with convection barrier over one without is strongly influenced by the temperature the collector operates at. In large solar fields, where the temperature rise within the same row is usually very high (from 40 °C up to 85 °C), both types of collectors may be used together to maximize the energy output. Collectors without foil may be used in the first part of the row, where the fluid temperature is still relatively low, to provide the first temperature increase. On the other hand, collectors with foil may be best exploited in the second part of the string, where higher temperatures are reached. Nevertheless, also the higher cost of collectors with foil must be taken into account, to verify whether the improved efficiency is worth the extra investment.

Nomenclature

a_1	first order heat loss coefficient, (W m^{-2} K^{-1})
a_2	second order heat loss coefficient, (W m^{-2} K^{-2})
b_0	first order IAM coefficient, (-)
b_1	second order IAM coefficient, (-)
FEP	fluorinated ethylene propylene
G	total irradiance on the collector plane, (W m^{-2})
IAM	incidence angle modifier = $1 - b_0 \cdot (1/\cos\theta - 1) - b_1 \cdot (1/\cos\theta - 1)^2$, (-)
NPV	net present value, (Danish crown, DKK)
T_a	ambient temperature, (°C)
T_m	fluid mean temperature, (°C)
T^*_m	reduced temperature difference = $(T_m - T_a)/G$, (K m^2 W^{-1})
η_0	zero-loss efficiency, (-)
η	efficiency of solar collector = $\eta_0 - a_1 \cdot T^*_m - a_2 \cdot G \cdot (T^*_m)^2$, (-)
θ	incidence angle, (°)

2. Method

To carry out the optimization analysis on the collector row composition, a TRNSYS simulation model was developed based on the design and control strategy of an actual solar collector field, more specifically the field in Braedstrup (Denmark), installed by the Danish company ARCON Solar A/S. Design of the field and 1-year (June 2013-May 2014) measured data of solar radiation, flow rate and inlet and outlet temperature were kindly made available by ARCON Solar and PlanEnergi, and then used as input for the TRNSYS model.

2.1. Description of the solar collector field

The solar collector field in Braedstrup was built in 2007, with an overall transparent area of 8,000 m^2. An extension of 10,608 m^2 was added in 2012 and is investigated in the current study. This new solar field consists of 847 collectors with convection barrier (model HT-SA 28-10), arranged in 72 rows spaced by 5.5 m. Most of the collectors (60%) are arranged in 14 module rows, while the remaining 40% is installed in shorter rows (Fig. 1).

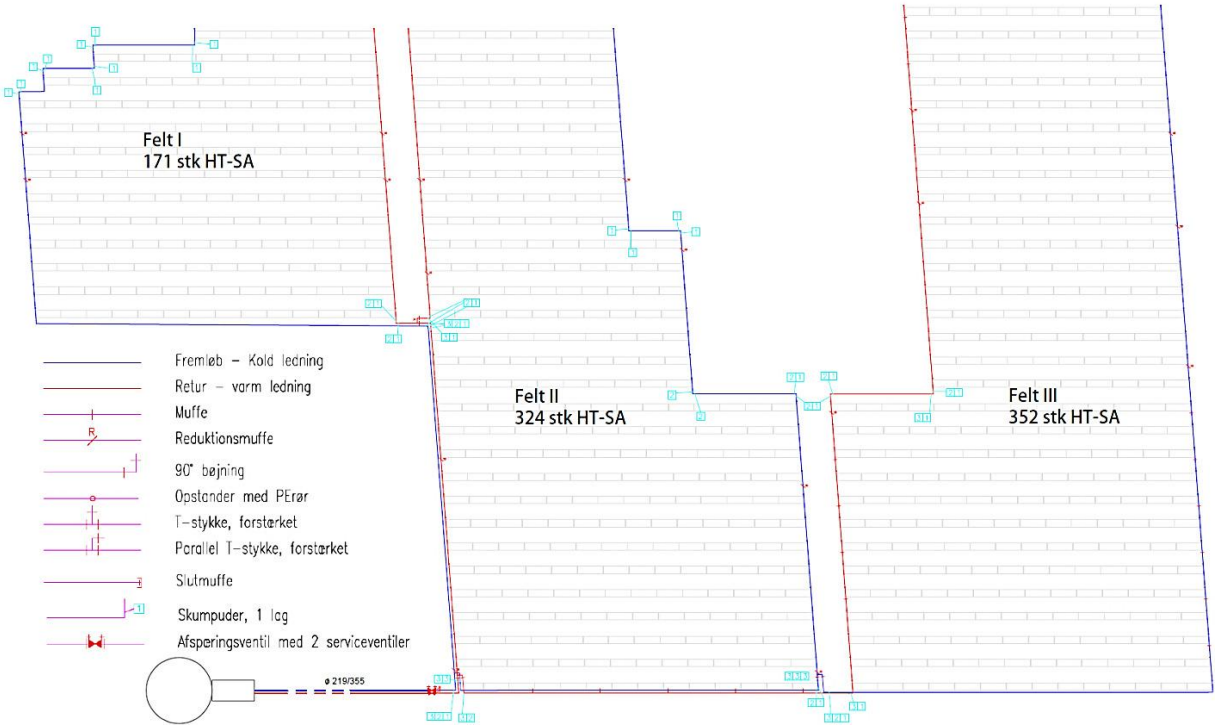

Fig. 1. Layout of the 10,608 m^2 collector field in Braedstrup (source: ARCON Solar A/S).

The collectors are tilted by 35° and are south oriented. For space reasons, the building containing the heat exchanger between solar collector loop and the water loop is shown in the bottom left corner of Fig. 1, relatively close to the solar collector field, while it is actually located approximately 500 m away. The field uses a mixture of propylene glycol and water with a 30% weight concentration as solar collector fluid. The inlet temperature is about 40 °C while the outlet temperature is about 90 °C.

2.2. Description of the TRNSYS model

One-year measured data (June 2013-May 2014) of total radiation on the collector plane, ambient temperature, flow rate through the entire collector field and supply temperature were given to TRNSYS as input, while the outlet temperature was used only as basis of comparison to check the correct operation of the model.

As the purpose of this study is to optimize the composition of a single row, the developed TRNSYS model simulates the behaviour of one row only, consisting of 14 collectors, which represents the most common configuration in Braedstrup field (Fig. 1). Because only the total field flow rate was measured, the ratio between the row flow rate and the field flow rate was assumed equal to the ratio between row area and field collector area, which guarantees approximately the same outlet temperature from each row.

Although the field is made of solar collectors of type HT-SA 28-10, manufactured by ARCON Solar, two other ARCON models (HT-A and HT-SA 35-10) were used in this study, as they are similar to the original model and more detailed information were available from previous studies [6]. The two HT 35-10 collectors are mostly identical in terms of design and technical specifications, with an aperture area of 12.56 m^2 and 18 horizontal copper tubes connecting two manifolds [7,8]. The only relevant difference between the two collectors is a 0.025 mm thick fluorinated ethylene propylene (FEP) foil interposed between the absorber and cover in the model HT-SA (Fig. 2), in order to decrease the convection losses.

The two collectors were tested between 2012 and 2013 [6], according to the standard norm EN 12975-2 and their efficiency was calculated for a 45° tilt angle, 25 litres per minute flow rate and using a mixture of water and propylene glycol with a 40% weight concentration as solar collector fluid.

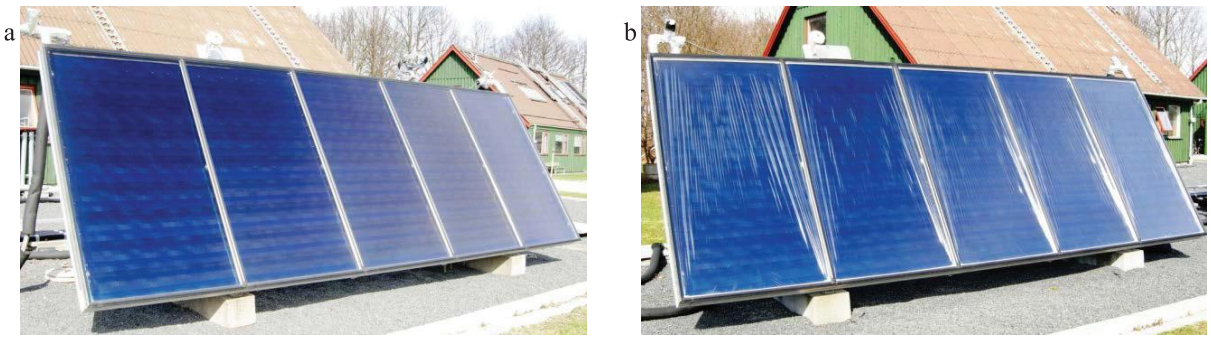

Fig. 2. Solar collector HT-A (a) and HT-SA (b) at Department of Civil Engineering at Technical University of Denmark.

As the operating conditions used in Braedstrup plant differ from those used in the efficiency tests in [6], a simulation model was created in Soleff, software developed at the Technical University of Denmark [9]. This model was first validated against the experimental results from [6], and then used to predict the efficiency parameters for a 30% glycol/water mixture and 35° tilt angle, which were then used as input for the collector Type 539 in the TRNSYS model [10]. The collector parameters given as input to Type 539 are listed in Table 1, while the collector efficiency curves are shown in Fig. 3 for a solar irradiance of 800 W m^{-2}. In the diagram it is possible to appreciate the effect of the FEP foil on the zero-loss efficiency and convection losses, as described in Section 1.

Table 1. Collector parameters used as input for the collector Type 539 in the TRNSYS model.

Collector characteristic	HT-A 35-10	HT-SA 35-10
Zero-loss efficiency η_0, (-)	0.850	0.816
First order heat loss coefficient a_1, (W m^{-2} K^{-1})	3.093	2.418
Second order heat loss coefficient a_2, (W m^{-2} K^{-2})	0.0111	0.0085
First order IAM coefficient b_0, (-)	0.045	0.070
Second order IAM coefficient b_1, (-)	0.089	0.080
Collector thermal capacity, (kJ/K)	78.5	78.5

Because the diffuse radiation was not measured in the solar collector field in Braedstrup, Type 546 was used to evaluate the diffuse component according to Erbs correlation [11], given the total radiation on the collector plane, horizontal extraterrestrial radiation and position of the sun in the sky. Shadow effect from other rows was considered by using Type 30a. Given the significant length of the supply pipes (560 m and 474 m for forward and return pipe respectively), these were taken into account by Type 604b, which modelled plug flow, thermal losses and pipe thermal capacity.

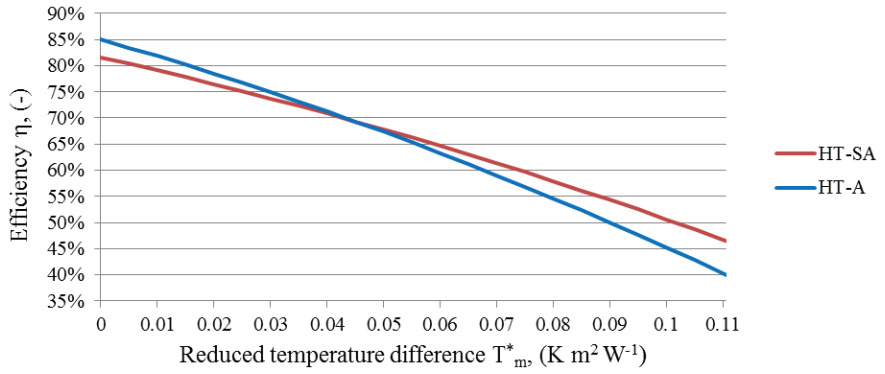

Fig. 3. Efficiency of the HT-A and HT-SA collector for a solar irradiance G=800 W m^{-2}.

After verifying the correct operation of the model, this was used to carry out a parametric analysis, varying the composition of the row by increasing the number of HT-A collectors. Computing and comparing the useful energy outputs in the different cases, it was possible to determine the best row composition from an energy point of view.

2.3. Economic analysis

The most efficient solution from an energy point of view may not be the most effective from an economic point of view. For this reason a simple economic analysis, based on the Net Present Value (NPV) method, was carried out as well. In this way the most cost-effective solution could be identified.

In order to carry out this analysis, the parameters listed in Table 2 were used. The cost of the solar collectors, their maintenance and their lifetime were communicated by ARCON Solar. The costs of the solar collectors include also installation and piping. The maintenance cost was said to be the same for both collector models, as no need of replacement of the FEP foil is expected during the collector lifetime, and, even if the FEP foil breaks, this is replaced by the collector manufacturer at their own expense. The lifetime of 20 years is meant as the period during which the collectors are supposed to maintain their original efficiency. This kind of solar collectors are usually kept in operation for longer than 20 years, but the same performance is not guaranteed afterwards.

The interest rate was assumed equal to 6%, as in similar project studies in Denmark [12], and the energy price was read from [13] as energy price for the customer without the 25% VAT.

The collector efficiency, and therefore the yearly energy production, was assumed constant throughout the expected lifetime of the solar collector field. Energy losses from the district heating network were neglected.

Table 2. Parameters used in the economic analysis

Economic parameter	Value
Turnkey price of a HT-A 35-10 collector, (DKK/m^2)	1750
Turnkey price of a HT-SA 35-10 collector, (DKK/m^2)	1850
Energy price, (DKK/MWh)	574.50
Maintenance cost, (DKK/MWh)	2.00
Minimum expected lifetime of the solar collector field, (years)	20
Interest rate, (%)	6%

3. Results

3.1. Comparison between TRNSYS model and measurements

To check the correct operation of the TRNSYS model, its results were compared against the measured data from Braedstrup, both in terms of return temperature from the solar collector field and useful energy delivered to the heat exchanger. As in Braedstrup all collectors are equipped with FEP foil, the row configuration used as comparison consisted of 14 HT-SA collectors.

In the considered year (June 2013-May 2014), the energy transferred to the heat exchanger in the TRNSYS simulation was approximately 72.8 MWh, only 1.2% higher than the measured one. Nevertheless, on a seasonal basis the deviations had higher values and opposite trend. In fact, the periods June-December 2013 and January-May 2014 were characterized by average deviations of +7% and -8%, weighted on the monthly transferred energy. As the flow rate and the inlet temperature used in the TRNSYS model were the measured ones, the difference was caused by the different outlet temperature at the end of the return pipe, before the solar collector fluid entered the heat exchanger. The comparison between measured and simulated return temperatures is shown in Fig. 4. The outlet temperature computed by the model followed the measured temperature profile, despite some deviations for high irradiance values. It can be seen how the return temperature calculated by the TRNSYS model was lower than the measured one, if data from 2014 were used (Fig. 4.a). On the other hand, the TRNSYS return temperature was higher, when data from 2013 were considered (Fig. 4.b). No significant intervention was done on the field in the winter 2013-2014, so the abrupt change in the performance of the solar collector field was unexpected.

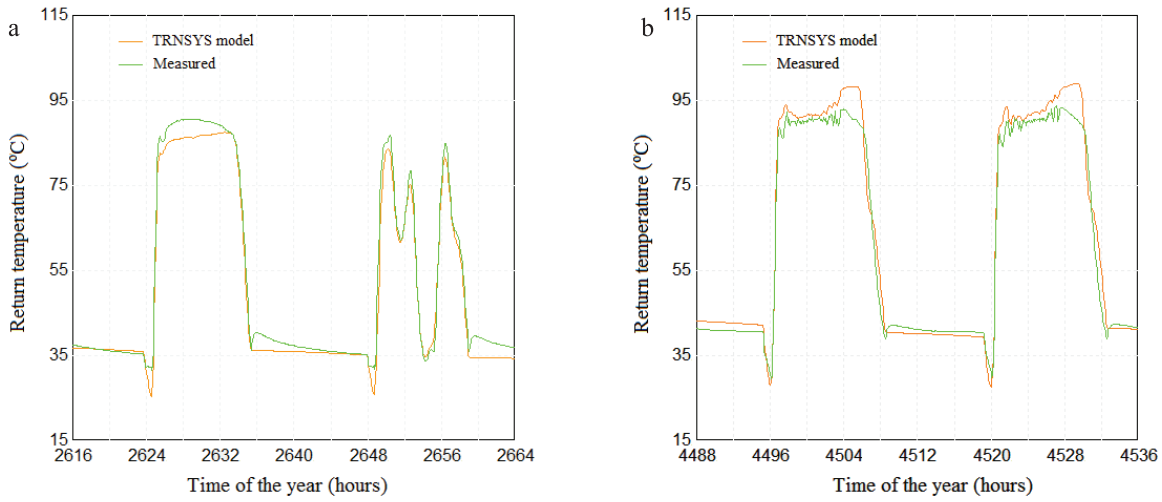

Fig. 4. Comparison between simulated and measured return temperature from the solar collector field: (a) April 20th and 21st, 2014; (b) July 7th and 8th, 2013.

On the basis of the available information, only some hypothesises could be made. The higher energy output of the TRNSYS model in 2013 was most likely due to the fact that the model assumed perfectly uniform flow distribution in the different rows, which might not be the case. Additionally, the heat losses from pipes were slightly underestimated, as only one collector row was modelled. Finally, pollen and dust on the collector cover or presence of moisture on the inner surface of the glass might reduce the actual performance of the collectors in real-world operation. Regarding the lower energy output in the first half of 2014, this seemed to be caused by underestimated irradiance measured by the silicon pyranometer Soldata 80spc, manufactured by SolData Instruments and installed in Braedstrup field. The irradiance measured in Braedstrup was compared to the horizontal irradiance from a DMI (Danish Meteorological Institute) climate station in Horsens, 20 km away from the solar collector field, where a NovaLynx 8101 Star pyranometer (first class according to ISO 9060) was installed. The comparison was done between the days May 29th-30th 2014 and June 2nd-3rd 2013, as they were characterized by clear sky conditions and almost identical solar declination. Considering an interval of a couple of hours around midday, the ratio between the irradiance in Braedstrup and that in Horsens in late May 2014 was about 7 % lower than the same ratio calculated for early June 2013, thus supporting the hypothesis that the silicon pyranometer underestimated the actual solar irradiance reaching the solar collector field, maybe because of dirt on the pyranometer cover or due to aging.

3.2. Useful energy output

After this comparison, calculations were carried out increasing the number of HT-A collectors placed in the first part of the row. Fig. 5 shows the monthly solar radiation reaching a unit area of solar collector during operation of the pumps, and the utilization factor of solar radiation for differently composed rows. The utilization factor is defined as the ratio between the row useful energy output and the collected radiation defined above.

For the sake of clarity, not all the utilization factor curves are shown in Fig. 5, as it would be difficult to distinguish them, but only those with a relevant difference between each other are displayed.

On the other hand, results for all the possible row combinations are listed in Table 3 in terms of yearly energy output and relative difference with respect to a composition consisting of 14 HT-SA collectors. From the values listed in Table 3, it is possible to see that the best performance was achieved by a row consisting of HT-SA collectors only. Nevertheless, introducing up to five HT-A collectors in the first part of the row did not significantly decrease the energy output, as the relative difference with respect to the row composed by 14 HT-SA collectors was lower than 1%. Further replacement of HT-SA collectors with HT-A models increasingly deteriorated the row performance, up to a 7% reduction in the case where only HT-A modules were used.

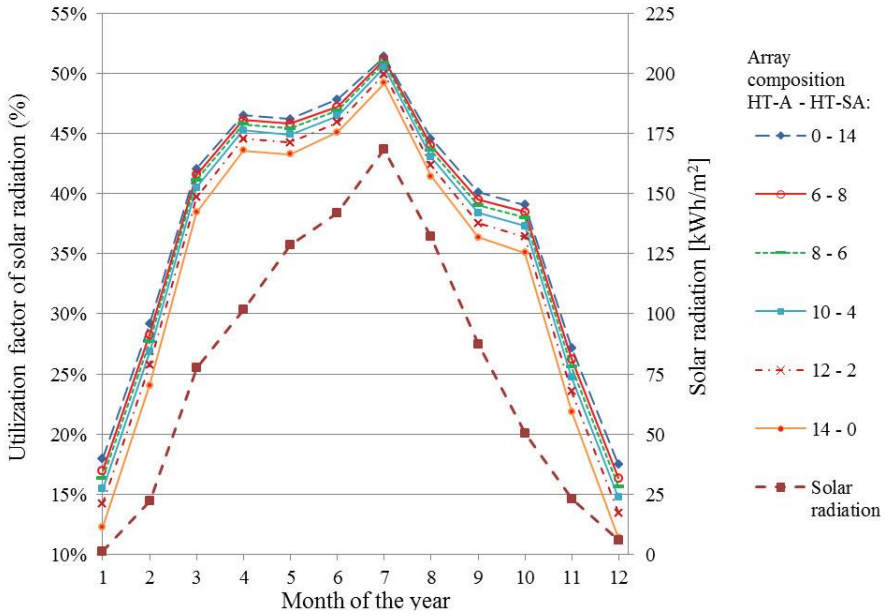

Fig. 5. Monthly utilization factor of solar radiation for different row compositions (left axis) and monthly solar radiation per unit area of collector (right axis), using weather data measured at Braedstrup field between June 2013 and May 2014.

Table 3. Yearly energy output from the collector row and relative difference with respect to a 14 HT-SA composition, using weather data measured at Braedstrup field between June 2013 and May 2014.

Row composition HT-A - HT-SA:	Yearly energy output, (MWh)	Relative difference, (%)
0 - 14	74.0	0%
1 - 13	74.0	-0.1%
2 - 12	73.9	-0.1%
3 - 11	73.8	-0.3%
4 - 10	73.7	-0.5%
5 - 9	73.5	-0.7%
6 - 8	73.2	-1.1%
7 - 7	72.9	-1.5%
8 - 6	72.6	-2.0%
9 - 5	72.2	-2.5%
10 - 4	71.7	-3.1%
11 - 3	71.2	-3.9%
12 - 2	70.5	-4.7%
13 - 1	69.8	-5.7%
0 - 14	68.9	-6.9%

3.3. Economic assessment

Under the assumptions made in Section 2.3, an investment analysis was carried out and its results are reported graphically in Fig. 6, both in terms of net present value of the installation after 20 years and payback time of the investment. It can be seen that the net present value of the row had a maximum (approximately 164,000 DKK) for the configuration consisting of five HT-A and nine HT-SA collectors.

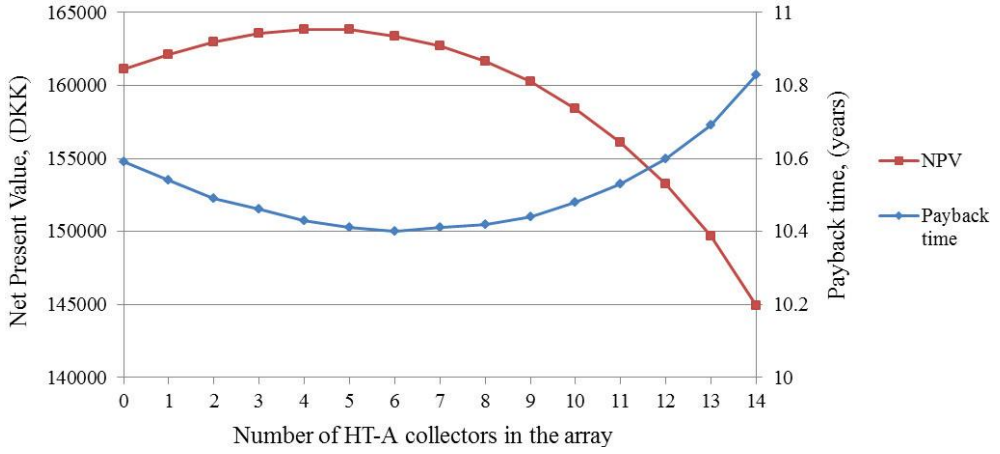

Fig. 6. Net Present Value (NPV) of the row at 20 years (left axis) and payback time of the investment (right axis).

Row configurations with a number of HT-A collector between two and seven presented very similar net present values (relative difference lower than 1%), while for an increasing presence of the HT-A model in the row this value decreased to a minimum value of approximately 145,000 DKK (-11.5% with respect to the highest NPV).

Regarding the payback time of the investment, this was found almost independent of the row configuration and with an average value of approximately ten years and a half (maximum value of 10.8 years for a 14 HT-A collector row and minimum value of 10.4 years for a 6 HT-A collector row). This value is in good agreement with the payback times usually estimated for solar collector fields in Denmark [14].

4. Discussion and conclusions

A TRNSYS model was developed in this study, in order to analyse the performance of differently composed solar collector rows, consisting of 14 collectors, both with and without polymer foil as convection barrier. The model was built based on measured data from the Danish solar collector field in Braedstrup and using two different solar collectors available on the Danish market.

The results returned by the model were compared to measurements coming from the plant. The model returned a value of useful energy output 7% higher than the measured one in the period June-December 2013, and then 8% lower in the period January-May 2014. As no significant intervention was done on the field in the winter 2013-2014, only some hypothesises about the reason of such a change in performance could be made. The higher energy output of the TRNSYS model in 2013 was most likely a consequence of some assumptions made in the model, such as uniform flow distribution in the different rows, clean and moisture-free collector cover throughout the year and slightly underestimated heat losses from supply and return pipes. The lower energy output in the first half of 2014 seemed to be caused by underestimated irradiance measured by the silicon pyranometer installed in Braedstrup field. Comparison between the irradiance measured in Braedstrup and the horizontal irradiance from a nearby DMI climate station supported this hypothesis. The reason for such an underestimation might be accumulated dirt on the flat cover of the silicon pyranometer, as this was not regularly cleaned.

The parametric analysis carried out on the row composition proved that the best performance in terms of yearly useful energy output was given by a row consisting of HT-SA modules only (74 MWh), assuming weather conditions as those recorded between June 2013 and May 2014. Nevertheless, rows with up to five HT-A collectors, installed in the first part of the row, presented very similar energy outputs, less than 1% different (Table 3). Although the replacement of HT-SA collectors with HT-A models reduced the performance, the effect was not so significant, as the collectors were replaced at the very beginning of the row, where the fluid temperature was not so high and hence the difference in efficiency between the two collector models was small. Nevertheless, when additional HT-A collectors were introduced, the performance of the row increasingly deteriorated, with a 7%

reduction in the case where only HT-A collectors were used. This was in agreement with the expectations, as in this case HT-A collectors were used also in a relatively hot part of the row, where thermal losses were more important than the transmittance of the cover.

From Fig. 5 it can be seen that the presence of the FEP foil played a more or less significant role depending on the season. Comparing the row with only HT-SA collectors to the case where only HT-A collectors were used, the additional gain in the first case was more important in winter months, when the temperature difference between collector operating temperature and ambient temperature is larger. In this case convection losses play a significant role, which the FEP foil helps reduce. So, the highest deviation occurred in December, with 6 percentage point difference in utilization factor of solar radiation, and the lowest in July, with 2 percentage point difference.

The economic analysis, carried out according to the method of the net present value and in a 20 year lifetime scenario, showed that the most cost-effective solution was given by a row consisting of five HT-A and nine HT-SA collectors. This is due to the fact that this configuration yielded a yearly energy output slightly lower (-0.7%) than the best case scenario, but also required a lower initial investment cost (-2%). The payback time was approximately the same in all scenarios, so it could not be used as a significant parameter to identify the best solution.

Since the solar collectors are expected to last more than 20 years, a longer lifetime could be assumed. In this case, the most cost-effective solution in terms of net present value would shift toward row compositions consisting of a larger number of HT-SA collectors. In fact, the additional yearly energy production would have a longer timespan to pay back the extra investment. Nevertheless, the collector efficiency after 20 year operation is not guaranteed to be the same as for brand new collectors, which makes it difficult to make forecast. Information about how the efficiency curves of the two different collector change over time are needed, if an analysis in the longer term is desired. Additionally, it must be noted that measured data from a specific year (June 2013-May 2014) were used in this study. Different yearly weather conditions influence the useful energy output of the solar collector field and thus affecting the results of the economic analysis.

References

[1] J. E. Nielsen and J. Windeleff, Solar District Heating in Denmark; 2014.
[2] S. Furbo, B. Perers and F. Bava, Thermal Performance of Solar District Heating Plants in Denmark, in EuroSun 2014 Conference Proceedings, Aix-les-Bains (France); 2014.
[3] J. Fan, Z. Chen, S. Furbo, B. Perers and B. Karlsson, Efficiency and lifetime of solar collectors for solar heating plants, in 29th ISES Biennial Solar World Congress 2009, Johannesburg (South Africa); 2009.
[4] ARCON Solar A/S, ARCON Solar Collector Type HT-HEATboost 35/10; 2013.
[5] ARCON Solar A/S, ARCON Solar Collector Type HT-HEATstore 35/10; 2013.
[6] F. Bava and S. Furbo, Comparative test of two large solar collectors for solar field applications, in EuroSun 2014 Conference Proceedings, Aix-les-Bains (France); 2014.
[7] SP Technical Research Institute of Sweden, Technical Report on HT-A 35-10, Ref. PX12871-01; 2011.
[8] ARCON Solar A/S, ARCON Solar collector Type HT-SA 35/10; 2011.
[9] P. B. Rasmussen and S. Svendsen, SolEff Program til beregning af solfangeres effektivitet; 1996.
[10] TESS - Thermal Energy Systems Specialists, TESSLibs 17 Component Libraries for the TRNSYS Simulation Environment, Volume 10 Solar Library Mathematical Reference; 2012.
[11] D. G. Erbs, S. Klein and J. A. Duffie, Estimation of the diffuse radiation fraction for hourly, daily and monthly-average global radiation, Solar Energy, vol. 28, pp. 293-302, 1982.
[12] P. K. Olsen, H. Lambertsen, R. Hummelshøj, B. Bøhm, C. H. Chrisiansen, S. Svendsen, C. T. Larsen and J. Worm, A new low-temperature district heating system for low-energy buildings, in The 11th International Symposium on District Heating and Cooling, Reykjavik (Iceland); 2008.
[13] J. Tang, Fjernvarmeprisen i Danmark 2013, Dansk Fjernvarme; 2013.
[14] http://www.solvarmedata.dk/index.asp?secid=228.

Paper III

A numerical model for pressure drop and flow distribution in a solar collector with U-connected absorber pipes

Federico Bava and Simon Furbo

Solar Energy 134 (2016) 264–272

Solar Energy 134 (2016) 264–272

Contents lists available at ScienceDirect

Solar Energy

journal homepage: www.elsevier.com/locate/solener

A numerical model for pressure drop and flow distribution in a solar collector with U-connected absorber pipes

Federico Bava *, Simon Furbo

DTU Civil Engineering, Technical University of Denmark, Brovej, Building 118, 2800 Kgs. Lyngby, Denmark

ARTICLE INFO

Article history:
Received 9 February 2016
Received in revised form 14 April 2016
Accepted 10 May 2016

Keywords:
Solar collector
U-configuration
Pressure drop
Flow distribution

ABSTRACT

This study presents a numerical model calculating the pressure drop and flow distribution in a solar collector with U-type harp configuration in isothermal conditions. The flow maldistribution in the absorber pipes, caused by the different hydraulic resistances, was considered to evaluate the pressure drop across the collector. The model was developed in Matlab and is based on correlations found in literature for both friction losses and local losses, and was compared in terms of overall pressure drop against experimental measurements carried out on an Arcon Sunmark HT 35/10 solar collector at different flow rates and temperatures for water and water/propylene glycol mixture. For collector pressure drops higher than 1.4 kPa, the relative difference between the model and measurements was within 5% for water and 7% for water/propylene glycol mixture. For lower pressure drops the relative difference increased, but remained within the accuracy of the differential pressure sensor. The flow distribution was mainly affected by the flow regime in the manifolds. Turbulent regime throughout the manifolds entailed a more uniform distribution across the absorber pipes compared to laminar regime. The comparison between calculated flow distributions and results from previous literature showed a good agreement.

1. Introduction

The pressure drop over a solar collector should be known and taken into account, when connecting collectors in a solar collector field. In fact, the pressure drop impacts the flow distribution throughout the field, affecting the heat transfer rate in the collectors and hence their efficiency, and determines the requirements of the pumps that need to be installed to supply the field in the most efficient way.

The standard norm ISO 9806 does not strictly prescribe a specific fluid when performing the pressure drop test of a solar collector. It states that "the fluid used in the collector for the test shall be water or a mixture water/glycol (60/40), or a mixture recommended by the manufacturer. The temperature of the fluid shall be (20 ± 2) °C" (ISO 9806). Therefore, if different fluids are used to test different collectors, the test results cannot be directly compared (Kovacs et al., 2012). Additionally, the conditions during the test may differ significantly from the actual operating conditions of the collector, both in terms of fluid type and operating temperature. For this reason, it could be useful to have a model able to derive the pressure drop of a collector for different temperatures and fluids, starting from a single test carried out in a specific operating condition.

When considering large flat plate collectors, the most common design is a number of parallel pipes connecting two manifolds. This configuration allows a high ratio between pipe length and absorber area, without too large pressure drops. On the other hand, the parallel pipe design has the disadvantage of non-uniform flow distribution in the different parallel pipes. The flow distribution in flat plate collectors with parallel pipes has been the topic of many investigations, as it may strongly affect the collector efficiency. In fact, several studies show that the efficiency decreases for higher flow maldistribution, as a consequence of non-uniform outlet temperatures for the different collector pipes. Chiou (1982) developed a method to determine how much the collector efficiency is deteriorated by flow maldistribution, but he did not calculate the flow distributions himself. He defines a *flow nonuniformity parameter* as the root mean square deviation of the absorber pipe flow rates and concludes that the deterioration of the collector efficiency is proportional to approximately the square of such parameter. Wang and Wu (1990) propose a discrete numerical model to predict the flow and temperature distribution in collector arrays with vertical pipes, both in U-type and Z-type configuration, taking into account buoyancy force. The U-type array presents a higher maldistribution and hence its efficiency is more penalized

* Corresponding author.
E-mail address: febav@byg.dtu.dk (F. Bava).

http://dx.doi.org/10.1016/j.solener.2016.05.012
0038-092X/

compared to the Z-type array. The flow rate in the absorber pipes for the U-type array decreases monotonically with the distance from the manifold inlet. The same trend is found by Jones and Lior (1994), who considered a single collector with vertical pipes, instead of an entire array, and neglected buoyancy effect. The flow is assumed isothermal, as buoyancy and temperature dependence of the thermophysical properties are expected to play a negligible role, as argued in the authors' previous work (Jones and Lior, 1987). Weitbrecht et al. (2002) carried out both an experimental and analytical study on the flow distribution in a Z-type collector in isothermal conditions. They investigated the influence that the inset of a pipe into the manifold has on the pressure drop across the tee junction. However, only laminar flow and one specific tee geometry were considered. Still, the effort of investigating pressure drops in tees with inset is noteworthy. In fact, the pipe inset is often neglected or simplified in other studies, but can play a role in the flow distribution by increasing significantly the pressure drop compared to tees with sharp edges (Ohnewein et al., 2015).

Fan et al. (2007) studied the flow and temperature distribution in a large solar collector with 16 U-connected horizontal tubes with quadrilateral cross section. A numerical model, based on CFD calculations and taking into account buoyancy, and experimental measurements are compared. The results show that the flow distribution is dominated by friction (and hence buoyancy can be neglected), if the velocity in the collector pipes is high compared to the temperature rise across the collector. In large solar collector fields in Denmark each row usually consists of 10–25 collectors (Windeleff and Nielsen, 2014), so the temperature rise in each collector is relatively small, while the flow rate is relatively high. Consequently, it can be considered that buoyancy plays a minor role in the flow distribution in this kind of installations. As the focus of the present study was on large solar collectors for collector field applications, the assumption of no buoyancy was made and the flow was assumed isothermal.

The aim of the study was to develop a numerical model for calculating the pressure drop and flow distribution in a U-type harp collector under isothermal conditions. The model, whose source code is publicly available online (Bava, 2015) and can be easily customized by other users, takes only a couple of seconds to perform a simulation. The model is based on a very common design of solar collector, so it can be used to evaluate geometry improvements to achieve more uniform flow distribution. Both laminar and turbulent regimes were considered, and an effort was made to take into account the effect of the pipe inset into the manifolds. The reliability of the model was verified by comparing its results against experimental measurements and previous literature findings.

2. Material and method

2.1. Numerical model

2.1.1. Pressure drop correlations

In a solar collector, as well as in any other hydraulic circuit, the total pressure drop is given by the sum of two types of pressure losses: friction (or major) losses and local (or minor) losses. Friction losses occur in pipe flow because of viscous effects generated by the pipe surface. Local losses are due to variations of momentum. Valves, bends, tees and abrupt changes in pipe cross section are examples of components causing local pressure losses.

The friction loss along a straight pipe of constant cross section can be calculated by the Darcy–Weisbach equation:

$$\Delta p = \lambda \frac{l}{D_h} \frac{\rho w^2}{2} \tag{1}$$

where

Δp is the pressure drop [Pa],
λ is the Darcy friction factor [–],
l is the pipe length [m],
D_h is the pipe hydraulic diameter, which equals the inner diameter for a full flow circular pipe [m],
ρ is the fluid density [kg m^{-3}],
w is the mean fluid velocity [m s^{-1}].

The friction factor depends on the type of flow regime and, if this is turbulent, on the roughness of the pipe as well. The parameter indicating whether a flow is laminar or turbulent is the Reynolds number, defined as

$$Re = \frac{w \rho D_h}{\mu} \tag{2}$$

where

Re is the Reynolds number [–],
μ is the fluid dynamic viscosity [Pa s].

Density and viscosity are properties characteristic of each fluid and are dependent on the temperature. Water and propylene glycol/water mixtures are the most common fluids used in solar thermal applications. Thermophysical properties of water are well known and are easily found in literature. For the density, the correlation (Eq. (3)) proposed by Furbo (2015) was used, while the dynamic viscosity was evaluated through equation (Eq. (4)) proposed by Kestin et al. (1978):

$$\rho = 1000.6 - 0.0128\ T^{1.76} \tag{3}$$

$$\log\{\mu(T)/\mu(T = 20\ ^\circ\mathrm{C})\} = \{1.2378 - 1.303 \cdot 10^{-3} \cdot (20 - T) + 3.06 \cdot 10^{-6} \cdot (20 - T)^2 + 2.55 \cdot 10^{-8} \cdot (20 - T)^3\} \cdot (20 - T)/(T + 96) \tag{4}$$

where T is the fluid temperature [°C].

Given the large variability of the properties of propylene glycol/water mixtures found in literature and in product datasheets, these were experimentally determined with an Anton Paar DMA 4100 densimeter and an Anton Paar AMV 200 viscometer. Three samples with glycol concentration of 40%, 45% and 50% were tested at temperatures between 20 °C and 80 °C with an intermediate step of 10 °C. The experimental data points were then interpolated with the polynomial expressions (Eq. (5)) and (Eq. (6)):

$$\rho = 1013 - 0.2682T + 0.7225x - 1.94 \cdot 10^{-3}T^2 - 4.964 \cdot 10^{-3}xT \tag{5}$$

$$\mu = (-2.881 - 6.721 \cdot 10^{-3}T + 0.2839x + 1.959 \cdot 10^{-3}T^2 - 7.036 \cdot 10^{-3}xT - 1.883 \cdot 10^{-5}T^3 + 4.862 \cdot 10^{-5}xT^2) \cdot 10^{-3} \tag{6}$$

where x is the mass concentration of propylene glycol in the mixture [%].

Laminar flow regime is characterized by low values of Reynolds number. In literature it is often stated that, for fully developed flow in a circular pipe, laminar flow occurs for $Re < 2300$, and turbulent flow for $Re > 4000$ (Holman, 2002). The flow regime between laminar and turbulent is referred to as transitional regime. In reality, the exact value at which change in flow regime occurs is extremely difficult to determine and depends on whether small disturbances are present. In the developed model, the flow was assumed laminar for $Re < 2300$, and turbulent for $Re > 3100$, as a result of a series of

tests carried out to evaluate transition in flow regime in the HT collector pipes. More detailed information about how these tests were performed and analyzed is reported in Appendix A.

In case of laminar flow, the Darcy friction factor was calculated through the Hagen–Poiseuille law:

$$\lambda = 64/Re \tag{7}$$

For turbulent flow the Blasius correlation for smooth pipes (Eq. (8)) was used, as the collector manifolds and pipes were made of commercial copper tubes, characterized by very small absolute roughness (Binder, 1973).

$$\lambda = 0.3164/Re^{0.25} \tag{8}$$

Beside the Blasius correlation, other friction factor correlations were implemented in the model, such as those proposed by Colebrook (1939) and Haaland (1983) for turbulent flow in pipes of known roughness, and by Joseph and Yang (2010) for any flow regime in smooth pipes.

Following the example of Jones and Lior (1994), the friction factor in the transition region ($2300 < Re < 3100$) was calculated by linear interpolation between the value obtained from (Eq. (7)) for $Re = 2300$ and that obtained from (Eq. (8)) for $Re = 3100$.

Regarding local losses, in the solar collector under investigation the only discontinuities were represented by the tees connecting the absorber pipes to the manifolds. The correlations used to model the pressure losses in tees were mainly obtained by Idelchik (1994). For the sake of simplicity, these correlations are not reported here, but can be found as part of the code of the developed model (Bava, 2015). Though, Idelchik's correlations refer to tees with sharp edges and without any inset, while the collector under investigation had 2–3 mm inset of the absorber pipes into the manifold. As even short insets have been proven to be able to affect the pressure drop across tees (Ohnewein et al., 2015), Idelchik's correlations were corrected based on the results from Ohnewein et al. (2015). In Ohnewein et al. (2015) Figs. 33–38 present the measured pressure drop coefficients in different types of tee junctions for different inset lengths and different flow rate ratios between side passage and combined passage of the tee junction. In the same diagrams also Idelchik's pressure drop coefficients for turbulent conditions are reported, even when the Reynolds number in the combined passage of the tee junction is very low (for example $Re = 500$ in Fig. 37). For this reason, in order to make a fair comparison, the coefficients proposed by Ohnewein et al. were compared to those from Idelchik, using turbulent or laminar correlations accordingly. Among the different pressure drop coefficients proposed by Ohnewein et al., those with an inset length/manifold diameter ratio closer to that of the investigated collector (see Section 2.2) were chosen. Based on the comparison, the following conclusions were drawn:

- Good agreement was found between Ohnewein et al.'s and Idelchik's pressure drop coefficients in case of straight passage in a diverging tee junction both in laminar and turbulent conditions;
- Good agreement was found in case of side passage in a diverging tee junction in laminar conditions, assuming that at $Re = 3500$ in the combined passage of the tee junction the flow is still laminar;
- In case of side passage of a diverging tee junction in turbulent conditions, Ohnewein et al. measured pressure drop coefficients about 0.75 times those predicted by Idelchik;
- In case of straight passage of a combining tee junction in turbulent conditions, Ohnewein et al. measured pressure drop coefficients about 2.2 times higher than those predicted by Idelchik.

Hence, Idelchik's correlations were corrected accordingly and implemented in the model. Given the collector geometry, the above mentioned pressure drop coefficients for isolated tee junctions could be used to evaluate the pressure losses along the manifolds, which, according to Miller (2009), is allowed when the distance between two consecutives tees is three times longer than the manifold diameter.

2.1.2. Matlab implementation

Using the pressure drop correlations described in the previous section, a numerical model was developed in Matlab to compute the flow distribution and the resulting pressure drop across a collector. The input data to the model are the dimensions of the collector hydraulics and operating conditions of the heat transfer fluid (glycol content, flow rate and fluid temperature). The fluid temperature, which is assumed to be constant throughout the collector, is used to determine the density and viscosity of the fluid. Additionally, the flow is considered to be fully developed.

Given an initial flow rate as input, the model assumes that the flow is uniformly distributed in all absorber pipes. A uniform flow distribution would cause the pressure drop to increase from one strip to the next (see strip numbering in Fig. 1), as the fluid path becomes longer due to additional manifold segments. In reality, the pressure drop must be the same, irrespective of the path the fluid follows, resulting in an adjustment of the flow rate in each absorber pipe. In order to calculate the true flow distribution, the numerical model solves iteratively the set of equations (Eq. (9)), which impose both the conservation of mass across the collector (first line in Eq. (9)) and the uniformity of pressure drop along the different hydraulic paths (from second line downward in Eq. (9)):

$$\begin{pmatrix} 1 & 1 & 1 & 1 & 1 & 1 \\ k_{1,j}\cdot\dot{m}_{1,j} & -k_{2,j}\cdot\dot{m}_{2,j} & 0 & 0 & 0 & 0 \\ 0 & k_{2,j}\cdot\dot{m}_{2,j} & -k_{3,j}\cdot\dot{m}_{3,j} & 0 & 0 & 0 \\ \vdots & \vdots & \vdots & \vdots & \vdots & \vdots \\ 0 & 0 & 0 & 0 & k_{N-1,j}\cdot\dot{m}_{N-1,j} & -k_{N,j}\cdot\dot{m}_{N,j} \end{pmatrix} \times \begin{pmatrix} \dot{m}_{1,j+1} \\ \dot{m}_{2,j+1} \\ \dot{m}_{3,j+1} \\ \vdots \\ \dot{m}_{N,j+1} \end{pmatrix} = \begin{pmatrix} \dot{m}_{tot} \\ 0 \\ 0 \\ \vdots \\ 0 \end{pmatrix} \tag{9}$$

where

$\dot{m}$ is the mass flow rate [kg s^{-1}],
k is a hydraulic resistance coefficient [kg^{-1} m^{-1}], defined so that the product $(k_i \cdot \dot{m}_i^2)$ corresponds to the pressure drop (in Pascal) across the i-th hydraulic path. The factor k_i is representative of the pressure drop along the i-th absorber pipe, which is proportional to the square of the flow rate $\dot{m}_i$, as well as the pressure drop across the manifold segments and tees included in the i-th hydraulic path, properly normalized to the flow rate $\dot{m}_i$,
$1, 2, \ldots, N$ subscripts denote the hydraulic path and N is the total number of hydraulic paths,
tot subscript refers to the total flow rate supplied to the collector,
j subscript denotes the iteration number.

The iterative procedure is continued until the difference in the absorber pipe flow rates between two consecutive iterations is lower than 0.1%. With this convergence constraint a typical calculation is performed in a couple of seconds for a computer with quad-core CPU, 2.4 GHz CPU frequency and 8 GB memory.

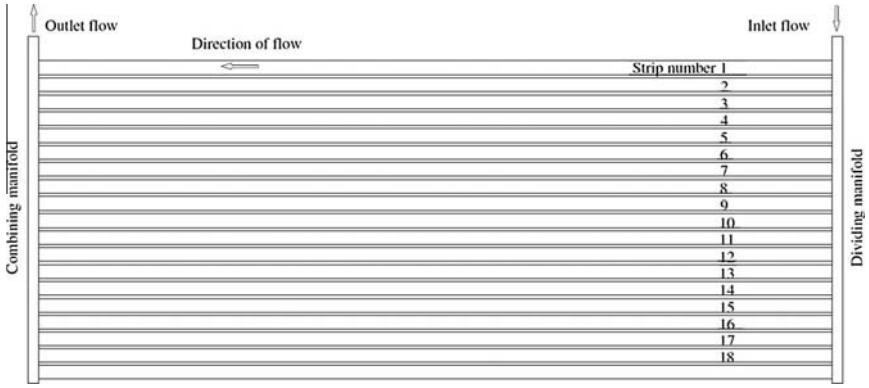

Fig. 1. Sketch of a U-type absorber with horizontal absorber pipes. Adapted from Fan et al. (2007).

The entire Matlab code used to carry out the present study is publicly available online (Bava, 2015).

2.2. Experimental setup for pressure drop measurement

The developed model was based on the design of U-type large scale collectors. These collectors have a number of horizontal absorber pipes welded to absorber strips and connecting two vertical manifolds located along the sides of the collector with their outlet at the top corners (Fig. 1).

The selection of this design was motivated by the fact that this is the most frequently adopted when manufacturing large collectors for solar heating field applications. In fact, these collectors are easy to assemble and quick to connect to one another when installed side by side in a field.

To validate the model in terms of overall collector pressure drop, the results were compared to measurements carried out on a large scale collector in different operating conditions. The tested collector was an Arcon Sunmark HT-SA 35/10 module, having an aperture area of 12.60 m^2. The collector piping was made of copper and had circular cross sections. The 18 absorber pipes were 5.80 m long, had an inner diameter of 9.1 mm and an intermediate spacing of 122 mm. The manifolds had an inner diameter of 32.9 mm.

A differential pressure sensor TA-SCOPE from IMI Hydronics was used to measure the pressure drop across the collector. The instrument nominal accuracy is given by the higher value between 0.1 kPa and 1% of the measured value.

The volume flow rate supplied to the collector was measured by a Kamstrup MP115 electromagnetic flow meter. Its accuracy is stated to be within ±0.50%. Additionally, the instrument was calibrated with water and propylene glycol/water mixture at different fluid temperatures and flow rates, and its nameplate calibration factor was confirmed.

Transparent plastic tubes were connected to the inlet and outlet of the collector at one end and to the pressure sensor at the other end, as shown in Fig. 2. The transparent pipes made it easier to verify that no air was present in the circuit, which otherwise would alter both the flow rate and differential pressure measurements. As the plastic pipes could not be connected exactly at the inlet and outlet of the solar collector (Fig. 3), the pressure losses occurring in between needed to be evaluated, in order not to assign them to the collector.

Fluid temperature was measured both at the inlet and outlet of the collector by type *T* thermocouples (copper/constantan junction).

Pressure drop measurements were carried out for flow rates between 0.08 and 0.72 l s^{-1} (0.3–2.6 m^3 h^{-1}) and at temperatures of approximately 25 °C, 55 °C and 70 °C, with water and a 50% propylene glycol/water mixture as heat transfer fluid. The tests were performed in cloudy sky conditions, so that the temperature rise across the collector was negligible and the assumption of isothermal flow introduced in the model was fulfilled.

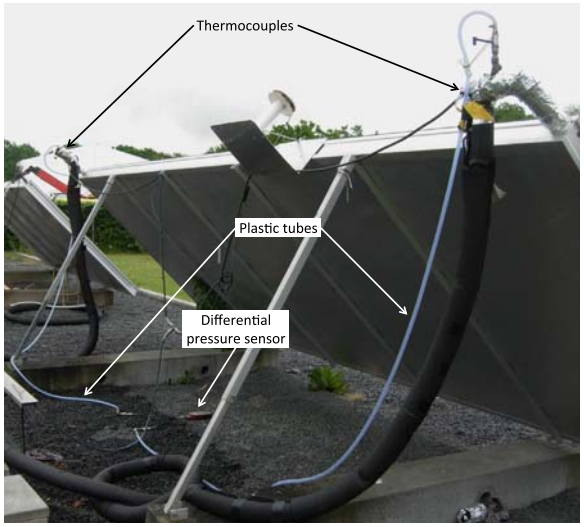

Fig. 2. Back of the HT-SA 35/10 solar collector with plastic pipes arrangement for pressure drop measurement.

3. Results

3.1. Collector pressure drop

The comparison between the measured and calculated pressure drops as function of the flow rate is shown in Figs. 4 and 5. Given the configuration of the hydraulic circuit, it was possible to test volume flow rates up to 2.6 m^3 h^{-1}, corresponding to pressure drops of approximately 9–10 kPa. The lower boundary of the tested flow rate was determined by the error of the differential pressure sensor, which became increasingly predominant when measuring pressure drops lower than 1 kPa. The error bars for the measured pressure drops represent the maximum value between the accuracy of the differential pressure sensor (i.e. the higher value between 0.1 kPa and 1% of the measured value) and the standard deviation of the measured values. For sake of simplicity of the diagrams, the error bars relative to the measured flow rates are not shown, as they are much smaller compared to the uncertainty of the differential pressure measurements. In fact, for all tested flow

Fig. 3. Detail of collector outlet with connection for the differential pressure sensor.

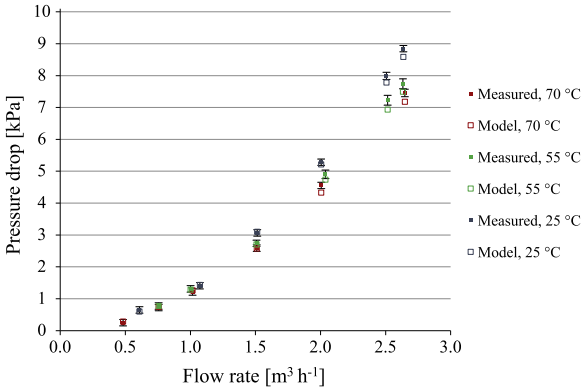

Fig. 4. Comparison between measured and calculated pressure drops for water.

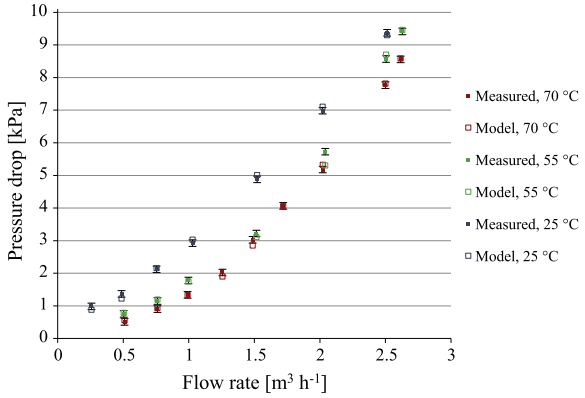

Fig. 5. Comparison between measured and calculated pressure drops for 50% propylene glycol/water mixture.

rates, the highest of the ratios between standard deviation and mean value was 0.43%, and most of them were lower than 0.20%. Consequently, they were always lower than the nameplate accuracy of the flow meter (±0.50%) and more than twice as small as the accuracy of the differential pressure sensor.

The pressure drop values given by the model matched the measured values with a reasonable accuracy. For values higher than 1 kPa, the highest relative difference between model and measurements was equal to 5% for water. Regarding the glycol/water mixture, the highest relative difference was 10% for a measured pressure drop of 1.37 kPa, while in the other cases it was within 7%.

For values lower than 1 kPa, the relative differences were slightly higher. The highest deviation (15%) was found for the lowest pressure drop (0.2 kPa). However, this deviation was within the accuracy range of the differential pressure sensor (0.1 kPa). Apart from this, no particular trend of discrepancy could be identified with respect to flow rate, temperature or fluid type, as both positive and negative deviations are found (see Figs. 4 and 5). Fig. 4 shows that for water at high flow rates ($V \geqslant 1.5\ m^3\ h^{-1}$ at 25 °C and $V \geqslant 2.0\ m^3\ h^{-1}$ for at 55 °C and 70 °C) the model underestimated the actual pressure drop by 3–5%. An underestimation of the friction factor in the corresponding range of Reynolds number ($Re_{pipe} > 5200$) was at first assumed as possible cause of these deviations. However, other data points in the same range of Reynolds number did not show similar deviations. Additionally, in order to increase the friction factor for this range of Reynolds number in such a way that these deviations were minimized, the roughness of copper pipes should have been assumed 10 times higher than that usually reported in literature (Binder, 1973). Such a correction did not seem acceptable, also based on the results of some surface roughness tests carried out on similar collector pipes. Hence, the assumption of smooth pipes was maintained.

Beside the accuracy of the instruments, other sources of error might be the assumptions made in the model, such as linear interpolation between laminar and turbulent conditions in case of transitional regime and fully developed flow throughout the pipes.

In both diagrams, the typical quadratic relation between pressure drop and flow rate can be observed, as the different groups of points are approximately aligned along parabolic trajectories. Additionally, the influence of the fluid temperature on the pressure drop across the collector can be noted by comparing the different series of points within the same diagram. As expected, a fluid flow at lower temperature caused a higher pressure drop for the same flow rate.

3.2. Flow distribution

The flow distribution was expressed in terms of dimensionless flow rate in the absorber pipes, defined by (Eq. (10)) as:

$$V_i' = \frac{V_i}{\left(\sum_{i=1}^{N} V_i\right)/N} \tag{10}$$

where

V_i' is the dimensionless flow rate flowing in the i-th absorber pipe [–],

V_i is the volume flow rate in the i-th absorber pipe [$m^3\ h^{-1}$],

N is the number of absorber pipes [–].

3.2.1. Comparison with previous literature

As no validation in terms of flow distribution could be performed in the test rig, the model results were compared with data found in literature. Results from the simulation model of Jones and Lior (1994) were chosen for comparison, because of the similarity in collector design as well as the identical assumption of isothermal flow. In Jones and Lior's paper, model results obtained for a

U-type harp collector having 8 or 16 absorber pipes are presented. The absorber pipes are 1.83 m long and can have a diameter of 0.25, 0.50 and 0.75 times the manifold diameter, which is 2.54 cm. The manifolds length is 0.915 m. As heat transfer fluid water at 60 °C is assumed and the flow rate is varied in such a way that the Reynolds number at the manifold inlet is 3210, 9640 and 16,100 in different cases. Darcy friction factors are evaluated using Colebrook equation (Colebrook, 1939) for $Re > 3000$ and Hagen–Poiseuille law (Eq. (7)) for $Re < 2100$. Linear interpolation between the two is used for the transition regime. The roughness of the pipe material is not specified in the paper, but it is said to be intermediate between that for clean copper and steel. A value of 0.016 mm was therefore selected in the model proposed in the present paper. Regarding tee junctions, the schemes reported by Jones and Lior imply that sharp edge tees were considered. The pressure change across the tee junctions is evaluated based on momentum conservation and constant pressure regain coefficients ($\gamma = 0$ for converging tee junction and $\gamma = 0.9$ for diverging tee), with no distinction between laminar and turbulent regime. Additionally, the energy loss coefficient at the entrance and exit of the absorber pipes is assumed to be constant and equal to 1.2. The last two assumptions may not be very accurate, as pressure drops in tees are shown to be very sensitive to the tee geometry and flow characteristics (Idelchik, 1994; Ohnewein et al., 2015). However, to make the comparison between the two models fair, the same assumption was made in the proposed model and the pressure drop correlations for tees in turbulent regime were used also in the laminar region.

The comparison between the flow distributions found by Jones and Lior and those given by the proposed model are shown in Fig. 6 for two different cases. The first refers to a collector with 8 pipes and a ratio between pipe and manifold diameters of 0.50. The second case refers to a collector with 16 pipes and a diameters ratio of 0.25. This resembles more closely the geometry of a large scale collector on which the present model was based. In both cases the Reynolds number at the manifold inlet was 9640.

In Fig. 6 it can be seen that the two couples of profiles presented a very similar trend, with the presented model predicting a more uniform flow distribution compared to Jones and Lior's. The difference was relatively small, with maximum deviations of 5% and 1% in case of 8 and 16 pipes respectively, and it was most likely due to the different correlations used to estimate the energy losses in the tee junctions.

Another difference between the two models was the trend of the curves in the bottom pipes. Due to the assumption made by Jones and Lior about the constant pressure regain coefficients, the profiles returned by their model were strictly decreasing. On the other hand, the pressure drop coefficients from Idelchik (1994) used in the proposed model allowed a slight increase in flow in the last pipes, as shown in the case with $N = 8$ in Fig. 6. This happened because the pressure drop across the side passage of diverging tee junctions decreased with the reduction in the manifold flow rate more significantly than the increase in hydraulic resistance given by the other hydraulic components (tee junctions and manifold segments).

A good agreement between the two models was found for most of the other combinations of Reynolds number and diameters ratio proposed by Jones and Lior in their paper, with maximum deviations of 5%. Exceptions were the results obtained for a diameters ratio of 0.75. In this case, Jones and Lior's model predicted a much stronger non-uniformity, with the top pipe having a flow rate up to four times higher than in the bottom pipe. In the same conditions, the proposed model predicted a ratio between of the two flow rates of approximately two. The difference between the models was caused by the different correlations used to evaluate the pressure drops in the tee junctions. In case of a large diameters ratio, the pressure drop across the absorber pipes is not predominant any more, and the pressure drops across the tee junctions play a more important role in determining the flow distribution.

3.2.2. Effect of flow regime on flow distribution

Using the developed model, it was possible to calculate the flow distribution inside the HT 35/10 collector at different flow rates and fluid types. Two cases were considered, one with water at 70 °C (Fig. 7) and the other with water at 20 °C (Fig. 8). Due to the different fluid viscosity at different temperatures, these two cases allowed to study the flow distribution at similar flow rates, but in different flow regimes.

The flow distributions shown in Figs. 7 and 8 decrease from the top to the bottom pipe, but with different profiles. In case of water at 70 °C (Fig. 7), the distribution was more uniform, especially at flow rates higher or equal to 1.5 $m^3\ h^{-1}$, for which the parameter V' ranged from 0.92 to 1.09. At these flow rates the flow across the absorber pipes and in the largest part of the manifold was turbulent. At a flow rate of 0.7 $m^3\ h^{-1}$, the flow regime in the manifold was turbulent in the first 15 pipes and consequently the flow distribution was still roughly uniform. Conversely, in the last three manifold segments the flow regime switched to laminar, causing a stronger decrease of the flow rates in the last absorber pipes and a wider spread of the V' values.

In case of water at 20 °C (Fig. 8), the laminar regime in the pipes and most of the manifolds caused a much less uniform flow distribution. This is particularly evident at the lower flow rates of 0.5 and 1 $m^3\ h^{-1}$, where V' varied more strongly, in a range between 0.66 and 1.25. For higher flow rates the portion of manifolds experiencing turbulent conditions increased and the flow distribution became more uniform, similar to the profiles shown in Fig. 7.

Through the developed model, it was also possible to study the contribution to the total pressure drop of the single hydraulic com-

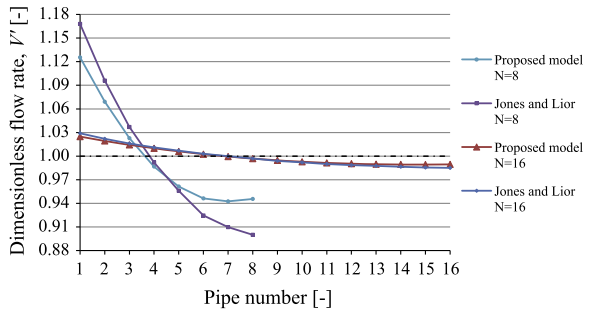

Fig. 6. Comparison in flow distribution between Jones and Lior's model and the proposed model.

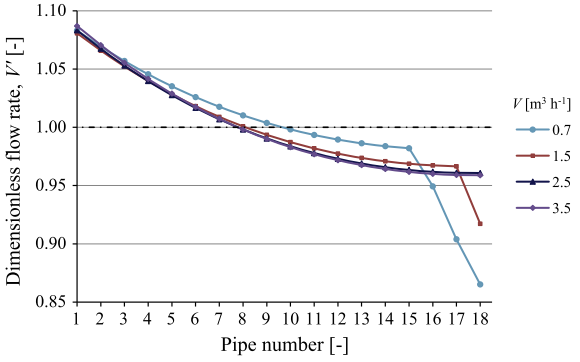

Fig. 7. Flow distribution in the absorber pipes at different flow rates for water at 70 °C.

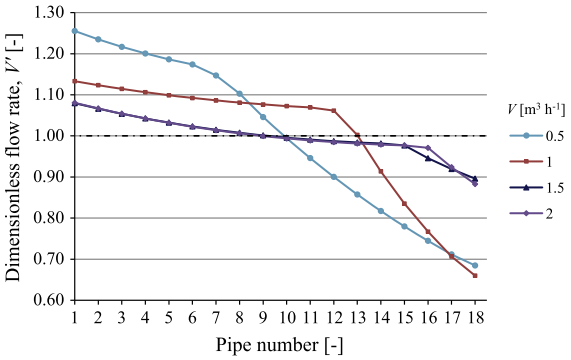

Fig. 8. Flow distribution in the absorber pipes at different flow rates for water at 20 °C.

ponents, such as absorber pipes, manifolds and tee junctions. Although the pressure drop across the absorber pipes played the most significant role in both cases, its importance for the different paths was quite different, depending on the flow regime. In case of turbulent regime in all absorber pipes, the pressure drop along these represented 86–90% of the total collector pressure drop for the top pipe, and 66–71% for the bottom pipe. The remaining part was caused by forward and return manifolds as well as tee junctions. In case of laminar regime, the pressure drop in the absorber pipe was 87–92% of the total for the top pipe, and 44–50% for the bottom pipe.

4. Discussion

4.1. Pressure drop

As expected, when testing the two heat transfer fluids at the same temperature and flow rate, the pressure drop for the glycol/water mixture was larger than for water, because of the much higher viscosity. For the same reason, the pressure drop for both fluids was higher at lower temperatures. Nevertheless, this effect was much more relevant for the 50% glycol/water mixture than for water. This was due to two main factors. Firstly, the kinematic viscosity of water decreases by a factor of 2.7 when the temperatures increases from 20 °C to 80 °C, while that of a 50% glycol/water mixture decreases by a factor of 5 for the same temperature variation. Secondly and more importantly, the higher viscosity of the glycol/water mixture at about 20 °C caused the flow regime in the absorber pipes to be laminar, even at the highest tested flow rate of 2.5 $m^3\ h^{-1}$. This entailed much higher friction factors compared to those obtained at higher temperatures.

Despite its secondary importance, the higher density also contributed in increasing the pressure drop at lower temperatures. The effect was more important for the glycol/water mixture, as its density varies by about 4% in the range 20–80 °C, compared to 2% for water.

It can also be noted that the pressure drop for glycol/water mixture at 70 °C was very similar to that of pure water at 20 °C. This was due to the fact that the two fluids have very similar kinematic viscosity and density in these conditions ($\nu \approx 1 \cdot 10^{-6}\ m^2\ s^{-1}$, $\rho \approx 1000\ kg\ m^{-3}$). This means that the pressure drop curves for glycol/water mixtures at relatively high temperature may be indirectly evaluated using water at sufficiently low temperature.

4.2. Flow distribution

The results given by the model showed a decrease in flow rate from the top to the bottom pipes, because only friction was considered as driving force, so that the longer the hydraulic path, the higher the resistance. This is in agreement with the findings of Wang and Wu (1990), Jones and Lior (1994), and Fan et al. (2007).

A large difference appeared to exist when comparing flow distributions characterized by a different flow regime. Turbulent flow in the manifolds entailed relatively small pressure losses both in manifold segments and tees, compared to those occurring across the absorber pipes. So, these additional pressure drops could be compensated by a slight unbalance in the collector flow distribution. This is shown in Fig. 7 by the flow distributions referring to the flow rates of 2.5 and 3.5 $m^3\ h^{-1}$. The extent of the unbalance in flow distribution, which was needed to compensate the pressure drop caused by manifolds segments and tees, was also affected by the flow regime in the absorber pipes. Due to the geometry of the HT 35/10 collector, the flow regime in all absorber pipes was turbulent, when it was turbulent in the entire manifold. Given the weak dependence of the friction factor in the turbulent region on the Reynolds number (see Eq. (8)), the friction pressure drop in the absorber pipes can be considered proportional to the square of the fluid velocity, so that small variations in flow rate cause larger variations in pressure drop. For this reason, a slight unbalance in flow distribution is sufficient to give the right pressure drop along each hydraulic path.

Fig. 7 also shows that when turbulent regime was established throughout the collector, then the flow distribution was not significantly affected by the total flow rate, which is in agreement with previous findings (Jones and Lior, 1994).

At lower flow rates ($V \leqslant 1.5\ m^3\ h^{-1}$ in Fig. 7), only part of the manifolds was in turbulent conditions, so that laminar equations applied to the last manifold segments and tees. As both pressure drop coefficients for tees and friction factor coefficients are much higher in laminar regime than in turbulent regime, the flow rate in the last absorber pipes needed to diminish abruptly in order to cause the same pressure drop as the previous hydraulic paths, causing higher flow non-uniformity.

On the other hand, when using water at 20 °C (Fig. 8), the higher viscosity resulted into laminar regime in the absorber pipes and in larger part of the manifolds. At lower flow rates ($V \leqslant 1\ m^3\ h^{-1}$), the flow regime in all absorber pipes was laminar, while it was initially turbulent in the manifold and then, as more fluid was diverted to the absorber pipes, laminar. The precise tee junction after which the change in flow regime occurred can be identified looking at the change in slope in the curves in Fig. 8: a milder slope corresponds to turbulent flow in the manifold, while a steeper slope to laminar flow. The flow distribution at these flow rates was much less uniform than in the turbulent case (Fig. 7). The main reason for this behavior was that the local loss coefficients for tees in laminar regime are more sensitive to flow conditions than in turbulent regime, so they varied more significantly from one pipe to the next. As the hydraulic resistance between two consecutive pipes differed more significantly, this needed to be compensated by a larger difference in flow rates. A secondary reason is the linear dependence of the friction pressure drop on the fluid velocity in laminar conditions (see Eqs. (1) and (7)), which, compared to the quadratic dependence in turbulent conditions, required larger variations in flow rate to compensate the varying pressure drop across the absorber pipes.

The distribution became more uniform at higher flow rates, as a longer part of the manifolds experienced turbulent conditions and the regime inside the absorber pipes became transitional ($V = 1.5\ m^3\ h^{-1}$) and then turbulent ($V = 2\ m^3\ h^{-1}$).

The fact that the modeled flow distributions become more uniform at higher flow rates seems to be in disagreement with previous literature. For example, Jones and Lior (1994) show that the flow distribution in a harp collector (both in Z- and U-configuration) is approximately independent of the Reynolds

number at the manifold inlet, and hence of the total flow rate. Only for the highest ratio between absorber pipe and manifold diameters ($d/D = 0.75$), the flow distribution at the lowest flow rate ($Re_{inlet} = 3210$) was slightly more uniform than at higher flow rates ($Re_{inlet} = 9640$ and $Re_{inlet} = 16{,}100$). The reason for the different trend found through the proposed model was mainly the use of different correlations for tee junctions, depending on the flow regime. As an example, Fig. 9 shows the modeled flow distributions in a HT-SA 35/10 collector at different manifold inlet Reynolds numbers, using turbulent correlations for tee junctions regardless of the actual flow regime. In this case the trend of the flow distributions was in agreement with Jones and Lior (1994). However, given the good agreement between the measurements from Ohnewein et al. at low Reynolds number and Idelchik's laminar correlations, it was decided to keep the latter in the model.

As mentioned, isothermal flow was assumed in the model. In real operating conditions, the temperature of the heat transfer fluid would increase along the absorber pipes. If the temperature rise is relatively small, the fluid properties do not change significantly and using the mean fluid temperature is an acceptable simplification. Nevertheless, in case of uneven flow distribution and uniform solar irradiance on the collector, a pipe with a lower flow would experience a larger temperature rise and a higher mean fluid temperature. The fluid viscosity would be lower, and thereby the friction factor and hydraulic resistance would be smaller. Consequently, the flow distribution in case of non-isothermal conditions would partly balance itself, resulting in a more uniform distribution compared to isothermal conditions. The effect is expected to be more relevant in case of laminar flow, because of the stronger flow maldistribution (Fig. 8) and the direct proportionality between friction factor and fluid viscosity (see Eqs. (2) and (7)).

Flow maldistribution in a harp collector causes a decrease in the collector efficiency. In fact, absorber pipes having lower flow rates and hence higher temperatures suffer higher heat losses. The warmer fluid at the exit of these pipes is tempered down by the colder fluid coming from the absorber pipes supplied with higher flow rates. The mixing of flows at different temperatures causes a lower temperature rise across the collector compared to the case with uniform flow distribution and identical temperature rise across each absorber pipe. Consequently, the overall collector efficiency decreases. The negative effect of the flow maldistribution on the collector efficiency is increased primarily by the degree of maldistribution and secondly by the collector heat loss coefficient. The quantitative relationship between flow maldistribution and collector efficiency degradation is out of the scope of this investigation. However, an estimation of this effect can be found in Chiou (1982). In fact, defined a *flow nonuniformity parameter* as the root mean square deviation of the absorber pipe flow rates, the deterioration of the collector efficiency is expected to be proportional to approximately the square of such parameter.

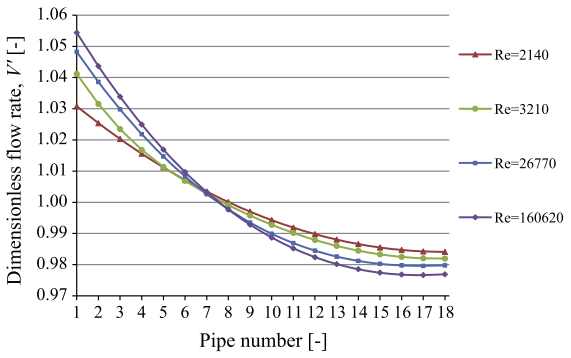

Fig. 9. Flow distribution in the absorber pipes of a HT-SA 35/10 collector for different manifold inlet Reynolds numbers.

5. Conclusions and future perspective

A model for estimating the pressure drop and flow distribution across a solar collector with U-type configuration in isothermal conditions was developed. The pressure drops calculated by the model were compared to measurements carried out on a solar collector. The flow distributions were compared to previous literature findings.

For pressure drops higher than 1 kPa, all relative differences between model and measurements were within ±7%, apart from one point. For lower pressure drops the relative difference increased, but always within the accuracy of the differential pressure sensor.

Flow rate and viscosity were the main factors influencing the pressure drop, so different fluids having similar values for these two parameters gave almost identical pressure drops.

The flow distribution was mainly affected by the flow regime in the manifolds. Turbulent regime throughout the manifolds entailed a more uniform flow distribution compared to laminar flow. This was mainly due to the strong dependence of the local losses for the tee junctions in laminar conditions. The comparison between calculated flow distributions and results from literature gave a good agreement in most of the cases.

The presented model is planned to be used for the development of a numerical model for evaluating the flow distribution in large solar collector fields for district heating applications. In fact, flow rate and temperature levels in such fields vary depending of several boundary conditions, such as solar irradiance, fluid type, forward and return temperatures of the district heating network. Moreover, due to the temperature rise across a collector row, each collector experiences a different mean fluid temperature. In order to evaluate the flow distribution across the collector field, a flexible and accurate model is needed to calculate the pressure drop across each collector in different operating conditions.

Additionally, regarding the flow distribution, the model can be used to optimize the design of collector. Aspects which may be investigated are the ratio between manifold diameter and absorber pipe diameter, length of the absorber pipes and effect of pipe inset into the manifold. The results could be used by collector manufacturers to design their products in such a way that a more uniform flow distribution is achieved under typical operation, and thereby improve the collector efficiency.

Acknowledgements

The authors are thankful to the Marie-Curie Actions – Initial Training Network research programme of the European Union which supported the first author through the SolNet-SHINE project. The authors are also grateful to the company Arcon-Sunmark A/S for having made available the HT-SA collector used during the study.

Appendix A

To evaluate the Reynolds number at which transition in flow regime occurred, the following procedure was followed. The pressure drop across the collector was measured while varying gradually the fluid inlet temperature and keeping a constant flow rate. The test was performed in cloudy sky conditions, so that the inlet and outlet temperature were approximately the same. Due to non-uniform flow distribution, the different absorber pipes had different flow rates. Using the presented numerical model, it was possi-

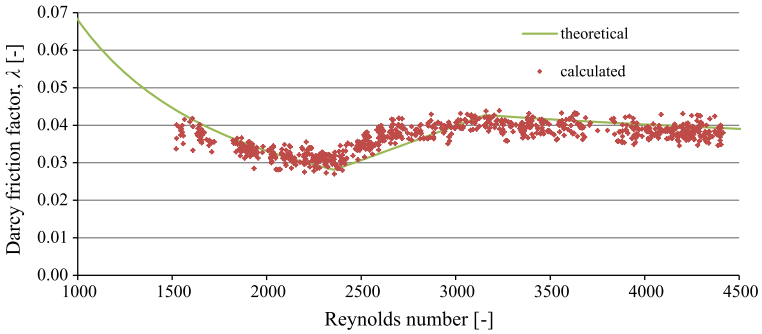

Fig. A1. Comparison between theoretical and calculated Darcy friction factor. The theoretical friction factor curve is obtained from (Eq. (7)) for $Re < 2300$, (Eq. (8)) for $Re > 3100$ and linear interpolation between the two in between these values.

ble to identify the pipe having a value of flow rate closer to the flow rate which would occur in case of perfectly uniform flow distribution. For the selected pipe, the numerical model was also used to isolate the pressure drop caused by the absorber pipe from that caused by the manifolds and tee junctions. The Darcy friction factor was finally calculated through (Eq. (1)), using the pipe pressure drop and a fluid velocity corresponding to a perfectly uniform flow distribution.

The comparison between the so calculated Darcy friction factor and the theoretical one is shown in Fig. A1. In the diagram the curved referred to as "theoretical" friction factor is obtained from (Eq. (7)) for $Re < 2300$, from (Eq. (8)) for $Re > 3100$ and from linear interpolation between the two for the intermediate Reynolds numbers. The data points refer to the results of a test performed with a 42% glycol/water mixture, a total flow rate of 1.98 m^3/h and a mean fluid temperature increasing from 30 °C to 70 °C during 2.5 h.

References

Bava, F., 2015. <https://github.com/febav/CollectorPressureDrop.git> (accessed 09/01/2016).

Binder, R.C., 1973. Fluid Mechanics, fifth ed. Prentice Hall, Englewood Cliffs, USA.

Chiou, J.P., 1982. The effect of non-uniform fluid flow distribution on the thermal performance of solar collector. Sol. Energy 29 (6), 487–502.

Colebrook, C.F., 1939. Turbulent flow in pipes, with particular reference to the transition region between smooth and rough pipe laws. J. Inst. Civil Eng. 11, 133–156.

Fan, J., Shah, L.J., Furbo, S., 2007. Flow distribution in a solar collector panel with horizontally inclined absorber strips. Sol. Energy 81 (12), 1501–1511.

Furbo, S., 2015. Using water for heat storage in thermal energy storage (tes) systems. In: Cabeza, L.C. (Ed.), Advances in Thermal Energy Storage Systems. Woodhead Publishing-Elsevier, Cambridge, United Kingdom, pp. 31–47.

Haaland, S.E., 1983. Simple and explicit formulas for the friction factor in turbulent flow. J. Fluids Eng. (ASME) 105 (1), 89–90.

Holman, J.P., 2002. Heat Transfer, ninth ed. McGraw-Hill, New York, USA.

Idelchik, I.E., 1994. Handbook of Hydraulic Resistance, third ed. CRC Press, Boca Raton, USA.

ISO Standard 9806, 2014. Solar Energy – Solar Thermal Collectors – Test Methods. International Organization for Standardization (ISO), Geneva, Switzerland.

Jones, G.F., Lior, N., 1987. Conjugate heat transfer and flow distribution in an assembly of manifolded finned tubes. In: Kitto, J.B., Jr., Robertson, J.M. (Eds.), Maldistribution of Flow and its Effect on Heat Exchanger Performance. ASME HTD, pp. 127–136.

Jones, G.F., Lior, N., 1994. Flow distribution in manifolded solar collectors with negligible buoyancy effects. Sol. Energy 52 (3), 289–300.

Joseph, D.D., Yang, B.H., 2010. Friction factor correlations for laminar, transition and turbulent flow in smooth pipes. Physica D 239, 1318–1328.

Kestin, J., Sokolov, M., Wakeham, W.A., 1978. Viscosity of liquid water in the range −8 °C to 150 °C. J. Phys. Chem. Ref. Data 7, 941–948.

Kovacs, P., Persson, M., Wahlgren, P., Jensen, S., 2012. Quality Assurance in Solar Thermal Heating and Cooling Technology – Pressure Drop Over a Solar Flat Plate Collector Using Various Heat Transfer Fluids. Deliverable D2.2 – R2.13 of Project IEE/08/593/SI2.529236 <http://www.estif.org/> (accessed 18/12/2015).

Miller, D.S., 2009. Internal Flow Systems, second ed. Miller Innovations, Bedford, United Kingdom.

Ohnewein, P., Hausner, R., Preiß, D., 2015. Hydraulikdesign von parallelen Kollektormodulen in solarthermischen Großanlagen. Neue Energien 2020 – ParaSol project <http://www.solarthermalworld.org/keyword/parasol> (accessed 05/04/2016).

Wang, X.A., Wu, L.G., 1990. Analysis and performance of flat plate solar collector arrays. Sol. Energy 45 (2), 71–78.

Weitbrecht, V., Lehmann, D., Richter, A., 2002. Flow distribution in solar collectors with laminar flow conditions. Sol. Energy 73 (6), 433–441.

Windeleff, J., Nielsen, J.E., 2014. Solar District Heating in Denmark. Danish Energy Agency and PlanEnergi.

Paper IV

A numerical model to evaluate the flow distribution in a large solar collector field

Federico Bava, Janne Dragsted and Simon Furbo

Solar Energy 143 (2017) 31–42

Solar Energy 143 (2017) 31–42

Contents lists available at ScienceDirect

Solar Energy

journal homepage: www.elsevier.com/locate/solener

A numerical model to evaluate the flow distribution in a large solar collector field

Federico Bava *, Janne Dragsted, Simon Furbo

DTU Civil Engineering, Technical University of Denmark, Brovej, Building 118, 2800 Kgs. Lyngby, Denmark

ARTICLE INFO

Article history:
Received 13 July 2016
Received in revised form 26 October 2016
Accepted 13 December 2016

Keywords:
Solar collector
Solar collector field
Flow balancing
Flow distribution
Parallel connection

ABSTRACT

This study presents a numerical model to evaluate the flow distribution in a large solar collector field, with solar collectors connected both in series and in parallel. The boundary conditions of the systems, such as flow rate, temperature, fluid type and layout of the collector field can be easily changed in the model. The model was developed in Matlab and the calculated pressure drop and flow distribution were compared with measurements from a solar collector field. A good agreement between model and measurements was found. The model was then used to study the flow distribution in different conditions. Balancing valves proved to be an effective way to achieve uniform flow distribution also in conditions different from those for which the valves were regulated. For small solar collector fields with limited number of collector rows connected in parallel, balancing valves are not strictly necessary if the pressure drop across the collector rows is much higher than the pressure drop along the longest distribution pipe.

1. Introduction

1.1. Background

An increasing number of large solar collector fields have been built in Europe in the last years. The main market for this technology has been Denmark, with 77% of the total collector area installed in European large scale solar heating plants at the end of 2015 (Mauthner et al., 2016). This development has been driven by some specific factors, such as high taxation on fossil fuels and widespread use of district heating (DH), to which large collector areas can be connected (Furbo et al., 2015). At the end of 2015, Denmark had more than 800,000 m^2 of solar collector fields, and more plants are expected to be installed in the next years (Fig. 1). Also the size of the collector fields has been increasing. In 2015 the current largest collector field was installed in Vojens, with a collector area of 70,000 m^2 (Mauthner et al., 2016). In 2016 a 150,000 m^2 collector field is expected to be completed in Silkeborg (EnergySupply, 2016).

The larger the solar collector field and the number of collector rows, the higher the risk of non-uniform flow distribution from one row to another and decreased thermal performance. In fact, identical collector rows supplied with different flow rates reach different outlet temperatures. Mixing flows at different temperatures causes a lower temperature rise across the collector field compared to the case with uniform flow distribution and identical outlet temperatures. If different rows have a different number of collectors (and different aperture areas), these should be supplied by different flow rates, proportional to the collector row area, resulting in the same outlet temperature for all rows.

1.2. Literature review

Flow distribution in solar thermal systems has been the topic of many investigations, both at collector level and array level. The negative effect of the flow maldistribution on the thermal performance of a single collector with parallel channels was investigated by Chiou (1982). He presents a method to determine how much the collector efficiency is penalized by the flow maldistribution. Wang and Wu (1990) developed a numerical model to predict the flow distribution in collector arrays with vertical pipes, both in U-type and Z-type configuration. Compared to the Z-type configuration, the U-type presents a higher maldistribution, with the flow rates in the absorber pipes decreasing monotonically with the distance from the array inlet. The same trend is found by Jones and Lior (1994), who considered a single collector with vertical pipes, instead of an entire array. Weitbrecht et al. (2002) present both an experimental and analytical study on the flow distribution in a Z-type collector in isothermal conditions, verifying the results from Wang and Wu (1990) and Jones and Lior (1994). They conclude that a more uniform flow distribution is

* Corresponding author.
E-mail address: febav@byg.dtu.dk (F. Bava).

http://dx.doi.org/10.1016/j.solener.2016.12.029
0038-092X/

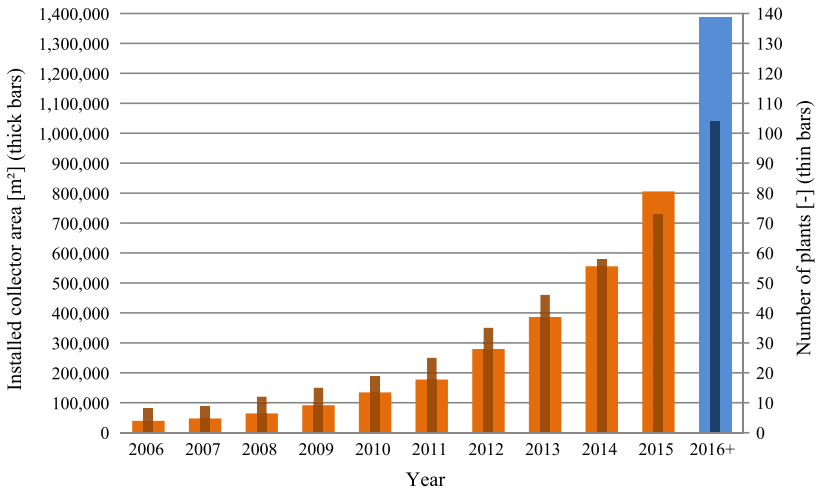

Fig. 1. Historical development of solar collector fields for DH applications in Denmark: installed collector area and number of operating (orange) and upcoming (blue) plants at the end of 2015 (Trier, 2016).

achieved when the pressure losses in the absorber pipes are much higher than in the manifolds. Fan et al. (2007) studied the flow and temperature distribution in a solar collector for large collector fields applications. Calculations with a CFD model and experimental measurements are compared. The authors conclude that the flow distribution is determined by friction (and hence buoyancy can be neglected), if the velocity in the collector pipes is high compared to the temperature rise across the collector. Bava and Furbo (2016) propose a numerical model to evaluate the pressure drop and flow distribution in a collector with horizontal U-connected pipes. Based on the findings of Fan et al. (2007), the authors argue that in large collector fields for DH applications the relation between the fluid velocity in the absorber pipes and the temperature rise across the collector is such that buoyancy can be neglected. The model was validated against measurements carried out on a collector for solar assisted DH plants.

Uniform flow distribution is of great importance also for the efficient operation of the entire collector field, but it is often overlooked (Dorantes et al., 2014). Ideally, the layout of a collector array should keep the pipe lengths as short and the flow distribution as uniform as possible. Shorter pipe lengths entail lower material and installation costs, lower thermal losses from the distribution lines, reduced pressure drop and consequently lower pumping power. Since reduction in pipe length and uniform flow distribution cannot be optimized simultaneously, a compromise between the two needs to be found. Rohde and Knoll (1976) investigate different hydraulic solutions for minimizing the flow maldistribution in a collector field of 12 collector rows connected in parallel. These solutions include various size manifolds, orifices and balancing valves. The last two are proposed as the best solutions, both in terms of performance and cost. It is noted that a configuration of valve settings maintains the desired flow distribution only at a certain flow rate. Finally, laminar flow produces less uniform flow distribution than turbulent flow. Also Knabl et al. (2014) present different solutions to achieve uniform flow distribution. A solution consists of maintaining a constant pipe diameter in the supply and return pipe. An example is represented by the first large collector fields built in Sweden, such as Falkenberg (1989) and Nykvarn II (1991). Another possibility is to adopt a Z-configuration (or reverse return). Though, both these solutions entail higher costs due to the additional material. Balancing valves can be installed in each row, but these increase the investment cost, installation time and maintenance (in case of defective valves). Installing pipes with different diameters within each collector row is a cheaper solution, but must be calculated in advance exactly, as a later adjustment would be very expensive.

1.3. Solar collector fields for DH applications

In Denmark the majority of large collector fields are installed next to a heating plant supplying a DH network. The inlet temperature to the collector field is determined by the return temperature from the DH network. Typical return temperatures are in the interval 35–45 °C (Windeleff and Nielsen, 2014). The control strategy of the collector field aims at reaching a constant outlet temperature, by continuously regulating the total flow rate based on the solar irradiance (Heller, 2000). The desired outlet temperature is the DH supply temperature. Typical supply temperatures are in the interval 70–85 °C (Windeleff and Nielsen, 2014). The temperature drop across the heat exchanger should be considered. When sufficiently high temperatures cannot be reached, for example in periods with low solar irradiance, the additional energy is provided by an auxiliary energy source.

Most of the Danish collector fields are made of 12–14 m^2 flat plate harp collectors (Windeleff and Nielsen, 2014). The diameter of the supply and return pipes to and from the collectors is progressively decreased as the fluid is diverted to the collector rows. A uniform flow distribution across the collector field is achieved by installing balancing valves at the inlet of each collector row. Unlike orifices, the setting of these valves can be changed if needed, so providing a higher flexibility. Additionally, if coupled with an on/off valve at the row outlet, balancing valves can be used for maintenance purposes. For example, in case of leakage in a row, this can be isolated, while the rest of the collector field continues its normal operation. The setting of the valves is usually chosen in such a way that the desired flow distribution is achieved in nominal operating conditions, i.e. high solar irradiance, high flow rate, nominal inlet and outlet temperatures. As found by Rohde and Knoll (1976), these valve settings provide a perfectly uniform flow distribution only in a specific operating condition, while deviations can be expected in other conditions.

Being able to evaluate these deviations is of great interest, as it allows understanding how the collector field performance is affected by off-design conditions. Additionally, it is of particular importance with respect to critical conditions such as incipient stagnation and anti-freezing mode. A collector row supplied with

a lower flow rate is more likely to experience stagnation or freezing. This represents a risk for the entire system and penalizes the overall performance. If one row is not supplied by the proper flow rate and so reaches too high temperatures, this may trigger an alarm signal, which interrupts the normal operation of the collector field with consequent loss of useful energy production. On the other hand, when the system switches to anti-freezing mode, the solar collector fluid (usually 30–40% propylene glycol/water mixture (Windeleff and Nielsen, 2014)) is circulated across the collector field. Rows supplied with lower flow rates are more likely to incur into freezing in case of extended cold periods.

The aim of this study was to develop a numerical model for calculating the flow distribution across a large collector field. The reliability of the model was verified by comparing its results against experimental measurements. Different scenarios were treated to analyze how different operating conditions, layouts and design choices can affect the flow distribution. The Matlab source code of the model is publicly available online (Bava, 2016) and can be edited to treat different configurations.

2. Material and method

2.1. Numerical model

2.1.1. Pressure drop correlations

To evaluate the flow distribution in a parallel hydraulic system, the relation between flow rate and pressure drop across each component needs to be known. In a parallel hydraulic system, the fluid flow distributes so that the pressure drop along each hydraulic path is the same. Consequently, hydraulic paths characterized by higher hydraulic resistance will receive lower flow rates. As the relation between pressure drop and fluid velocity is neither generally linear nor constant, the flow distribution across a parallel system changes depending on the total flow rate. Also variations of the fluid viscosity and density can affect the flow distribution.

In a solar collector field it is possible to distinguish three main types of hydraulic components: solar collectors, pipes (distribution pipes and row inlet/outlet) and fittings (bends, tee junctions, valves, etc.).

The pressure drop characteristic of a solar collector can be difficult to find in technical datasheets, as it is not compulsory for the manufacturer to provide (ISO, 2014). Even if provided, this relation is usually given for a specific fluid and temperature. So, care should be taken when using other fluids and/or temperatures.

In this study the collector pressure drop was calculated using the model proposed by Bava and Furbo (2016). The modeled collector was a HTHEATStore 35/08 from the company Arcon-Sunmark A/S (SP, 2015). This is a flat plate harp collector with U-type configuration and an aperture area of 12.60 m^2. Its 18 absorber pipes are 5.80 m long, have an inner diameter of 7.3 mm and an intermediate spacing of 122 mm. The manifolds have an inner diameter of 32.9 mm. The calculated pressure drop is shown in Fig. 2 as function of temperature and flow rate for a 35% propylene glycol/water mixture. The thermophysical properties of the fluid were evaluated through (Eq. (8)) and (Eq. (9)).

The friction loss along a straight pipe of constant cross section can be calculated by the Darcy-Weisbach equation:

$$\Delta p = \lambda \frac{l}{D_h} \frac{\rho w^2}{2} \tag{1}$$

where

Δp is the pressure drop [Pa],
λ is the Darcy friction factor [–],
l is the pipe length [m],
D_h is the pipe hydraulic diameter, which equals the inner diameter for a full flow circular pipe [m],
ρ is the density of the fluid [kg m^{-3}],
w is the mean fluid velocity [m s^{-1}].

In case of Reynolds numbers (Re) lower than 2300, laminar flow regime was assumed (Holman, 2002) and the Darcy friction factor was calculated through the Hagen-Poiseuille law (Eq. (2)):

$$\lambda = 64/Re \tag{2}$$

For $Re > 4000$, the flow was assumed turbulent (Holman, 2002) and the friction factor was calculated through the Haaland (1983) correlation for rough pipes (Eq. (3)), as the distribution pipes were made of steel with roughness $\varepsilon = 10^{-4}$ m (Li and Svendsen, 2013).

$$\lambda^{-1/2} = -1.8\log_{10}\left\{\left[\varepsilon/(3.7D_h)^{1.11} + 6.9/Re\right]\right\} \tag{3}$$

where ε is the absolute surface roughness of the pipe inner surface [m].

The Haaland correlation is an explicit, and hence faster to solve, formulation of the Colebrook (1939) equation. Beside the mentioned correlations, other correlations were implemented in the model, such as those proposed by Colebrook (1939) for turbulent flow in rough pipes, by Blasius (1913) for turbulent flow in smooth pipes and by Joseph and Yang (2010) for any flow regime in smooth pipes.

Following the example of Jones and Lior (1994), the friction factor in the transition region ($2300 < Re < 4000$) was calculated by linear interpolation between the value obtained from (Eq. (2)) for $Re = 2300$ and that obtained from (Eq. (3)) for $Re = 4000$.

Regarding local losses in fittings, such as bends, tee junctions, and changes of flow section area, correlations from Idelchik (1994) were used. Regarding balancing valves, the relation between flow rate and pressure drop is usually provided by the manufacturer in terms of flow factor K_v (Eq. (4)):

$$K_v = V\sqrt{\frac{SG}{10^{-5}\Delta p}} \tag{4}$$

where

V is the fluid flow rate [m^3 h^{-1}],
SG is the fluid specific gravity [–].

The K_v values are given as function of the valve setting and refer to water and fluids with similar viscosity. Deviations from the nominal K_v value are expected for other types of fluid and at flow rates significantly smaller than the valve nominal flow rate (IMI Hydronic, 2015a). In these cases, corrections need to be applied. In this study, valves from IMI-Hydronic were used and their K_v values in different operating conditions were estimated though the software HySelect (IMI Hydronic, 2014).

2.1.2. Fluid properties

Usually propylene glycol/water mixtures are used as solar collector fluid in solar collector fields. For the relevant thermophysical properties of these mixtures, the following correlations were implemented in the model (Conde, 2011).

$$\rho = 508.4 - 0.1824x + 965.8T^* + 0.2803xT^* - 472.2 \cdot (T^*)^2 \tag{5}$$

$$c_p = 4476 + 608.6 - 715.0T^* - 1939xT^* + 478.7 \cdot (T^*)^2 \tag{6}$$

$$\ln \mu = -1.028 - 0.1003x - 19.94T^* + 0.1464xT^* + 14.6205 \cdot (T^*)^2 \tag{7}$$

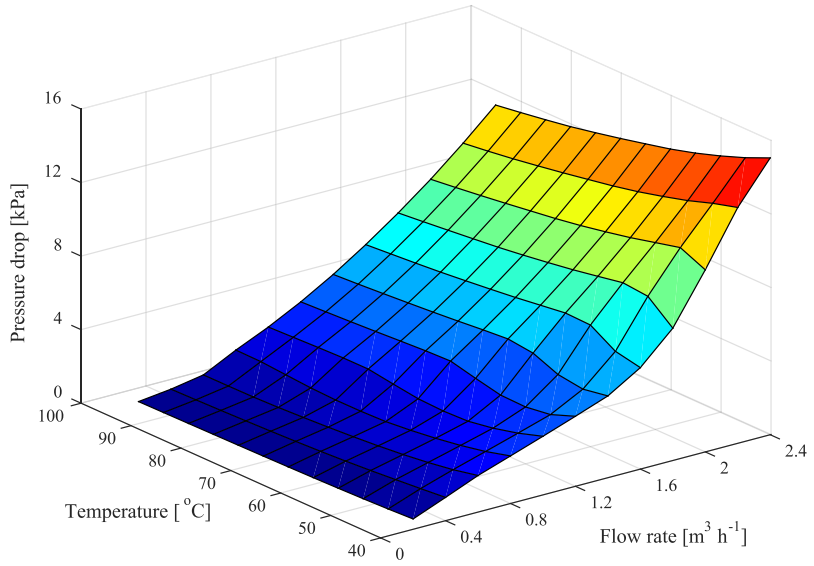

Fig. 2. Pressure drop of a HTHEATstore 35/08 collector as function of temperature and flow rate for 35% propylene glycol/water mixture.

where

c_p is the specific heat of the fluid [J kg^{-1} K^{-1}],
μ is dynamic viscosity of the fluid [Pa s],
x is the mass concentration of propylene glycol in the mixture [%],
T^* is a factor defined as $T^* = 273.15/(T + 273.15)$, where T is the fluid temperature [°C].

A large variability of the properties of propylene glycol/water mixtures was found when comparing different sources in literature (Conde, 2011; George and Sastry, 2003; Melinder, 2007; Sun and Teja, 2004; Tsierkezos and Palaiologou, 2009) or product datasheets (DOW, 2008; Skovrup, 2005). In fact, different commercial propylene glycols may contain different amounts and types of additives to prevent corrosion. Additionally, propylene glycol is known to suffer acidic degradation and hence change its composition over time, especially when exposed to high temperatures (Clifton et al., 1985; Rossiter et al., 1985). For these reasons, when performing the model validation, a sample of propylene glycol/water mixture was taken from the specific collector field and its density and viscosity were experimentally determined. For this purpose, an Anton Paar DMA 4100 densimeter and an Anton Paar AMV 200 viscometer were used. The mixture (glycol mass content of 35%) was tested at temperatures between 20 °C and 80 °C with an intermediate step of 10 °C. The experimental data points were then interpolated with the expressions (Eq. (8)) and (Eq. (9)). The specific heat was not determined, as it was not needed for the validation.

$$\rho = 1038.3 - 0.4419T - 1.940 \cdot 10^{-3}T^{-2} \tag{8}$$

$$\mu = \begin{cases} -1.449 \cdot 10^{-8}T^3 + 3.066 \cdot 10^{-6}T^2 - 2.337 \cdot 10^{-4}T + 7.289 \cdot 10^{-3} & \text{if } T < 38 \\ 0.1803T^{-1.232} & \text{if } T > 38 \end{cases} \tag{9}$$

2.1.3. Matlab implementation

Using the pressure drop correlations and the fluid properties described in the previous sections, a numerical model was developed in Matlab to compute the flow distribution in a solar collector field. To provide the necessary input data to the model, the layout of the collector field, pressure drop in the collectors, valves and settings, dimensions of distribution pipes and type of fittings must be known. Also the fluid type and operating conditions, such as field flow rate and fluid inlet temperature, need to be inserted. The temperature profile along the collector rows, used to evaluate the fluid properties, can be estimated in two ways. The first possibility is to define an outlet temperature, equal for all collector rows, and a linear temperature profile is assumed along the collector row. For the second possibility, the collector efficiency coefficients and weather conditions, such as solar irradiance on the collector plane and ambient temperature, must be provided instead. The temperature profile across each collector row is then calculated solving the differential equation (Eq. (10)), which assumes steady state conditions.

$$\dot{m}c_p \frac{dT}{dA} = G\eta_0 K_\theta - a_1 \cdot (T - T_{amb}) - a_2 \cdot (T - T_{amb})^2 \tag{10}$$

where

$\dot{m}$ is the mass flow rate [kg s^{-1}],
A is the gross/aperture collector area [m^2],
G is the hemispherical solar irradiance on the collector plane [W m^{-2}],
η_0 is the peak efficiency of the solar collector coherent with the definition of A [–],
K_θ is the incident angle modifier [–],
a_1 is the first order heat loss coefficient coherent with the definition of A [W m^{-2} K^{-1}],
a_2 is the second order heat loss coefficient coherent with the definition of A [W m^{-2} K^{-2}],
amb subscript denotes ambient temperature.

The solution of (Eq. (10)) represents the temperature profile along the collector row and is given by (Eq. (11)):

$$T(A) = \frac{d \cdot \tan\left[\frac{1}{2}(Kd + Ad)\right] - b}{2a} \tag{11}$$

where

a is parameter defined as $a = -a_2/\dot{m}c_p$,
b is parameter defined as $b = 2a_2T_{amb} - a_1/\dot{m}c_p$,
c is parameter defined as $c = G\eta_0K_\theta + a_1T_{amb} - a_2T_{amb}^2/\dot{m}c_p$,
d is parameter defined as $d = \sqrt{4ac - b^2}$,
K is the integration constant, defined based on the inlet temperature boundary condition T_{in} [°C] as $K = \frac{2}{d}\tan^{-1}\left(\frac{b+2aT_{in}}{d}\right)$

As can be seen from (Eq. (11)), the temperature profile along a collector row is function of its flow rate, so rows supplied lower flow rates reach higher temperatures.

Given an initial total flow rate as input, the model assumes that the flow is uniformly distributed across the collector field. To calculate the true flow distribution, the numerical model solves iteratively the set of equations (Eq. (12)), which impose both the conservation of mass across the collector field (first line in (Eq. (12))) and the uniformity of pressure drop along the different hydraulic paths (from second line downward):

$$\begin{pmatrix} 1 & 1 & 1 & 1 & 1 & 1 \\ k_{1,j}\cdot\dot{m}_{1,j} & -k_{2,j}\cdot\dot{m}_{2,j} & 0 & 0 & 0 & 0 \\ 0 & k_{2,j}\cdot\dot{m}_{2,j} & -k_{3,j}\cdot\dot{m}_{3,j} & 0 & 0 & 0 \\ \vdots & \vdots & \vdots & \vdots & \vdots & \vdots \\ 0 & 0 & 0 & 0 & k_{N-1,j}\cdot\dot{m}_{N-1,j} & -k_{N,j}\cdot\dot{m}_{N,j} \end{pmatrix} \begin{pmatrix} \dot{m}_{1,j+1} \\ \dot{m}_{2,j+1} \\ \dot{m}_{3,j+1} \\ \vdots \\ \dot{m}_{N,j+1} \end{pmatrix} = \begin{pmatrix} \dot{m}_{tot} \\ 0 \\ 0 \\ \vdots \\ 0 \end{pmatrix} \tag{12}$$

where

k is a hydraulic resistance coefficient [$kg^{-1}\ m^{-1}$],
1, 2, …, N subscripts denote the collector row and N is the total number collector rows,
tot subscript refers to the total flow rate supplied to the solar collector field,
j subscript denotes the iteration number.

The hydraulic resistance coefficient k_i is defined so that the product $(k_i\cdot\dot{m}_i^2)$ corresponds to the pressure drop (in Pascal) along the entire i-th hydraulic path. The value of k_i is representative of the pressure drop along the i-th collector row, which is proportional to the square of the row flow rate $\dot{m}_i$, as well as the pressure drop across the supply/return pipes segments and tees included in the i-th hydraulic path, properly normalized to the flow rate $\dot{m}_i$. In general, k_i is defined by a formulation of the type (Eq. (13)):

$$k_i = k_i' + \sum_{y=1}^{i}\left(k_y''\frac{\dot{m}_{y-1\to y}^2}{\dot{m}_i^2}\right) \tag{13}$$

where

k_i' [$kg^{-1}\ m^{-1}$] is the contribution to the coefficient k_i such that the product $(k_i'\cdot\dot{m}_i^2)$ gives the pressure drop in those components whose pressure drop is proportional to the square of the row flow rate, such as collectors, row inlet/outlet, and balancing valves.
k_y'' [$kg^{-1}\ m^{-1}$] is the contribution to the coefficient k_i such that the product $\left(k_y''\cdot\dot{m}_{y-1\to y}^2\right)$ gives the pressure drop in the components of the (y–1 → y)-th distribution line segment, such as supply/return pipe segments and tee junctions,
$y-1\to y$ subscript denotes the supply/return pipe segment between the ($y-1$)-th and y-th collector row.

The system of equations (Eq. (12)) is iteratively solved until the maximum difference in the collector row flow rates between two consecutive iterations is lower than 0.1%. Assuming a collector array with 24 hydraulic paths, such as that used in this study, a typical calculation is performed in approximately 0.1 s for a computer with quad-core CPU and 2.4 GHz CPU frequency.

The Matlab code of the model is publicly available online (Bava, 2016).

2.2. Description of the solar collector field

2.2.1. Collector field layout

The developed model was based on the layout of the solar collector field near Høje Taastrup (Denmark). The layout of the collector field is shown in Fig. 3. The collector field had a collector area of 3024 m^2 and consisted of two subfields, having 12 collector rows each. Each row was made up of 10 HTHEATStore 35/08 collectors (Section 2.1.1) and the row distance was 5.5 m. The collectors had a tilt angle of 43° and an orientation of 2.5°W. The supply pipes ran along the outer sides of the collector field (blue lines in Fig. 3). One return pipe collected the fluid in the middle of the field (red line in Fig. 3). Pumps, heat exchanger, expansion vessels and control system were located in the technical building in the north-east corner of the collector field. Because there was no auxiliary heating plant nearby, the outlet temperature from the collector field had always to reach approximately the DH supply temperature. The collector field was usually operated between an inlet temperature of 50–55 °C and an outlet temperature of 90–95 °C. The flow rate ranged between 8 and 50 $m^3\ h^{-1}$.

The distribution pipes were made of preinsulated steel pipes. The pipes between the technical building and the collector field, along which the entire field flow rate flows, had an inner diameter of 10.7 cm. The diameter progressively decreased as part of the flow rate was diverted to the collector rows. For each collector row the supply line had a diverging tee junction which directed part of the supplied fluid to the collector row through the row inlet. The row inlet consisted of two preinsulated steel pipes, connected to each other through a balancing valve. The balancing valves installed in the collector field were of type STAD20 in rows 1–11 and STAD25 in rows 12–24 (IMI Hydronic, 2015a). In the middle of the field, the flows coming from each couple of side-by-side rows merged through a merging tee junction and flowed into the return pipe through a converging tee junction. Before the merging tee junction, each row outlet was equipped with a three way ball valve. This valve, together with the balancing valve at the row inlet, could be used to isolate a specific row from the rest of the field, when maintenance was needed.

The heat transfer fluid in the collector field was a 35% propylene glycol/water mixture (Section 2.1.2).

2.2.2. Measuring equipment

To measure the flow rate in the different collector rows, a differential pressure sensor TA-SCOPE from IMI Hydronic was used (IMI Hydronic, 2015b). The balancing valves are equipped with two measuring points, one before and one after the valve member. From the measured pressure drop across the valve and the valve flow factor (Eq. (4)), the flow rate is calculated. The TA-SCOPE device is also equipped with a temperature sensor, so that, by specifying the type of fluid, it calculates its density and viscosity and corrects the flow factor accordingly. The nominal accuracy of the differential pressure sensor is given by the higher value between

Fig. 3. Layout of Høje Taastrup solar collector field. Blue and red lines represent supply and return pipes respectively (adapted from Arcon-Sunmark A/S). (For interpretation of the references to colour in this figure legend, the reader is referred to the web version of this article.)

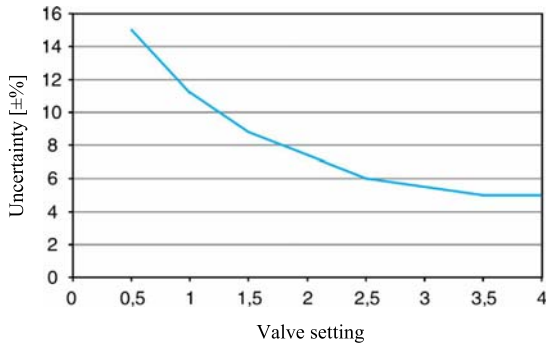

Fig. 4. Uncertainty on the measured flow rate across a STAD valve as function of the valve setting (IMI Hydronic, 2015a).

0.1 kPa and 1% of the measured value. However, when using the TA-SCOPE sensor to evaluate the flow rate across a STAD valve, the accuracy is worse. Fig. 4 shows the expected uncertainty as function of the valve setting. As the uncertainty increases sharply at low valve settings, it is generally advised to use a setting higher than two. This rule of thumb was respected in Høje Taastrup collector field, where the lowest valve setting was 2.2.

A first series of measurements on the field flow distribution showed that the difference in the row flow rates was lower than the uncertainty of the measurement method. A validation of the model in these conditions would not have been completely decisive, as the error band of the measured points would be larger than the differences in flow rate that the model is meant to predict. Consequently, a second series of measurements was carried out. This time the setting of the first 10 balancing valves in the eastern subfield were modified, so to induce a stronger flow maldistribution, which could be more easily detected.

As the total field flow rate was expected to be the most important parameter affecting the flow distribution, three different flow rates were tested: a high flow rate of approximately 50 $m^3 h^{-1}$, which is the highest flow rate supplied to the field in full load conditions; a low flow rate of 14 $m^3 h^{-1}$, which was regarded as the lowest flow rate still able to cause a pressure drop across the valves high enough to make the measurement meaningful; and an intermediate flow rate of 30 $m^3 h^{-1}$. As measuring the flow rate in all the rows took approximately 30–40 min, it was important that the operating conditions of the collector field were kept as constant as possible during this procedure. Hence, the measurements were performed during a cloudy day, to avoid significant temperature variations, and the pump was run at constant speed. The relevant operating conditions during the tests are listed in Table 1.

The volume flow rate to the collector field was measured by an electromagnetic flow meter with an accuracy of 0.5%. The fluid temperature was measured by RTD temperature sensors with accuracy of 0.25 °C. The temperature was monitored at the beginning of the supply pipe and at the end of the return pipe, as well as at the inlet and outlet of four collector rows. The pressure in the system was measured by piezoresistive pressure sensor with maximum accuracy of 0.5%. In the solar collector loop there were three of these sensors: one after the pump, one right before the heat exchanger and one after the heat exchanger. The first and the second sensor could hence be used to evaluate the pressure drop across the collector field.

The instantaneous values of the monitored data were recorded once per minute.

Table 1
Operating conditions while measuring the field flow distribution in Høje Taastrup solar collector field.

	Test 1	Test 2	Test 3
Duration [min]	29	32	38
Field flow rate [$m^3 h^{-1}$]	50.3 ± 0.3%	30.4 ± 0.3%	14.1 ± 0.6%
Inlet temperature [°C]	45.0 ± 1.2	46.7 ± 1.2	50.0 ± 0.5
Outlet temperature [°C]	45.1 ± 1.2	47.5 ± 1.3	50.5 ± 0.6

2.3. Investigated scenarios

Using the developed model, the field flow distribution was evaluated in different scenarios:

- Case 1. The operating conditions used for the simulation were similar to those actually used in Høje Taastrup collector field. The inlet temperature was 55 °C and the solar irradiance on the collector plane was varied with the total flow rate in such a way that the outlet temperature was approximately 95 °C (see (Eq. (11))). A 35% propylene glycol/water mixture was assumed as collector fluid (Eqs. (5)-(7)). The same settings of the balancing valves as used in Høje Taastrup in case of normal operation were assumed in the model.
- Case 2. The effect of a fluid temperature close to the freezing point was investigated. In case of very cold temperatures, the solar collector fluid is circulated in the collector loop to prevent freezing. Collector rows supplied with lower flow rates are more likely to freeze in case of extended cold periods. As the viscosity of propylene glycol/water mixtures is strongly dependent on the temperature, it is important to verify that also in these conditions all collector rows receive a sufficient flow. According to DOW (2008), the freezing point of a 35% propylene glycol/water mixture should is −16 °C. Consequently, a slightly higher fluid temperature of −13 °C was assumed in the model simulations.
- Case 3. The operating conditions were the same as in case 1, but no balancing valves were installed. A method for achieving good flow distribution without balancing valves consists in keeping constant the diameters of the supply and return pipes throughout their length. This approach was for example used in the first large collector fields built in Sweden (Section 1.2).
  This case was divided in two subcases. Subcase 3.1 used the same distribution pipes as in case 1, so the pipe diameter changed along the pipe length. In subcase 3.2 constant diameters in supply and return pipes were assumed, more specifically 8.25 cm for the supply pipe and 10.7 cm for the return pipe. Additionally, to avoid unbalance between the two subfields, the technical building was assumed to be located right above where row 1 and 13 face each other (see Fig. 3).
- Case 4. The number and the composition of the collector rows were the same as in the previous cases, but the rows were now all connected in parallel. The resulting layout is shown in Fig. 5. Three different subcases were investigated. In subcases 4.1 and 4.2 the diameter of the supply and return pipes was progressively decreased as more fluid was diverted. The diameters of the pipes were chosen from commercially available preinsulated pipes (Logstor, 2005) and in such a way that the highest fluid velocity was lower than 1.65 m/s. The difference between the two subcases was that in subcase 4.1 balancing valves were regulated to obtain a more uniform flow distribution at the flow rate of 50 $m^3\ h^{-1}$. In subcase 4.2 no valves were used. Finally, in subcase 4.3 the diameter of the distribution pipes was kept constant and equal to 10.7 cm, i.e. the largest pipe diameter used in subcases 4.1 and 4.2. The operating conditions were the same as in case 1.

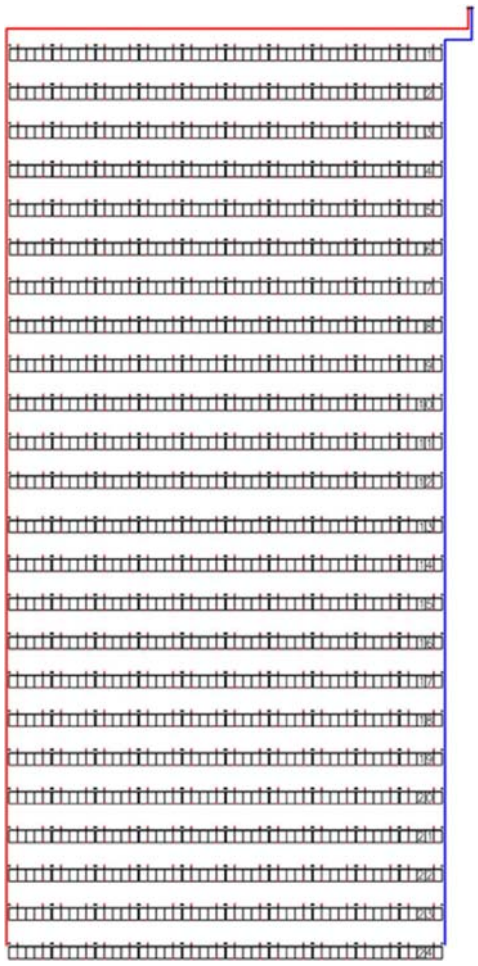

Fig. 5. Layout of the collector field in case 4 (adapted from Arcon-Sunmark A/S).

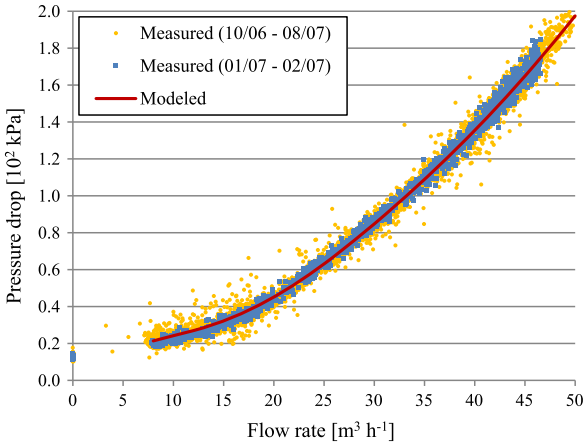

Fig. 6. Comparison between measured and modeled pressure drop across Høje Taastrup collector field as function of the field flow rate.

3. Results

3.1. Validation of the model

3.1.1. Pressure drop across the collector field

The comparison between the measured and calculated pressure drops as function of the flow rate is shown in Fig. 6. The measured data are from the period June 10th–July 8th 2015. To reduce the scatter of the data caused by transient periods with fast variation of the field flow rate, only the data points where the flow rate differed less than 10% from the previous recorded value are shown. In Fig. 6 the data points referring to the period 1st–2nd July are highlighted. These days presented clear sky conditions. Due to the control strategy (Section 1.3), the flow rate varied smoothly following the solar irradiance. The inlet and outlet temperature were fairly

constant throughout the day and equal to 56 °C and 95 °C respectively. These boundary conditions were used as input for the model to calculate the pressure drop across the collector field (continuous curve in Fig. 6).

At null flow the measured pressure difference was approximately 13 ± 1 kPa. This was because the two manometers (see Section 2.2.2) had an elevation difference of 1.36 m, which caused different hydrostatic pressures. Apart from this offset, the typical quadratic relation between pressure drop and flow rate was observed, as the measured points are approximately aligned along a parabolic trajectory.

The pressure drop curve calculated by the model fits the measured data accurately. The coefficient of determination R^2 between the measured data and the model is 0.97, if the entire data set is used, and 0.98, if only data from the period 1st–2nd July are used.

3.1.2. Flow distribution

The flow distribution was expressed in terms of dimensionless flow rate in the collector rows, defined as:

$$V'_i = \frac{V_i}{\left(\sum_{i=1}^{N} V_i\right)/N} \tag{14}$$

where

V'_i is the dimensionless flow rate in the i-th collector row [–],
V_i is the volume flow rate in the i-th collector row [$m^3\ h^{-1}$],
N is the number of collector rows [–].

Figs. 7–9 show the measured and modeled flow distribution in terms of dimensionless flow rate for field flow rates of 50, 30 and 14 $m^3\ h^{-1}$. The shown error bars are based on the information contained in Fig. 4.

The difference in flow distribution between the eastern subfield (rows 1–12) and the western subfield (rows 13–24) is easily recognized. In the eastern subfield the valve settings were changed so to introduce a stronger maldistribution than in normal operation. The settings of the first 10 valves were modified, so to cause a decreasing flow rate profile. In the western subfield the valve settings were not changed, so the flow distribution was much more uniform.

To evaluate the accuracy of the model, the root-mean-square deviation (*RMSD*) is introduced (Eq. (15)).

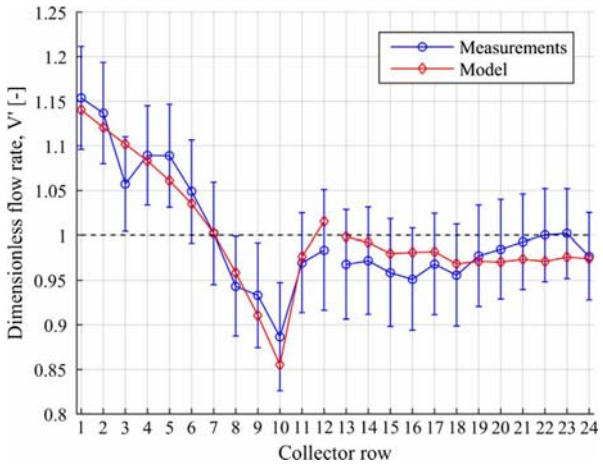

Fig. 7. Comparison between measured and modeled flow distribution for a field flow rate of 50 $m^3\ h^{-1}$.

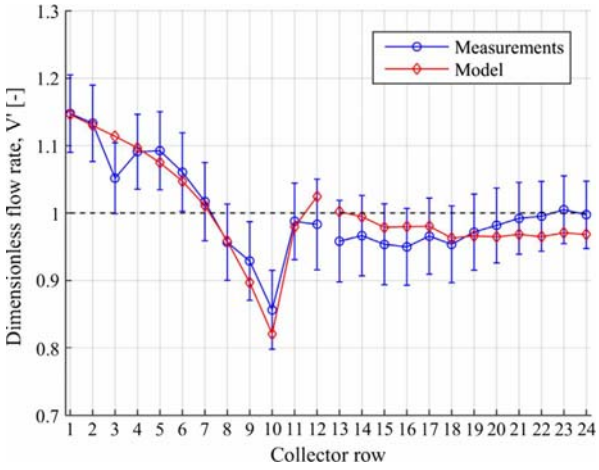

Fig. 8. Comparison between measured and modeled flow distribution for a field flow rate of 30 $m^3\ h^{-1}$.

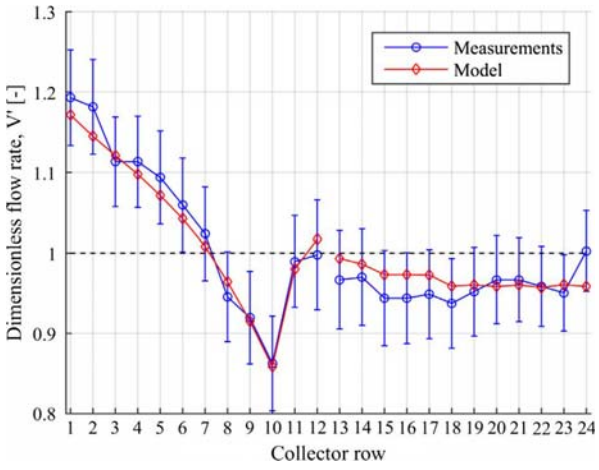

Fig. 9. Comparison between measured and modeled flow distribution for a field flow rate of 14 $m^3\ h^{-1}$.

$$RMSD = \sqrt{\frac{\sum_{i=1}^{N}(\hat{z}_i - z_i)^2}{N}} \tag{15}$$

where

z is the measured value of the investigated parameter,
$\hat{z}$ is the estimator of the investigated parameter.

To make the different RMSDs immediately comparable irrespective of the field flow rate, the RMSDs were evaluated using the dimensionless flow rate V' (Eq. (14)). Table 2 lists the RMSDs

Table 2
RMSD and maximum deviation between measured and modeled flow distributions in terms of dimensionless flow rates.

	Test 1	Test 2	Test 3
Field flow rate [$m^3\ h^{-1}$]	50.3	30.4	14.1
RMSD (V')	0.022	0.027	0.020
Max. deviation (row number)	4.2% (3)	5.9% (3)	4.4% (24)

and the maximum relative difference for the three flow distribution tests.

An overall good agreement between measurements and model was found, with the RMSD ranging between 0.020 and 0.027. The highest deviations were between 4.2% and 5.9% depending on the tested flow rate. It is also noted that at the lowest flow rate of 14 $m^3 h^{-1}$ the measured flow distribution is less uniform that in the other two cases. Especially the very first rows received higher fractions of the total flow rate, with dimensionless flow rates up to 1.20. Conversely, in the other two tests, this value did not exceed 1.15.

3.2. Investigated scenarios

3.2.1. Case 1: normal operating conditions

The calculated flow distribution in case 1 is shown in Fig. 10 for different field flow rates.

In the simulated scenarios the RMSD was used as main parameter to evaluate the degree of maldistribution. Unlike in the model validation, the term of comparison was now the uniform distribution profile ($z = 1$ in Eq. (15)).

It can be noted that the higher the flow rate, the more uniform the flow distribution. At flow rates equal to or higher than 30 $m^3 h^{-1}$ the RMSD was approximately constant and equal to 0.015. At lower flow rates this value increased up to 0.025 for a flow rate of 8 $m^3 h^{-1}$. The highest deviation from the ideal flow rate was lower than 6%, and the maximum difference between highest and lowest row flow rates was within 8%.

For the different flow rates, the pressure drop across the field was in agreement with Fig. 6.

3.2.2. Case 2: temperature close to freezing point

Fig. 11 shows the model results in case 2, which differs from case 1 only in the fluid temperature, now assumed constant and equal to −13 °C.

Despite the much higher viscosity of the glycol/water mixture at low temperature, the flow distribution was very uniform. The maximum deviation of row flow rate from the perfectly uniform case was 3.5%. Unlike case 1, higher flow rates did not necessarily entail a more uniform flow distribution. In fact, the value of RMSD varied from a minimum of 0.005 at 20 $m^3 h^{-1}$ to a maximum of 0.018 at 50 $m^3 h^{-1}$.

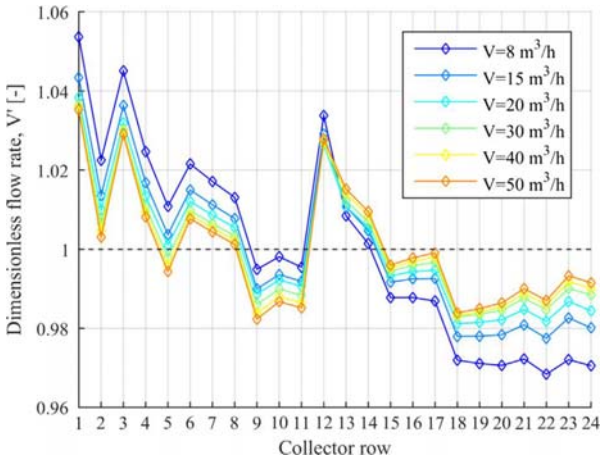

Fig. 10. Modeled flow distributions in Høje Taastrup solar collector field for different field flow rates, assuming normal operating conditions (case 1).

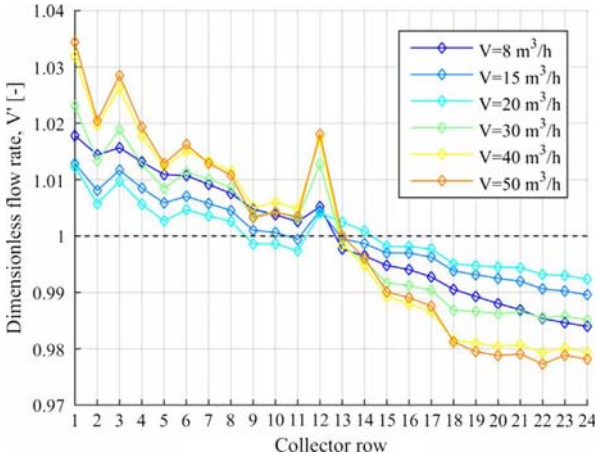

Fig. 11. Modeled flow distributions in Høje Taastrup solar collector field for different field flow rates in case of low temperature (case 2).

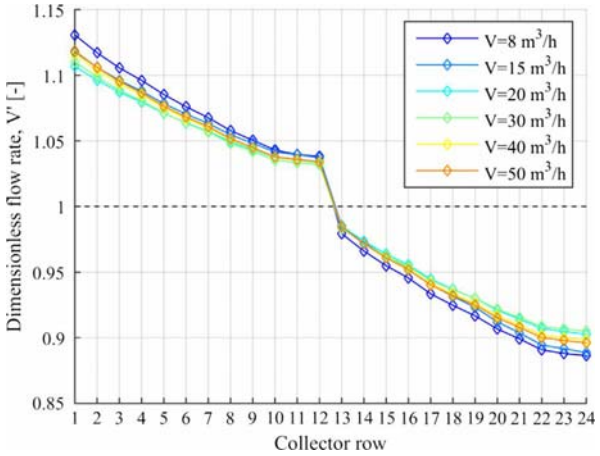

Fig. 12. Modeled flow distributions for different field flow rates in subcase 3.1.

3.2.3. Case 3: no balancing valves

In subcase 3.1 only the balancing valves were removed, while the layout and the dimensions of the distribution pipes were maintained as in case 1. The resulting flow distributions are presented in Fig. 12. Given the longer pipe length from the pump to the western subfield, this solution caused this subfield to be supplied with a much lower flow rate (12–14% lower compared to the eastern subfield depending on the field flow rate). Within the same subfield the relative difference between the lowest and the highest collector row flow rate was 6–8% depending on the field flow rate. The RMSDs in this case were much higher, ranging between 0.068 and 0.082.

In subcase 3.2 the diameters of the supply and return pipes were maintained constant and each of them equal to the largest installed diameter (8.25 cm for the supply pipe and 10.7 cm for the return pipe). Given the symmetry of the resulting field layout, the flow distribution was identical in both subfields. Hence, Fig. 13 shows the flow distribution only for the eastern subfield. Due to the constant pipe diameters, the relative difference between the lowest and the highest collector row flow rate was 5–6% depending on the field flow rate, so slightly better than in subcase 3.1.

Without balancing valves and due to the larger pipe diameters, the pressure drop across the collector field was approximately 20–25% smaller compared to case 1. However, as the connection

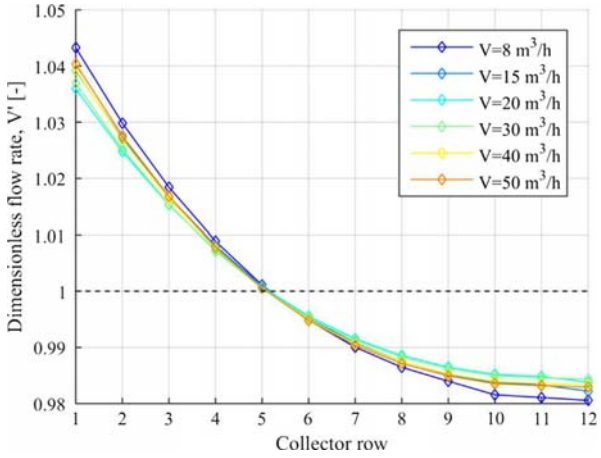

Fig. 13. Modeled flow distributions for different field flow rates in subcase 3.2.

to the DH network is located in the north-east corner of the field, the additional 2 × 65 m pipes to carry the fluid to this point would result in a reduction of 10% only.

3.2.4. Case 4: different field layout: 24 rows in parallel

Looking at Fig. 13 it may be thought that balancing valves are not strictly necessary to reach a good flow distribution. For this reason, a different collector field layout (Fig. 5) was investigated to verify whether this could be generalized. Fig. 14 presents the flow distributions in subcase 4.1 with balancing valves, subcase 4.2 without balancing valves and subcase 4.3 without balancing valves and constant distribution pipe diameter. For each subcase the two flow rates, which gave the most and least uniform distribution, are shown.

It can be noted that only subcase 4.1, which makes use of balancing valves, gave a uniform flow distribution. As expected the better distribution was found for the flow rate of 50 $m^3\,h^{-1}$ (RMSD = $3.5 \cdot 10^{-3}$), at which the balancing valves were regulated. In this case the flow rate in each row never differed more than 1% from the perfectly uniform distribution. This deviation increased at lower flow rates and at 8 $m^3\,h^{-1}$ it was within 2%, while the RMSD was 0.01.

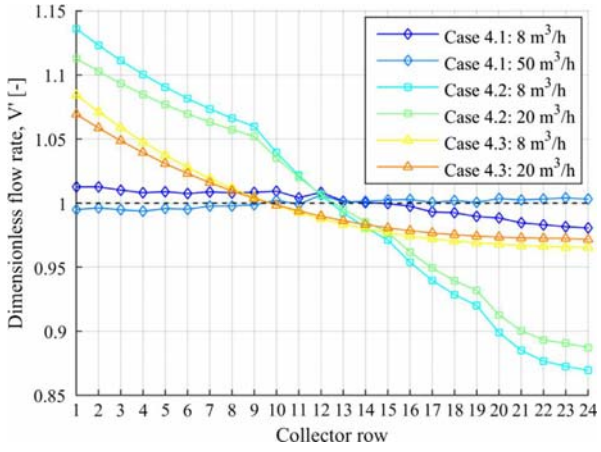

Fig. 14. Modeled flow distribution in the different subcases of case 4. Case 4.1 with balancing valves; Case 4.2 without balancing valves and decreasing diameter of the distribution pipes; Case 4.3 without balancing valves and constant diameter of the distribution pipes and equal to the larger pipe diameter of Case 4.2.

Removing the balancing valves while decreasing the distribution pipe diameter with the flow rate (subcase 4.2) gave the highest maldistribution, with deviations up to 13% compared to perfectly uniform distribution. Comparing the highest and the lowest row flow rate, the former was about 30% higher than the latter. The RMSD was 0.086 at 8 $m^3\,h^{-1}$ and 0.073 at 20 $m^3\,h^{-1}$. Maintaining constant diameter along the entire length of the distribution pipes (subcase 4.3) improved the flow distribution compared to subcase 4.2, and the highest row flow rate was 12% higher than the lowest row flow rate. The RMSDs decreased to 0.036 and 0.030 at 8 and 20 $m^3\,h^{-1}$, but were still considerably higher than in case 4.1.

4. Discussion

4.1. Validation of the model

From Figs. 7–9 and Table 2, an overall good agreement between modeled results and measurements can be noted, with the RMSD ranging between 0.020 and 0.027.

In the eastern subfield the measured and modeled flow distribution profiles presented the same trend, with the only exception represented by the third row. In fact, this collector row was characterized by the highest deviation between measured and modeled flow rate in both test 1 and 2 (Table 2). For this row the measured flow rate was significantly lower than the flow rate in the neighboring rows in all the three tests. This was most likely due to some additional flow resistance in this collector row, maybe due to some obstruction or dirt clog. In fact, also the original setting of its balancing valve was larger (and hence the valve more open) than the valve settings of neighboring rows and had the same value as the valve in the 11th collector row, significantly farther away. This means that, already when balancing the flow at the start-up phase of the collector field, it was noted that, in order for the third row to receive the design flow rate, its valve had to be opened more than expected. It is not reasonable to assume that this difference was caused by an inaccurate correlation for its tee junction used by the model. In fact, being the two subfields symmetric, a similar behavior should appear in the corresponding collector row (the 15th) in the western subfield.

At the lowest flow rate, row 24 had the highest deviation between measurement and model (Table 2). In this case the accuracy of the differential pressure sensor might play a significant role. Given the low flow rate and the completely open balancing valve, the pressure drop across the valve was very low (0.5 kPa). As the accuracy of the TA-SCOPE sensor is 0.1 kPa (Section 2.2.2), the measurement error can be higher than that shown in Fig. 4.

4.2. Investigated scenarios

Comparing the scenario in normal operating conditions (Fig. 10) with the validation results (Figs. 7–9), it can be seen that the correct setting of the balancing valves significantly improved the flow distribution.

The most uniform flow distribution occurred at the highest flow rate of 50 $m^3\,h^{-1}$. This was expected, as the balancing valves were set to give a uniform distribution at the nominal field flow rate, i.e. the highest flow rate the collector field operates at. This was about 55 $m^3\,h^{-1}$ in Høje Taastrup collector field.

As the relation between flow rate and pressure drop varies differently for the different components in the collector loop, a higher maldistribution is likely to occur when the field flow rate increasingly deviates from the nominal one. Despite this, the balancing valves resulted in a good flow distribution in all simulated conditions. The highest relative difference between row flow rate and

its ideal value was always well within 10%, which is considered the maximum acceptable deviation according to the German standard VDI (2004).

A good flow distribution was found also in case 2 (Fig. 11) with low fluid temperature. A variation in flow distribution could have been expected, due to strong temperature dependence of the kinematic viscosity of the glycol/water mixture. In fact, this increased approximately 20 times when the mixture temperature decreased from 75 °C to −13 °C. Despite the very strong variation, all components in the circuit experienced this low viscosity, so the flow distribution was not significantly affected.

The effect of removing the balancing valves was investigated in case 3.1 (Fig. 12). There was a significant flow unbalance between the two subfields, because the supply pipe to the western subfield was 122 m longer compared to the eastern subfield. If a collector field with the same layout as in Høje Taastrup was designed without balancing valves, the distribution pipes should be symmetrical to avoid unbalance between the two subfields (case 3.2). This scenario was inspired by the first collector fields built in Sweden, such as Falkenberg and Nykvarn II. These plants were built connecting in parallel collector rows of 10 collectors each. The collectors had a U-type harp design, very similar to a HTHEATstore 35/08. Both plants were relatively small (5500 m^2 in Falkenberg and 3500 m^2 in Nykvarn II) and could achieve a uniform flow distribution without balancing valves, due to the regular layout and constant pipe diameter. Similarly, case 3.2 presented an acceptable flow distribution, as shown in Fig. 13. This was possible due to the relatively small area of the collector field (3024 m^2) and the limited number of rows connected in parallel (12 in each subfield). In this configuration the pressure drop across the collector row played the most significant role, representing 85–88% of the entire pressure drop along the hydraulic path for the first row and 76–81% for the last one. The required head of the pump in case 3.2 was 10% lower than in case 1.

However, collector fields having more collector rows connected directly in parallel are less likely to achieve uniform flow distribution (case 4.2 and 4.3), unless balancing valves are installed (case 4.1). Maintaining a large and constant diameter for the entire length of the distribution pipes help reduce the maldistribution (case 4.3), but this solution entails higher cost and heat losses due to the increased pipe size.

Comparing the results of simulations with different layouts, it was found that in absence of balancing valves the rule of thumb (Eq. (16)) is generally valid, if the flow regime both in the distribution pipes and in the collectors is turbulent.

$$\frac{\max(V_i) - \min(V_i)}{\max(V_i)} \approx 0.5 \frac{\Delta p_{distr.pipe}}{\Delta p_{row}} \tag{16}$$

where

$\max(V_i)$ is the highest volume flow rate in a collector row [$m^3\ h^{-1}$],

$\min(V_i)$ is the lowest volume flow rate in a collector row [$m^3\ h^{-1}$],

$\Delta p_{distr.pipe}$ is the pressure drop along the longest distribution pipe supplying a collector row [Pa],

Δp_{row} is the pressure drop across a collector row supplied by the average flow rate [Pa],

For example, in order for the highest and the lowest row flow rate to differ less than 10%, the pressure drop along the longest supply and return pipes should be lower than 20% of the pressure drop across the average collector row. Fig. 15 represents (Eq. (16)) and shows the investigated scenarios 3.2, 4.2 and 4.3 along with other selected cases, to make the data set more complete.

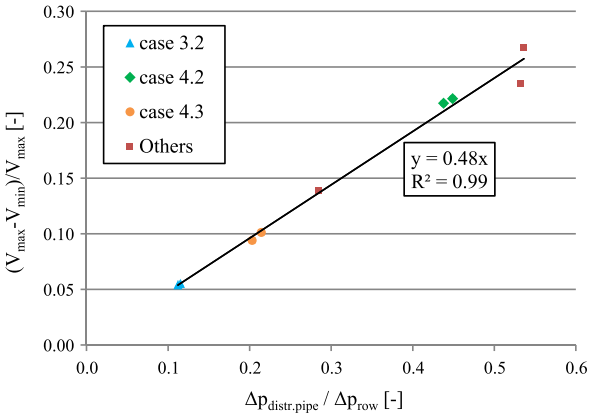

Fig. 15. Maximum deviation in row flow rate as function of the ratio between the pressure drop along the longest distribution line and the average pressure drop in a collector row.

4.3. Effect of the flow regime on the flow distribution

From Figs. 12 and 13 it can be noted that, in absence of balancing valves, higher flow rates did not necessarily entail a more uniform flow distribution. Fig. 13 shows that the lowest flow rate had the highest maldistribution. Increasing the flow rate up to 20 $m^3\ h^{-1}$ gave a more uniform flow distribution, while for even higher flow rates this became less uniform. To analyze this trend in more detail, Fig. 16 shows the RMSD as function of both flow rate and average *Re* in the absorber pipes of the collectors. The diagram was based on the same collector field layout and operating conditions as in case 3.2, with the only difference of the fluid temperature, assumed constant and equal to 55 °C. This allowed having the same *Re* in all the collectors of the same row and simplified the analysis.

At low flow rates ($V < 20\ m^3\ h^{-1}$), the flow regime in the collectors was still laminar while that in the distribution pipes was mainly turbulent with the exception of the very last pipe segments. In these conditions, a higher field flow rate increased the flow maldistribution. In fact, the increase in pressure drop in the

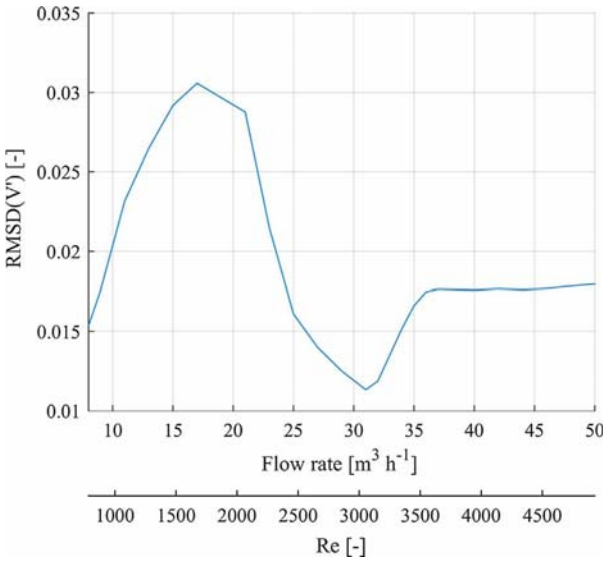

Fig. 16. Profile of the RMSD of the dimensionless flow rate V' as function of the field flow rate and average Reynolds number in the collector absorber pipes.

distribution pipes (approximately quadratic with the flow rate in turbulent regime) was sharper than that in the collector rows (approximately linear in laminar regime). At higher flow rates ($V = 20–30\ m^3\ h^{-1}$), the regime in the collector absorber pipes became progressively transitional. Given the assumption of linear interpolation made in the transition region (Section 2.1.1), the pressure drop was proportional to the cube of the fluid velocity, so the flow distribution improved rapidly and the RMSD decreased to its minimum. Finally, when the field flow rate was high enough to cause turbulent regime in all components ($V \geqslant 35\ m^3\ h^{-1}$), the flow distribution became slightly less uniform and almost independent of the flow rate.

5. Conclusions

A model for estimating the flow distribution in a solar collector field was developed. The model results were compared against measurements, both in terms of pressure drop and flow distribution across a collector field. Good agreement was found.

By using the model, different scenarios were investigated. Installing balancing valves in each collector row proved to be a reliable way to guarantee uniform flow distribution. Although the valves were set in nominal conditions, the deviations occurring at different conditions were still within the generally accepted range of ±10%.

Relatively small fields with few collector rows and regular layout can also achieve good flow distribution without balancing valves. Keeping a constant and large pipe diameter along the entire distribution line favors a uniform distribution and decreases the pressure drop across the collector field. The final solution should be selected based on economic considerations, taking into account the cost of the pipes and valves, increased heat losses and decreased pressure drop.

For very large collector fields with a high number of rows, balancing valves seems to be the most reliable solution to achieve good flow distribution.

Acknowledgements

The authors are thankful to the Marie-Curie Actions - Initial Training Network research programme of the European Union which supported the first author through the SolNet-SHINE project. The authors are also grateful to the company Arcon-Sunmark A/S and the DH company Høje Taastrup Fjernvarme for providing useful information necessary to develop the model and for granting access to the solar collector field in Høje Taastrup.

References

Bava, F., 2016. Field flow distribution model. <https://github.com/febav/FieldFlowDistribution> (accessed 13/07/2016).
Bava, F., Furbo, S., 2016. A numerical model for pressure drop and flow distribution in a solar collector with horizontal U-connected pipes. Sol. Energy 134, 264–272. http://dx.doi.org/10.1016/j.solener.2016.05.012.
Blasius, P.R.H., 1913. Das Aehnlichkeitsgesetz bei Reibungsvorgangen in Flüssigkeiten. Forschungsheft 131, 1–41.
Chiou, J.P., 1982. The effect of nonuniform fluid flow distribution on the thermal performance of solar collector. Sol. Energy 29, 487–502.
Clifton, J.R., Rossiter, W.J., Brown, P.W., 1985. Degraded aqueous glycol solutions: pH values and the effects of common ions on suppressing pH decrease. Sol. Energy Mater. 12, 77–86.
Colebrook, C.F., 1939. Turbulent flow in pipes, with particular reference to the transition region between smooth and rough pipe laws. J. Inst. Civ. Eng. 11, 133–156.
Conde, M., 2011. Thermophysical properties of brines – Models, Conde Engineering. Zurich (Switzerland) <http://www.mrc-eng.com> (accessed 13/07/2016).
Dorantes, R., García, G., Salazar, C., Oviedo, H., González, H., Alanis, R., Salazar, E., Martín-Dominguez, I.R., 2014. Thermal and hydraulic design of a solar collector field for a primary school pool. Energy Proc. 57, 2515–2524. http://dx.doi.org/10.1016/j.egypro.2014.10.262.
DOW, 2008. Engineering and Operating Guide for DOWFROST and DOWFROST HD Inhibited Propylene Glycol-based Heat Transfer Fluids <http://www.dow.com/heattrans/literature/> (accessed 13/07/2016).
EnergySupply, 2016. Danmarks største solenergianlæg på vej ved Silkeborg <http://www.energy-supply.dk/article/view/235192/> (accessed 13/07/2016).
Fan, J., Shah, L.J., Furbo, S., 2007. Flow distribution in a solar collector panel with horizontally inclined absorber strips. Sol. Energy 81, 1501–1511. http://dx.doi.org/10.1016/j.solener.2007.02.001.
Furbo, S., Perers, B., Bava, F., 2015. Thermal performance of solar district heating plants in Denmark. In: Conference Proceedings of EuroSun 2014. Aix-les-Bains (France). http://dx.doi.org/10.18086/eurosun.2014.19.11.
George, J., Sastry, N.V., 2003. Densities, dynamic viscosities, speeds of sound, and relative permittivities for water + alkanediols (propane-1,2- and -1,3-diol and butane-1,2-, -1,3-, -1,4-, and -2,3-diol) at different temperatures. J. Chem. Eng. Data 48, 1529–1539. http://dx.doi.org/10.1021/je0340755.
Haaland, S.E., 1983. Simple and explicit formulas for the friction factor in turbulent flow. J. Fluids Eng. 105, 89–90.
Heller, A., 2000. Large Scale Solar District Heating Evaluation, Modelling and Designing PhD Thesis. Technical University of Denmark (DTU), Department of Buildings and Energy (accessed 13/07/2016) <http://orbit.dtu.dk/files/5300211/R-046_PhD_Thesis.pdf>.
Holman, J.P., 2002. Heat Transfer. McGraw-Hill, New York, USA.
Idelchik, I.E., 1994. Handbook of Hydraulic Resistance. CRC Press, Boca Raton, USA).
IMI Hydronic, 2015a. STAD Balancing valves DN 15–50 <http://www.imi-hydronic.com> (accessed 13/07/2016).
IMI Hydronic, 2015b. TA-SCOPE <http://www.imi-hydronic.com> (accessed 13/07/2016).
IMI Hydronic, 2014. HySelect User Manual <http://www.imi-hydronic.com> (accessed 13/07/2016).
ISO, 2014. ISO Standard 9806: Solar Energy – Solar Thermal Collectors – Test Methods. International Organization for Standardization (ISO), Geneva, Switzerland.
Jones, G.F., Lior, N., 1994. Flow distribution in manifolded solar collectors with negligible buoyancy effects. Sol. Energy 52, 289–300. http://dx.doi.org/10.1016/0038-092X(94)90496-0.
Joseph, D.D., Yang, B.H., 2010. Friction factor correlations for laminar, transition and turbulent flow in smooth pipes. Phys. D 239, 1318–1328. http://dx.doi.org/10.1016/j.physd.2009.09.026.
Knabl, S., Fink, C., Ohnewein, P., Mauthner, F., Hausner, R., 2014. Requirements and guidelines for collector loop installation, Deliverables of IEA-SHC Task 45 Large scale solar heating and cooling systems. IEA-SHC http://task45.iea-shc.org/fact-sheets (accessed 13/07/2016).
Li, H., Svendsen, S., 2013. District heating network design and configuration optimization with genetic algorithm. J. Sustain. Dev. Energy Water Environ. Syst. 1, 291–303. http://dx.doi.org/10.13044/j.sdewes.2013.01.0022.
Logstor, 2005. Logstor Industry Catalogue <https://www.logstor.com/documentation> (accessed 13/07/2016).
Mauthner, F., Weiss, W., Spörk-Dür, M., 2016. Solar Heat Worldwide: Markets and Contribution to the Energy Supply 2014. IEA Solar Heating & Cooling Programme <http://www.iea-shc.org/data/sites/1/publications/Solar-Heat-Worldwide-2016.pdf> (accessed 13/07/2016).
Melinder, A., 2007. Thermophysical Properties of Aqueous Solutions Used as Secondary Working Fluids PhD Thesis. Royal Institute of Technology (KTH), Department of Energy Technology.
Rohde, J.E., Knoll, R.H., 1976. Analysis of a solar collector field water flow network. Cleveland (Ohio, USA) <http://ntrs.nasa.gov/archive/nasa/casi.ntrs.nasa.gov/19760024583.pdf> (accessed 13/07/2016).
Rossiter, W.J., Godette, M., Brown, P.W., Galuk, K.G., 1985. An investigation of the degradation of aqueous ethylene glycol and propylene glycol solutions using ion chromatography. Sol. Energy Mater. 11, 455–467.
Skovrup, M.J., 2005. SecCool API. IPU-Refrigeration and Energy Engineering <http://www.ipu.dk/Indhold/koele-og-energiteknik/Seccool.aspx> (accessed 13/07/2016).
SP, 2015. Solar Keymark Certificate HTHEATstore 35/08. Borås (Sweden) <http://www.solarkeymark.dk> (accessed 13/07/2016).
Sun, T., Teja, A.S., 2004. Density, viscosity and thermal conductivity of aqueous solutions of propylene glycol, dipropylene glycol, and tripropylene glycol between 290 K and 460 K. J. Chem. Eng. Data 49, 1311–1317. http://dx.doi.org/10.1021/je049960h.
Trier, D., 2016. Personal Communication with D. Trier (PlanEnergi).
Tsierkezos, N.G., Palaiologou, M.M., 2009. Ultrasonic studies of liquid mixtures of either water or dimethylsulfoxide with ethylene glycol, diethylene glycol, triethylene glycol, tetraethylene glycol, 1,2-propylene glycol and 1,4-butylene glycol at 298.15 K. Phys. Chem. Liq. 47, 447–459. http://dx.doi.org/10.1080/00319100802104855.
VDI, 2004. VDI-Richtlinie: VDI 6002 Blatt 1 Solare Trinkwassererwärmung - Allgemeine Grundlagen - Systemtechnik und Anwendung im Wohnungsbau.
Wang, X.A., Wu, L.G., 1990. Analysis and performance of flat-plate solar collector arrays. Sol. Energy 45, 71–78.
Weitbrecht, V., Lehmann, D., Richter, A., 2002. Flow distribution in solar collectors with laminar flow conditions. Sol. Energy 73, 433–441.
Windeleff, J., Nielsen, J.E., 2014. Solar District Heating in Denmark. Danish Energy Agency and PlanEnergi.

Paper V

A numerical model to evaluate the flow distribution in large solar collector fields in different operating conditions

Federico Bava, Janne Dragsted and Simon Furbo

Proceedings of EuroSun 2016 Conference

Conference Proceedings

EuroSun 2016
Palma de Mallorca (Spain), 11 - 14 October 2016

A numerical model to evaluate the flow distribution in large solar collector fields in different operating conditions

Federico Bava, Janne Dragsted and Simon Furbo

DTU Civil Engineering, Technical University of Denmark, Kgs. Lyngby (Denmark)

Abstract

A numerical model to evaluate the flow distribution in a large solar collector field was developed in Matlab and is presented in this study. Model and measurements from a solar collector field were compared and a good agreement was found. The model was then used to study the flow distribution in different array layouts. Balancing valves proved to be an effective way to achieve uniform flow distribution also in conditions different from those for which the valves were regulated, as well as in case of irregular layouts with different compositions of the collector rows. A Tichelmann connection gave a uniform flow distribution, especially if the distribution pipe diameter is reduced so to give a constant pressure drop gradient. The reduction in power output from the collector field was approximately proportional to the square of the root-mean-square deviation of the flow distribution, but was generally small, at least under the considered assumptions.

Keywords: *solar collector, solar collector field, flow balancing, flow distribution, parallel connection.*

1. Introduction

1.1. Background

An increasing number of large scale solar collector fields have been built in Europe in the last years. Of the total collector area installed at the end of 2014, 77% was located in Denmark (Mauthner et al., 2016). The development in this country has been driven by specific factors, such as high taxation on fossil fuels and widespread use of district heating (DH), to which large collector areas can be connected (Furbo et al., 2015). More than 800,000 m^2 of collector fields were installed in Denmark at the end of 2015 and this number is expected to grow in the next future (Mauthner et al., 2016). Also the size of the collector fields has been increasing. The current largest field in Vojens has a collector area of 70,000 m^2 (Mauthner et al., 2016), but by the end of 2016 a 150,000 m^2 collector field should be completed in Silkeborg (EnergySupply, 2016).

The larger the collector fields and the higher the number of collector rows, the larger the risk of non-uniform flow distribution. Non-uniform flow distribution cause non-uniform temperature distribution across the collector field, so decreasing the thermal performance. The negative effect of flow maldistribution on the thermal performance was investigated by Chiou (1982), who treated this effect in a single collector with parallel channels. He presents a method to determine how much the collector efficiency is penalized by the flow maldistribution. Defined a *flow nonuniformity parameter* as the root mean square deviation of the channels flow rates, he concludes that the deterioration of the collector efficiency is proportional to the 1.8^{th}-1.9^{th} power of such parameter. Wang and Wu (1990) presented a model to calculate the flow distribution in collector arrays with vertical pipes, both in U- and Z-configuration. The U-configuration presents a higher maldistribution than the Z-configuration. Fan et al. (2007) investigated through CFD calculations the flow and temperature distribution in a large collector for solar assisted DH plants. Model results and measurements are compared. The authors conclude that the flow distribution is driven by friction (and so buoyancy can be neglected), if the velocity in the collector pipes is high compared to the temperature rise across the collector. Bava and Furbo (2015) propose a numerical model to calculate the pressure drop and flow distribution in a U-type harp collector. Based on the conclusions of Fan et al. (2007), the authors argue

that in large collector fields for DH applications the relation between the fluid velocity in the absorber pipes and the temperature rise in the collector is such that buoyancy can be neglected. The model was compared against measurements carried out on a collector for solar assisted DH plants and good agreement was found.

Ideally, the layout of a collector array should be with short pipe lengths and uniform flow distribution. Though, it is not possible to optimize both these aspects simultaneously, so a compromise must be found. Rohde and Knoll (1976) analyzed different options to minimize the flow maldistribution in a collector field of 12 rows connected in parallel. The options included various size manifolds, manifold area changes, different locations of the inlets and exits to the manifolds, orifices and balancing valves. The last two are presented as the best solutions, both in terms of performance and cost. It is observed that a specific configuration of valve settings maintains the desired flow distribution only at a specific total flow rate. The topic of flow distribution in collector fields is also treated by Knabl et al. (2014). Maintaining a constant and large diameter in the distribution pipes or adopting a Tichelmann configuration (Fig. 6.b) improves the flow distribution. However, both options have higher costs due to the longer/larger pipes. Balancing valves are another possibility, but these increase the cost, installation time and maintenance (in case of defective valves). A cheaper solution is to install differently sized pipes in the collector rows, but the hydraulic design must be calculated in advance and very precisely, as a later adjustment would be very expensive.

In Danish solar collector fields, the pipe diameter of the distribution pipes is progressively reduced, as fluid is diverted to the collector rows. Balancing valves are then installed in each row to obtain a uniform flow distribution. These are regulated to achieve the desired flow distribution in full-load conditions (high flow rate, high solar radiation, nominal inlet/outlet temperatures), so that the outlet temperature from all rows is the same. This is done by supplying the different rows with flow rates proportional to the collector row area.

1.2. Sizing distribution pipes and balancing valves in solar collector fields: HySelect software

The design of the hydraulic network of a solar collector array can be a time-consuming and cumbersome procedure to be carried out manually. Hence, software able to carry out the same task can be extremely useful, making the job of planners and designers much easier. A program which can be used for this purpose is the commercial software *HySelect* from IMI Hydronic Engineering (IMI Hydronic, 2014). The software can be used to design and balance generic hydraulic networks, and so solar collector fields as well, in terms of pipe size, pump head, types and settings of balancing valves. The software returns the valve type and valve settings which should be applied to achieve a user-defined flow distribution. Additionally, it makes easy to optimize the pipe diameters (based on several pipe dimension standards) to fulfill fluid velocity or pressure gradient constraints. The software also contains built-in libraries of the thermophysical properties of a variety of fluids, including those most commonly used in solar heating systems, such as water and ethylene/propylene glycol-water mixtures. When designing a branched system, the program automatically adds and considers the pressure drop caused by the resulting tee junctions and bends. HySelect is intuitive to use and extremely fast in returning the results.

Despite these strengths, the software has some limitations. First of all, its reduced flexibility. As mentioned above, the program returns the valve setting configuration which guarantees a certain flow distribution. It does not calculate the flow distribution itself. Consequently, once a system has been balanced for specific boundary conditions (e.g. total flow rate and fluid temperature), it is not possible to analyze how the flow distribution varies, if the boundary conditions are changed. Secondly, the fluid temperature is assumed constant throughout the system. This approximation does not seem very accurate when designing solar collector fields for DH application, where the temperature rise across the collector field can be 40-50 K. Furthermore, the thermophysical properties (especially viscosity) of glycol-water mixtures are known to be strongly dependent on the temperature (see Section 2.1.2). Thirdly, complex layouts, having for example a common return pipe such as in Fig. 3, cannot be designed. Finally, the correlations used for evaluating the pressure drop in tee junctions are not in agreement with the literature (Idelchik, 1994). No reference to a literature source is provided and the used correlations are not stated in the software manual (IMI Hydronic, 2014). The difference between HySelect and Idelchik's correlations for pressure drops in tee junctions is shown in Fig. 1. The diagram was obtained assuming a distribution pipe from which 10 parallel circuits parted. The distribution pipe and the circuit pipes had diameter of 81 mm and 36 mm respectively. The system was supplied with a total flow rate of 20 $m^3 h^{-1}$, uniformly distributed in the 10 parallel circuits.

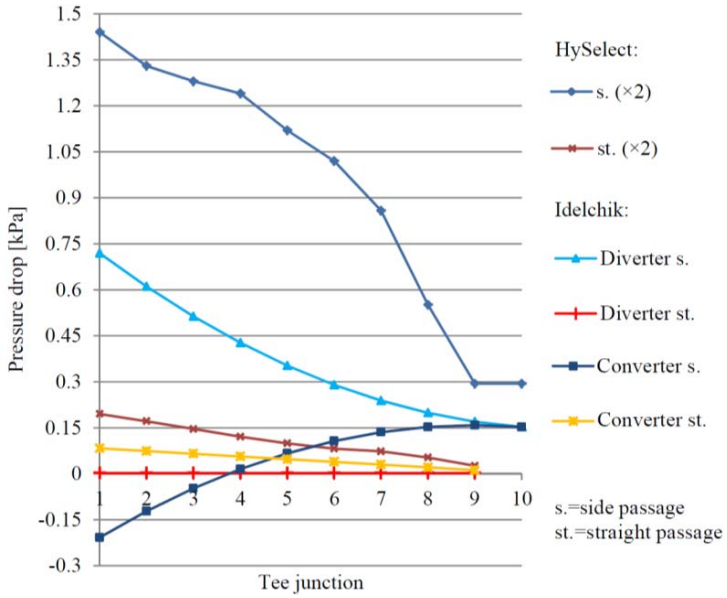

Fig. 1: Comparison between HySelect and Idelchik's correlations for pressure drop in tee junctions.

The fluid was water at 75 °C. Looking at Fig. 1, it is first of all noted that HySelect does not show the different contributions of the diverging and converging tee junctions, but only the overall pressure drop. Secondly, comparing the pressure drops in the diagram, it can be seen that for the straight passage the combined pressure drops from HySelect are approximately twice as large as the pressure drops that Idelchik's correlations give for the straight passage of the converging tee. On the other hand, the pressure drop in straight passage of the diverging tee junction predicted by Idelchik is negligible compared to that in the converging tee junction. Consequently, it could be neglected in the calculations without introducing a significant error. Regarding the side passages, the combined pressure drop from HySelect is between two and four times higher than Idelchik's pressure drop for the side passage of the diverging tee junction.

2. Material and method

2.1. Numerical model

2.1.1. Pressure drop correlations

To calculate how a fluid flow distributes in a branched system, it is necessary to know the relation between flow rate and pressure drop across each component. In fact, the fluid flow distributes in such a way that the pressure difference between two points is the same, regardless of the hydraulic path which connects one to the other. Because the relation between pressure drop and fluid velocity depends on factors such as Reynolds number, flow regime, etc., the flow distribution in a branched system may vary in different conditions.

In a collector field three main categories of hydraulic components can be identified: solar collectors, pipes and fittings (bends, tee junctions, valves, etc.).

The pressure drop characteristic of a solar collector is not always given in the technical datasheets and - even when provided - it usually refers to a specific fluid type and temperature. Different fluids and/or temperatures can affect the pressure drop. In this study the model proposed by Bava and Furbo (2016) was used to evaluate the pressure drop across each solar collectors, more specifically a HTHEATStore 35/08 from Arcon-Sunmark A/S (SP, 2016a). The HTHEATStore 35/08 is a flat plate harp collector with 18 U-connected absorber pipes. The pipes are 5.80 m long and have an inner diameter of 7.3 mm. The two manifolds are 2.24 m long and have an inner diameter of 32.9 mm. The collector gross area is 13.57 m^2 and its efficiency coefficients are η_0=0.757, a_1=2.2 W m^{-2} K^{-1} and a_2=0.007 W m^{-2} K^{-2} with respect to the collector gross area. Fig. 2 shows the modeled pressure drop for a 35% propylene glycol/water mixture, whose physical properties were evaluated through (Eq. 5) and (Eq. 7).

The friction loss along the distribution pipes was calculated by the Darcy-Weisbach equation (Eq. 1):

$$\Delta p = \lambda \frac{l}{D_h} \frac{\rho w^2}{2} \qquad \text{(Eq. 1)}$$

In (Eq. 1) Δp [Pa] denotes the pressure drop; λ [-] the Darcy friction factor; l [m] the pipe length; D_h [m] the pipe hydraulic diameter, which equals the inner diameter for a full flow circular pipe; ρ [kg m^{-3}] the fluid density and w [m s^{-1}] is the mean fluid velocity.

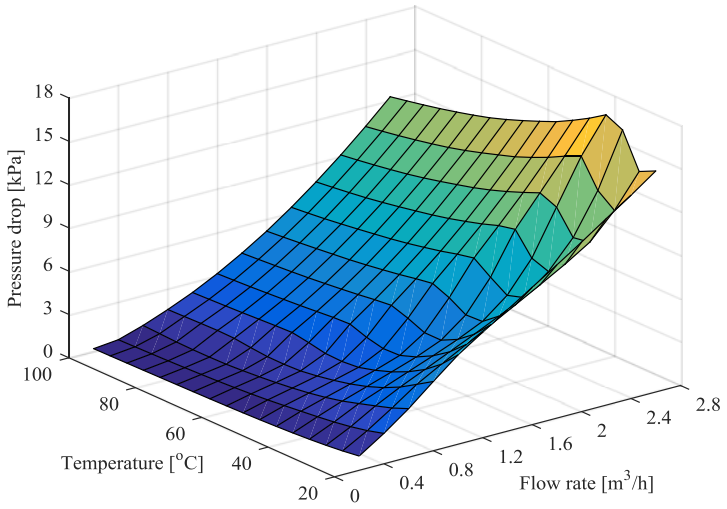

Fig. 2: Pressure drop in a HTHEATstore 35/08 collector as function of temperature and flow rate for 35% propylene glycol/water mixture.

Laminar regime was assumed for Reynolds numbers Re<2300, while turbulent regime was assumed for Re>4000 (Holman, 2002). According to the flow regime, the friction factor was calculated through the Hagen-Poiseuille law (Eq. 2) and the Haaland (1983) correlation (Eq. 3) respectively. The roughness of steel pipes was assumed to be ε=10^{-4} m. In the transition region (2300<Re<4000) the friction factor was evaluated by linearly interpolating the value obtained from (Eq. 2) at Re=2300 and that from (Eq. 3) at Re=4000.

$$\lambda = 64/Re \qquad \text{(Eq. 2)}$$

$$\lambda^{-1/2} = -1.8 \log_{10}\{[\varepsilon/(3.7\, D_h)^{1.11} + 6.9/Re]\} \qquad \text{(Eq. 3)}$$

Correlations from Idelchik (1994) were used to estimate the local losses in fittings, such as bends, tee junctions, changes of flow section area, etc. Regarding the balancing valves, the manufacturers usually provide the pressure drop characteristic as flow factor K_v (Eq. 4):

$$K_v = V \cdot [SG/(\Delta p \cdot 10^{-5})]^{1/2} \qquad \text{(Eq. 4)}$$

In (Eq. 4), V [m^3 h^{-1}] represents the volume flow rate and SG [-] the fluid specific gravity.

The flow factor is mainly function of the valve setting. However, deviations from the nominal K_v value can be expected with fluids different from water and flow rates significantly smaller than the valve nominal flow rate (IMI Hydronic, 2015). In these cases, the nominal K_v value should be corrected. In this study, valves from IMI-Hydronic were used and their corrected flow factors were evaluated through HySelect software.

2.1.2 Fluid properties

Propylene glycol/water mixtures with glycol concentration of 30-40% (Windeleff and Nielsen, 2014) are normally used as heat transfer fluid in solar assisted DH plants. In this study, the thermophysical properties of these mixtures were evaluated using the correlations proposed by Conde (2011).

$$\rho = 508.4 - 0.1824x + 965.8T^* + 0.2803xT^* - 472.2\cdot(T^*)^2 \qquad \text{(Eq. 5)}$$

$$c_p = 4476 + 608.6 - 715.0T^* - 1939xT^* + 478.7\cdot(T^*)^2 \qquad \text{(Eq. 6)}$$

$$\ln \mu = -1.028 - 0.1003x - 19.94T^* + 0.1464xT^* + 14.6205\cdot(T^*)^2 \qquad \text{(Eq. 7)}$$

When comparing the thermophysical properties of propylene glycol reported in literature (Conde, 2011; DOW, 2008; George and Sastry, 2003; Melinder, 2007), a large variability was found. So, for the model validation, a sample of propylene glycol/water mixture was taken from the collector field and its properties were determined with an Anton Paar DMA4100 densimeter and an Anton Paar AMV200 viscometer. The sample (35% glycol) was tested every 10 °C in the range 20-80 °C. The following correlations were found:

$$\rho = 1038.3 - 0.4419T - 1.940 \cdot 10^{-3} T^2 \qquad \text{(Eq. 8)}$$

$$\mu = \begin{cases} -1.449 \cdot 10^{-8} T^3 + 3.066 \cdot 10^{-6} T^2 - 2.337 \cdot 10^{-4}\, T + 7.289 \cdot 10^{-3} & if\ T < 38\ °C \\ 0.1803 T^{-1.232} & if\ T > 38\ °C \end{cases} \qquad \text{(Eq. 9)}$$

In (Eq. 5)-(Eq. 9), ρ [kg m^{-3}] denotes the density, c_p [J kg^{-1} K^{-1}] the specific heat, μ [Pa s] the dynamic viscosity, x [%] the mass concentration of propylene glycol in the mixture, while T^* is a factor defined as T^*=273.15/(T+273.15), where T [°C] is the fluid temperature.

2.1.3 Matlab implementation

Based on the above mentioned correlations, a numerical model was developed in Matlab, to calculate the flow distribution in a solar collector field. The layout of the collector field, the collector pressure drop, valves types and settings, dimensions of distribution pipes, fittings and the operating conditions (fluid type, field flow rate and fluid inlet temperature) need to be specified in the model. The temperature profile along the collector rows can be evaluated in two ways. The first is that a unique outlet temperature, equal for all collector rows, is defined in input and a linear temperature profile is assumed along the collector row. The second option requires the collector efficiency parameters, solar irradiance and ambient temperature. The temperature profile in each row is given by the solution of (Eq. 10), which assumes steady state conditions.

$$\dot{m}\, c_p \frac{dT}{dA} = G\, \eta_0\, K_\theta - a_1 \cdot (T - T_{amb}) - a_2 \cdot (T - T_{amb})^2 \qquad \text{(Eq. 10)}$$

In (Eq. 10), $\dot{m}$ [kg s^{-1}] is the mass flow rate, A [m^2] is the gross/aperture collector area, G [W m^{-2}] is the hemispherical solar irradiance on the collector plane, η_0 [-] is the peak efficiency of the solar collector coherent with the definition of A, K_θ [-] is the incident angle modifier, a_1 [W m^{-2} K^{-1}] and a_2 [W m^{-2} K^{-2}] are the first and second order heat loss coefficients coherent with the definition of A, T [°C] is the fluid temperature and while T_{amb} [°C] is the ambient temperature.

To determine the actual distribution, the set of equations (Eq. 11) is solved iteratively. (Eq. 11) imposes both the mass conservation across the collector field (first line in (Eq. 11)) and the uniformity of pressure drop along the different hydraulic paths (from second line downward):

$$\begin{pmatrix} 1 & 1 & 1 & 1 & 1 & 1 \\ k_{1,j} \cdot \dot{m}_{1,j} & -k_{2,j} \cdot \dot{m}_{2,j} & 0 & 0 & 0 & 0 \\ 0 & k_{2,j} \cdot \dot{m}_{2,j} & -k_{3,j} \cdot \dot{m}_{3,j} & 0 & 0 & 0 \\ \vdots & \vdots & \vdots & \vdots & \vdots & \vdots \\ 0 & 0 & 0 & 0 & k_{N-1,j} \cdot \dot{m}_{N-1,j} & -k_{N,j} \cdot \dot{m}_{N,j} \end{pmatrix} \begin{pmatrix} \dot{m}_{1,j+1} \\ \dot{m}_{2,j+1} \\ \dot{m}_{3,j+1} \\ \vdots \\ \dot{m}_{N,j+1} \end{pmatrix} = \begin{pmatrix} \dot{m}_{tot} \\ 0 \\ 0 \\ \vdots \\ 0 \end{pmatrix} \qquad \text{(Eq. 11)}$$

In (Eq. 11), k [kg^{-1} m^{-1}] is a hydraulic resistance coefficient; the subscripts 1, 2, ..., N denote the collector row and N is the total number collector rows; the subscript *tot* refers to the total flow rate supplied to the solar collector field and the subscript j denotes the iteration number. The factor k_i is defined so that the product $\left(k_i \cdot \dot{m}_i{}^2\right)$ represents the pressure drop along the entire i-th hydraulic path. The value of k_i takes into account both the pressure drop along the i-th collector row, proportional to the square of the row flow rate $\dot{m}_i$, and the pressure drop along the portion of distribution pipes and tees included in the i-th hydraulic path, properly normalized to the flow rate $\dot{m}_i$.

The system (Eq. 11) is iteratively solved until the maximum difference in the collector row flow rates between two consecutive iterations is lower than 0.1%.

2.2. Description of the solar collector field and experimental setup

The developed model was based on the layout of the solar collector field installed near Høje Taastrup (Denmark). The layout is shown in Fig. 3. The collector field (gross collector area of 3257 m^2) consisted of

two subfields of 12 collector rows each. The rows consisted of 10 HTHEATStore 35/08 collectors each and were 5.5 m apart from each other. Because near the collector field there was no auxiliary heating plant, the control strategy aimed at reaching an outlet temperature from the collector field which was approximately the DH supply temperature. Nominal inlet and outlet temperatures of the field were 50-55 °C and 90-95 °C respectively, and the flow rate ranged between 8 and 50 $m^3 h^{-1}$, depending on the solar irradiance.

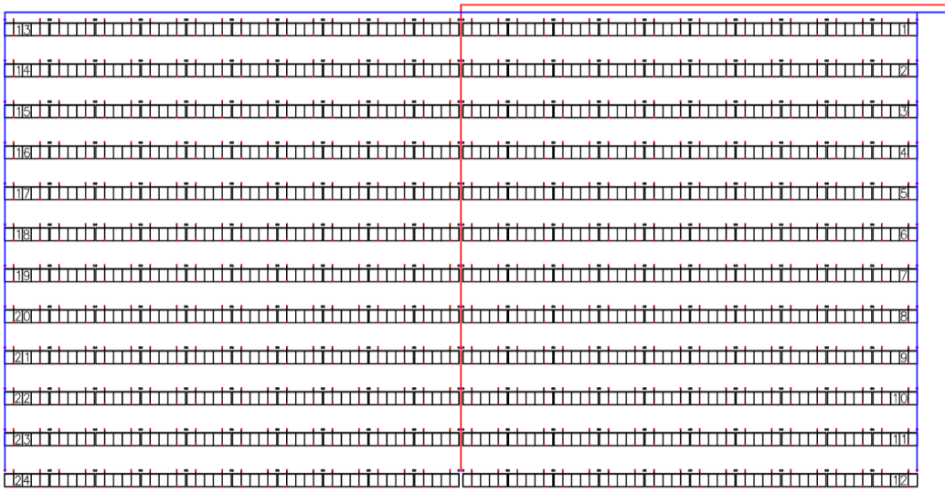

Fig. 3: Layout of Høje Taastrup solar collector field: blue and red lines represent supply and return pipes respectively (adapted from Arcon-Sunmark A/S).

The distribution pipes were made of preinsulated steel pipes. The largest inner diameter was 10.7 cm and it progressively became smaller as more fluid was diverted to the collector rows. At the inlet of each row a balancing valve was installed. In the middle of the field, the flows from each couple of row outlets were merged and then directed into the return pipe. The heat transfer fluid was a 35% propylene glycol/water mixture (Section 2.1.2).

To measure the flow distribution in the collector field, a differential pressure sensor TA-SCOPE from IMI Hydronic was used. The balancing valves have two measuring points, one before and one after the valve member. By measuring the pressure drop across the valve, the flow rate can be calculated through (Eq. 4). Specifying the type of fluid in the device, this calculates the fluid density and viscosity thanks to the built-in temperature sensor and corrects the valve flow factor. The maximum relative error when measuring the flow rate with this method is shown in Fig. 4. The error increases rapidly for low valve settings, so it is recommended to use settings higher than two. In Høje Taastrup collector field the lowest setting was 2.2.

The volume flow rate to the field was measured by an electromagnetic flow meter with accuracy of 0.5%.

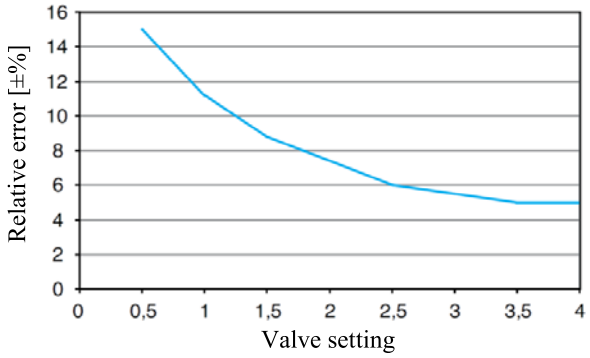

Fig. 4: Relative error on the measured flow rate across a STAD valve as function of the valve setting (IMI Hydronic, 2015).

At first, the flow distribution was measured keeping the same valve settings as in normal operation. However, the difference in the row flow rates was lower than the measurement error. Hence, the measurements were repeated after changing the setting of the first 10 valves in the eastern subfield, so to

introduce a higher maldistribution, which could be more easily detected. The flow distribution across the collector field was measured for a total flow rate of 50.3±0.3% $m^3\ h^{-1}$. The test was carried out in a cloudy day, so that the temperature across the field was constant (45.0±1.3 °C) during the entire duration of the test.

3. Results and discussion

3.1. Validation of the model

To compare the flow distributions at different field flow rate, the dimensionless row flow rate was introduced. The dimensionless flow rate V_i' in the *i*-th collector row is defined by (Eq. 12) as:

$$V'_i = \frac{V_i}{(\sum_{i=1}^{N} V_i)\cdot A_{row,i}/A_{field}} \qquad \text{(Eq. 12)}$$

In (Eq. 12), V [$m^3\ h^{-1}$] is the row flow rate, A [m^2] is the collector area, subscript i denotes the collector row number and N is the total number of collector rows. So, the dimensionless flow rate V'_i represents the ratio between the actual flow rate in the *i*-th collector row and the ideal flow rate in case of uniform distribution.

The measured and modeled flow distributions in terms of dimensionless flow rate are shown in Fig. 5. It is easy to recognize the effect that the change in first 10 valve settings had on flow distribution in the eastern subfield (rows 1-12) compared to the western subfield (rows 13-24). In the eastern subfield the row flow rates decreased progressively in the first 10 rows, only to return to their nominal value in the last two rows, whose valves were not changed. In the western subfield, where the valve settings were not modified, the row flow rates were much more similar to each other.

The agreement between model and measurements was evaluated through the root-mean-square deviation (*RMSD*) (Eq. 13).

$$RMSD = \sqrt{\frac{\sum_{i=1}^{N}(\hat{V}_i' - V_i')^2 \cdot b_i}{N}} \qquad \text{(Eq. 13)}$$

In (Eq. 13), V_i' [-] is the dimensionless form (Eq. 12) of measured flow rate in the *i*-th collector row in case of the model validation, while V_i'=1 in case of the investigated scenarios (Section 3.2); $\hat{V}_i'$ is the dimensionless form (Eq. 12) of modelled flow rate in the *i*-th collector row. The parameter b_i is a weight defined by (Eq. 14). If all rows are identical, *b*=1.

$$b_i = A_{row,i}/(A_{field}/N) \qquad \text{(Eq. 14)}$$

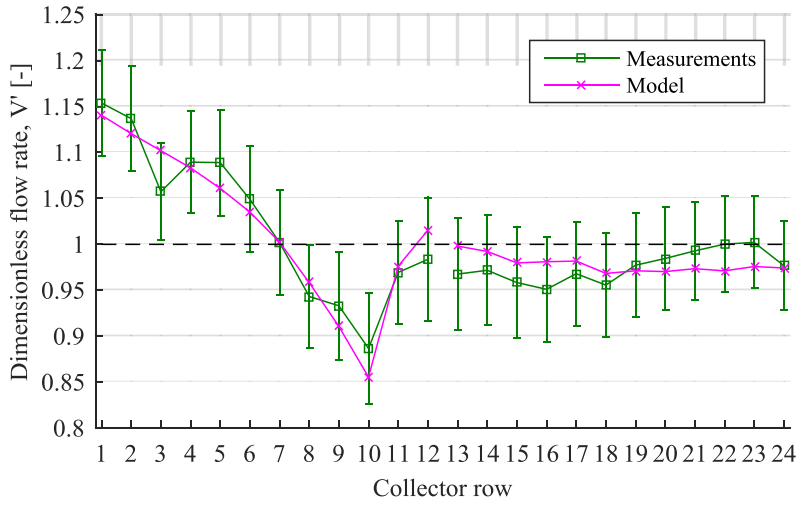

Fig. 5: Comparison between measured and modeled flow distribution for a field flow rate of 50.3 $m^3\ h^{-1}$.

Measurements and model showed an overall good agreement, with a RMSD of 0.022. In the eastern subfield the measured and modeled flow distribution profiles had the same trend, except for the third row, characterized by the highest deviation between measurement and model. In fact, the measured flow rate was

significantly lower compared to the neighboring rows. This deviation was most likely caused by additional flow resistance in this collector row, maybe due to some obstruction or dirt clog. Also the original setting of its balancing valve was larger (and hence the valve more open) than the valve settings of neighboring rows. So, already when balancing the flow at the start-up phase of the collector field, it was noted that, in order for the third row to receive the design flow rate, its valve had to be opened more than expected.

3.2. Investigated scenarios

Using the developed model, the flow distribution across a solar collector field was evaluated in different scenarios. A 35% propylene glycol/water mixture was assumed as collector fluid and its fluid properties were evaluated through (Eq. 5-Eq. 7). The following scenarios were investigated:

- Case 1. The operating conditions used for the simulation were similar to those actually used in Høje Taastrup collector field. The inlet temperature was 55 °C and the solar irradiance on the collector plane was varied with the flow rate so that the outlet temperature was about 95 °C (Eq. 10). The same balancing valves settings as those used in Høje Taastrup collector field in normal operation were used in the model.
- Case 2. As shown by the experience of the first solar collector fields built in Sweden in 80'-90', good flow distribution can be achieved without balancing valves in case of collector array with regular geometry and constant diameter of the distribution pipes. To see the effect that a more complex geometry would have on the flow distribution in case of no balancing valves, the layout of the collector field was modified as shown in Fig. 6.a. The 24 rows were now connected all in parallel and they had a different number of collectors. Because in this case the collectors were 204 instead of 240 (case 1), the highest field flow rate was proportionally decreased from 50 m^3 h^{-1} to 42.5 m^3 h^{-1}. Two different subcases were considered. In case 2.2 the diameter of the supply and return pipes decreased as fluid was diverted to the collector rows. In case 2.1 the pipe diameter of the distribution pipes was kept constant and equal to 10.7 cm, i.e. the largest diameter in subcases 2.2. Pipes commercially available for this kind of application (Logstor, 2005) were used. The field inlet and outlet temperature was 50 °C and about 85 °C respectively.

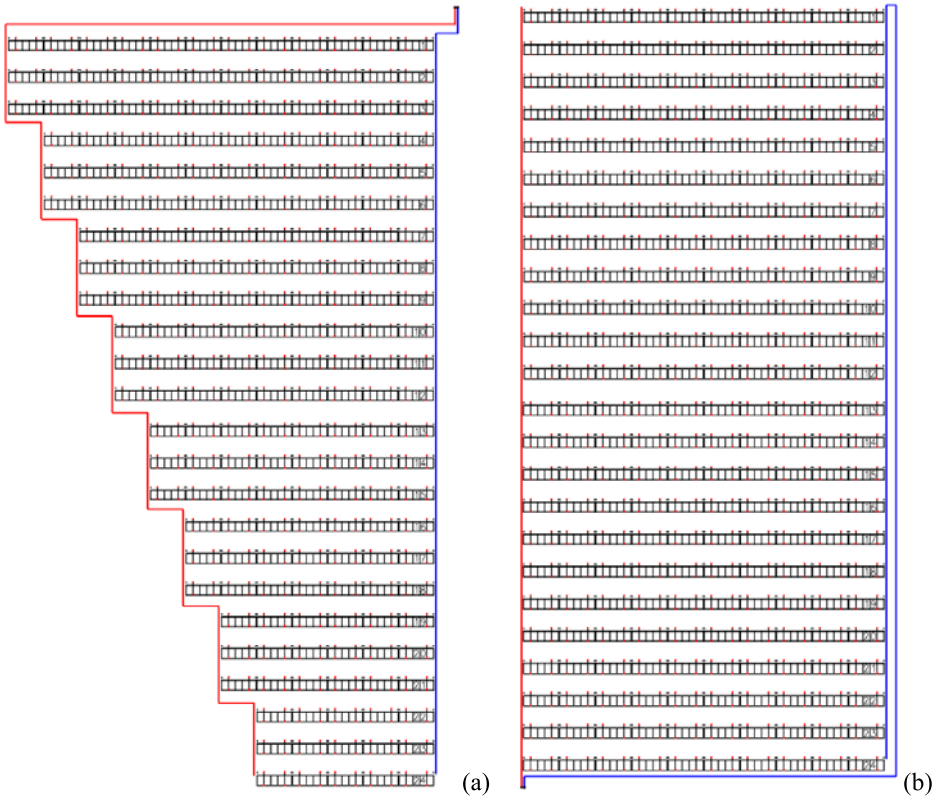

Fig. 6: Layout of the collector field assumed in case 2 (a) and in case 3 (b) (adapted from Arcon-Sunmark A/S).

- Case 3. This scenario used a Tichelmann connection (Fig. 6.b), which is expected to give a fairly uniform configuration due to the identical length for each hydraulic path. Hence, no valves were installed. As in case 2, two subcases were considered: case 3.1, having a constant pipe diameter of the distribution

pipe, and case 3.2, with decreasing pipe diameter according to the flow rate in each pipe segment. As in case 1, the inlet temperature was 55 °C and field outlet temperature was about 95 °C.

3.2.1. Case 1: normal operating conditions

The flow distribution in this case is shown in Fig. 7 for different field flow rates.

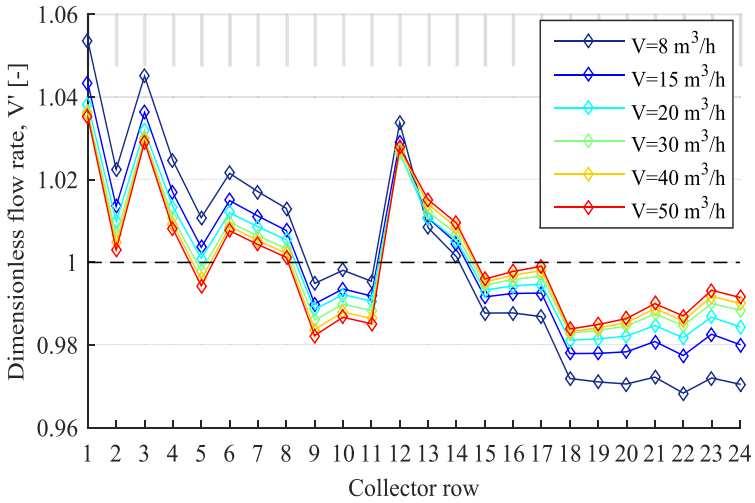

Fig. 7: Modeled flow distributions in Høje Taastrup solar collector field for different field flow rates, assuming normal operating conditions (case 1).

Also in the simulated scenarios the RMSD was used as the main parameter to quantify the level of maldistribution. Though, as no measurements were carried out for the simulated scenarios, the uniform distribution profile was now taken as term of comparison and hence z=1 in (Eq. 13) for any value of i.

Fig. 7 shows that the higher the flow rate, the more uniform the flow distribution. For V≥30 m^3 h^{-1}, the RMSD was approximately constant and equal to 0.015. At lower flow rates this value increased up to 0.025 for a flow rate of 8 m^3 h^{-1}. This was expected, as the balancing valves were set to give a uniform distribution at the nominal field flow rate, i.e. the highest flow rate the collector field operates at. The highest deviation between row flow rates and perfectly uniform flow distribution was lower than 6%, and the maximum difference between highest and lowest row flow rates was within 8%. Hence, the flow distribution can be considered acceptable for all the considered flow rates, as it differs from the ideal case less than 10%, which is considered the maximum acceptable deviation according to the German standard (VDI, 2004).

3.2.2. Case 2: Collector rows with different number of collectors

This scenario considered only cases where no balancing valves were installed, as these would give uniform flow distribution when properly regulated. The flow distribution in the two investigated subcases is shown in Fig. 8, with the subcase 2.1 characterized by much stronger maldistribution than subcase 2.2.

Given the field layout (Fig. 6.a), the collector rows became shorter while getting farther away from the pumping station. As the collector row represented the main contribution in terms of pressure drop along a hydraulic path, rows with fewer collectors had a much lower hydraulic resistance. So, in absence of balancing valves, these rows diverted flow rates higher than their design value. In case of constant pipe diameter in the distribution pipes (case 2.1) the flow maldistribution was higher with the RMSD ranging between 0.40-0.43 depending on the flow rate. The maximum deviation occurred in the last three rows, with flow rates about twice as high as the nominal value. The distribution was not very uniform, but still considerably better, in case 2.2, where the diameter was progressively decreased. In this case, the maximum deviation was only 40% and the RMSD was in the range 0.18-0.20. In fact, in case of constant diameter the fluid velocity progressively decreased in the pipe segments, making their contribution to the pressure drop of the entire hydraulic path very small. In order for all hydraulic paths to give the same pressure drop, the flow rate in the rows with fewer collectors had to increase significantly. Conversely, decreasing the pipe diameter gave similar pressure gradient in the different pipe segments. This increased the resistance of the hydraulic

paths of the collector rows which lay farther away, resulting in a more uniform flow distribution.

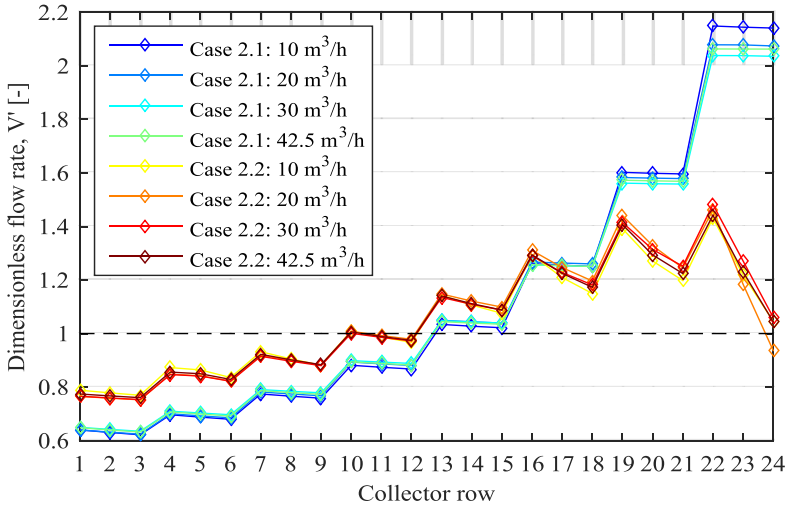

Fig. 8: Modeled flow distributions for different field flow rates in case 2.

3.2.3. Case 3: Tichelmann connection

Fig. 9 shows the flow distribution in the subcases 3.1 and 3.2. For sake of clarity, for each subcase only two flow rates, which gave the most and least uniform distribution, are shown. In both scenarios the Tichelmann connection assured a good flow distribution with deviations from the perfectly uniform case no larger than 4%. Subcase 3.2 achieved a slightly better distribution (RMSD=0.008-0.010) compared to subcase 3.1 (RMSD=0.014-0.016). In the latter, the choice of keeping a constant pipe diameter resulted into a U-shape flow distribution profile. In fact, although the pipe length was the same for each hydraulic path, the paths in more central position (rows 9-13) were supplied with lower flow rates. This was due to the fact that these paths included distribution pipes segments with higher flow rates (and hence higher pressure drop) compared to the more peripheral paths. In subcase 3.2 the distribution pipe diameter was progressively varied, so that the fluid velocity was similar in all pipe segments. This resulted in similar pressure drops and hence a more uniform flow distribution. Varying the pipe diameter also saved pipe material (steel and insulation), reducing cost and thermal losses. The main drawback of a Tichelmann connection is the longer pipe length.

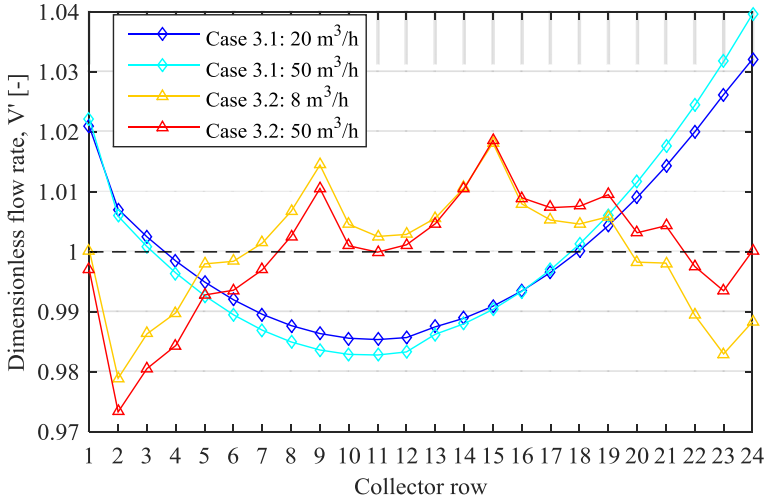

Fig. 9: Modeled flow distributions for different field flow rates in case 3.

3.3. Effect of the flow maldistribution on the thermal performance of the collector field

Modifying the row composition of the collector field shown in Fig. 6.a, different degrees of flow maldistribution were caused. The effect on the power output of the collector field is shown in Fig. 10 for two collector types, a HTHEATStore 35/08 (SP, 2016a) (Section 2.1.1) and a HTHEATBoost 35/08 (SP, 2016b)

(η_0=0.786, a_1=2.97 W m^{-2} K^{-1} and a_2=0.009 W m^{-2} K^{-2}). The collectors differed only for the presence of a polymer foil, working as convection barrier, between glass cover and absorber in the HTHEATBoost model. The loss in power output was calculated with respect to the case where the collector row flow rates were exactly proportional to the collector row area. The power output, P_{out} [W], was calculated through (Eq. 15):

$$P_{out} = \sum_{i=1}^{N} \left(\dot{m}_i \cdot c_{p,i}(\bar{T}_i) \cdot \left(T_{out,i} - T_{in} \right) \right) \qquad \text{(Eq. 15)}$$

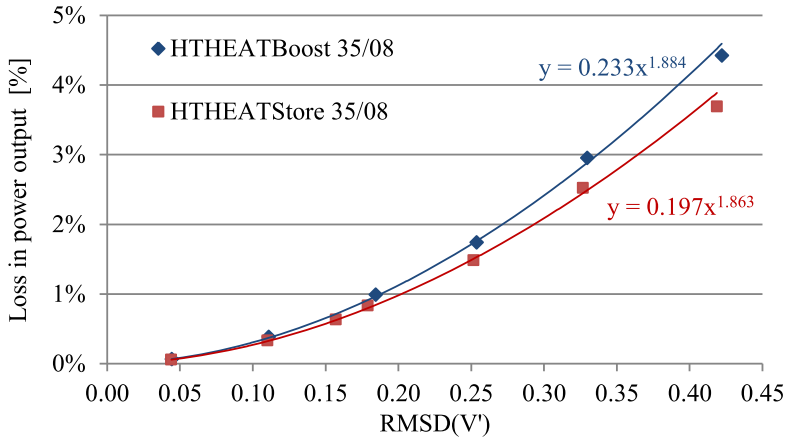

Fig. 10: Maximum reduction in power output of a solar collector field as function of the flow maldistribution.

It can be seen that the reduction in power output is proportional to the RMSD of the flow distribution to the 1.9th power, very similar to the result of Chiou (1982) for a single collector (Section 1.1). The loss in power output is relatively small, within 5% for RMSDs up to 0.4. However, it should be noted that in the current study pipe losses were neglected and the collector efficiency was assumed independent of the collector flow rate. In reality, lower efficiency is expected at low flow rates, especially if these cause laminar regime in the absorber pipes (Bava and Furbo, 2014). Slightly stronger effect on the power output would result, if these aspects were taken into account too. As expected, the performance of the collector field made of HTHEATBoost modules was more affected by the flow maldistribution. In fact, given the higher heat loss coefficients of this collector, its efficiency was more penalized in those rows which were supplied with lower flow rates and hence reached unnecessarily higher temperatures.

4. Conclusions

A model for calculating the flow distribution in a solar collector field was developed. The model results were compared against measurements and a good agreement was found.

The model was used to study different scenarios. Balancing valves in each collector row guaranteed good flow distribution in all the operating conditions. Although the valves were set in full load conditions, the deviations occurring at different operating conditions were still within the range of ±10%.

A Tichelmann connection gave a good flow distribution also without balancing valves. Reducing the pipe diameter of the distribution pipes was a good measure to improve the distribution and decrease the pipe cost.

In case of irregular field layout with collector rows having a different number of modules, balancing valves seemed to be the only way to reach uniform flow distribution.

5. Acknowledgements

The authors are thankful to the Marie-Curie Actions - Initial Training Network research programme of the European Union which supported the first author through the SolNet-SHINE project. The authors are also grateful to the company Arcon-Sunmark A/S and the DH company Høje Taastrup Fjernvarme for providing useful information necessary to develop the model and for granting access to the solar collector field.

6. References

Bava, F., Furbo, S., 2016. A numerical model for pressure drop and flow distribution in a solar collector with horizontal U-connected pipes. Solar Energy 134, 264–272.

Chiou, J.P., 1982. The effect of nonuniform fluid flow distribution on the thermal performance of solar collector. Solar Energy 29, 487–502.

Conde, M., 2011. Thermophysical properties of brines – Models, Conde Engineering, Zurich.

DOW, 2008. Engineering and Operating Guide for DOWFROST and DOWFROST HD Inhibited Propylene Glycol-based Heat Transfer Fluids.

EnergySupply, 2016. Danmarks største solenergianlæg. http://www.energy-supply.dk/article/view/235192/.

Fan, J., Shah, L.J., Furbo, S., 2007. Flow distribution in a solar collector panel with horizontally inclined absorber strips. Sol. Energy 81, 1501–1511.

Furbo, S., Perers, B., Bava, F., 2015. Thermal performance of solar district heating plants in Denmark, in: Conference Proceedings of EuroSun 2014. Aix-les-Bains (France).

George, J., Sastry, N. V., 2003. Densities, Dynamic Viscosities, Speeds of Sound, and Relative Permittivities for Water + Alkanediols (Propane-1,2- and -1,3-diol and Butane-1,2-, -1,3-, -1,4-, and -2,3-Diol) at different Temperatures. Journal of Chemical and Engineering Data 48, 1529–1539.

Haaland, S.E., 1983. Simple and Explicit Formulas for the Friction Factor in Turbulent Flow. Journal of Fluids Engineering (ASME) 105, 89–90.

Holman, J.P., 2002. Heat transfer, 9th ed. McGraw-Hill, New York.

Idelchik, I.E., 1994. Handbook of hydraulic resistance, 3rd ed. CRC press, Boca Raton.

IMI Hydronic, 2015. STAD Balancing valves DN 15-50. IMI Hydronic Engineering. Online at http://www.imi-hydronic.com/en/products-solutions/balancing-and-control/balancing-valves/.

IMI Hydronic, 2014. HySelect User Manual. IMI Hydronic Engineering. Online at http://www.imi-hydronic.com/en/knowledge-tools/hydronic-tools-software/balance-control/ta-select-4/.

Knabl, S., Fink, C., Ohnewein, P., Mauthner, F., Hausner, R., 2014. Requirements and guidelines for collector loop installation, Deliverables of IEA-SHC Task 45 Large scale solar heating and cooling systems. Online at http://task45.iea-shc.org/fact-sheets.

Mauthner, F., Weiss, W., Spörk-Dür, M., 2016. Solar Heat Worldwide. Markets and Contributions to the Energy Supply 2014. Online at http://www.iea-shc.org/solar-heat-worldwide.

Melinder, Å., 2007. Thermophysical Properties of Aqueous Solutions Used as Secondary Working Fluids. Royal Institute of Technology, KTH.

Rohde, J.E., Knoll, R.H., 1976. Analysis of a solar collector field water flow network. Lewis Research Center, Cleveland (Ohio, USA).

SP - Technical Research Institute of Sweden, 2016a. Solar Keymark Certificate No. SP SC0842-14: HTHEATstore 35/08 . Borås (Sweden). Online at http://www.solarkeymark.dk/.

SP - Technical Research Institute of Sweden, 2016b. Solar Keymark Certificate No. SP SC0840-14: HTHEATboost 35/08 . Borås (Sweden). Online at http://www.solarkeymark.dk/.

VDI, 2004. VDI-Richtlinie: VDI 6002 Blatt 1 Solare Trinkwassererwärmung - Allgemeine Grundlagen - Systemtechnik und Anwendung im Wohnungsbau.

Wang, X.A., Wu, L.G., 1990. Analysis and performance of flat-plate solar collector arrays. Solar Energy 45, 71–78.

Windeleff, J., Nielsen, J.E., 2014. Solar District Heating in Denmark.

Paper VI

Development and validation of a detailed TRNSYS-Matlab model for large solar collector fields for district heating applications

Federico Bava and Simon Furbo

Energy 135C (2017) 698–708

Energy 135 (2017) 698–708

Contents lists available at ScienceDirect

Energy

journal homepage: www.elsevier.com/locate/energy

Development and validation of a detailed TRNSYS-Matlab model for large solar collector fields for district heating applications

Federico Bava*, Simon Furbo

DTU Civil Engineering, Technical University of Denmark, Brovej, Building 118, 2800, Kgs. Lyngby, Denmark

ARTICLE INFO

Article history:
Received 13 February 2017
Received in revised form
19 June 2017
Accepted 25 June 2017
Available online 26 June 2017

Keywords:
Solar collector field
TRNSYS
Simulation
Flow regime
Flow distribution

ABSTRACT

This study describes the development of a detailed TRNSYS-Matlab model to simulate the behavior of a large solar collector field for district heating application. The model includes and investigates aspects which are not always considered by simpler models, such as flow distribution in the different rows, effect of the flow regime on the collector efficiency, thermal capacity of the components and effect of shadows from row to row. The model was compared with measurements from a solar collector field and the impact of each aspect was evaluated. A good agreement between model and measurements was found. The results showed that a better agreement was achieved, when a flow regime-dependent efficiency of the collector was used. Also the precise flow distribution in the collector field improved the model accuracy, but it must be assessed if the aimed level of accuracy justifies the much longer programming and computing time. Thermal capacity was worth being considered only for the bulkier components, such as the longer distribution and transmission pipes. The actual control strategy, which regulates the flow rates in the solar heating plant, was accurately reproduced in the model, as proved by the good agreement with the measurements.

1. Introduction

1.1. Background

To reach the CO_2-reduction goals agreed at the COP21 conference in Paris, reduce energy imports and cut costs for households and businesses, the European Union will act on several fronts. Among these, a key role should be played by the spread of district heating (DH) and the integration of renewable energy sources into DH networks [13].

Approximately 80% of the energy demand of European residential buildings is used for space heating and domestic hot water preparation [20]. Because solar thermal collector can efficiently and economically provide energy at the temperature levels required by these applications, they seem a perfect candidate to cover this demand. Although solar heating systems are fairly common in the single-family house sector, large solar thermal plants for DH are still rare, except for a few countries, and represented less than 1% of the total installed water collector capacity at the end of 2016 [42].

Approximately 5000 DH networks are currently in operation in Europe, supplying 10% of the total heat demand [2]. Of these, about 300 are solar assisted DH systems at the end of 2016 [42]. However, the contribution of solar energy to DH in Europe is expected to increase. According to the SDHtake-off project, supported EC-Programme IEE Intelligent Energy Europe, a solar fraction of 1% by 2020 and of 5% by 2050 is realistic [32,34].

Although several large solar plants for DH have been installed in Germany, Austria and Sweden [32], Denmark is still the main market for this technology, with 79% of the total collector area installed in Europe at the end of 2016 [42]. In the Scandinavian country some specific factors, such as high taxation on fossil fuels and widespread use of DH, has lead this development [14]. At the end of 2016, Denmark had more than 1,300,000 m^2 of solar collector fields [39]. Additionally, the size of the collector fields has been constantly increasing and at the end of 2016 a 156,000 m^2 collector field was completed in Silkeborg [28]. An even larger installation may come about in the next years, if the project for a 450,000 m^2 collector field is realized in Graz, Austria [30].

In a scenario where solar collector fields become increasingly larger and supply increasingly higher solar fractions, even small performance improvements in relative terms can lead to a large increase in the overall energy production in absolute terms. Hence,

* Corresponding author.
E-mail address: febav@byg.dtu.dk (F. Bava).

http://dx.doi.org/10.1016/j.energy.2017.06.146
0360-5442/

Nomenclature

A_{field}	collector area of the collector field, [m^2]
a_1	heat loss coefficient of collector at T_m-T_{amb} = 0 K, [W m^{-2} K^{-1}]
a_2	temperature dependence of the heat loss coefficient of collector, [W m^{-2} K^{-2}]
c_p	specific heat, [J kg^{-1} K^{-1}]
DH	district heating
F_f	correction factor for heat exchanger fouling, [−]
G_{tot}	hemispherical solar irradiance, [W m^{-2}]
$\dot{m}$	mass flow rate, [kg s^{-1}]
nom	subscript referring to nominal conditions
Q_{sol}	theoretical solar energy output from the collector field, [W]
Re	Reynolds number, [−]
$RMSD$	root-mean-square deviation
s_i	uncertainty of the function/variable i
T_m	mean fluid temperature in the collector field, [°C]
T_{amb}	ambient temperature, [°C]
UA	overall heat transfer coefficient of the heat exchanger, [W K^{-1}]
η_0	peak collector efficiency, [−]

it is important to be able to predict the behavior and performance of these plants in the most accurate way. If correct sizing, control strategy and design improvements can be accurately evaluated in advance and implemented already in the planning phase, later and more expensive interventions can be avoided. Additionally, detailed simulation models can be used for on-line simulations, which use real-time measured data as input [25], to continuously monitor the plant and verify whether this meets the expected performance.

So, the aim of this study was to develop a detailed simulation model of a large solar collector field for DH application. The model was developed in TRNSYS-Matlab. The model treated aspects which are usually neglected in simpler models, such as flow distribution, collector efficiency dependence on the flow regime, etc., in order to evaluate their impact on the overall model accuracy. The reliability of the model was verified by comparing its results against experimental measurements.

The paper is structured as follows. Section 1.2 presents a literature review on modeling of solar heating systems and the challenges that were addressed in this study. Section 2 describes the collector field used for the model validation and the developed TRNSYS model. Section 3 presents and analyzes the results of the TRNSYS subsystems used to calibrate single model components, as well as the comparison between the results of the model of the solar heating plant and the measurements. The titles of the subsections of Sections 2 and 3 are almost identical, so that for each component the reader can easily move from the methodology subsection to the corresponding result and discussion subsection. Section 4 summarizes the main conclusions.

1.2. Literature review

Le Denn [21] distinguishes the available simulation tools for large solar collector fields for DH applications in two categories. The first category includes dedicated solar DH tools, such as F-Easy [24], Fjernsol-II [26], SDH Online-Calculator [9] and Sunstore 4 Tool [8]. The second category includes generic software, such as TRNSYS [18], energyPRO [12], Polysun [41] and RETScreen [23].

The programs of the first category are mainly feasibility tools, suitable for rough estimation of the system performance on yearly or monthly basis. They are simple to use, but offer limited detail and few possibilities of customization, so they were discarded for this study. Of the second category, TRNSYS was identified as the most suitable simulation program, as it offered different advantages compared to the other tools. First of all, TRNSYS comes with a wide library of validated component models. Besides the original TRNSYS component library, other libraries [33,38] or single components have been developed by different institutions or programmers. Additionally, TRNSYS users can write and compile their own components, or customize existing ones by editing their source code. Finally, TRNSYS can interact with other software, such as Matlab, while a simulation is running. All these possibilities give a high flexibility in the use of the software, which was hence chosen for this study.

TRNSYS has been widely used for simulation of solar thermal systems. Numerous articles report on studies where TRNSYS was successfully used to simulate domestic or small case solar thermal systems. A selection of these is presented in the review by Saleem et al. [31]. Larger parabolic trough collector fields connected to power plants have been modeled in TRNSYS [1,6,7]. In the field of solar DH, Raab et al. [27] developed and validated a TRNSYS model to simulate the solar assisted DH system in Hannover. Sibbitt et al. [35] used TRNSYS in the design phase of the solar DH system of Drake Landing Solar Community in Canada. The monitored data of the installed system were in satisfactory agreement with the model. Bava et al. [5] modeled a single collector row in the collector field by Brædstrup II, Denmark. The comparison between simulation results and measurements shows that inaccurate solar radiation measurements and decreased collector efficiency (caused for example by dirty glass cover) may compromise the agreement between model and monitored data.

In most of the mentioned studies, the collector field was only a part of the entire system and hence was treated with little detail, usually by a single collector component. Consequently, aspects such as flow distribution across the collector field are not considered, although they may have an impact on the collector field performance [10]. This is especially valid nowadays, when the collector fields have become increasingly larger. Additionally, modeling the entire collector field as a single component entails that also the distribution pipes in the model do not have the actual layout or fluid content. This can easily lead to an advance or delay of the model response compared to reality. To address this problem, the TRNSYS model developed in this study was made interact with a previously validated Matlab model [3], so to accurately take into account the exact flow distribution across the collector field (see Section 2.2.2.2).

Another simplification consists of assuming the collector efficiency expression constant. Among the different operating conditions which can affect the collector efficiency, the flow regime in the absorber pipes has great importance [4,15]. Most collectors are tested using water as heat transfer fluid and in condition of turbulent flow. If the collector is supplied with propylene glycol/water mixtures, laminar regime may take place, reducing its efficiency. Therefore, using the certificate collector efficiency as input to the model is likely to cause an overestimation of the collector performance compared to real-world operation. To reproduce the behavior of the collectors in a more realistic way, the collector efficiency from the collector test report was corrected to take into account the different heat transfer fluid through a collector simulation program. Additionally, a new TRNSYS collector component was developed, to account for the effect of the flow regime on the collector efficiency.

Other aspects which are often neglected for sake of simplicity, but which were considered in this study, are thermal capacity of pipes, distinction between beam and diffuse radiation and shadow effect from one row to another.

2. Material and method

This section describes the solar collector field used for the model validation and the TRNSYS model itself. The collector field is described in terms of hydraulic layout, system components, measuring equipment and control strategy. Regarding the TRNSYS model, the list of utilized components as well as the reasons and considerations behind their choice are presented.

2.1. Description of the solar collector field

2.1.1. Collector field design

The TRNSYS model presented in this paper was developed based on the solar collector field near Høje Taastrup, Denmark (Fig. 1). As can be seen from the layout in Fig. 2, the collector field consisted of two subfields, having 12 collector rows each. Each row was composed of 10 HTHEATStore 35/08 collectors [37] from the company Arcon-Sunmark A/S. The collectors were harp flat plate collectors with 18 horizontal absorber pipes and a gross area of 13.57 m^2. The collector field gross area was 3257 m^2. The declared collector efficiency is reported in Table 1. The row distance was 5.5 m. The collector tilt angle was 43° and the orientation 2.5° W. The solar collector fluid was a 35% propylene glycol/water mixture [3]. Normal operating temperatures for the collector field were of 50–55 °C in inlet and 90–95 °C in outlet. The flow rate ranged from 8 to 50 $m^3\ h^{-1}$ (0.04–0.26 L $min^{-1}\ m^{-2}$) depending on the solar irradiance.

Fig. 1. Aerial picture of Høje Taastrup solar collector field (source: Arcon-Sunmark A/S).

Both supply and return pipes of the primary loop (or solar collector loop) were made of preinsulated steel pipes [22] with progressively decreasing diameter, as part of the flow was diverted to the collector rows. As seen in Fig. 2, supply pipes (in blue) supplied the collector rows from the outer sides of the collector field, while a single return pipe (in red) collected the heated fluid in the middle of the field. Balancing valves were installed and regulated at the inlet of each collector row, to guarantee a uniform flow distribution across the collector field [3].

The technical building (top-right corner in Fig. 2) hosted pumps, expansion vessels, control system, measuring equipment and the plate heat exchanger, which connected primary and secondary side.

The secondary side was connected to the DH main network through 550 m long transmission pipes. To avoid supplying too cold fluid to the network in the start-up phase, a bypass is installed at the end of the transmission pipes and it is used to recirculate the fluid until a temperature of at least 65 °C, compatible with the DH network, is reached.

2.1.2. Measuring equipment

Electromagnetic flow meters with an accuracy of ±0.5%

Table 1
Declared and simulated efficiencies of HTHEATStore 35/08 collector based on the gross area of 13.57 m^2.

	Fluid	η_0 [−]	a_1 [W m^{-2} K^{-1}]	a_2 [W m^{-2} K^{-2}]
Declared efficiency [37]	water	0.757	2.199	0.007
Soleff efficiency (test conditions)	water	0.757	2.260	0.006
Soleff efficiency (turbulent)	35% glycol	0.756	2.318	0.006
Soleff efficiency (laminar)	35% glycol	0.727	2.357	0.005

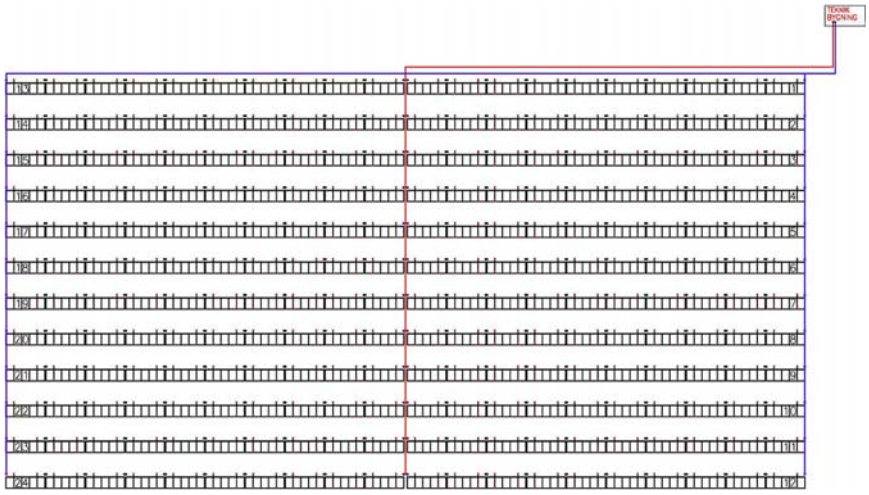

Fig. 2. Layout of Høje Taastrup solar collector field: blue and red lines represent supply and return pipes respectively (adapted from Arcon-Sunmark A/S). (For interpretation of the references to colour in this figure legend, the reader is referred to the web version of this article.)

measured the volume flow rate in both primary and secondary side. The temperature of the heat transfer fluids was measured by resistance thermometers with an accuracy of 0.25 K. The temperature was monitored at the beginning of the supply pipe, at the end of the return pipe, at the inlet and outlet of collector rows 1, 11, 13 and 23 (Fig. 2), at each inlet and outlet of the heat exchanger, and at the end of the transmission pipes. The ambient temperature in the field was measured too.

The solar irradiance on the collector field was measured by pyranometers in different parts of the collector field. Three photovoltaic cell pyranometers [36] were installed next to one another in the collector field and used in the control strategy. However, this kind of sensors is known to degrade over time, underestimating the actual solar irradiance. For this reason, four Kipp & Zonen thermopile pyranometers were added. A secondary standard CMP11 pyranometer and a first class CM5 pyranometer equipped with shadow ring were placed in the middle of the collector field on top of a collector, to measure the total and diffuse irradiance on the collector plane. The diffuse irradiance was corrected to account for the shadow ring using Drummond's [11] model. From the total and the diffuse irradiance, the beam component was determined. Other two secondary standard CM11 pyranometers were placed at the north-east and north-west corner of the collector field to measure possible differences between morning and afternoon incident radiation due to reflection from the collectors.

The instantaneous values of the monitored data were recorded once per minute. The sampling time used for control purposes was on the other hand much shorter (<1 s).

2.2. Description of the TRNSYS model

TRNSYS is a transient system simulation tool having a modular structure. A TRNSYS project is set up by interconnecting different modules, which build up the system which is to be simulated. The following sections explain which components built up the model, why they were chosen and how they were connected. A detail of the overall TRNSYS model of Høje Taastrup collector field is shown in Fig. 3. Simpler models were developed to calibrate single components, as described in the following sections.

Perers and Furbo [25] identify several aspects which should be taken into account, to develop accurate simulation models for large solar collector fields. These range from accurate weather data to choice of the component models, from flow distribution across the collector field to thermal capacity of the components. So the following sections also describe how these different aspects were addressed in this study.

2.2.1. Weather data and time resolution

Accurate weather data, including the distinction between beam and diffuse irradiance on the collector plane, should be used as input [25]. Both solar irradiance and ambient temperature were measured in the collector field by high class thermopile pyranometers (see Section 2.1.2). The measured weather data, as well as all other relevant monitored data from Høje Taastrup collector field, were loaded into the TRNSYS model by the data reader Type 9c [18].

To simulate the collector array shading, Type 30 [18] was used. The so corrected diffuse and beam irradiances were input to all collector rows except the front ones, which were not shaded.

According to Perers and Furbo [25]; the time resolution is also very important. Usually hourly mean values are available, but higher time resolution is desirable to test control algorithms. Hence, all recorded data (1 min time step) were used without averaging.

2.2.2. Model components

Regarding the components models, Perers and Furbo [25] suggest using already validated models instead of detailed theoretical components, to save both programming and computing time. Hence, almost all components used in the simulation model were

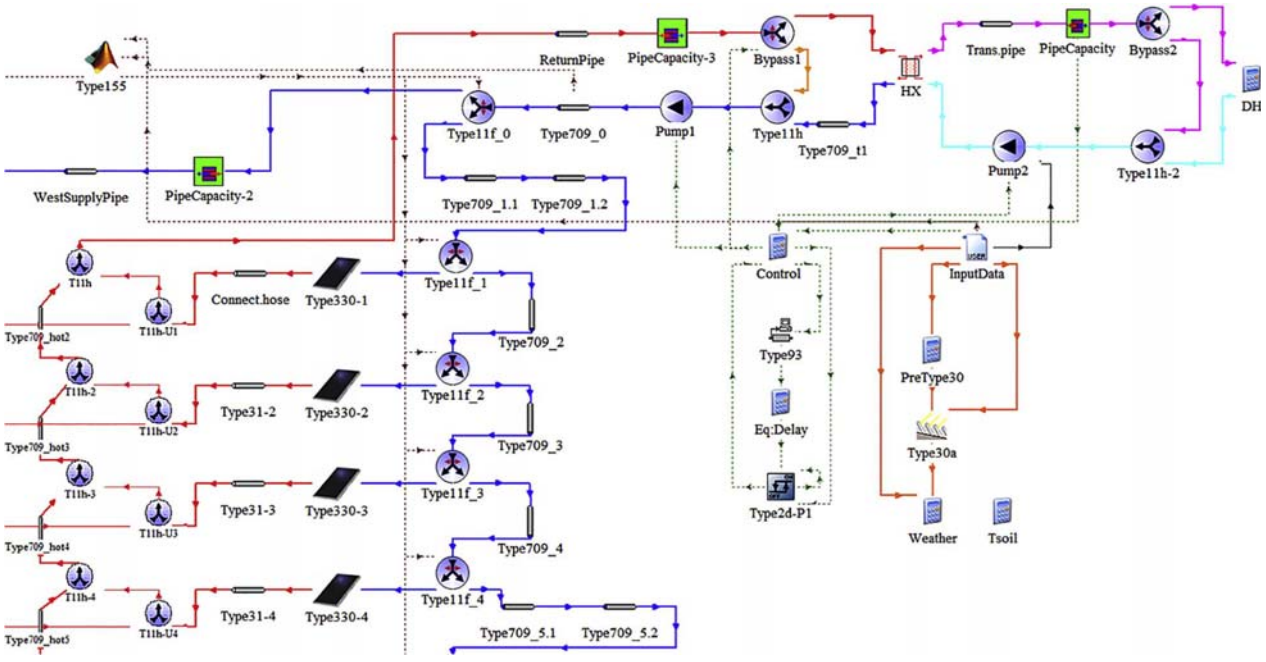

Fig. 3. Detail of the TRNSYS model of Høje Taastrup solar heating plant. For sake of clarity, only the first four collector rows of the eastern subfield are shown. Blue and red connections represent the supply and return pipes of the solar collector glycol loop; purple and pale blue connections represent the supply and the return pipes with water to/from the DH network. (For interpretation of the references to colour in this figure legend, the reader is referred to the web version of this article.)

taken from existing and well-established TRNSYS libraries [18,33,38].

2.2.2.1. Collector type components. A collector model which is compatible with the collector test standard ISO 9806 [16] should be used [25]. To be able to consider aspects which are usually neglected when simulating solar collector fields, Type 330 was used. This is an in-house model developed by editing Type 539 [38] with some desired features added. First of all, Type 330 makes use of a different efficiency expression depending on the flow regime in each node in which the collector is divided. Consequently, this collector type requires two efficiency expressions, one for laminar and one for turbulent regime. This may be a problem, as collector certificates provide only one efficiency expression, usually for turbulent conditions. In this study, a simulation model of the investigated collector HTHEATStore 35/08 [37] was developed with the software Soleff [29], based on the collector design and the operating conditions used during the efficiency test. The good agreement between the certificate efficiency and the simulated efficiency (RMSD = 0.12%) proved the reliability of the Soleff model. The model was then used to calculate the collector efficiency in laminar and turbulent conditions for a 35% glycol/water mixture. The coefficients of the declared and simulated efficiencies are listed in Table 1.

Considering the operating conditions in Høje Taastrup collector field (see Section 2.1.1) and assuming Re = 2300 as threshold between laminar and turbulent flow, about one third of the collectors experienced laminar flow. For this reason, it was relevant to have a different efficiency expression in case of laminar flow.

A second feature of Type 330 is the possibility for the user to specify an incidence angle modifier (IAM) for diffuse radiation, instead of having it internally calculated as in Type 539. Another feature consists of the wider range of incidence angle where the IAM-expression for beam radiation is used. The range is chosen depending on the data available in the technical datasheet of the collector which is to be simulated. The original Type 539 linearizes the IAM for angles between 60° and 90°.

To evaluate whether the improvements introduced in Type 330 had an effect, three different collector type variants were analyzed. The first used Type 539 and the declared collector efficiency (Table 1). The second made use of Type 330 and the Soleff efficiency equation for turbulent conditions (Table 1), regardless of the actual flow regime in the absorber pipes of the collectors. In the third variant, all features of Type 330 were enabled. For sake of simplicity, the first and second variants of Type 330 are referred to as Type330a and Type330b in the rest of the paper. To focus on the behavior of the different collector variants and avoid the influence of external factors, such as control strategy and secondary side temperatures, only the primary side of the collector field was modeled, and the measured flow rate, collector field supply temperature and weather data were given as input. The modeled return temperatures from the collector field in the three scenarios were compared to the measurements. Different types of weather conditions were considered: clear sky, cloudy sky with fluctuating solar radiation and overcast sky.

2.2.2.2. Flow distribution. To take into account the flow distribution in the collector field, each single collector row was modeled. As TRNSYS cannot solve problems of flow distribution in hydraulic networks, Type 155 [18] passed the necessary inputs to a Matlab program [3]. Matlab evaluated the flow distribution in the different collector rows and returned the result to TRNSYS, where the total flow was then distributed to the different rows accordingly.

To evaluate the impact of modeling the exact flow distribution, the detailed model using Type 330b (Section 2.2.2.1) was compared to a simpler model. The simpler model differed from the detailed one, as the entire collector array was simulated through a single Type330b. Additionally, the supply and return pipes were modeled by a pipe component each (see Section 2.2.2.3). The pipe length used as input in the pipe components was the average distance between the technical building and each collector row. The thermal capacity of the pipes was proportionally scaled (see Section 2.2.2.3).

2.2.2.3. Pipes and heat exchanger. Type 709 [38] was chosen to model the distribution pipes, as it had a better agreement with the measurements, compared to Type 31 [18] and Type 604 [38]. However, unlike Type 604, Type 709 does not consider the thermal mass of the pipe material, which may be relevant, especially in case of long transmission pipes. To take this aspect into account and evaluate its impact on the accuracy of the model, the thermal capacity Type 306 [33] was added to the longest distribution and transmission pipes. Specific TRNSYS projects were built, simulating only the investigated pipes. In this way, all the other simplifications of the model, which could have an effect on the simulation results, were excluded. The pipes investigated in detail were the supply pipe to the western subfield (see Figs. 2 and 3) and the transmission pipe from the heat exchanger to the DH network (see Section 2.1.1 and Fig. 3). These were chosen because their inlet and outlet temperatures were monitored. Additionally, the flow rate in the transmission pipe was directly measured, while the flow rate in the western supply pipe could be estimated based on the measured primary flow rate and the flow distribution model (Section 2.2.2.2). Pipe dimensions and material properties were also known. Finally, these pipes had the largest thermal mass, so they were the most relevant to investigate with respect to thermal inertia effect. The model used the measured inlet temperature and flow rate as input, and the resulting outlet temperatures were compared with the measured.

To accurately model the plug flow along the pipes, all distribution pipes segments were simulated, as well as connection hoses between consecutive collectors (Type 31 in Fig. 3). This also allowed taking into account the heat losses from the connection hoses. The soil temperature to calculate the heat losses from the buried pipes was evaluated through Type 77 [18].

The plate heat exchanger between the solar collector loop (primary side) and the DH network (secondary side) was modeled through Type 5b [18]. This type offers the possibility of inserting a variable heat transfer coefficient. A specific TRNSYS project, simulating only the heat was developed to calibrate Type 5b against measurements. Measured flow rates and inlet temperatures were given as input to Type 5b and the heat transfer coefficient was varied so to obtain the best agreement between measured and modeled outlet temperatures.

2.2.3. Control strategy

The control strategy implemented in the model was based on the information received by the plant designer Arcon-Sunmark A/S. The control strategy aimed at reaching a constant outlet temperature, by continuously regulating the total flow rate based on the solar irradiance. The desired outlet temperature is the DH supply temperature, increased by the temperature drop across the heat exchanger. As the collector field was not located near an auxiliary energy source, the collector field outlet temperature must meet the DH requirements, if the energy is to be delivered to the DH network.

The main principles of the control strategy in Høje Taastrup solar heating plant can be summarized as follows. The relation (Eq. (1)) gives the theoretical solar energy output Q_{sol}, which is then used to regulate the primary pump flow rate (Eq. (2)). The primary pump is denoted as *Pump 1* in Fig. 3.

$$Q_{sol} = A_{field}\left(G_{tot}\ \eta_0\ - a_1\cdot(T_m - T_{amb}) - a_2\cdot(T_m - T_{amb})^2\right) \quad (1)$$

$$\dot{m} = \max\left[\dot{m}_{min},\ Q_{sol}/(c_p\cdot(T_{out,setpoint} - T_{in}))\right] \quad (2)$$

T_m is the mean temperature between the measured collector field inlet temperature T_{in} and the desired outlet temperature $T_{out,setpoint}$. The solar irradiance G_{tot} is measured by the photovoltaic cell pyranometers (see Section 2.1.2).

The condition for the primary pump to turn on is that either Q_{sol} is higher than a certain threshold, or one of the monitored fluid temperatures in the collector field is higher than a preset value. The turn-off condition is the negation of the turn-on condition, delayed by the time needed to discharge the energy content of the hot return pipes. Because at the start-up of the primary pump in the morning the primary loop is still relatively cold, the flow bypasses the heat exchanger and is recirculated across the collector field (*Bypass1* in Fig. 3). When the field outlet temperature is sufficiently high, the primary bypass is closed and the secondary pump is turned on. The secondary pump is regulated so that the heat capacity rate on both sides of the heat exchanger is the same. At the start-up of the secondary pump, the bypass installed at the end of the transmission pipes (*Bypass2* in Fig. 3) recirculates the fluid until a temperature of 65 °C, compatible with the DH network, is reached.

In the TRNSYS model, most of the control strategy is implemented in an Equation block, while the turn-on/off conditions and the time delay are set by a differential controller Type 2d and Type 93 respectively [18].

A detail of the overall TRNSYS model, which implemented also the control strategy of the solar heating plant, is shown in Fig. 3. The only measured values used as input were the weather conditions (irradiance and ambient temperature) and the return temperature from the DH network. The accuracy of the model was tested, by comparing simulated and measured temperatures, energy outputs and flow rates under different weather conditions.

3. Results and discussion

This section presents and analyzes the results from the validation of the single components or subsystems, such as solar radiation sensors, solar collector, heat exchanger and pipes. Based on these results, the parameters of the single components could be accurately determined and used in the model of the solar heating plant. Secondly, the validation of the model of the plant is presented.

3.1. Solar radiation measurements

Fig. 4 shows the relative difference between the total solar irradiance measured by the photovoltaic cell pyranometers and that from the thermopile CMP11 pyranometer in a clear sky day. It can be seen that for high irradiances (G_{tot}>800 W m^{-2}), the photovoltaic pyranometers underestimated the solar irradiance by 7–8%. At lower irradiances (and larger incidence angles) the difference increased, up to 27% for G_{tot} = 200 W m^{-2}. The non-perfect overlap of morning and afternoon data must have been caused by a small difference in the orientation of the pyranometers, with the CMP11 sensor oriented slightly more eastward than the photovoltaic sensors.

As all sensors had been recently cleaned, the difference in the reading cannot be attributed to soiling, but was likely caused by degradation of the photovoltaic cell. Repeated measurements in similar sky conditions gave similar results. Conversely, lower

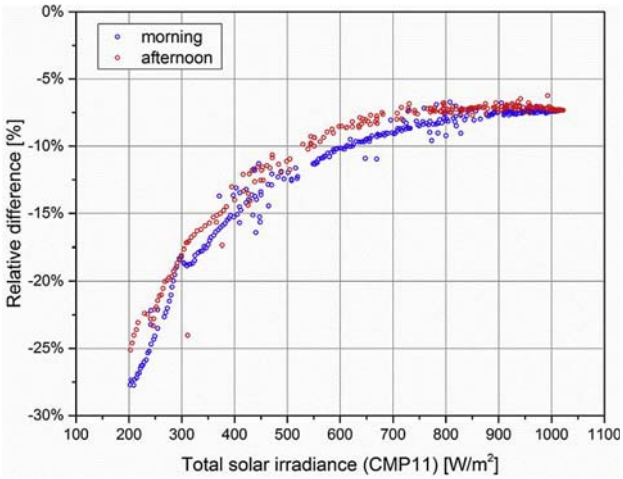

Fig. 4. Relative difference in the hemispherical solar irradiance between photovoltaic cell and thermopile CMP11 pyranometer.

differences (≤5%) were found in case of overcast sky. This led to the conclusion that the large deviations between photovoltaic and thermopile pyranometer in the early morning and late afternoon were caused by larger incidence angles rather than low solar radiations.

The significant decrease in sensitivity of the photovoltaic pyranometer over time is a problem which is often observed with this type of sensors. However, photovoltaic cell sensors have the advantage of much lower price and much shorter response time (some milliseconds [36]), compared to a thermopile sensor (5–20 s [17]). If the instantaneous measured solar irradiance is used for control purposes, a fast response time of the sensor is of key importance and photovoltaic cell sensors could be preferred. However, they should be regularly checked and their sensitivity corrected, if needed. Additionally, the strong directional response (i.e., dependence of the measured radiation on the incidence angle) of the photovoltaic pyranometer suggests introducing a second correction to account for this effect.

Given the significant difference between the solar irradiance measured by the photovoltaic cell pyranometers and that from the thermopile pyranometers, it was important to use the two of them properly. Hence, the irradiance measured by the photovoltaic cell was used in the control strategy of the model, as it was used in the actual solar heating plant. The irradiance measured by the thermopile pyranometers provided the weather data input to the collector TRNSYS types.

3.2. Collector type components

With all three collector type variants, the collector field return temperature calculated by the model was always higher than the measured, if the efficiencies listed in Table 1 were used. To have a good agreement between the two, the peak collector efficiency η_0 had to be reduced by 7.3% for Type 330b and Type 539, and by 7.8% for Type 330a. For each type variant, the exact reduction was chosen so that the modeled daily energy output from the collector field differed from the measured one less than ±1%.

The good accuracy of the measurement equipment (Section 2.1.2) excluded the presence of faults in the measured data used as input for the model. Additionally, these data were also carefully checked to spot possible outliers. Secondly, the presence of temperature sensors at the inlet and outlet of some collector rows allowed having a clear focus on the behavior of the single rows. This

excluded the influence of possible biased heat losses and plug flow in the pipes. In each modeled collector row, the only components were the collector (Type 539 or 330) and the pipe Type 31, to take into account plug flow and heat losses in the connection hoses. Hence, it was concluded that the disagreement between modeled and measured outlet temperature was most likely due to a difference between the actual collector efficiency and the efficiency from Soleff, based on the test report. As the variation of the heat loss coefficients (for example, due to moist insulation) could not be evaluated, the reduction in performance was entirely attributed to the decreased transmittance of the glass cover, which can be caused by soiling, dirt and moisture on the glass cover. The pollution from the motorway running just 150 m away might have a more negative effect than less traffic-congested areas.

Table 2 shows the RMSD between measured and modeled temperatures at the end of the return pipe from the solar collector field. If ranked in order of better agreement with the measurements, the three collector types were Type 330b, Type 539 and Type 330a.

So, the enhancements introduced in Type 330b improved the agreement between model and measurements, compared to the original Type 539. However, Type 539 performed better than Type 330a. This can be explained by the fact that the flow regime in the collector was laminar at low flow rates, which, according to (Eq. (2)), occurred in case of low solar irradiance. Low irradiance was measured either in the early morning and late afternoon of clear sky days or in cloudy days. In these conditions, the overall IAM used by Type 539 was lower than that used by Type 330. In fact, in the early morning and late afternoon, at incidence angles larger than 60°, Type 539 linearizes the IAM, which is hence lower than that calculated by Type 330 (Section 2.2.2.1). In cloudy conditions, when the fraction of diffuse radiation is significant, the IAM for diffuse radiation calculated by Type 539 was lower than that used by Type 330. Type 330 used a value of 0.94, as stated by the collector test report [37]. These two different effects (use of turbulent efficiency also at low flow, and lower IAM at low radiation) almost canceled each other out in Type 539. Consequently, this type was slightly less accurate than Type 330b. Conversely, Type 330a overestimated the collector efficiency in case of low flow and low irradiance, and hence had the least accurate agreement.

3.3. Flow distribution

According to the Matlab model, the flow distribution in the collector field was fairly uniform in all the tested conditions. The maximum relative difference between the modeled flow rate in a collector row and that in case of a perfectly uniform flow distribution was lower than 6%. The maximum difference between highest and lowest row flow rates was lower than 10%, which is the maximum deviation in flow distribution in solar collector arrays recommended by the German standard VDI [40].

Because of the fairly uniform flow distribution, it could be expected that neglecting this aspect would not affect the agreement between model and measurements. To verify this hypothesis, a simpler model where the entire collector array was simulated by only one collector type was developed.

Table 3 lists the RMSDs between measured and modeled field return temperatures, both for the model taking into account the flow distribution and for the simpler model. As expected, the simpler model had higher deviations (by about 1 K) compared to the more detailed model. Also in terms of energy output from the collector field, the simpler model differed more significantly from the measurements. Assuming the same decrease in the peak collector efficiency for both models (−7.3%), the simpler model differed between +0.5% and +2.6%, compared to ±1% of the detailed model (Section 3.2).

So taking into account the flow distribution improved the accuracy of the model compared to a perfectly uniform flow distribution scenario. There are different reasons why the more detailed scenario gave a better agreement. Firstly, modeling each segment of the distribution pipes, instead of using an average pipe length, allowed reproducing accurately the plug flow along the pipes and hence the time delay that the fluid takes to reach the single collector rows. Considering this aspect improves the accuracy of the model mainly in terms of RMSD of the outlet temperature, as temperature fluctuations are in phase when comparing model and measurements. Secondly, if the flow distribution in the collector field is not uniform, this reduces slightly the energy output of the field, which the model is able to reproduce. Finally, if all pipe segments are modeled, the heat losses can be calculated more accurately. This aspect had however a limited impact, because being the pipes well insulated, the impact of the heat losses was negligible in both models.

However, modeling the flow distribution was the most demanding and time consuming part, both in terms of programming and computing time. When TRNSYS used a time step of 1 min, and convergence and integration relative tolerances of 0.001, a simulation of 2 days of normal operation was performed in approximately 2.5 min by a computer with quad-core CPU, 2.4 GHz CPU frequency and 8 GB memory. The computing time was about 4 times shorter, when Matlab was not called to calculate the flow distribution, and 50 times shorter for the simpler model, which used only one collector component to model the entire array. Therefore, the trade-off between increased accuracy and longer programming and computing time should be considered case by case. For example, a slower but more precise model could be desirable in case of on-line simulations. Conversely, a simpler but faster model is a better solution for preliminary evaluations or feasibility studies.

3.4. Pipes and thermal capacity

The effect of thermal capacity was investigated adding Type 306

Table 2
RMSD (in Kelvin) between measured and modeled return temperatures from the collector field with different collector type models.

Date	Weather	Type 539	Type 330a	Type 330b
12/07/2015	overcast	2.05	1.99	1.74
13/07/2015	cloudy	2.26	2.07	2.05
14/07/2015	sunny	1.43	1.48	1.30
16/07/2015	sunny	1.13	1.42	1.05
17/07/2015	cloudy	1.71	1.95	1.72
24/07/2015	overcast	1.99	2.24	1.75
Mean		1.81	1.97	1.69

Table 3
RMSD (in Kelvin) between measured and modeled return temperatures from the collector field in case flow distribution is modeled (Detailed model) or not (Simpler model).

Date	Detailed model	Simpler model
12/07/2015	1.74	2.94
13/07/2015	2.05	2.77
14/07/2015	1.30	2.06
16/07/2015	1.05	2.10
17/07/2015	1.72	2.65
24/07/2015	1.75	1.97
Mean	1.69	2.44

to the supply pipe to the western subfield and the transmission pipe from the heat exchanger to the DH network. Measured inlet temperature and flow rate were given as input to the model, and the model outlet temperatures were compared with the measured. Two different types of days were analyzed: July 14 and 16, mainly clear sky days; July 13 and 17, characterized by fast fluctuation in solar irradiance due to continuously moving clouds.

Table 4 lists the RMSDs between measured and modeled pipe outlet temperature of the investigated pipes. It should be noted that the listed values were obtained taking into account the thermal mass of the steel pipe only and neglecting that of the pipe insulation. This choice was motivated by the fact that this simplification had no or negative effect on the RMSDs. In fact, the thermal capacity of the insulation accounted only for 20% of that of the steel pipe. Additionally, because of its low thermal conductivity, only a portion of the insulation thermal mass would actually be involved in the dynamic response of the pipe. Finally, Type 306 models the thermal mass as a lumped capacity, characterized by one temperature and one heat transfer coefficient between fluid and solid part of the pipe. This simplification can be regarded as accurate for the steel pipe, due to its high thermal conductivity and small thickness, but not for the insulation.

The remaining deviation between measured and modeled pipe outlet temperature could be caused by several factors, such as measurement accuracy and limitations of the model to reproduce the exact pipe conditions. Additionally, the measured data available, which were used as input for the model, were instantaneous values with recording time of 1 min (Section 2.1.2). Hence, the pipe model assumed constant inlet temperature and flow rate over 1 min, although this might not be necessarily the case, especially in conditions of fluctuating solar radiation and consequent fast variation of the pump speed (see also Section 3.6).

Because considering the thermal capacity of the pipes improved the agreement between model and measurements, Type 306 was added to the longest pipes in the model, i.e. the western supply pipe, the common return pipe from the collector field and the transmission pipes to the DH.

3.5. Heat exchanger

A good agreement between modeled and measured outlet temperatures from the heat exchanger was found, if the overall heat transfer coefficient of Type 5b was given by (Eq. (3)).

$$UA = F_f (UA)_{nom} \left(\frac{\dot{m}}{\dot{m}_{nom}} \right)^{0.6} \quad (3)$$

According to the technical specifications of the heat exchanger, the heat transfer coefficient in nominal conditions was $UA_{nom} = 440$ kW K^{-1}. However, to fit the model with the measured temperatures, it was necessary to introduce a correction factor for fouling $F_f = 0.77$. A second correction was added to take into account the reduced convective heat transfer coefficient at flow rates lower than the nominal one, $\dot{m}_{nom} = 58$ m^3 h^{-1}.

As the difference in heat transfer coefficient UA between the technical specifications of the heat exchanger and real-world operation was significant, it was important to correct the model accordingly. Because flow rates and inlet/outlet temperatures across a heat exchanger are usually monitored, it is convenient to calibrate the heat exchanger model against measurements. For this purpose, one day of data with variable flow rate can be sufficient and improves the accuracy considerably.

The heat exchanger outlet temperatures obtained by using (Eq. (3)) were compared with the measurements from days with different sky conditions. The results are summarized in Table 5. The days July 14 and 16 were characterized by clear sky conditions and hence smooth variations of the flow rates, while July 13 and 17 had fast fluctuations of the flow rate due to passing clouds (see Fig. 5). On the clear sky days, the RMSD between model and measured outlet temperatures was about 0.4–0.7 K on both primary and secondary side. On the cloudy days, characterized by rapidly varying flow rate, the RMSD was slightly higher (1.2–1.5 K). These larger deviations can be explained by the recording time of the measured data used as model input, as in Section 3.4. Adding the thermal capacity of both fluid content and metal plates to the heat exchanger through Type 306 had negligible effect on the RMSD in most cases, so this aspect was neglected in all other simulations.

3.6. Control strategy and overall TRNSYS model

The overall TRNSYS model reproduced in detail the solar heating plant in Høje Taastrup, both in terms of components and control strategy. The only external boundary conditions required by the model were the return temperature from the DH and weather conditions.

The good agreement between measurements and model can be appreciated in Fig. 5. Fig. 5 shows some of the measured and modeled data for two different types of weather conditions. As can be seen, July 13 was characterized by moving clouds and so fast fluctuations of the solar radiation, which caused higher deviations between measurements and model.

Table 6 presents an overview of the comparison between model and measurements in terms of fluid temperatures in different parts of the system, gross and net produced energy and flow rate in the primary side. The gross energy output from the collector field was calculated whenever the primary pump was in operation. So it also includes the energy collected during pre-heating of the primary loop, when the primary bypass was open. The energy delivered to the DH network was calculated at the end of the transmission line, when the supply temperature was higher than 65 °C (Section 2.2.3). The cumulated flow is the time integral of the flow rate. The RMSD of the different temperatures is the deviation between measured and modeled values. Taking into account the accuracy of the measuring equipment (see Section 2.1.2) and the density and

Table 4
RMSD (in Kelvin) between measured and modeled pipe outlet temperatures with and without taking into account the thermal capacity (Cap.) of the steel pipe.

	13/07/2015	14/07/2015	16/07/2015	17/07/2015
West supply pipe (no Cap.)	1.87	1.67	1.93	3.12
West supply pipe (with Cap.)	1.15	1.20	1.45	1.91
Transmission pipe (no Cap.)	3.03	1.14	2.38	3.49
Transmission pipe (with Cap.)	2.19	1.05	0.71	1.48

Table 5
RMSD (in Kelvin) between measured and modeled outlet temperatures from the heat exchanger, with and without taking into account its thermal capacity (Cap.).

	13/07/2015	14/07/2015	16/07/2015	17/07/2015
Outlet on primary side (no Cap.)	1.39	0.64	0.53	1.24
Outlet on primary side (with Cap.)	1.38	0.63	0.53	1.23
Outlet on secondary side (no Cap.)	1.30	0.72	0.44	1.54
Outlet on secondary side (with Cap.)	1.15	0.69	0.47	1.52

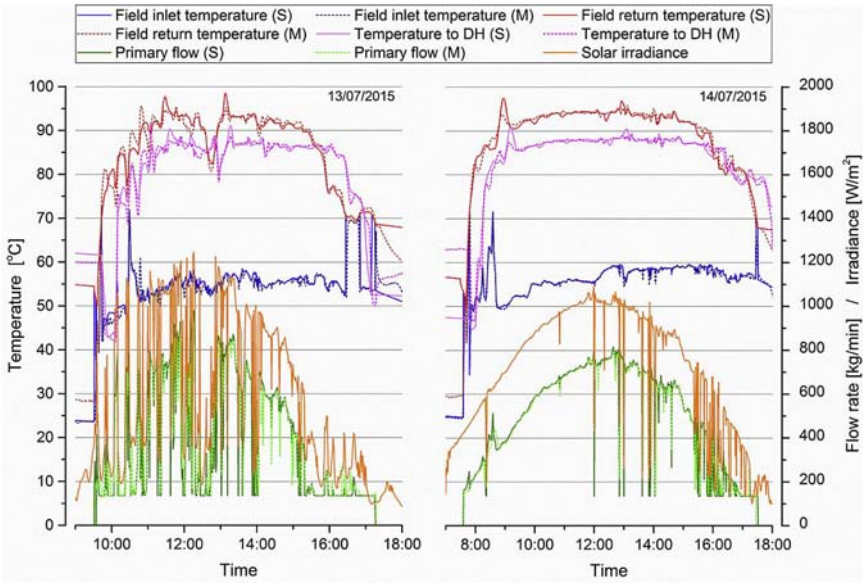

Fig. 5. Comparison between measurements (M) and simulation results (S) based on the data from 13 to 14 July 2015.

Table 6
Comparison between measurements (M) and simulation results (S) of the overall TRNSYS model.

		12/07/2015	13/07/2015	14/07/2015	16/07/2015	17/07/2015
Gross energy output from field (M)	MWh	2.42	6.63	11.4	11.7	8.63
Gross energy output from field (S)	MWh	2.34	6.58	11.4	11.8	8.62
Deviation in gross energy output	%	−3.3%	−0.8%	0%	0.9%	−0.1%
Energy supplied to DH (M)	MWh	2.31	6.48	11.4	11.6	8.44
Energy supplied to DH (S)	MWh	2.27	6.47	11.3	11.7	8.45
Deviation in energy to DH	%	−1.7%	−0.2%	−0.9%	0.9%	0.1%
Cumulated primary flow (M)	kg	$8.24 \cdot 10^4$	$1.79 \cdot 10^5$	$2.92 \cdot 10^5$	$2.99 \cdot 10^5$	$2.29 \cdot 10^5$
Cumulated primary flow (S)	kg	$8.03 \cdot 10^4$	$1.78 \cdot 10^5$	$2.95 \cdot 10^5$	$3.02 \cdot 10^5$	$2.29 \cdot 10^5$
Deviation in primary flow	%	−2.5%	−0.6%	1.0%	1.0%	0%
RMSD ($T_{\text{supply to field}}$)	K	1.37	1.20	1.33	1.10	1.28
RMSD ($T_{\text{return from field}}$)	K	2.82	2.37	1.48	1.76	2.59
RMSD ($T_{\text{supply to DH}}$)	K	3.77	2.20	1.43	1.89	2.29

specific heat of the heat transfer fluids, the uncertainty of the measured energy outputs and cumulated flow rates was calculated through the formula for propagation of error (Eq. (4)):

$$s_f = \sqrt{\left(\frac{\partial f}{\partial x}\right)^2 s_x^2 + \left(\frac{\partial f}{\partial y}\right)^2 s_y^2 + \cdots + \left(\frac{\partial f}{\partial z}\right)^2 s_z^2} \tag{4}$$

where s_f is uncertainty of the function f (e.g., the energy output from the collector field) and s_i is the uncertainty of the function variable i, (e.g., volume flow rate, density and specific heat of the fluid, inlet and outlet temperature).

Based on (Eq. (4)), the uncertainty on the measured energy outputs was 1.5% for the days in the period July 13–17, and 1.7% for July 12. The uncertainty on the measured mass flow rate was 0.8%.

The tabled values show the good agreement between model and measurements. In terms of energy and cumulated primary flow, the model differed from the measurements no more than 1%, with the only exception being the overcast day July 12.

As expected, the temperature deviations were higher in the days characterized by fluctuating solar radiation (July 13 and 17), compared to clear sky days. The main reason for this is that, although both measured and simulated data were available once per minute, this 1 min time step had a different meaning in the two cases. In the measured data, 1 min is the recording time step, after which the instantaneous measured value of all monitored parameters was recorded. No information of what happened between one recording and the next was stored. In the simulation, 1 min was the time step used by the model to calculate the output parameters. Inputs, such as solar radiation and return DH temperature, and calculated parameters, such as flow rates, were assumed constant during the time step. This simplification is reasonable, when the input parameters change slowly, such as in clear or overcast sky conditions. Higher deviations can be expected, in case of higher frequency changes, for example in a cloudy day.

A second reason may be the different response time of the real pump and the pump model. The latter reacted instantly to a change in Q_{sol} (Eq. (2)), while the former had certain inertia. This effect was more evident in case of rapidly moving clouds and consequent fast variation of the pump speed.

Deviations in field return temperature were observed in the early morning, especially in presence of fluctuating solar radiation (Fig. 5). On the other hand, July 14 (clear sky day) had a better agreement between measured and modeled temperature profiles, although some misalignment is still visible in the first hours of operation. This might be caused by the simplified modeling of the collector heat capacity. The current standard ISO 9806 [16] accounts for the collector heat capacity through a single value (the

effective thermal capacity), which may not be sufficient to reproduce completely the dynamic response of the collector. Firstly, among the collector characteristic parameters determined by the quasi-dynamic test method [16], the effective thermal capacity may not always accurately be identified, due to the constant inlet temperature constraint, which limits the dynamic response of the collector [19]. Secondly, because of how the test is performed, the calculated effective thermal capacity is affected by the residence time of the fluid in the collector, and hence may change at different flow rates. Additionally, the test method assumes a lumped heat capacity, without distinction between fluid and solid parts of the collector. However, it is reasonable to expect that the different components, such as fluid, metal parts and insulation, have a different dynamic response. Consequently, a value of effective thermal capacity, which may give a realistic response during normal operation, may not be as accurate in other phases, such as start-up and/or cooling down of the collector. However, the different effect of the collector thermal capacity between model and actual plant affected mainly the dynamic response of the collector field, and not its energy output. In fact the deviations between model and measured gross energy output in the morning only were not higher than 1%.

The simulation results for July 12, day characterized by overcast sky conditions, had a lower agreement with the measurements compared to the other days. Both the simulated gross energy output from collector field and the simulated energy delivered to the DH network were lower than the measured ones (−3.5% and −1.7% respectively). The main reason for this was found in the lower cumulated flow rate in the simulation compared to the measurements. The simulated and measured flow rates had extremely similar profiles, proving the good ability of the model control strategy to reproduce the actual one. However, the measured data showed some sudden and very brief peaks of the flow rates, which could not be reproduced by the model control strategy, because not justified by the recorded weather data. As mentioned above, the fact that the measured data are the instantaneous (and not average) values of the monitored data may explain part of the discrepancy. This explained also the higher RMSD of the investigated temperatures, as even temporary differences in flow rates immediately affect the plug flow, causing a shift and mismatch of the temperature profiles. Secondly, the gross energy production on this day was fairly low (2.42 MWh), between 2.7 and 4.8 times lower than the other investigated days. So, even modest absolute differences between model and measurements caused stronger relative differences, compared to days with higher energy output.

In Table 6 the data from July 24 are not shown. In fact, taking advantage of the overcast sky conditions, some manual calibration of the plant was performed in this occasion. Hence, the control strategy did not follow the equations described in Section 2.2.3, so it was pointless to compare the measured and modeled flow rate, and consequently all the other quantities.

4. Conclusions and future perspective

The developed TRNSYS-Matlab model showed a good agreement with the measurements in different weather conditions. Although the exact results presented in this study refer to the specific case of Høje Taastrup solar heating plant, they can be used to draw some general considerations and conclusions which should be taken into account when analyzing measurements from other solar heating plants or when modeling this kind of installations. The following conclusions can be drawn:

- Accuracy of the input data is of key importance for precise modeling. Special attention should be paid to solar radiation sensors, which should be recalibrated, if their sensitivity is suspected of varying.
- If the collectors experience laminar flow for a relevant fraction of their normal operating conditions, a collector model, such as Type 330, with efficiency equations defined differently depending on the flow regime, can improve the accuracy.
- Considering the exact flow distribution in the collector field improves the accuracy, but it requires much longer programming and computing time. Depending on the aimed level of accuracy, this aspect may be considered or not.
- The thermal capacity of pipes may be considered for longer pipes only, otherwise its role is negligible.
- The heat transfer coefficient of a heat exchanger should be estimated through measurements rather than from technical specifications, so to include aspects, such as fouling and flow rate dependence.
- It was possible to reproduce the actual control strategy of the solar heating plant, maintaining a good agreement between model results and measurements.

The presented model is meant to be used to investigate different improvements measures in terms of operating conditions and control strategies, which may enhance the performance of the plant and provide a more constant return temperature from the collector field. The improvements measured which are planned to be investigated are improvements of the control strategy (such as more detailed input and closed-loop control), different heat transfer fluids in the primary loop and different temperature levels. Additionally, one year simulations in the above mentioned conditions will elucidate their impact on the yearly performance.

Acknowledgements

The authors are thankful to the Marie-Curie Actions - Initial Training Network research programme of the European Union which supported the first author through the SolNet-SHINE project. The authors are also grateful to the company Arcon-Sunmark A/S and the DH company Høje Taastrup Fjernvarme for providing useful information necessary to develop the model and for granting access to the solar collector field in Høje Taastrup.

References

[1] Abdel Dayem AM, Nabil Metwally M, Alghamdi AS, Marzouk EM. Numerical simulation and experimental validation of integrated solar combined power plant. Energy Procedia 2014;50:290–305. http://dx.doi.org/10.1016/j.egypro.2014.06.036.
[2] AEBIOM. EU handbook - district heating markets [WWW document]. 2012. URL, http://www.crossborderbioenergy.eu/fileadmin/crossborder/DH_MarketHandbook.pdf [Accessed 13 December 2016].
[3] Bava F, Dragsted J, Furbo S. A numerical model to evaluate the flow distribution in large solar collector fields in different operating conditions. Sol Energy 2017;143:31–42. http://dx.doi.org/10.1016/j.solener.2016.12.029.
[4] Bava F, Furbo S. Comparative test of two large solar collectors for solar field application. In: Proceedings of EuroSun 2014 Conference. Aix-les-Bains, France; 2014. http://dx.doi.org/10.18086/eurosun.2014.16.03.
[5] Bava F, Furbo S, Perers B. Simulation of a solar collector array consisting of two types of solar collectors, with and without convection barrier. Energy Procedia 2015;70:4–12. http://dx.doi.org/10.1016/j.egypro.2015.02.091.
[6] Biencinto M, Bayón R, Rojas E, González L. Simulation and assessment of operation strategies for solar thermal power plants with a thermocline storage tank. Sol Energy 2014;103:456–72. http://dx.doi.org/10.1016/j.solener.2014.02.037.
[7] Biencinto M, González L, Valenzuela L. A quasi-dynamic simulation model for direct steam generation in parabolic troughs using TRNSYS. Appl Energy 2016;161:133–42. http://dx.doi.org/10.1016/j.apenergy.2015.10.001.
[8] CIT Energy Management. Sunstore4 tool [WWW document]. 2013. URL, http://sunstore4.eu/use-results/sunstore4-tool/ [Accessed 13 December 2016].
[9] Deschaintre L. Development of a solar district heating online calculation tool. Energy Procedia 2014;48:1065–75. http://dx.doi.org/10.1016/

j.egypro.2014.02.121.
[10] Dorantes R, García G, Salazar C, Oviedo H, González H, Alanis R, et al. Thermal and hydraulic design of a solar collector field for a primary school pool. Energy Procedia 2014;57:2515–24. http://dx.doi.org/10.1016/j.egypro.2014.10.262.
[11] Drummond AJ. On the measurement of sky radiation. Arch für Meteorol Geophys Bioklimatol 1956;7:413–36. http://dx.doi.org/10.1007/BF02242969.
[12] EMD International A/S. energyPRO [WWW Document]. 2016. URL, http://www.emd.dk/energypro/ [Accessed 13 December 2016].
[13] European Commission. Communication from the commission to the european parliament, the council, the european economic and social committee and the committee of the regions: an EU strategy on heating and cooling. 2016. http://dx.doi.org/10.1017/CBO9781107415324.004.
[14] Furbo S, Perers B, Bava F. Thermal performance of solar district heating plants in Denmark. In: Conference proceedings of EuroSun 2014. Aix-les-Bains, France: International Solar Energy Society (ISES); 2015. http://dx.doi.org/10.18086/eurosun.2014.19.11.
[15] Hausner R, Fechner H. Influence of the flow condition (laminar/turbulent) in the fluid tube on the collector efficiency factor of a fin absorber. In: Proceedings of EuroSun 1998 conference. Portoroz, Slovenia; 1998.
[16] ISO. ISO Standard 9806: solar energy – solar thermal collectors – test methods. Geneva, Switzerland. 2014.
[17] Kipp & Zonen. CMP/CMA series manual. 2006.
[18] Klein SA, Beckman WA, Mitchell JW, Duffie JA, Duffie NA, Freeman TL, et al. TRNSYS 17 a transient system simulation program. Solar Energy Laboratory, University of Wisconsin-Madison; 2012.
[19] Kong W, Perers B, Fan J, Furbo S, Bava F. A new Laplace transformation method for dynamic testing of solar collectors. Renew Energy 2015;75:448–58. http://dx.doi.org/10.1016/j.renene.2014.10.026.
[20] Lapillonne B, Pollier K, Samci N. Energy efficiency trends for households in the EU [WWW Document]. 2015. URL, http://www.odyssee-mure.eu/publications/efficiency-by-sector/household/household-eu.pdf.
[21] Le Denn A. Solar district heating guidelines: calculation tools and methods [WWW document]. 2014. URL, http://solar-district-heating.eu [Accessed 13 December 2016].
[22] Logstor. Logstor industry catalogue. 2005.
[23] Natural Resources Canada. RETScreen [WWW document]. 2016. URL, http://www.nrcan.gc.ca/energy/software-tools/7465 [Accessed 13 December 2016].
[24] Nielsen JE, Battisti R. Solar district heating guidelines: feasibility study [WWW document]. 2012. URL, http://solar-district-heating.eu [Accessed 13 December 2016].
[25] Perers B, Furbo S. IEA-SHC tech sheet 45.A.4 simulation of large collector fields [WWW document]. 2014. URL, http://task45.iea-shc.org/fact-sheets [Accessed 13 December 2016].
[26] PlanEnergi. Fjernsol II [WWW document]. 2013. URL, http://www.solarkey.dk/fjernsol.htm [Accessed 30 March 2017].
[27] Raab S, Mangold D, Müller-Steinhagen H. Validation of a computer model for solar assisted district heating systems with seasonal hot water heat store. Sol Energy 2005;79:531–43. http://dx.doi.org/10.1016/j.solener.2004.10.014.
[28] Rasmussen FL. Rekordanlæg bliver klar på rekordtid. Fjernvarmen - Dan Fjernvarmes Mag 2016;7:20–3.
[29] Rasmussen PB, Svendsen S. SolEff, Program til beregning af solfangeres effektivitet. 1996.
[30] Reiter P, Poier H, Holter C. Big solar Graz: solar district heating in Graz - 500,000 m^2 for 20% solar fraction. In: Proceedings of EuroSun 2016 conference. Spain: Palma de Mallorca; 2016.
[31] Saleem MS, Haider A, Abas N. Review of solar thermal water heater simulations using TRNSYS. In: 2nd international conference on power generation systems and renewable energy technologies, PGSRET 2015; 2015. p. 68–73. http://dx.doi.org/10.1109/PGSRET.2015.7312251.
[32] Schubert M, Holter C, Soell R. Solar District Heating (SDH): technologies used in large scale SDH plants in Graz – operational experiences and further developments. In: Proceedings of 12th international symposium on district heating and cooling. Tallinn, Estonia; 2010. p. 140–2.
[33] Schwarzbözl P. A TRNSYS model library for solar thermal electric components (STEC). 2007. Reference Manual.
[34] SDHtake-off. SDHtake-off - solar district heating in Europe. 2012.
[35] Sibbitt B, McClenahan D, Djebbar R, Thornton J, Wong B, Carriere J, et al. The performance of a high solar fraction seasonal storage district heating system - five years of operation. Energy Procedia 2012;30:856–65. http://dx.doi.org/10.1016/j.egypro.2012.11.097.
[36] SolData. SolData 80spc pyranometer - data and application notes [WWW document]. 2016. URL, http://www.soldata.dk/pyr-80spc.htm [Accessed 30 March 2017].
[37] SP. Solar Keymark certificate HTHEATstore 35/08 No. SP SC0843-14. Borås, Sweden. 2016.
[38] TESS. TESSLibs 17 component libraries for the TRNSYS simulation environment. 2012.
[39] Trier D. Personal communication with d. Trier (PlanEnergi). 2016.
[40] VDI. VDI-Richtlinie: VDI 6002 Blatt 1 Solare Trinkwassererwärmung - Allgemeine Grundlagen - systemtechnik und Anwendung im Wohnungsbau. 2004.
[41] Vela Solaris. Polysun simulation software [WWW document]. 2016. URL, http://www.velasolaris.com/ [Accessed 30 March 2017].
[42] Weiss W, Spörk-Dür M, Mauthner F. Solar heat worldwide - global market development and trends in 2016 [WWW document]. 2017. URL, http://www.solarthermalworld.org/keyword/solar-heat-worldwide-2017 [Accessed 19 June 2017].

Paper VII

Impact of different improvement measures on the thermal performance of a solar collector field for district heating

Federico Bava and Simon Furbo

Under review at *Energy* journal

Impact of different improvement measures on the thermal performance of a solar collector field for district heating

Federico Bava* and Simon Furbo

DTU Civil Engineering, Technical University of Denmark, Brovej 118, 2800 Kgs. Lyngby (Denmark)

* Tel.: +45 45251700, Email: febav@byg.dtu.dk

Abstract

The paper describes the impact of different measures to improve the thermal performance of a solar heating plant for district heating applications. The impact of the different measures was evaluated through a TRNSYS-Matlab model, which had been previously validated. The model included details such as the effect of the flow regime in the absorber pipes on the collector efficiency, flow distribution in the collector field, thermal capacity of the pipes and effect of shadows from row to row. The improvement measures included variation of the temperature levels in the collector field, accurate input to the control strategy, feedback control on the outlet temperature of the solar collector field, control strategy based on weather forecast and use of different heat transfer fluids. The results showed that accurate input to the control strategy, especially in terms of actual solar radiation on the collectors, improved the yearly energy output of the plant by about 3%. If accurate input is not technically or economically feasible, the addition of a feedback control on the field outlet temperature can be an alternative solution. The integration of weather forecast in the control strategy did not give relevant improvements. Higher glycol concentrations in the solar collector fluid gave better results than lower concentrations, as the higher frost protection guaranteed by the former outweighed the better thermophysical properties of the latter.

Keywords: solar heating plant; solar collector field; TRNSYS; modeling; control strategy.

Nomenclature

A_{field}	collector area of the collector field	[m^2]
a_1	heat loss coefficient of collector at $T_m - T_{amb} = 0$ K	[W m^{-2} K^{-1}]
a_2	temperature dependence of the heat loss coefficient of collector	[W m^{-2} K^{-2}]
c_p	specific heat	[J kg^{-1} K^{-1}]
DH	district heating	
E_{DH}	energy delivered to DH	[GWh]
$E_{DH,w}$	energy to DH, weighted on the temperature difference $\Delta T_{s\text{-}DH}$	[GWh]
$E_{DH\ 2.5}$	energy to DH at a temperature T_{toDH}, such that $\Delta T_{s\text{-}DH} < 2.5$ K	[GWh]
$E_{DH\ 5}$	energy to DH at a temperature T_{toDH}, such that 2.5 K $< \Delta T_{s\text{-}DH} <$ 5 K	[GWh]
E_{el}	electricity consumption	[MWh]
E_{frost}	energy injected into the collector field in frost protection operation	[GWh]
F_f	correction factor for heat exchanger fouling	[-]
G_{tot}	total solar irradiance on the collector plane	[W m^{-2}]
K	proportional gain constant (in PID controllers)	
$\dot{m}$	mass flow rate	[kg s^{-1}]
nom	subscript referring to nominal conditions	
Q_{sol}	theoretical power output from the collector field	[W]
P_{el}	electrical power	[W]
t	time	[s]
T_{amb}	ambient temperature	[°C]
T_d	derivative time (in PID controllers)	[s]
T_i	integral time (in PID controllers)	[s]
T_{in}	inlet temperature to the collector field	[°C]
T_m	mean fluid temperature in the collector field	[°C]
T_{out}	outlet temperature from the collector field	[°C]
$T_{setpoint}$	set point outlet temperature for the collector field	[°C]
$T_{DH,r}$	return temperature in the DH network	[°C]
$T_{DH,s}$	supply temperature in the DH network	[°C]
T_{toDH}	temperature of the fluid delivered to the DH network (after shunt)	[°C]

u	control signal from PID control	[-]
UA	overall heat transfer coefficient of the heat exchanger	[W K^{-1}]
$\dot{V}$	volume flow rate	[m^3 s^{-1}]
Δt	time interval	[s]
$\Delta T_{s\text{-}DH}$	temperature difference $T_{DH,s} - T_{toDH}$	[K]
$\Delta T_{set\text{-}out}$	temperature difference $T_{setpoint} - T_{out}$	[K]
ε	effectiveness of the heat exchanger	[-]
η_0	peak collector efficiency	[-]

1. Introduction

1.1. Background

Space heating and domestic hot water preparation account for approximately 80% of the energy demand of European residential buildings [1]. An efficient way to provide heat to buildings in densely populated areas is through district heating (DH). In Europe there are about 5000 DH networks, which provide 10% of the total heat demand [2]. As the heat demand required by residential buildings is at relatively low temperatures, solar thermal collectors are a good candidate to cover this demand in a sustainable and efficient way.

However, the combination of these two technologies, i.e. solar collectors feeding into DH networks, is relatively recent and still rare, except for a few countries. Of the 5000 DH networks in operation in Europe, about 150 are solar assisted DH systems [3]. This scenario may change in the coming years, as the European Union has set a target of 1% solar fraction in DH by 2020 and of 5% by 2050 [4].

Denmark is currently the only example for a mature and commercial market for solar DH. At the end of 2015, 77% of the total collector area of large collector fields in Europe was installed in Denmark [5]. During 2016, the installed area of solar heating plants for DH in Denmark increased by more than 60% compared to 2015 [6]. Among the newly installed plants, the one in Silkeborg is currently the world largest collector field with a collector area of 156,000 m^2 [7].

If solar heating plants are to play a significant role in the heat supply of DH networks, it is desirable to have models able to simulate and predict in an accurate way the performance of these plants. These models could be for example used to optimize sizing, design and control strategy in the planning phase, avoiding later and more expensive interventions. They could also be used to check whether the plant performs as expected, by running on-line simulations using real-time measured data as model input [8].

Hence, the aim of this study was to evaluate a number of optimization measures for large solar collector fields for DH application, by using a TRNSYS-Matlab model. The model had been previously developed and validated against measurements from a large solar collector field [9]. The model considered aspects which are usually neglected in simpler models, such as flow distribution across the collector field, collector efficiency dependence on the flow regime and thermal inertia of the system components.

1.2. Literature review

Le Denn [10] identifies different simulation tools which can be used to model solar collector fields for DH applications. Programs such as F-Easy [11], Fjernsol-II [12], SDH Online-Calculator [13] and Sunstore 4 Tool [14] are feasibility tools, with limited level of detail and few possibilities of customization. However, they can give a rough estimation of the system performance. Higher level of detail and customization is offered by generic software, such as TRNSYS [15], energyPRO [16], Polysun [17] and RETScreen [18].

The advantages of TRNSYS compared to other software are described in [9]. It is worth mentioning the large number of validated component models in the original TRNSYS library, as well as in the TESS [19] and STEC [20] libraries, and the possibility for users to create their own components, either by writing new source code or by editing the code of existing components.

TRNSYS is well known and commonly used to simulate solar thermal systems. Saleem et al. [21] present a review of several articles, describing how domestic and small solar thermal systems were successfully modeled in TRNSYS. There are also examples of TRNSYS simulations treating large parabolic trough collector fields [22–24]. Regarding solar assisted DH, TRNSYS was used to model the collector field of Brædstrup II (Denmark) [25] and the solar assisted DH system in Hannover [26]. Sibbitt et al. [27] used the

software to design the solar DH system in Drake Landing (Canada). The model had a good agreement with later collected monitored data.

Most simulation models simplify the modelling of the collector field, usually using a single collector component and one or two pipe components to represent it. Therefore, the exact plug flow in the pipes and the flow distribution across the collector field cannot be reproduced. Another simplification which is usually accepted is the assumption that the collector efficiency expression is constant, although the flow regime in the collector pipes can have a strong influence on the collector efficiency [28,29]. Water is commonly used as heat transfer fluid in solar collector testing and often entails turbulent flow in the absorber pipes. If a propylene glycol/water mixture is supplied to the same collector, the higher viscosity may cause laminar flow, decreasing the collector efficiency. Other aspects that are seldom considered can be the thermal capacity of the components and shadow from a collector row to another.

2. Methodology

2.1. Description of the solar collector field

The TRNSYS model used in this study had been previously developed and validated against measurements from the solar collector field installed nearby Høje Taastrup, Denmark (Figure 1). The 240 collectors were arranged in two symmetrical subfields (Figure 2), for a total gross area of 3257 m^2. Each subfield had 12 collector rows, 5.5 m apart from each other, and each row had 10 HTHEATStore 35/08 collectors [30] from the company Arcon-Sunmark A/S. These flat plate collectors had a gross area of 13.57 m^2 and a harp design with 18 horizontal absorber pipes. The collector efficiency coefficients are listed in Table 1. The collectors had a tilt of 43° and an orientation of 2.5° W. A 35% propylene glycol/water mixture [31] circulated in the solar collector loop. The operating temperatures of the collector field depended on the supply and return temperatures in the DH network (see Section 2.2.1). The flow rate varied between 8 and 67 $m^3\ h^{-1}$ (0.04−0.34 liter $min^{-1}\ m^{-2}$) depending on the solar irradiance on the collector field. The solar irradiance was measured by photovoltaic cell pyranometers [32]. A fairly uniform flow distribution in the different rows was achieved though balancing valves installed at the inlet of each row [31].

Figure 1: Aerial picture of Høje Taastrup solar collector field (source: Arcon-Sunmark A/S).

A plate heat exchanger transferred heat from the solar collector loop (primary side) to a water loop (secondary side). In the water loop two 550 m long transmission pipes directly connected the secondary side of the heat exchanger to the DH network. Both primary and secondary side were equipped with a bypass, which allowed recirculation of the heat transfer fluid until fluid temperatures compatible with the DH network were reached. Conversely, if the fluid temperature at the end of the forward transmission pipe was too high, this could be lowered through a shunt (see Section 2.2.2.1 and Figure 3). The temperature of the heat transfer fluids was measured at each inlet and outlet of the heat exchanger (before and after the primary and secondary bypass). Additionally, the fluid temperature was measured at the inlet of the first collector and at the immediate outlet of the last collector in 4 of the 24 collector rows.

No auxiliary heating plant was located near the collector field, so the supply temperature from the solar heating plant had to be as close as possible to DH supply temperature.

Figure 2: Layout of Høje Taastrup solar collector field: blue and red lines represent supply and return pipes respectively (adapted from Arcon-Sunmark A/S).

2.2. Description of the TRNSYS model

The detailed description of the TRNSYS-Matlab model used in this study is given in [9]. The following sections summarize the main characteristics of the model, and describe the differences between the model used in this study and the original version described in [9]. A detail of the TRNSYS model is shown in Figure 3.

Unless otherwise specified, the weather data used in the simulations were taken from the Meteonorm weather data file for the location of Copenhagen-Taastrup, contained in the standard TRNSYS library [15]. A time step of 3 minutes, and convergence and integration relative tolerances of 0.001 were used in the simulations. Under these conditions one-year simulation took approximately 75 minutes for a computer with quad-core CPU, 2.4 GHz CPU frequency and 8 GB memory.

2.2.1. Temperature levels and weather conditions

The following conditions were applied for the TRNSYS model. The inlet and outlet temperature of the collector field varied depending on the return and supply temperature in the DH network. Based on the information received from the DH network operator, the following DH temperatures were used in the model. The DH return temperature was 40 °C in the winter months, from October to March (included). In the summer period from May to August (included), the DH return temperature was 50 °C. In fact, because of the lower heat demand (only domestic hot water preparation), the return temperature was not lowered as much as in winter, when also space heating was required. In April and September the DH return temperature was calculated as linear interpolation between the winter and summer temperature.

The DH supply temperature was function of the average ambient temperature. If the daily average ambient temperature was higher than 5 °C, the supply temperature was 70 °C. For ambient temperatures lower than -12 °C, the supply temperature was 90 °C. For ambient temperatures between 5 °C and -12 °C, the supply temperature was calculated by linear interpolation between 70 °C and 90 °C.

2.2.2. Control strategy

2.2.2.1. Normal operation

The actual control strategy of Høje Taastrup solar heating plant was accurately reproduced in the TRNSYS model. The main goal of the control strategy was to reach a constant outlet temperature at the end of the

forward transmission pipe. This required that the outlet temperature from the collector field was fairly constant, which was obtained by continuously regulating the flow rate to the field based on the solar irradiance measured at the site. The outlet temperature set point for the collector field was the DH supply temperature (see Section 2.2.1), increased by the temperature drop across the heat exchanger and transmission pipe. In the control strategy of the plant this temperature increase was set constant. In the model reference case, a temperature increase of 6 K was used, assuming 5 K as temperature drop across the heat exchanger and 1 K for other losses.

The main points of the control strategy can be summarized as follows. The theoretical power output from the collector field (Q_{sol}) was calculated through (Eq. 1), and was then used to regulate the primary pump flow rate $\dot{m}$ (Eq. 2).

$$Q_{sol} = A_{field}(G_{tot}\,\eta_0 - a_1 \cdot (T_m - T_{amb}) - a_2 \cdot (T_m - T_{amb})^2) \qquad \text{(Eq. 1)}$$

$$\dot{m} = \min\left[\dot{m}_{max}, \max\left[\dot{m}_{min}, Q_{sol}/\left(c_p \cdot \left(T_{setpoint} - T_{in}\right)\right)\right]\right] \qquad \text{(Eq. 2)}$$

In (Eq. 1) the temperature T_m is the mean between the measured inlet temperature to the collector field (T_{in}) and the outlet temperature set point ($T_{setpoint}$); G_{tot} is the measured solar irradiance on the collectors; $\dot{m}_{max}$ and $\dot{m}_{min}$ are the maximum and minimum flow rate the primary pump operated at.

For the primary pump to turn on, either Q_{sol} had to be higher than a certain threshold, or the temperature measured at the outlet of a collector row had to be higher than a predefined value. The pump turned off, when none of the turn-on conditions were fulfilled. In the early morning, before the start-up of the primary pump, the primary loop was relatively cold. So, a bypass (*Bypass 1* in Figure 3) was used to recirculate the fluid in the collector field without passing through the heat exchanger (pre-heating of the primary side). The bypass was closed, as soon as the outlet temperature from the collector field exceeded a predefined value. Simultaneously the secondary pump started and it was regulated so that the heat capacity rate (i.e. the product of mass flow rate and specific heat) on both sides of the heat exchanger was the same. This maximized the performance of the heat exchanger. As at the start-up of the secondary pump the water in the long transmission pipes was relatively cold, also the secondary side had a pre-heating phase, during which the water was recirculated through the bypass at the end of the transmission pipes (*Bypass 2* in Figure 3). When the fluid temperature at the end of the forward transmission pipe was sufficiently high, the secondary bypass was closed and energy was delivered to the DH network. In case that the fluid temperature at the end of the forward transmission pipe was higher than the DH supply temperature, a shunt was used to temper the temperature down, by pumping some of the cooler DH return water into the forward transmission pipe (*Shunt Pump* in Figure 3).

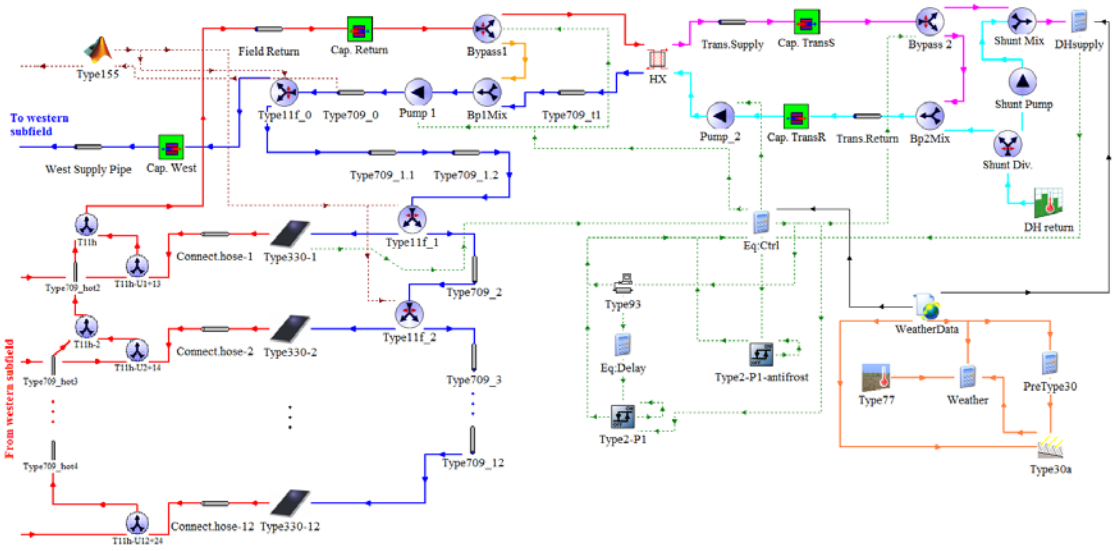

Figure 3: Detail of the TRNSYS model. For sake of clarity, only the first four collector rows of the eastern subfield are shown. Blue and red connections represent the supply and return pipes of the solar collector loop; purple and light blue connections represent the supply and the return pipes of the secondary side.

2.2.2.2. Frost protection

The 35% propylene glycol/water mixture in the solar collector loop ensured frost protection down to -16 °C [33,34]. However, in case of extended cold periods the fluid temperature in the collectors may decrease close to the freezing point. To avoid freezing in the collectors, a frost protection operation mode was implemented. The primary pump started, when any of the temperature sensors installed in the collectors fell below -12 °C, or when the ambient temperature was lower than -14 °C. In this way, the warmer fluid stored in the distribution pipes was circulated in the collector field, increasing the fluid temperature in the collectors. The pump turned off, when the temperature measured by all sensors installed in the collectors was at least -10 °C.

In case of extremely cold weather, this operation may not be able to stop the cooling of the solar collector fluid. If the fluid temperature in the collectors fell below -14 °C, the primary bypass was closed and the secondary pump started. Heat was transferred through the heat exchanger from the secondary side and the DH network to the primary side.

2.2.3. Collector model

All the components used in the model belong to well-established TRNSYS libraries [15,19,20], with the only exception of the collector Type 330. This type was developed by Bava and Furbo [9], editing the source code of Type 539 [19]. Compared to Type 539, some desired features were introduced. The main feature is that Type 330 accepts two sets of collector efficiency coefficients, one for turbulent and one for laminar flow. In each node in which the collector model is divided, either efficiency expression is used, depending on the flow regime in the node. The two efficiency expressions used in this study are shown in Table 1 and were found by Bava and Furbo [9] for the same collector and fluid type.

Table 1: Declared and simulated efficiencies of HTHEATStore 35/08 collector based on the gross area of 13.57 m^2 [9].

	Fluid	η_0 [-]	a_1 [W m^{-2} K^{-1}]	a_2 [W m^{-2} K^{-2}]
Declared efficiency [30]	water	0.757	2.199	0.007
Collector efficiency (turbulent)	35% glycol	0.756	2.318	0.006
Collector efficiency (laminar)	35% glycol	0.727	2.357	0.005

Additionally, if the incidence angle modifier (IAM) for diffuse radiation is known, this can be given as input to Type 330, instead of being internally calculated as in Type 539. Finally, the IAM-expression for beam radiation, which is linearized for angles larger than 60° in Type 539, can be used in a wider range of incidence angles, depending on which data are available in the collector test report.

2.2.4. Pipes and flow distribution

Distribution and transmission pipes were modeled through Type 709 [19]. The thermal mass of the pipe material, which may be relevant for the bigger pipes, was taken into account by Type 306 [20], which was added to the longer pipes of the plant, i.e. supply pipe to the western subfield, the common return pipe from the field and the transmission pipes.

To be able to simulate the flow distribution in the collector field, each single collector row and pipe segment were modeled. To calculate the flow distribution in the collector field, a Matlab program [31] was called every time step by Type 155 [15]. The flow distribution profile calculated by Matlab was passed to TRNSYS, which used it to distribute the total flow rate in the different collector rows.

2.2.5. Heat exchanger and pumps

Type 5b [15] was used to simulate the plate heat exchanger between primary and secondary side. The heat transfer coefficient used by Type 5b is given by (Eq. 3), determined based on measurements from the heat exchanger installed in the plant [9].

$$UA = F_f (UA)_{nom} \left(\frac{\dot{m}}{\dot{m}_{nom}}\right)^{0.6} \qquad \text{(Eq. 3)}$$

In (Eq. 3) UA_{nom} is the declared heat transfer coefficient of the heat exchanger in nominal conditions, equal to 440 kW K^{-1}; F_f is a correction factor for fouling, equal to 0.77; $\dot{m}$ is the primary flow rate across the heat exchanger and is equal to 58 m^3 h^{-1} in nominal conditions.

The primary pump was a Grundfos CR 90-2 centrifugal pump [35]. The Matlab model evaluating the flow distribution (see Section 2.2.4) also calculates the pressure drop in the primary loop. The good agreement between modeled and measured pressure drop in the system was proved by Bava et al. [31]. Combining the resulting system curve with the characteristics of the pump [35], it was verified that the electrical power of the pump followed the affinity laws for centrifugal pumps [36]. So, given the pump power at a specific point of operation ($\dot{V}_{nom}$ and $P_{el,nom}$ in (Eq. 4)), the power P_{el} for a flow rate $\dot{V}$ could be estimated through (Eq. 4):

$$P_{el} = P_{el,nom}\left(\frac{\dot{V}}{\dot{V}_{nom}}\right)^3 \qquad \text{(Eq. 4)}$$

The same assumption was made for the pump on the secondary pump.

2.3. Investigated scenarios

In the attempt of enhancing the performance of the solar heating plant, the model was used to investigate different scenarios. Firstly, a reference scenario, based on the description given in Section 2.2, was simulated. Then alternative scenarios were simulated to evaluate the impact of different improvement measures, such as variation of the temperature levels in the collector field, more accurate input to the control strategy, feedback control on the outlet temperature of the solar collector field, control strategy based on weather forecast and use of different heat transfer fluids.

When comparing the performance of the plant in different scenarios, the energy delivered to the DH network (E_{DH}) was not sufficient to describe the performance of the plant, as this parameter did not consider at which temperature the energy was delivered. So, the following energy indicators were introduced:

- $E_{DH\,2.5}$: energy delivered to DH at a temperature T_{toDH}, such that $\Delta T_{s\text{-}DH} = T_{DH,s} - T_{toDH} < 2.5$ K,
- $E_{DH\,5}$: energy delivered at a temperature T_{toDH}, such that $2.5\text{ K} < \Delta T_{s\text{-}DH} < 5$ K,
- $E_{DH,w}$: weighted energy to DH, defined as $E_{DH,w}=E_{DH}\,(1-0.008\,\Delta T_{s\text{-}DH}{}^2)$ (see Table 2). The weighted energy $E_{DH,w}$ was introduced as single parameter combining energy and temperature, so to make the comparison between different scenarios more immediate.

Table 2: Values of the factor $(1-0.008\,\Delta T_{s\text{-}DH}{}^2)$ *for different temperature differences* $\Delta T_{s\text{-}DH}$.

$\Delta T_{s\text{-}DH}$ [K]	≤0	1	2	3	4	5	7.5	10
$1-0.008\,\Delta T_{s\text{-}DH}{}^2$ [-]	1.00	0.99	0.97	0.93	0.87	0.80	0.55	0.20

3. Results and discussion

3.1. Reference case

In the reference case the yearly energy output from the collector field measured at the heat exchanger was 1.13 GWh (corresponding to 346 kWh m^{-2}), while the energy delivered to the DH was 1.08 GWh. Of this energy 85% was characterized by a $\Delta T_{s\text{-}DH}$ lower than 2.5 K, 12% had a $\Delta T_{s\text{-}DH}$ between 2.5 K and 5 K, and the remaining 3% had a $\Delta T_{s\text{-}DH}$ higher than 5 K. The energy delivered to the DH on a monthly basis is shown in Figure 4, together with the solar radiation on the collector plane. The yearly energy consumption of the pumps was 15.3 MWh, of which 11.2 MWh were absorbed by the secondary pump, 4 MWh by the primary pump and 0.1 MWh by the shunt pump. Frost protection mode without heat injection (Section 2.2.2.2) took place only 12 minutes during the entire year.

As expected, the performance of the solar heating plant was highest in summer, significantly lower in spring and autumn, and almost insignificant in winter. This was partly due to the lower solar radiation and ambient temperature during this season, but also to the higher temperature at which the collector field was operated to meet the DH temperature requirements (see Sections 2.2.1). Additionally, because the lower ambient temperatures cooled the collector field and pipes more during non-operation, more energy was required for pre-heating purposes. In the period November−February the monthly collected radiation during pre-heating represented between 16% (February) and 78% (December) of the total radiation collected during operation of the primary pump. In summer this fraction was about 3%−6%.

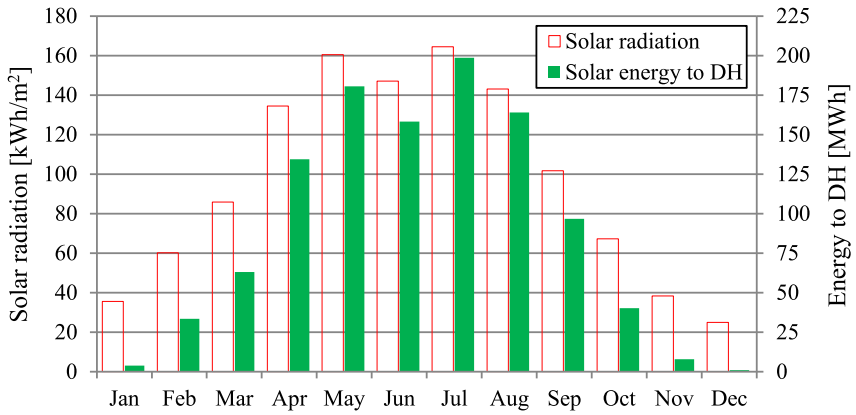

Figure 4: Monthly solar radiation on the collector plane (left axis) and solar energy delivered to the DH network (right axis) in the reference case.

As in winter the heat demand is highest, it would be beneficial to improve the performance of the collector field in this period, as addressed in Section 3.2.

3.2. Lower outlet temperature set points

In the attempt of increasing the performance of the collector field in winter, an upper boundary for the outlet temperature set point for the collector field was imposed (see (Eq. 5)) and progressively decreased in Cases 1−3.

$$T_{setpoint} = \min(T_{setpoint,max}, T_{DH,s}+5\ \text{K}+1\ \text{K}) \qquad \text{(Eq. 5)}$$

Doing so, the temperature at which energy was supplied to the DH network did not meet the DH temperature requirements any longer. However, as the solar fraction of the system was very small in winter, the DH network was assumed to be able to compensate the lower temperature fluid supplied by the solar heating plant.

The energy delivered to the DH during winter in the different scenarios, while progressively decreasing the maximum set point temperature, is listed in Table 3 (Cases 1−3; Case 7 is later described in Section 3.3). The lowest maximum set point considered was 76 °C, which was the same set point as in summer.

Table 3: Energy delivered to the DH in winter (November−March). For the reference case absolute values are reported; for the other cases, the relative variations from the reference case are listed.

	E_{DH}	$E_{DH,w}$	$E_{DH\ 2.5}$	$E_{DH\ 5}$	
Reference case	109.0	87.4	32.5	47.1	MWh
Case 1: $T_{setpoint,max}$=85 °C	+0.1%	-3.6%	-0.2%	-0.3%	%
Case 2: $T_{setpoint,max}$=80 °C	+0.3%	-10%	-3.0%	-16%	%
Case 3: $T_{setpoint,max}$=76 °C	+0.6%	-24%	-24%	-38%	%
Case 7: $T_{setpoint,max}$=80 °C	-1.0%	+12%	+164%	-79%	%

As seen from Table 3, decreasing the set point temperature (Cases 1−3) did not have a significant impact on the energy delivered to the DH during winter (only +0.6% in Case 3). On the other hand, because of the lower set point, the amount of energy delivered at temperatures close to the DH supply temperature decreased significantly. Hence, lowering the set point temperature in winter to improve the efficiency of the collector field did not bring significant advantages in terms of performance. The pumping energy was roughly the same as in the reference scenario.

3.3. Accurate inputs to the control strategy

The control strategy (Section 2.2.2.1) assumed that the solar irradiance measured by the pyranometers was the same as that received by the collectors. However, this was not strictly true, because the pyranometers were installed on top of the collectors, so they did not experience shadows from other collector rows. This difference may become particularly relevant in winter, when the solar altitude is low and the shadow effect from row to row can be significant. In summer, when the sun is higher on the horizon, there may not be

shading of the beam radiation, but partial shading of the diffuse radiation still occurs. Another simplification in the control strategy was to neglect the IAM of the collectors when calculating Q_{sol} (Eq. 1). Finally, a constant temperature drop across the heat exchanger was assumed (see Section 2.2.2.1 and (Eq. 5)), while this could be better evaluated through (Eq. 6), based on the characteristics of the heat exchanger [37].

$$T_{setpoint} = \frac{T_{DH,s} - T_{DH,r} \cdot (1-\varepsilon)}{\varepsilon} \qquad \text{(Eq. 6)}$$

In (Eq. 6) $T_{DH,s}$ and $T_{DH,r}$ are the supply and return temperature in the DH network, while ε is the effectiveness of the heat exchanger, defined by (Eq. 7) [37]:

$$\varepsilon = \left(\frac{UA}{\dot{m}\, c_p}\right) \Big/ \left(1 + \frac{UA}{\dot{m}\, c_p}\right) \qquad \text{(Eq. 7)}$$

The product $(\dot{m}\, c_p)$ is the lowest between the two products on the two sides of the heat exchanger. As the heat capacity rates in the primary and secondary loop were identical (see Section 2.2.2.1), either can be used in (Eq. 7).

Using the same maximum set point temperature of 80 °C as in Case 2, different scenarios were investigated, where the inputs to the control strategy were progressively made more representative of the actual conditions of the plant. More specifically the following scenarios were considered:

- Case 4: same as Case 2, but with $T_{setpoint}$ chosen as minimum value between 80 °C and the value returned by (Eq. 6).
- Case 5: same as Case 2, but in the definition of Q_{sol} (Eq. 1) the peak collector efficiency was decreased by the IAM for beam radiation, as calculated from the collector test report [30].
- Case 6: same as Case 2, but in the definition of Q_{sol} the total shaded radiation on the collector plane (as calculated by the TRNSYS shadow mask Type 30) was used.
- Case 7: $T_{setpoint}$ was calculated as in Case 4, and the total shaded radiation (as in Case 6) and the IAM (distinguishing beam and diffuse components) were used to calculate Q_{sol}.

Table 4 presents the yearly energy delivered to the DH network and the electricity consumption of the pumps in the above mentioned scenarios. The outlet temperature from the collector field in the different cases is shown in Figure 5 for the day June 7. In this day Cases 2, 5 and 6 used an outlet temperature set point of 76 °C (Eq. 5), while Cases 4 and 7 used 74.3 °C (Eq. 6).

Table 4: Yearly energy delivered to the DH and electricity consumption of the pumps. The percentage variations $\%\Delta E_{DH,w}$ and $\%\Delta E_{el}$ are calculated with respect to Case 2.

	E_{DH} [GWh]	$E_{DH,w}$ [GWh]	$\%\Delta E_{DH,w}$ [%]	$E_{DH\,2.5}$ [GWh]	$E_{DH\,5}$ [GWh]	E_{el} [MWh]	$\%\Delta E_{el}$ [%]
Case 2	1.08	1.04	-	0.92	0.11	15.4	-
Case 4	1.08	1.02	-1.1%	0.89	0.15	17.5	+12%
Case 5	1.07	1.04	+0.1%	0.94	0.09	14.5	-6%
Case 6	1.07	1.06	+2.0%	1.03	0.03	12.0	-28%
Case 7	1.08	1.07	+2.8%	1.05	0.01	12.6	-22%

Comparing Case 4 and Case 2, it is noted that the energy delivered to DH at the appropriate temperature decreased (see $E_{DH,w}$ and $E_{DH\,2.5}$ in Table 4), although the energy to DH (E_{DH}) was approximately constant. This was due to the lower $T_{setpoint}$ in Case 4 (74.3 °C) compared to Case 2 (76 °C). As in both scenarios the control strategy used the unshaded irradiance to determine the primary flow rate, while the collector field received the shaded irradiance, the higher $T_{setpoint}$ in Case 2 partially compensated this mismatch in irradiance and made the solar heating plant deliver energy at higher temperatures, closer to the DH supply temperature, as seen in Figure 5. This resulted in higher values of $E_{DH,w}$ and $E_{DH\,2.5}$. Other consequences of the lower set point in Case 4 were the higher flow rates (both on primary and secondary side) and so higher pumping energy.

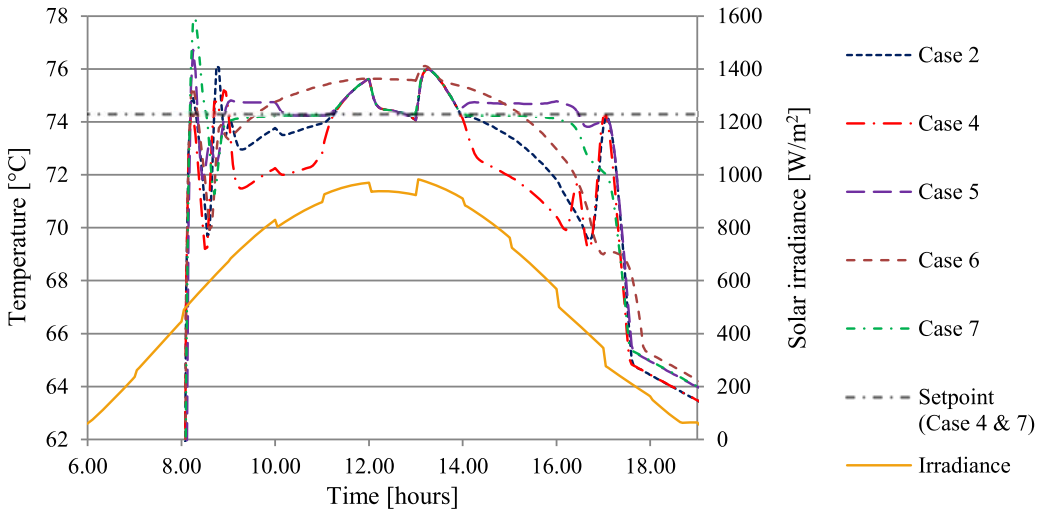

Figure 5: Outlet temperature from the collector field (Cases 2 and 4−7) and solar irradiance on the collector plane on June 7th.

In Case 5 the introduction of the IAM in the definition of Q_{sol} resulted in a lower flow rate to the collector field, especially in early morning and late afternoon, when the incidence angle was larger. This achieved a more constant outlet temperature during the day, as seen in Figure 5. Due to the higher average temperature in the collector field, the collector efficiency decreases compared to Case 2, resulting in a lower E_{DH}. However, as energy was delivered to DH at temperatures closer to the DH requirements, slightly higher $E_{DH,w}$ and $E_{DH\,2.5}$ were achieved. The lower flow rates entailed lower pumping energy too.

In Case 6 the use of the shaded radiation in the control strategy had the same effect of lowering Q_{sol} as in Case 5. However, the effect was more important, as shading effect played a more significant role than the IAM. So the weighted energy to DH ($E_{DH,w}$) increased by 2% and the pumping energy decreased by 28% compared to Case 2 on a yearly basis (Table 4).

Finally, in Case 7 the close agreement between the inputs to the control strategy and the conditions in which the plant operated resulted in an improved performance, with +2.8% in weighted energy to DH and -22% in pumping energy. Using shaded irradiance and IAM decreased in particular the pumping energy in the preheating phase (by 70%−80%), because of both lower power (due to lower flow rates) and shorter duration. The performance of the solar heating plant was especially increased in winter, when shadows and IAM played a more important role, as seen in Table 3 by comparing case 7 with the other scenarios. Figure 5 shows that the improved control strategy maintained the field outlet temperature fairly constant and very close to the set point.

From Figure 5 it can also be noted that in all scenarios the field outlet temperature exceeded the set point, when the solar irradiance was highest (around 12:00 and 13:30). In these periods the calculated flow rate based on Q_{sol} was higher than the maximum flow that the primary pump could supply (see Eq. 2). Hence, a slight overheating of the collector fluid could not be avoided.

Of the measures introduced in Cases 4−7, the use of a variable outlet temperature set point (Eq. 6) and the introduction of IAM for beam radiation can be easily implemented in real world, simply adding a few lines of code in the control algorithm of the plant. On the other hand, taking into account the shadow effect is less straightforward, as it would require additional measuring equipment to evaluate the diffuse and beam components of the solar radiation, as well as appropriate correlations to evaluate the shadow effect from row to row.

3.4. Feedback control on the field outlet temperature

From (Eqs. 1−2) it is noted that the outlet temperature set point was used to regulate the primary pump, while the actual outlet temperature did not affect the control strategy during normal operation. This open-loop control guaranteed good operation, as long as the measured data and the collector efficiency parameters used in the control strategy were close to the actual conditions at which the plant operated. However, if the inputs to the control strategy differ from the actual conditions (e.g., the pyranometers underestimate the actual

irradiance), a disagreement between field outlet temperature and set point can be expected.

To make the control more robust, a PID feedback control on the field outlet temperature was added (Type 23 [15]). If the outlet temperature differed from the set point, the control signal from the PID controller (u in (Eqs. 8−9)) was used to correct the flow rate $\dot{m}$ calculated by (Eq. 2).

$$\dot{m}_{corrected} = \dot{m} \cdot (1 + u) \quad \text{(Eq. 8)}$$

$$u = K\left(\Delta T_{set-out} + \frac{1}{T_i}\int \Delta T_{set-out}\, dt + T_d \frac{d(\Delta T_{set-out})}{dt}\right) \quad \text{(Eq. 9)}$$

The effect of the PID control when applied to Case 4 (see Section 3.3) was investigated in Case 4.1, to see whether this type of control could compensate the low accuracy of the inputs given to the control strategy. Additionally, two other scenarios (Cases 8 and 8.1) were investigated, where the irradiance value used for control purposes was assumed to be 10% lower than the actual irradiance on the collector field. In fact, silicon cell pyranometers, often used in solar collector field applications, are known to decrease their sensitivity over time [9]. The only difference between the two scenarios was that Case 8.1 implemented the PID controller.

Table 5 lists the yearly energy delivered to the DH network and the electricity consumption of the pumps in the above mentioned scenarios. The outlet temperature from the collector field in the different cases is shown in Figure 6 for the day June 7.

Table 5: Yearly energy delivered to the DH network and electricity consumption of the pumps with and without PID control on the field outlet temperature. The percentage variations $\%\Delta E_{DH,w}$ and $\%\Delta E_{el}$ of the Case 4.1 and 8.1 are calculated with respect to Case 4 and 8 respectively.

	E_{DH} [GWh]	$E_{DH,w}$ [GWh]	$\%\Delta E_{DH,w}$ [%]	$E_{DH\,2.5}$ [GWh]	$E_{DH\,5}$ [GWh]	E_{el} [MWh]	$\%\Delta E_{el}$ [%]
Case 4	1.08	1.02	-	0.89	0.15	17.5	-
Case 4.1	1.08	1.06	+3.9%	1.05	0.02	12.8	-27%
Case 8	1.05	1.04	-	1.03	0.01	10.3	-
Case 8.1	1.07	1.06	+1.9%	1.05	0.01	12.6	+22%

In Case 4.1 the feedback control compensated the overestimation of the solar irradiance in the control strategy. In fact, in the definition of Q_{sol} in Case 4 neither IAM nor shadows from row to row were considered. As the field outlet temperature in Case 4.1 was higher than in Case 4, the collector efficiency decreased and so did the energy delivered to the DH network E_{DH}. However, as this energy was at a temperature closer to the DH supply temperature, both $E_{DH,w}$ and $E_{DH\,2.5}$ increased. Additionally, the pumping energy decreased by 27% in Case 4.1 compared to Case 4, because to reach a higher temperature rise across the collector field, the flow rates had to decrease.

It can be seen that the energy indicators in Case 4.1 (in Table 5) were very similar to those in Case 7 (in Table 4). Also the outlet temperature profiles in the two cases were close to each other (see Figure 5 and Figure 6). This suggested that the integration of feedback control on the outlet field temperature had the same effect as providing accurate input parameters to the control strategy (Section 3.3). The distinction between beam and diffuse radiation, as well as the calculation of the shadow effect, can be easily performed in a simulation program like TRNSYS, but they are more demanding to achieve in real world, as they require additional equipment compared to a single pyranometer measuring the total radiation. Additionally the correlations used to estimate shading from row to row are likely to entail some degree of error. For these reasons, the integration of a PID controller to correct the primary flow rate seemed a more robust and economical solution. Because the PID control is a feedback control without any direct knowledge of the regulated system, it may show a poor behavior if used alone to regulate processes with long and/or variable time delays. This is why the solar heating plant was still mainly regulated by the feed-forward control (Eqs. 1−2), which relied on the actual physics of the plant, while the PID controller was introduced for minor corrections.

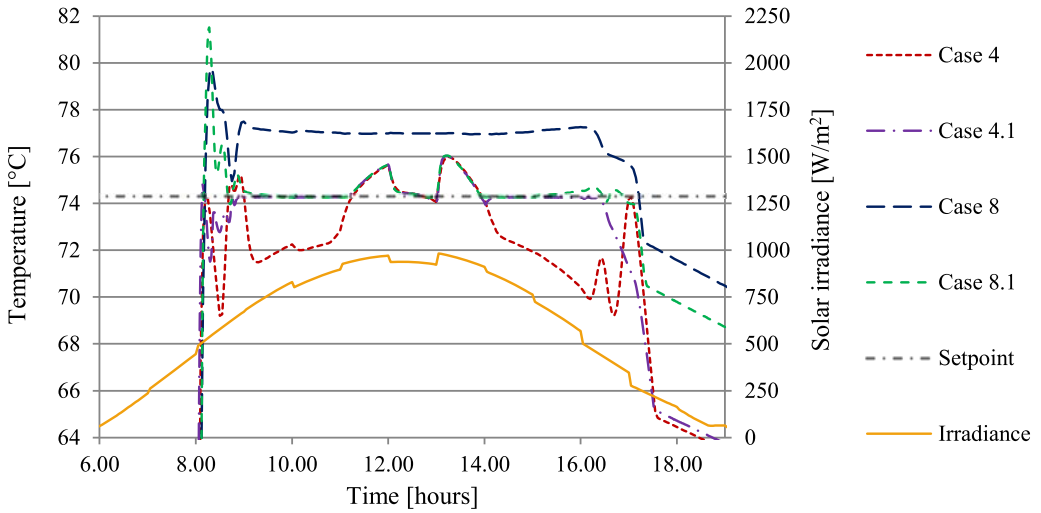

Figure 6: Outlet temperature from the collector field (Cases 4, 4.1, 8 and 8.1) and solar irradiance on the collector plane on June 7th.

In Case 8 the underestimation of the solar irradiance led to field outlet temperatures higher than the set point (see Figure 6). This penalized the collector efficiency, reducing the energy output of the collector field (Table 5). The addition of the PID control in Case 8.1 improved the plant performance by 1.6%. However, the higher flow rate required to avoid overheating of the solar collector fluid led to an increase of the pumping energy by 22%.

3.5. Control strategy and weather forecast

Assuming that the weather conditions at the plant location could be accurately forecast (for example using an all-sky camera), different scenarios were simulated, implementing weather forecast in the control strategy. In the model weather conditions were forecast simply reading in advance the weather data from the weather data file.

Two types of weather forecast were implemented: a short-term and a long-term forecast. In the short-term forecast, the weather conditions expected to occur in the next future (20 s, 30 s and 60 s ahead) were used to calculate Q_{sol} and anticipate the regulation of the primary pump, in the attempt of obtaining a more constant outlet temperature from the collector field in case of fluctuating irradiance.

In the long-term forecast, the upcoming weather conditions were used to predict the future energy output from the collector field. The condition (Eq. 10) was added to the start-up requirements of the primary pump (see Section 2.2.2.1). This condition required that the weather conditions over the future time interval Δt were at least sufficient for the operation of the collector field at the lowest flow rate and at nominal temperatures. Values of 15, 30 and 60 minutes were used as Δt.

$$\int_t^{t+\Delta t} Q_{sol}\, dt \geq \dot{m}_{min}\, c_p \left(T_{setpoint} - T_{in}\right) \Delta t \quad \text{(Eq. 10)}$$

This condition was added to avoid useless start-up and preheating of the plant, when the upcoming weather conditions would not allow normal operation for a minimum period of time.

As weather data from the Meteonorm data file in TRNSYS were interpolations of hourly values, they did not present fast fluctuations in solar irradiance, which were needed to evaluate the impact of the above mentioned control strategies. Hence, these simulations used measured data from Høje Taastrup plant [9] for an overall period of 20 days with different sky conditions (moving clouds, clear and overcast sky). Instantaneous values of total and diffuse irradiance on the collector plane, as well as ambient temperature, were available with 1 minute time step. Data sets with smaller time steps were created by interpolation of the measured data.

Neither approach led to relevant improvements in performance. In the short-term forecast the energy output from the collector field decreased slightly (-0.9% in the worst scenario) and the outlet temperature profile was not more constant in days with intermittent irradiance. The long-term forecast avoided the start-up of the plant in days characterized by mainly cloudy conditions with few and short sunny moments. However, the

effect over the entire period was irrelevant. The electricity consumption of the pumps was reduced by 0.1%, but the energy output from the collector field decreased by 0.3%.

3.6. Fluid types

As higher concentrations of glycol entail poorer fluid properties in terms of specific heat and heat transfer as well as higher pumping power, lower concentrations may be preferable. However, mixtures with lower concentrations have higher freezing points, so the plant may run in frost protection mode more often (Section 2.2.2.2), requiring additional pumping energy and heat injection from the DH network. To identify the best compromise between fluid properties and frost protection, scenarios using different fluids in the primary loop were simulated and their results were compared to Case 7, which used a 35% glycol/water mixture. More specifically, water and a 22% propylene glycol/water mixture were considered. The 22% glycol/water mixture was chosen for its freezing point of -8 °C [33,34], which reduced by 93% the number of hours of frost protection operation compared to the scenario using water (Figure 7).

The TRNSYS models using water and the 22% propylene glycol/water mixture differed from Case 7 in terms of collector efficiencies, which were calculated for the new fluids, according to what described in Section 2.2.3 and in [9]; characteristics of the primary pump for the new fluids (see Section 2.2.5) and fluid properties. Frost protection operated as described in Section 2.2.2.2, but its temperature set points were modified so that the differences between set points and freezing temperature of the new fluids were the same as for the 35% glycol/water mixture.

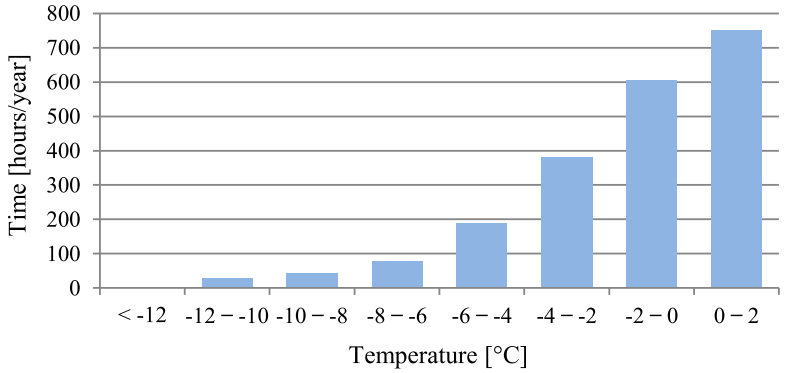

Figure 7: Frequency diagram of ambient temperatures below 2 °C in Høje Taastrup during the design reference year [15].

A summary of the results in terms of energy transferred between the solar heating plant and DH network, as well as electricity consumption of the pumps, is given in Table 6. Compared to a 35% propylene glycol/water mixture, the use of water and a 22% glycol/water mixture increased the energy output of the plant by 2.2% and 0.8%. The better thermophysical properties of the fluids improved the collector efficiency and decreased the pressure drop across the primary loop. This entailed a higher maximum flow rate of the primary pump, which reduced and/or avoided overheating of collector fluid above the set point temperature, especially in summer. However, the better thermal performance of the plant was outweighed by the energy required by the frost protection operation. This was especially true when using water, as 0.08 GWh were injected into the collector field in winter, in the face of an extra production of 0.02 GWh (mainly in spring-summer). Not only the net balance was negative, but as the DH heat demand is much higher in winter than in summer, the trade-off was disadvantageous. In case of the 22% glycol/water mixture this net balance was positive, but negligible.

Table 6: Yearly energy exchanged between solar heating plant and DH network, and electricity consumption of the pumps. The percentage variations $\%\Delta E_{DH,w}$ and $\%\Delta E_{el}$ are calculated with respect to Case 7.

	E_{DH} [GWh]	$E_{DH,w}$ [GWh]	$\%\Delta E_{DH,w}$ [%]	E_{frost} [GWh]	E_{el} [MWh]	$\%\Delta E_{el}$ [%]
Case 7 (35% glycol)	1.08	1.07	-	0	12.6	-
Case 9 (water)	1.10	1.09	+2.2%	0.08	13.4	+6%
Case 10 (22% glycol)	1.08	1.07	+0.8%	0.01	13.1	+4%

Additionally, the electricity consumption of the pumps increased. In fact, although the lower viscosities of water and 22% glycol/water mixture reduced the pumping energy in the primary loop by 0.5 MWh and 0.3 MWh respectively, the higher flow rate which could be supplied by the primary pump and the matched flow between primary and secondary pump increased the pumping energy on the secondary side (+1.1 MWh and +0.8 MWh respectively). Furthermore, the pumps ran more often for frost protection purposes (+0.2 MWh and +24 kWh respectively). The higher pumping energy was caused by the specific equipment and location of Høje Taastrup plant. If the collector field lay close to the DH network, and the primary pump could supply any flow rate expected by the control strategy (Eqs. 1−2) regardless of the fluid type, the electricity consumption of the secondary pump would be less significant and the use of fluids with lower viscosity would decrease the total pumping energy.

The limited increase in energy output from the plant did not seem to justify the higher risk of freezing connected to the use of fluids with lower glycol concentrations, unless this entailed some other clear advantages, which may include lower cost of the fluid, less maintenance and reduced risk of corrosion.

5. Conclusions

A detailed TRNSYS-Matlab model, which had been previously validated, was used to simulate the behavior and thermal performance of a solar heating plant for DH application in different scenarios. Based on the simulation results, the following conclusions can be drawn.

- The inputs to the control strategy should be as representative of the actual conditions of the plant as possible. For example, the measured solar irradiance should be corrected to take into account shadows from row to row as well as the IAM, before being used for control purposes.
- Lowering the set point temperature in winter improved the plant performance, only if more accurate IAM and shadows from row to row were considered.
- Feedback control on the field outlet temperature improved the performance of the plant, when the inputs to the control strategy differed from the actual operating conditions. Hence, this can be a valid alternative to more accurate input to the control strategy.
- Control strategies implementing weather forecast did not show significant improvements, which may justify the additional cost and complexity of the control system.
- Glycol/water mixtures minimizing or completely avoiding frost protection operation seemed to be preferable to mixtures with lower concentrations. The enhanced thermophysical properties of the latter barely compensated the additional energy required for frost protection.

6. Acknowledgements

The authors are thankful to the Marie-Curie Actions - Initial Training Network research programme of the European Union which supported the first author through the SolNet-SHINE project. The authors are also grateful to the company Arcon-Sunmark A/S and the DH company Høje Taastrup Fjernvarme for providing useful information to carry out this study.

7. References

[1] Gynther L, Lappillone B, Pollier K. Energy efficiency trends and policies in the household and tertiary sectors. An analysis based on the ODYSSEE and MURE databases. 2015.

[2] AEBIOM. EU Handbook - District Heating Markets 2012. http://www.crossborderbioenergy.eu/fileadmin/crossborder/DH_MarketHandbook.pdf (accessed December 13, 2016).

[3] Dalenbäck J-O, Werner S. Solar District Heating: Boundary Conditions and Market Obstacles 2012. http://www.solar-district-heating.eu/Documents.aspx (accessed December 13, 2016).

[4] Schubert M, Holter C, Soell R. Solar District Heating (SDH): Technologies used in large scale SDH plants in Graz – Operational experiences and further developments. Proc. 12th Int. Symp. Dist. Heat.

Cool., Tallinn, Estonia: 2010, p. 140–2.

[5] Mauthner F, Weiss W, Spörk-Dür M. Solar Heat Worldwide: Markets and Contribution to the Energy Supply 2014 2016. http://www.iea-shc.org/data/sites/1/publications/Solar-Heat-Worldwide-2016.pdf (accessed December 13, 2016).

[6] Trier D. Personal communication with D. Trier (PlanEnergi) 2016.

[7] Wittrup S. Verdens største solfangeranlæg i drift i Silkeborg. Ingeniøren 2017.

[8] Perers B, Furbo S. IEA-SHC Tech Sheet 45.A.4 Simulation of Large Collector Fields 2014. http://task45.iea-shc.org/fact-sheets (accessed December 13, 2016).

[9] Bava F, Furbo S. Development and validation of a detailed TRNSYS-Matlab model for large solar collector fields for district heating applications. Draft submitted to *Energy* journal, 2017.

[10] Le Denn A. Solar District Heating Guidelines: Calculation tools and methods 2014. http://solar-district-heating.eu (accessed December 13, 2016).

[11] Nielsen JE, Battisti R. Solar District Heating Guidelines: Feasibility study 2012. http://solar-district-heating.eu (accessed December 13, 2016).

[12] PlanEnergi. Fjernsol II 2013. http://www.solarkey.dk/fjernsol.htm (accessed March 30, 2017).

[13] Deschaintre L. Development of a solar district heating online calculation tool. Energy Procedia 2014;48:1065–75. doi:10.1016/j.egypro.2014.02.121.

[14] CIT Energy Management. Sunstore4 Tool 2013. http://sunstore4.eu/use-results/sunstore4-tool/ (accessed December 13, 2016).

[15] Klein SA, et al. TRNSYS 17 A Transient System Simulation program. Solar Energy Laboratory, University of Wisconsin-Madison; 2012.

[16] EMD International A/S. energyPRO 2016. http://www.emd.dk/energypro/ (accessed December 13, 2016).

[17] Vela Solaris. Polysun Simulation Software 2016. http://www.velasolaris.com/ (accessed March 30, 2017).

[18] Natural Resources Canada. RETScreen 2016. http://www.nrcan.gc.ca/energy/software-tools/7465 (accessed December 13, 2016).

[19] TESS. TESSLibs 17 Component Libraries for the TRNSYS Simulation Environment. 2012.

[20] Schwarzbözl P. A TRNSYS Model Library for Solar Thermal Electric Components (STEC). Reference Manual. 2007.

[21] Saleem MS, Haider A, Abas N. Review of Solar Thermal Water Heater simulations using TRNSYS. 2nd Int. Conf. Power Gener. Syst. Renew. Energy Technol. PGSRET 2015, 2015, p. 68–73. doi:10.1109/PGSRET.2015.7312251.

[22] Abdel Dayem AM, Nabil Metwally M, Alghamdi AS, Marzouk EM. Numerical simulation and experimental validation of integrated solar combined power plant. Energy Procedia 2014;50:290–305. doi:10.1016/j.egypro.2014.06.036.

[23] Biencinto M, Bayón R, Rojas E, González L. Simulation and assessment of operation strategies for solar thermal power plants with a thermocline storage tank. Sol Energy 2014;103:456–72. doi:10.1016/j.solener.2014.02.037.

[24] Biencinto M, González L, Valenzuela L. A quasi-dynamic simulation model for direct steam generation in parabolic troughs using TRNSYS. Appl Energy 2016;161:133–42. doi:10.1016/j.apenergy.2015.10.001.

[25] Bava F, Furbo S, Perers B. Simulation of a Solar Collector Array Consisting of two Types of Solar Collectors, with and Without Convection Barrier. Energy Procedia 2015;70:4–12. doi:10.1016/j.egypro.2015.02.091.

[26] Raab S, Mangold D, Müller-Steinhagen H. Validation of a computer model for solar assisted district heating systems with seasonal hot water heat store. Sol Energy 2005;79:531–43. doi:10.1016/j.solener.2004.10.014.

[27] Sibbitt B, McClenahan D, Djebbar R, Thornton J, Wong B, Carriere J, et al. The performance of a high solar fraction seasonal storage district heating system - Five years of operation. Energy Procedia 2012;30:856–65. doi:10.1016/j.egypro.2012.11.097.

[28] Hausner R, Fechner H. Influence of the flow condition (laminar/turbulent) in the fluid tube on the collector efficiency factor of a fin absorber. Proc. EuroSun 1998 Conf., Portoroz, Slovenia: 1998.

[29] Bava F, Furbo S. Comparative test of two large solar collectors for solar field application. Proc. EuroSun 2014 Conf., Aix-Les-Bains, France: 2014. doi:doi:10.18086/eurosun.2014.16.03.

[30] SP. Solar Keymark Certificate HTHEATstore 35/08 No. SP SC0843-14. Borås, Sweden: 2016.

[31] Bava F, Dragsted J, Furbo S. A numerical model to evaluate the flow distribution in large solar collector fields in different operating conditions. Sol Energy 2017;143:31–42. doi:10.1016/j.solener.2016.12.029.

[32] SolData. SolData 80spc Pyranometer - Data and application notes 2016. http://www.soldata.dk/pyr-80spc.htm (accessed March 30, 2017).

[33] Conde M. Thermophysical properties of brines – Models, Conde Engineering. Zurich (Switzerland): 2011.

[34] DOW. Engineering and Operating Guide for DOWFROST and DOWFROST HD Inhibited Propylene Glycol-based Heat Transfer Fluids. 2008.

[35] Grundfos. CR 90-2 A-F-A-E-HQQE - 96124077 2017. https://product-selection.grundfos.com (accessed January 27, 2017).

[36] Gülich JF. Centrifugal pumps. 2nd ed. Springer; 2010.

[37] Cengel YA, Ghajar AJ. Heat and Mass Transfer: Fundamentals and Applications. 5th ed. McGraw-Hill; 2015.

One day two men in their 30s bumped into each other, while hurrying up along the street. Noah halted, a bit annoyed by the distracted guy. But his annoyance turned into a surprised smile, when he recognized Ethan.
They had used to be very good friends in school, but had lost contact when moving away for university. They had not seen each other since then.
Glad for the unexpected reunion, they disregarded their agendas and went for a coffee.
After so many years they had a lot to catch up with: university time, current and past jobs, family, maybe acquaintances from the old days they were still in contact with...
While wondering how fast time runs away and how things can change so rapidly without actually changing at all, Ethan asked:

"Last time we were together, we were carefree teenager... now look at us! Grown-up responsible adults... How did that happen? When do you think you became a man?"

Noah pondered for a short while.

"...hum,
...maybe it was when I moved from my parents' house for university...
no, I think when I got my first real job and that check at the end of the month...
wait! When I got married to Erika; that must be it! ...
...or maybe when Elli was born... I don't know...
What about you? When do you think you became a man?"

After thinking about it for a moment, Ethan said:

"When I was a child, my father used to wake me up early on Sundays and we would go to see the sunrise from the pier. I remember that when the sun emerged completely from the horizon and the sunrays stung my eyes, my father would stand in front of me, shielding me from the light. My father's figure appeared impressive from there. Taut and solid, with shoulders wide enough to cover the entire sun, and light pouring around his body profile.
One day of late autumn, when I was about 25, I went back to visit my parents. On Sunday morning my father and I headed toward the pier. Dad was merely the shadow of his former self. His body curved and weak now. His skin loose, no longer filled by the former musculature.
The wind was brisk, when the sun started rising. My dad's eyes blurred and feeble. I saw them struggling against the strength of the morning light. So I stepped in front of him, my shadow shrouding his figure. I felt a light weight when he leaned on my back for support. Then, I feel, was when I became a man."

In the last years Denmark has seen a rapid increase in the number and size of solar collector fields for district heating application. As this trend is expected to continue, it is important to identify which factors affect the plant performance. If correct sizing, control and design are evaluated in advance and implemented in the planning phase, later and more expensive interventions can be avoided. This can be done by means of detailed simulation models, which have been the focus of this PhD study. Based on the results, guidelines on how to model and plan a solar heating plant were given.

DTU Civil Engineering
Technical University of Denmark

Brovej, Bygning 118
2800 Kongens Lyngby

www.byg.dtu.dk

ISBN 9788778774590
ISSN 1601-2917